ABSTRACT

Title of dissertation: CFD/Quasi-Steady Coupled Trim Analysis of *Diptera*-type Flapping Wing MAV in Steady Flight

Dissertation directed by: Dr. James D. Baeder, Department of Aerospace Engineering

The nuances in flapping wing aerodynamics are not yet fully understood to the extent where concepts can be translated to practical designs. Trimmed flight is a fundamental concept for aircraft in general. It describes the flight condition when there are no accelerations on the vehicle. From an engineering perspective, trim estimation is essential for performance analysis and flapping wing vehicle design. Without an efficient trim algorithm, trial-and-error based identification of the trimmed wing kinematics is computationally expensive for any flight condition, because the large number of simulations required make the process impractical. In a global sense the nature of forces produced by flapping wings closely resemble those on a helicopter blade, such that an analogy can be drawn between the two. Therefore, techniques developed for helicopter performance calculations are adapted and applied to the flapping wing platform particularly for analyzing steady flight.

Using a flight dynamic model of the insect, which comes embedded with simplified quasi-steady wing aerodynamics and is coupled to high-fidelity CFD analysis, trim solutions are obtained

in realistic time frames. This procedure is analogous to rotorcraft periodic coupling for trim. This multi-fidelity approach, where many quasi-steady calculations are combined with a judicious number of CFD simulations, may be used in parametric sweeps and design studies to improve hover and cruise performance.

It was shown that the coupled trim methodology based on the QS model is capable of driving the CFD towards a stable trim solution. In forward flight the trim procedure tilts the stroke plane resulting in lift generation during downstroke and propulsive force during upstroke. The airloads, thrust and power are affected by the trim parameters, and the CFD/QS methodology accurately accounted for these inter-dependencies. Also it is observed that power initially decreases as an insect goes from hover to forward flight. Furthermore, the lift-to-power ratio versus average lift was identified as a principal efficiency metric to assess the performance of flapping-wing vehicles for a given geometry and kinematic parameters.

CFD/Quasi-Steady Coupled Trim Analysis of *Diptera*-type Flapping Wing MAV in Steady Flight

by

Camli Badrya

Dissertation submitted to the Faculty of the Graduate School of the
University of Maryland, College Park in partial fulfillment
of the requirements for the degree of
Doctor of Philosophy
2016

Advisory Committee:

Professor James D. Baeder, Chair/Advisor
Professor Inderjit Chopra
Assistant Professor Anya R. Jones
Professor James Duncan
Professor Amir Riaz, Dean's Representative

Dedication

To the loving memory of my grandfather, Suliman Badrya (1936 - 2016).

Acknowledgments

Undertaking this PhD degree has been a truly life-changing experience. It would not have been possible to complete without the support and guidance I received from many people. First, I would like to express my deepest gratitude for my adviser, Professor James D. Baeder, for believing in me when I doubted myself. I still remember the first time I stepped through his office door. Back then, I didn't imagine that I would spend countless hours in his office learning the most significant lessons in my academic and professional life. Without his guidance, patience and positive encouragement, this PhD would not have been achieved. I'm honored to be his PhD student and grateful for the opportunity he has given me to grow as a research scientist.

Many thanks to my committee members Dr. Inderjit Chopra, Dr. Anya Jones, Dr. James Dancan and Dr. Amir Riaz for guiding me along the way with their most valuable insights. Thank you for being an outstanding committee! I could not have asked for a better members advising on my thesis. Especial thanks go to Dr. Bharath Govindarajan and Dr. Ananth Sridharan that helped and advised on this study. Much appreciation and thanks to the professors, staff and students of the department of Aerospace engineering for making my graduate experience pleasant and memorable. I am fond of the memories and experience I have had at UMD.

I was incredibly honored to be awarded a Fulbright Scholarship in 2011, to pursue my Master degree in the United States. Receiving a Fulbright Award opens many doors and provides educational and global networking opportunities.

I would like to acknowledge and thank the funder and sponsors for my Phd research and education: the Micro Autonomous Systems and Collaborative Technology Alliance MAST CTA.

I gratefully appreciate the support received through the collaborative work undertaken with the Army Lab water tank, especially Dr. Christopher M. Kroninger and Aaron Harrington, for providing this study with the experimental data. Also, thanks go out to Kenneth MacFarlane and Dr. J. Sean Humbert, University of Maryland, for providing the quasi-steady aerodynamic solver used in this study.

There are not enough words to describe my appreciation, admiration and gratitude to my parents, Roda and Alam Eldin Badrya. They have always stood by me throughout this journey with patience, care, compassion and unconditional love, always believing in me. My parents are the light guiding me on my path. I hope they will find some comfort and relief in knowing that because of them, I find the strength inside me to be a better person. I would like to express my special thanks and appreciation to Vivian and Norman Belmonte, for being generous, inspiring, kind and loving, for opening their home and hearts, treating me as one of their daughters and a member of their family. I'm so fortunate to have you in my life.

This thesis is dedicated to the memory of my beloved grandfather, whose role in my life was and continues to be immense. Every time we talked, you asked me when I would finish my studies, and I always answered soon. This past April you left us earlier than expected, and I want you to know I completed my studies, and I wish you were here to see that. Thank you grandpa for your unlimited love and support! I will always hold your memory and your beautiful smile in my heart for the rest of my life.

Finally I would like to thank my dear family and friends in Israel and United States who shared this journey with me, for their support and encouragement. To them, I owe my successes.

Table of Contents

List of Tables

List of Figures

Nomenclature

a_∞	Speed of sound
AR	Wing aspect ratio, AR$= b/\bar{c}$
b	Wing span
$\bar{c}$	Wing mean chord, $\bar{c} = S/b$
CG	Center of Gravity
C_T	Rotor thrust coefficient, $= T/\rho A\Omega^2 R^2$
f	Wing flap frequency, Hz
$\mathbf{F}$	External forces acting at the insect body
$\overline{F}_x$	Stroke-averaged wing aerodynamic force along the body longitudinal axis
$\overline{F}_z$	Stroke-averaged wing aerodynamic force in the z direction
$\overline{M}_y$	Aerodynamic pitching moment about CG
$\mathbf{g}$	Acceleration under gravity
$\mathbf{I}$	Inertia tensor
L	Characteristic length
m	Insect body mass
M_∞	Mach number
$\mathbf{M}$	Moments acting at the insect body CG
p, q, r	Rigid-body angular velocity components along body-fixed axes, rad/s
r_f	Reduced frequency
Re	Reynolds number

S	Wing area
u, v, w	Rigid-body velocity components along body-fixed axes, m/sec
x, y, z	Inertial coordinate system

Greek Symbols

α	Angle of attack
α_g	Wing geometric angle of incidence or pitch angle, (degrees)
β	Stroke plane tilt angle, degrees
γ	ratio of specific heats, 1.4 (air)
λ_i	Non-dimensional inflow velocity, $= v_i/\Omega R$
μ	Dynamic viscosity coefficient
ν	Kinematic viscosity coefficient
ρ	Flow density
ρ_∞	Free-strem density
Θ_{B}	Body pitch attitude, degrees
ϕ	Flap stroke azimuth, degrees
ϕ_{max}	Maximum stroke amplitude, half peak-to-peak,, (degrees)
ϕ_{off}	Flap stroke bias, degrees
Φ_{B}	Body roll attitude, degrees
ψ_B	Heading Euler angle

$\dot{\psi}_B$	Rate of turn, rad/s
ω	Body angular velocity vector
Ω	Angular velocity of blade rotation

List of Abbreviations

2D	Tow dimensional
3D	Three dimensional
CFD	Computational Fluid Dynamics
CRWENO	Compact-Reconstruction Weighted Es- sentially Non-Oscillatory
MUSCL	Monotonic Upstream-Centered Scheme
CPU	Central Processing Unit
GPU	Graphics Processing Unit
QS	Quasi-Steady
Re	Reynolds number
LEV	Leading Edge Vortex
MAV	Micro Air Vehicle

Chapter 1

Introduction

Insect flight has evolved over millions of years, enabling them to perform very advanced flight profiles. Insects are capable of a wide range of flight modes such as hover, forward flight, climb, descent, inverted flight, and perching on a variety of surfaces. This ability to simultaneously demonstrate superior maneuvering capability and sustained hover/cruise is of great practical interest for small-scale aerial platforms operating in confined locations. In the last two decades, an increased interest in bio-inspired flying platforms has given rise to a new class of small, highly maneuverable and hover-capable aircraft called Micro Air Vehicles (MAVs). While flapping-wing configurations offer several advantages over rotary-wing VTOL platforms at millimeter scales, the aerodynamics and design are more complex. Flapping wing kinematics are difficult to untangle into independent parameters, and at small scales the flowfield around these wings is both highly viscous and unsteady. Research over more than three decades has contributed much to understanding the aerodynamic basis of insect flight. However, although progress has been made toward establishing the principles underlying the design of insect wings, trimmed and controlled insect-like MAVs have not yet achieved. The tools developed should provide the MAVs designers with an accurate model for the steady and unsteady flow features that a flapping-wing vehicle encounters while it is in flight. Some of the challenges in the design of a flapping wing MAV are:

1. Flight efficiency in terms of lift-to-drag ratio at the low Reynolds numbers ($O(10^3)$) at which these MAVs operate.

2. Understanding the aerodynamic phenomena that occur on a flapping wing with insect-like kinematics.

3. The development of mathematical models and tools for aircraft design.

1.1 Motivation

Trim refers to a steady flight condition in which the translational and rotational accelerations are zero (sometimes termed "equilibrium of forces and moments"). Therefore, trim includes hover, steady level flight, steady climbing forward flight, steady level turn and steady climbing/descending turns of constant radii. Trim for a fixed-wing aircraft is defined as a steady flight condition in which the control settings, orientations and velocity of the vehicle produce forces and moments (inertial and aerodynamic) that exactly cancel out external forces (gravity), allowing the aircraft to remain in its state of uniform motion"indefinitely". The force distributions on a fixed-wing aircraft are fairly steady in nature, and so the loads, during trim, at any two instants in time will be near-identical. In contrast, the loads generated by a flapping wing are not steady. The presence of wing flapping motion requires a modification to the traditional definition of aircraft trim.

Trim analysis is important to find the trim variables and kinematics. As well, trim is needful to compare the performance of various flapping wing configurations at the same initial state is to identify the best flapping-wing MAV platform for a given mission profile. Such performance

comparisons must be made for a given flight condition, usually steady forward flight. Trim analysis can be used to determine the: a) operational envelope (max speed and max payload), b) flight performance (minimum power required), and c) the initial state for stability analysis. A rigorous trim analysis is a great design tool as it accounts for all the cross coupling between airloads and wing kinematics. Trim and power estimation are essential for performance analysis and flapping wing vehicle design.

Trim analysis has received minimal attention in literature. To determine the kinematics for steady flight, a trial-and-error based approach to adjust the wing kinematics to achieve vertical force equilibrium in hover was used, which was insufficient for other steady flight modes (i.e.: steady level flight). The other approach was used is trim analysis based on a reduced aerodynamic model (quasi-steady or blade element), which concerns with insufficient fidelity. Trim analysis based high-fidelity CFD approach, where properties of the entire flowfield and the time-resolved aerodynamic forces calculated with high accuracy, it incurs significant computational cost. Further, to compare various flapping wing platforms from an engineering perspective, the forces produced by the wing must be consistent with a given flight condition. Therefore, the kinematics may need to be readjusted during the CFD simulations to maintain force and moment balance. An efficient trim algorithm can reduce these runtimes significantly without compromising the accuracy of the solutions is essential. To obtain accurate airloads and trim kinematics, a high-fidelity flowfield model is required, which must be coupled to the trim process. Till date, an efficient framework incorporating a trim process coupled to a CFD model for a flapping wing vehicle is not in the literature. The present work seeks to address this deficiency.

Sun [12] noted that the nature of forces produced by flapping wings closely resembles those on a helicopter blade. While Sun refers to the aerodynamic and inertial loads in the context of stability analysis, this analogy — between a flapping wing vehicle and a helicopter — readily lends itself to the estimation of performance in steady flight for a flapping wing MAV by conducting trim analysis. In the current work techniques developed for helicopter performance calculation [13, 14] are adapted and applied to the flapping wing MAV platform to obtain CFD-coupled trim solutions.

In the present work, a flight dynamic model was developed, including an embedded quasi-steady aerodynamics model. This model provides qualitative trends that describe the coupling between wing kinematics and associated loads, but it does not capture unsteady aerodynamic effects due to shed vortices, a key phenomenon in flapping wing flight [5]. A higher-fidelity aerodynamic model is necessary to obtain accurate airloads; so a CFD analysis is used to obtain accurate aerodynamic loads on the wings. However, coupling the two models (trim and CFD) directly is computationally intensive. This dissertation outlines a methodology to achieve computationally efficient CFD-coupled trim solutions for a flapping wing platform at various forward flight speeds, drawing analogies and adapting techniques from helicopter dynamics. This work aims to provide an efficient algorithm to analyze trimmed flight of flapping-wing MAV and to reduce the analysis runtimes significantly without compromising the accuracy of the solutions.

Chapter 2

Background

Initial MAV design requirements were defined in 1997 by the US Defense Advanced Research Projects Agency (DARPA), through a program called “MAV - project” [15]. MAVs design requirements are: a) Small, where no dimension exceeds 15 cm (6 inches); b) Lightweight, where the gross take-off weight (GTOW) is less than 100 grams; c) Capable of a loiter time at least 60 minutes; and d) Capable of carrying at least 20 grams of payload. Later, in 2005 [16], DARPA announced Table. 2.1 summarizes the MAV requirements [17].

The need behind developing these vehicles is driven by civilian, research, commercial and military purposes. For military needs, MAVs can be used for intelligence, surveillance, and reconnaissance (ISR) missions; and for civilian purposes. Therefore, capabilities such as high maneuver, sustained hover and efficient cruise are very essential for small-scale platforms operating within confined environments in additional to DARPA sizing requirements.The following section discusses briefly the state of art of MAVs, reviewing the current candidates for this application along with technical challenges and opportunities.

Although in the last ten years progress has been made in this field, DARPA sizing requirements are still considered a great challenge to satisfy. There is no current vehicle with the maximum dimension less than 15 cm, that has an endurance of 60 minutes, and is capable of hovering with a GTOW less than 100 grams and payload of 20 grams. Figure 2.1 shows the capabilities of

Table 2.1: MAV design requirements [1]

Specification	Requirements	Details
Size	< 15.24 cm	Maximum dimension
Weight	100 g	Objective GTOW
Range	1 to 10 km	Operational range
Endurance	60 min	Loiter time on station
Altitude	< 150 m	Operational ceiling
Speed	15 m/s	Maximum flight speed
Payload	20 g	Mission dependent
Cost	\$1500	Maximum cost

current MAVs. The poor performance and efficiency of MAV systems arise from:

1. Lack of comprehensive understanding of aerodynamic mechanism at low Reynolds numbers ($\leq 4 \times 10^4$) [1].
2. Dearth of an appropriate mathematical model that represents all the flow physics.
3. Dearth of appropriate design tools for this class of miniature vehicles.
4. The limited existing technologies does not address the requirements of MAV design.

Assumptions and simplifications applied to the design of a full-scale flying vehicle (fixed and rotary wing) do not translate into this very relatively small scales.

Research on MAV platform design has been carried out along multiple fronts, and can be divided roughly into three main categories:

1. Fixed-wing MAVs
2. Rotary-wing MAVs
3. Bio-inspired flapping-wing MAVs

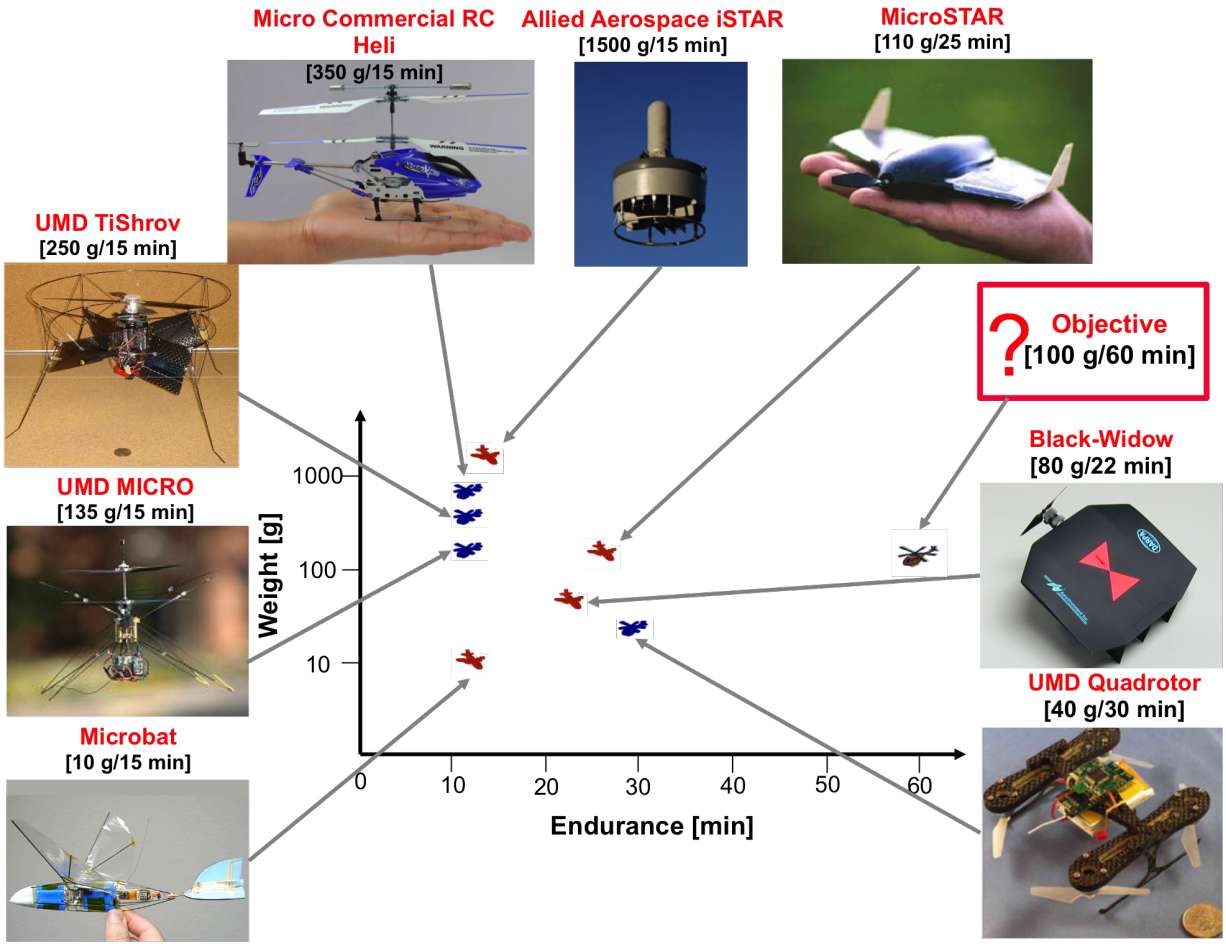

Figure 2.1: Endurance or hover time of early MAVs (2008) [2].

2.1 MAVs: State of the Art

The fixed-wing MAV configuration offers many advantages over other configurations. First, these systems are less complex in terms of aeromechanics, control; and design in comparison to other configurations. Second, in terms of performance, fixed-wing configurations have high lift-to-drag (L/D) ratios and are longitudinal stable. Many light-weight fixed wing MAVs have been developed, but have not met the sizing criteria defined by DARPA (i.e., less than 15 cm in dimension).A couple of more recent representative systems that were designed, based on fixed wings, for increased endurance are shown in Fig. 2.1. The AeroVironment WASP [18] micro UAV "flying wing" developed as a follow on the Black-Widow [18], set a new world record for MAVs endurance of one hour and 47 minutes. The Mosquito Micro UAV, developed by Israel Aerospace Industries, has a saucer (double ellipse) shaped plane and can carry a payload of a video camera [19]. The wing span, weight and endurance for several vehicles are given in Table 2.2.

Table 2.2: Fixed-wing MAVs key specifications

MAV Name	Wing span [cm]	Weight [grams]	Endurance [min]
AeroVironment Black-Widow	15.24	80	30
AeroVironment WASP	32	430	107
Lockheed MicroSTAR	60	110	25
Mosquito Micro UAV	30	250	40

Despite the advantages of a higher L/D ratio and relatively long endurance, fixed-wing MAVs suffer from major a disadvantage. These platforms are incapable of hovering, which makes them capable of many potential MAV missions, both indoors and outdoors. The important requirement that a MAV be capable of sustaining hover leads to the next type of MAV design: rotary-wing MAVs.

(a) Lockheed Martin MicroSTAR (b) Israel Aerospace Ind. Mosquito MAV

Figure 2.2: More recent fixed-wing MAVs.

The most significant advantage of rotating wing MAVs is their ability to hover. Rotary-wing MAVs represent the bulk of the vehicles that have been developed for MAV applications. A variety of vehicles have been designed successfully with traditional rotor configurations, such as:

1. Single main rotor, for example Micro RC helicopter
2. Coaxial rotors, for example the UMD MICRO MAV
3. Shrouded rotors configuration, such as the UMD TiShrov [20]
4. Quadrotor configuration, such as the Stanford's Mesicopter [21] and the UMD quadrotor.

Current rotary-wing MAVs have Reynolds numbers $O(10^4 - 10^5)$ due to the relatively high rotational speed of the blades. These systems show promising progress toward achieving DARPA's MAV requirements in term of weight, dimensions, and performance. Research on optimizing the rotor design to improve performance, especially in hover, has been carried out; but the 60 minutes endurance requirement is still a great technological challenge. The design of rotating-wing MAVs requires an understanding of the physics and the flow behavior at the lower MAV-scale Reynolds

numbers as compared to their full-scale counterparts. Aerodynamic principles for full scale rotary-wing vehicles at high Reynolds numbers do not always apply to small scale rotary-wing MAVs.

A few non-traditional rotary-wing designs have been studied as well. The University of Maryland developed successfully a class of flying vehicles based on the non-traditional rotary concept called Cyclocopter [22]. Some of the representative vehicles of a rotating-wing MAV are shown in Fig. 2.3. Table 2.3 presents key specifications of some the rotor-wing MAVs mentioned above.

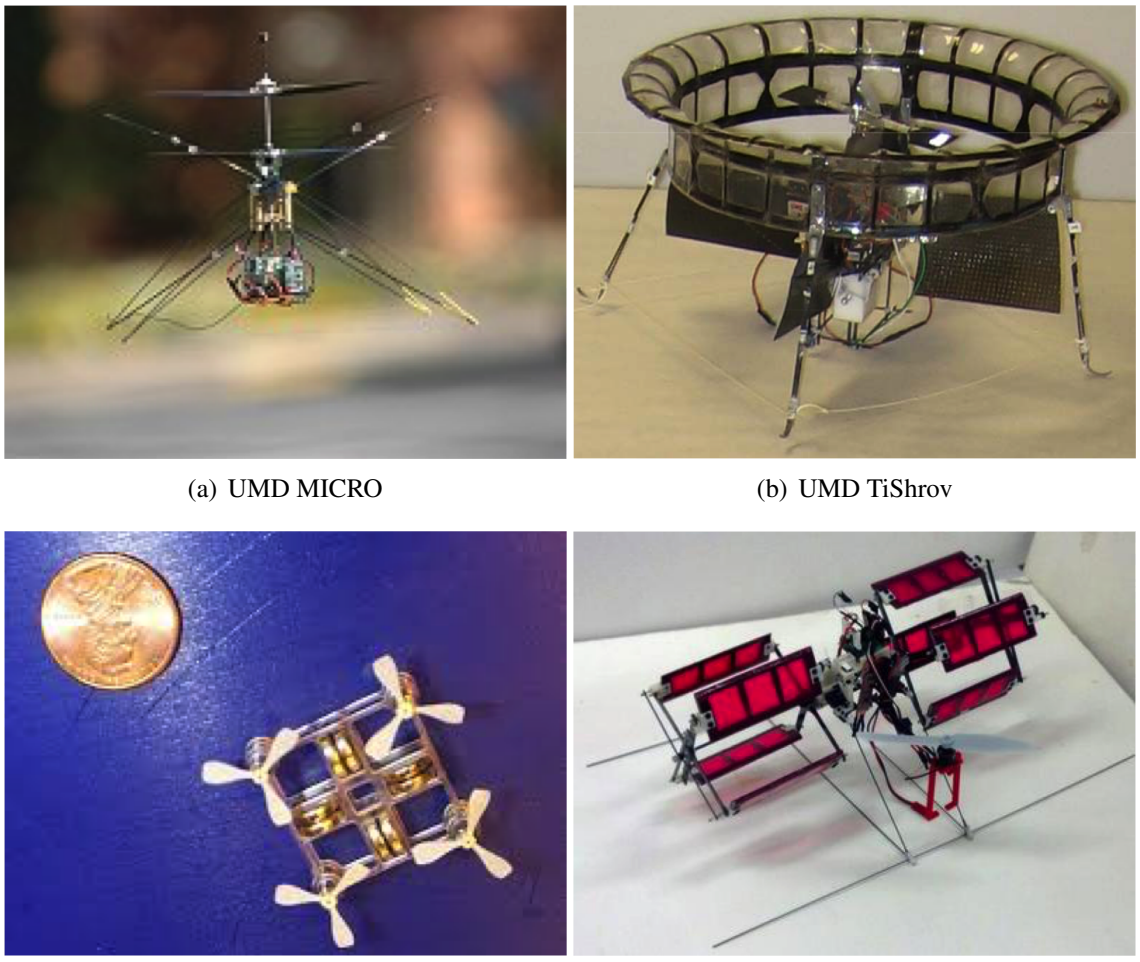

(a) UMD MICRO (b) UMD TiShrov

(c) Stanford Mesicopter (d) UMD Cyclocopter

Figure 2.3: Rotary-wing MAVs.

Table 2.3: Rotary-wing MAVs key specifications

MAV Name	Rotor	Weight [grams]	Hover endurance [min]
UMD MICRO	2 bladed teetering	135	20
UMD TiShrov	25 cm rotor dia.	230	8
UMD Cyclocopter	2 contra-rotating 3 bladed rotors	287	40
UMD MICRO Quadrotor	4 2-bladed rotors	45	31

Current technology has not produced a high performance MAV vehicle, but nature is full of very small, high performance fliers such as insects and birds. For very small vehicles, insect-inspired wing kinematics may lead to a viable MAV design.

Flapping-wing based MAVs are divided into two types, avian and insect-like kinematics as shown in Fig. 2.4. In the first type, Avian flappers or ornithopters (Fig. 2.4(a)), the flapping kinematics are similar to those of a birds' flight, where the flapping-stroke is perpendicular to the travel direction, the change in angle of incidence (defined as the angle between the wing chord and the flapping stroke) is relatively small, and the flapping frequency is low (order of magnitude of 10 Hz) [4]. Representative examples for avian flappers are the Microbat (Fig. 2.5(a)) developed by Caltech labs, DelFly (Fig. 2.5(b)) that has been developed at Delft University and the Lilienthal ornithopter studied at the University of Maryland. The ornithopter is not capable of hovering like insect or rotary-wing MAV, which is considered a barrier for MAVs application as previously discussed.

The second type are the insect-based flappers, where the kinematics are similar to insects; flapping stroke is not necessarily perpendicular to the the travel direction (Fig. 2.4(a)), and unlike for Avian kinematics the change in angle of incidence (pitch angle) is large and the flapping frequency is high (order of magnitude of 100 Hz [4]). Representative examples of insect-based MAV

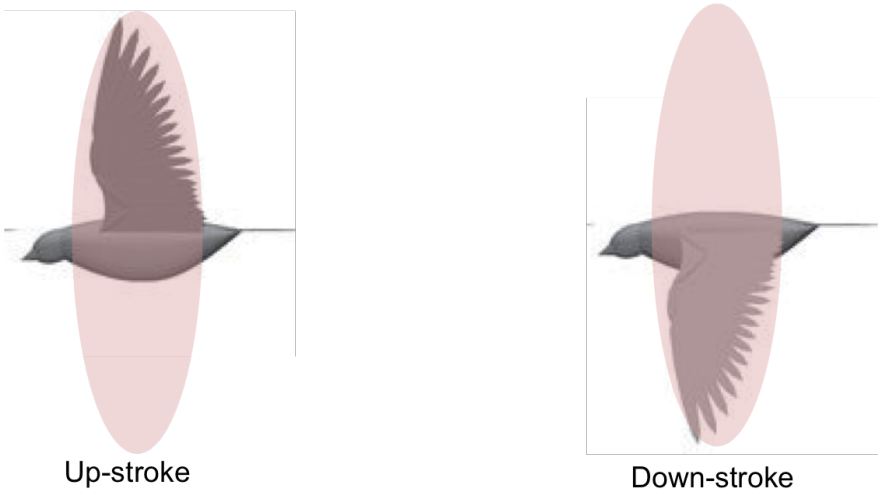

(a) Avian Stroke

(b) Insect Stroke

Figure 2.4: Avian and insect stroke, the shaded area represents the flapping stroke path.

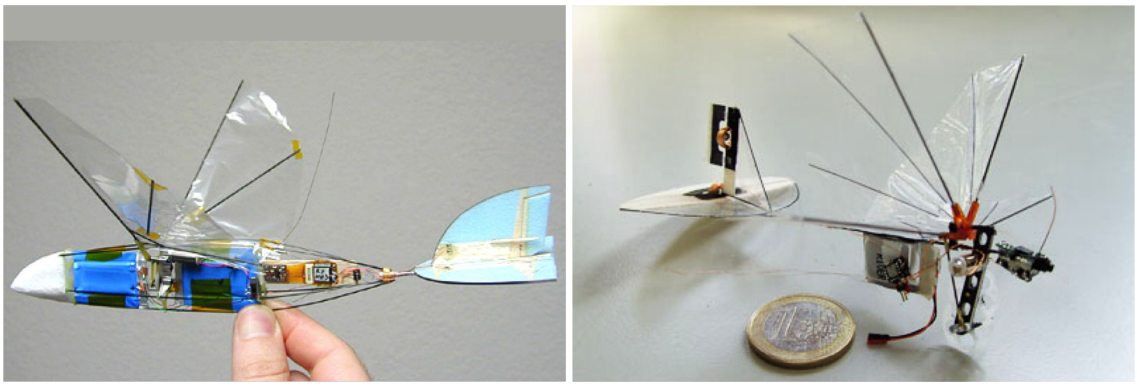

(a) Microbat, Caltech

(b) DelFly, Delft University

Figure 2.5: Avian flappers or Ornithopters.

are the AeroVironment Hummingbird (Hummingbirds fly more like insects than birds) (Fig. 2.6(a)). The Hummingbird is equipped with a small video camera for surveillance and reconnaissance purposes and for now operates in the air for up to 11 minutes, with the ability to operate both indoors and outdoors.

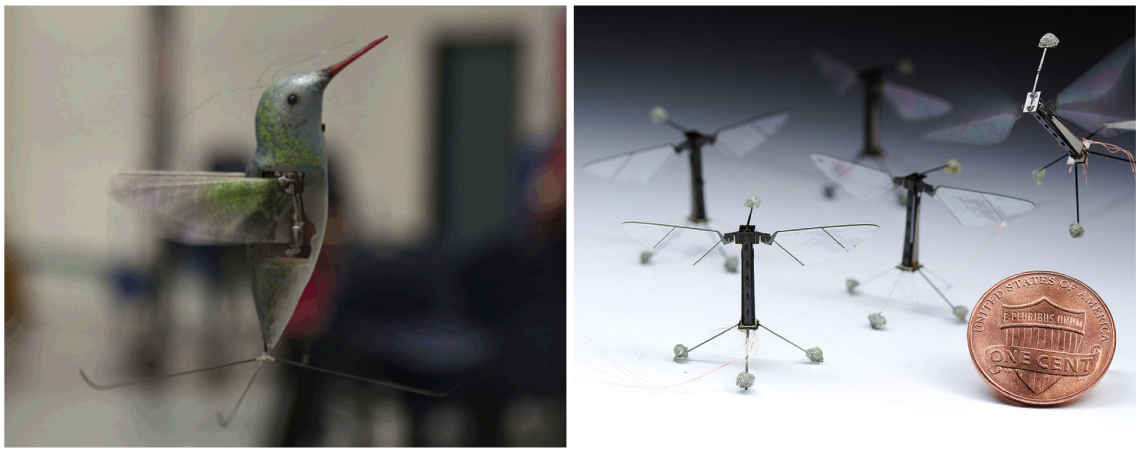

(a) Hummingbird, AeroVironment (b) Insect flapper, Harvard University

Figure 2.6: Insect flappers or Entomopters.

Despite the progress that has been achieved, a fully functional insect-based MAV seems to be a difficult goal to achieve at this point in time. Currently, there are many related projects undergoing research; perhaps the most notable development in this area comes from the Harvard University Microrobotics lab which has developed a bio-inspired robot with insect kinematics and geometric features with a weight of 80 mg, wing span of 3 mm, and wingbeat frequency of 120 Hz. This flapper was able to demonstrate a controlled vertical flight in hover (Fig. 2.6(b)), but only for a very short time [23].

Insect flight is very complex and the flowfield around the wings is highly viscous and unsteady. Despite these challenges, in order to develop a MAV that flies efficiently and has high

performance, the bio-inspired option should be considered. The challenges and technical barriers related to flapping-wing MAVs will be discussed in the next section.

2.2 Flapping-Wing MAVs: Challenges and Technical Barriers

The performance of current MAVs is vastly inferior to that of birds and insects in nature, with no flapping-wing vehicle able to achieve controlled flight for more than a few minutes. Yet, significant potential may be found in bio-inspired flapping-wing designs.

MAV design faces many unique challenges and obstacles that must be overcome to develop an efficient flapping-wing MAV platform. Of these, two are of particular interest in the current work.

1. **Aerodynamics at low Reynolds numbers**: At low Reynolds numbers, viscous effects are dominant compared to inertial forces. Significant viscous flow results in a large shear boundary layer (BL) that can causes high skin friction drag. Complex flow phenomena can take place within the BL, such as flow separation, transition, and reattachment. This type of flow morphology often results in early flow separation and stall. One of the parameters that characterizes airfoil aerodynamic efficiency is the lift-to-drag (L/D) ratio. L/D is a non-linear function of Reynolds number, as droping significantly with decreasing Re shown in Fig. 2.7. L/D depends not just on the flow conditions around the wing but also on its geometry (i.e. aspect ratio, wing shape) and surface roughness.

   Insects operate in a very sensitive low Reynolds numbers regime, and the physics of flight here is not completely clear, which raise a challenge for air vehicle design. For flapping-wing

design it is critical to develop analytical tools, computational models, and better understand experimental wind-tunnel and flight test data. The tools developed should provide the MAVs designers with an accurate model for the steady and unsteady flow features that a flapping-wing vehicle encounters while it is in flight. The development of an aerodynamic theory of flapping-wing flight and appropriate vehicle design tools for this low Reynolds regime are critical for the evolution of MAV technology.

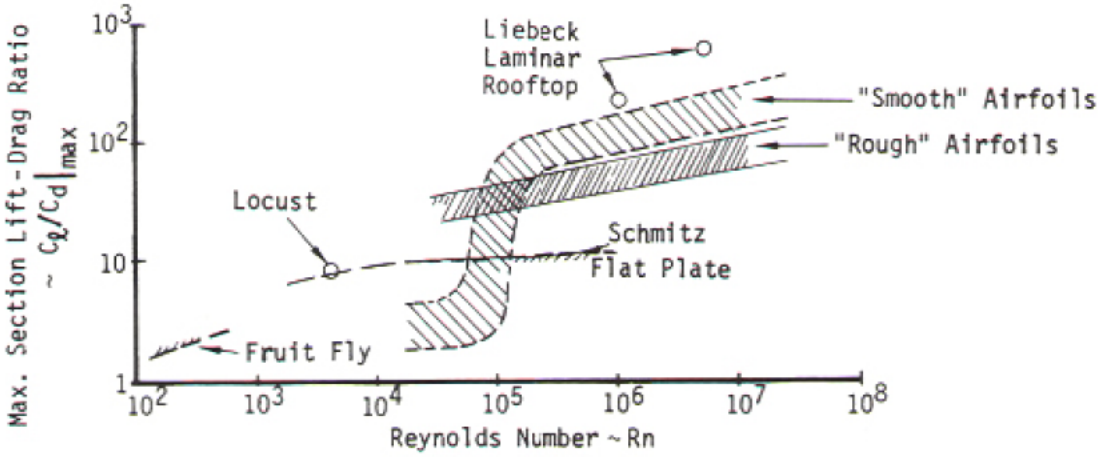

Figure 2.7: Maximum sectional lift-to-drag ratio versus Reynolds number for smooth and rough airfoils (McMasters and Henderson [3]).

2. **Wing geometry, kinematics and structure**: Insect wings have a low aspect ratio with order magnitude of $O(1)$. For example, a fruit fly wing has an aspect ratio of 2.4, and a hawk-moth wing has an aspect ratio of 5.3 [4]). The low aspect ratio emphasizes the effect of the tip vortices on the flow field and the forces generated. Another challenge encountered in flapping-wing flight is the level of unsteadiness in both the wing kinematics and the aerodynamic flow field. Insects flap their wings at high frequencies ($O(10-100)$), which results in

production of a strong vortical structure in the flow and large unsteady inertial forces that, in turn, result in large deformations in the wing structure [4].

From nature it appears that insects benefit from the flexibility of their wings. The role of insect wing flexibility has been identified in the literature [24], particularly in the context of flight efficiency, power, and stability and control. For biologically inspired flapping-wing MAVs, these mechanical, material and structure requirements should therefore be addressed. Development of a framework for large-strain comprehensive analysis of wing morphing and active shape deformation remains an active research topic [2].

The objective of this dissertation relates to insect-based flapping wing flight aerodynamics, and therefore the literature survey will mostly focus on topics related to insect flapping wings in the following sections.

2.3 Insect Flapping Wing Physical Phenomena

After three decades of research to understand and analyze insect flight, it is clear that insects rely on the production of unsteady forces to fly and maneuver. The unsteadiness here is related to two aspects:

1) Unsteady kinematics: Insect kinematics is complex, and can be performed by either two wings (i.e., fruitfully, bumblebee, hawkmoth) or four wings (dragonfly). Insects flap their wings at high frequency and high pitch angles; while the flapping configuration various for different insect species (i.e., figure of 8). Figure 2.8 describes the two-wing (*Diptera*) insect stroke, that can be divided into four motions: translational upstroke and downstroke along with supination and

pronation at the end of each of the translational strokes.

2) Unsteady forces: The nature of the forces produced by flapping wings are unsteady instantaneous (changing with time) forces. Therefore, steady-state aerodynamics theory can not be applied to explain all of the forces produced by flapping wings [25–27].

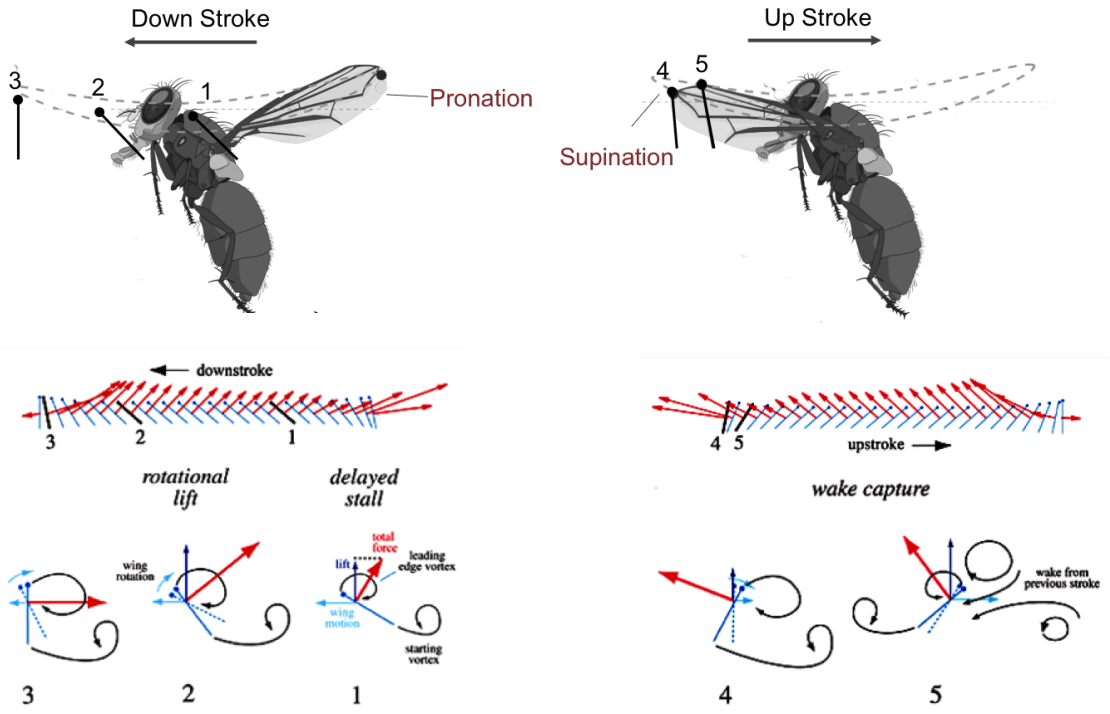

(a) Insect flapping stroke during downstroke (b) Insect flapping stroke during downstrok

Figure 2.8: Insect flapping stroke divided into four motions: 1) Downstroke (translational) 2) Upstroke (translational) 3) Pronations and 4) Supination. Blue arrows indicate the direction of wing movement and red arrows the direction and magnitude of the forces generated in the stroke plane, and the associated forces production mechanism [4, 5].

2.3.1 Flapping Wing Aerodynamics - Hover

Prior experimental and computational studies identified several unsteady flow phenomena that enable the production of sustained lift. The relevant conclusions from prior work are briefly

summarized in this section. Much of the earlier work in insect flight aimed to understand the force production mechanism in flapping wings; with most of this work performed in hover. From what has been observed, the force production mechanisms of insect during hovering flight can be classified into four major categories:

1. **Delayed Stall**, that is due to the leading edge vortex (LEV) : As the wing increases its angle of attack, the flow over the wing tends to separate, especially in the case of thin airfoil (similar to insect's wings) separation that occurs near the leading edge. However, the flow reattaches before it reaches the trailing edge. In such cases, a leading edge vortex (LEV) forms on the upper surface of the wing. Because the flow reattaches, the fluid continues to flow smoothly from the trailing edge and the Kutta condition is maintained. The presence of the attached leading edge vortex produces very high lift coefficients, a phenomenon termed "delayed stall". Delayed stall in insect flight was observed by Maxworthy (1979), who visualized the leading edge vortex on the model of a flying wing.

   The formation of a leading edge vortex (LEV) during the flapping flight, from the root of the wing to the tip as described in Fig. 2.9(a) is a common feature in insects flight [27–30]. The formation of the LEV is suggested to be because of dynamic stall mechanisms [5, 27, 28, 31], where a LEV is formed in the case of a rotational wing at high angle of attack. The attached bound vortex on the leading edge during wing translation enhances the lift [27, 32]. The LEV results in a low pressure area, which results in a large suction on the upper surface. This LEV has found to be stable during the flapping stroke, which means that it remains attached to the wing upper surface during the translational periods. The vortex can

maintain lift enhancement for 3 – 4 chords length of wing travel, before the LEV breakdown occurs at the end of the stroke. The reason contributing to the stability of the LEV remain partially unclear, but it was observed that for relatively higher Reynolds numbers (Re-5000, Hawkmoth, *Manduca sexta* [27, 33]) the LEV has a spiral structure (spanwise axial flow velocity), suggesting that this span-wise flow from root to the tip of the wing, allows the energy to be drained, and limits the LEV growth and delay its shedding. The LEV separated at approximately 75% of the wing span, forming a large tip vortex. But, for relatively lower Reynolds number (Re-120, fruitfly [5]), it was shown by Birch and Dickinson that the LEV remains stable, with weak span-wise flow at the vortex core, and no separation from the wing suggesting that the induced downwash from the tip and wake vorticity limited the LEV's growth by lowering the effective angle of attack, and delaying its shedding. Later work by Ansari et. al. [34] also showed that the spiral structure is more significant for higher Reynolds numbers (Re-500 to15,000). Also the strength of the LEV depends on Reynolds numbers [4], where the LEV strength increases with increasing Reynolds numbers [4, 34], and the separation point from the upper surface occurs at 60% span for Reynolds 6000, and the feature of stable LEV remains; the vortex didn't breakdown during the translation.

2. **Rapid Pitch-Up** or Rotational lift: [5,35] The LEV is a major source of lift enhancement for insect flight during the translational portions of the flap stroke. In addition, the rapid rotation of the wing at the end of the upstroke and downstroke (pronation and supination, Fig. 2.8) also results in lift generation. Kramer [36] was first to show that a wing rotating from low to high angles of attack results in a lift coefficient above the steady-stall value, known as the

"Kramer effect". The rotation effect in a flapping wing was investigated experimentally by Dickinson et al. [5, 6], and computationally by Sun and Tang [37]. Sun and Tang suggested that the vorticity associated with rapid pitch-up rotation results in lift enhancement. Sane and Dickinson [6] explained it as reestablishing the Kutta condition due to the change of the pitch angle during the rotation. Pitch-up rotation is influenced by the kinematics of the flapping wing.

3. **Wake capture**: Dickinson et al. [5, 6] observed from the experimental data of the Robofly, in hover that is shown in Fig. 2.9(b), two lift peaks (enhancement) were identified: The first due to the rotational forces (explained above) and the second as due to wake capture [5, 38]. This lift enhancement occurs when the wing starts the reversal motion at the end of each half-stroke (upstroke or downstroke). During this time the wing interacts with the previous flow field that consists of the trailed and shed vortices due to the supination/pronation, which results with transferring momentum from the flow to the wing, and generating additional lift. In other words, the wing is capable of extracting energy from the wake. The wake capture mechanism was observed also for normal-hovering [39, 40] while being absent in water-treading [40]. Indicating that the wake capture mechanism, similarly to rapid pitch-up, is affected by the kinematics.

4. **Clap and fling**: [41–44] Although not all the insect use this mechanism to generate lift, it is important to highlight it, as it was the first mechanism to be identified by Weis-Fogh [41] which aims to explain insect lift generation of the wasp *Encarsia formosa*. The wing at the beginning of the downstroke clap together and then peel apart (clap and fling). Insects

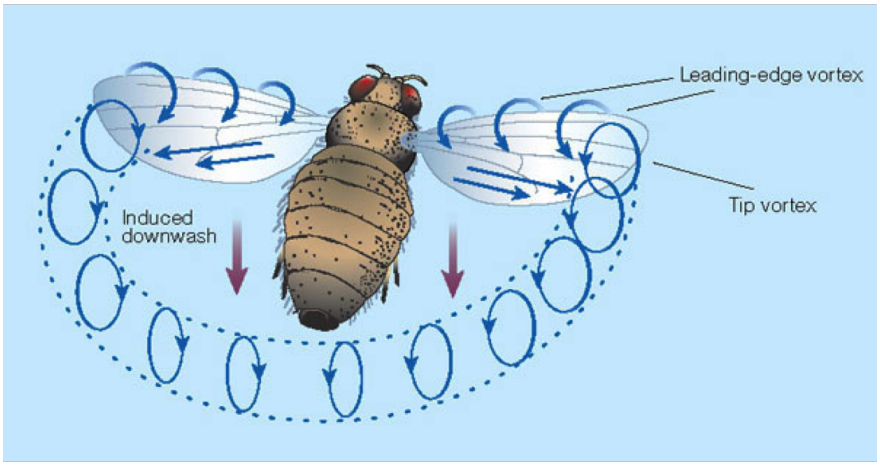

(a) Leading Edge Vortex- LEV

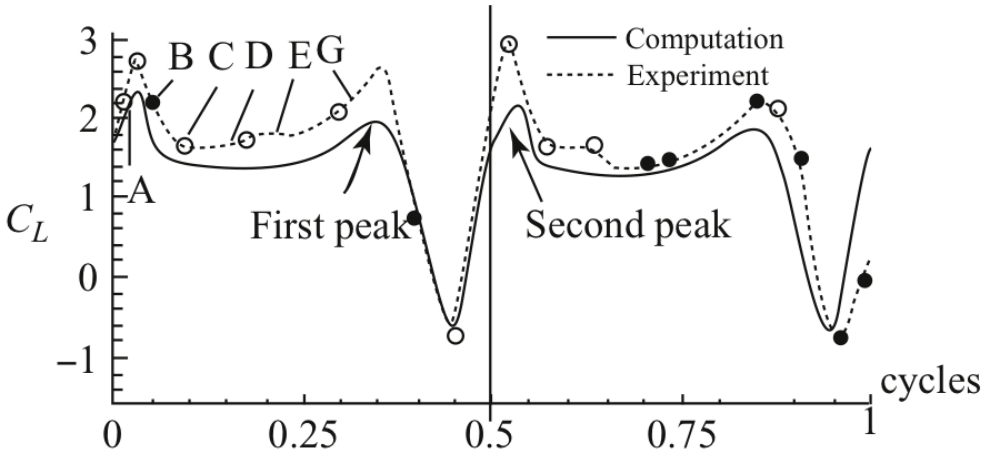

(b) Time history lift during a flapping cycle

Figure 2.9: (a) Airflow over the leading edge of the wing rolls up into a leading-edge vortex (LEV) [5, 6], (b) Flapping-wing lift generation as described by Dickinson et al. [5]. First peak is due to "Rotational force", and second peak due to "Wake capture".

utilize this mechanism when they are require high thrust for maneuver [45] or for lifting loads during their flight [46]. The wings during the clip and fling take advantage of the produced vortices.

5. In addition to the major lift enhancement resources listed above, there are more factors in the aerodynamic forces production that may influence the forces during the flapping cycle. One of these factors is the effect of acceleration or added mass of the fluid [47] on the generated forces. Added mass refers to the effect of the accelerated fluid mass on the wing inertia [48], which can be significant in flapping wing kinematics. The wing mass of an insect is relatively very small in comparison to the body mass, and many times can be neglected, but the mass of the accelerated fluid might not be, as suggested by Ellington, Lehmann and others [26, 49]. The other factor is wing flexibility, the role of insect wing flexibility has been identified in the literature [24, 50], and plays a key role in lift generation of flapping wing.

2.3.2 Forward Flight

Most of the studies have been restricted to hover, with only some limited foray into forward flight. David [51] and Willmott et al. [31] found an inverse relationship between the body axis angle and forward speed, such that the body angle decreases with an increase of the flight speed. In hover, the stroke plane is horizontal Fig. 2.8 (plane tilt is zero), while the body trims nose-up to achieve pitching moment balance. In forward flight, Willmott and Ellington observed a positive correlation between stroke plane angle and forward speed [31], by tilting the flapping plane forward, a component of thrust is achieved in the direction of insect travel. The angle of attack

depends on the plane angle and also on the inflow, therefore the instantaneous forces depends on the plane tilt.

Dickinson [52] conducted experiments on the Robofly mechanical wing in forward flight, and observed that lift and drag coefficients for a fixed angle of attack (with horizontal flapping stroke plane) are dependent upon advance ratio and wing position w.r.t to the flapping stroke (i.e., downstroke or upstroke). Nagai et al. [53] investigated the forces on an isolated flapping wing using both experiments and Navier-Stokes computional simulations in forward flight. A significant effect of the stroke plane tilt angle and advance ratio on the extent of stall delay and wake energy recovery was observed, along with asymmetry between the upstroke and the downstroke forces.

2.4 Aerodynamic Modeling of a Flapping Wing

There are three main approaches to explain the physical principles and estimate the generated aerodynamic forces and power to investigate flapping wings: 1. Formulate a simplified model, 2. Experimental studies, and 3. Computational simulations. This section will review briefly the simplified models of flapping-wings that have been suggested in the literature, along with computational approaches to investigate flapping-wing aerodynamics at low Reynolds numbers.

2.4.1 Simplified Flapping Wing Aerodynamic Model

Simplified flapping wing aerodynamic models were proposed to analyze insect flight characteristics and provide an estimation of the aerodynamics forces. Early models were based on different simple approaches; the common ones are based on momentum theory, vortex sheet, blade

element theory and quasi-steady aerodynamics [26, 50, 54–56]. These approaches have been used both individually and in combination, with varying degrees of success [57]

Momentum theory based on actuator disk has been used to analyze flapping wing and simplify the aerodynamic forces calculations [26, 54]. For this analysis a few assumptions were made: 1. Wing flapping frequency is high enough that the flapping plane can be simplified as an actuator disk; and 2. uniform velocity distribution occurs downstream of the wake. Using this approach, Weis-Fogh [54] calculated the induced downwash velocity at the flapping stroke in hover, assuming that the far wake velocity was twice the downwash velocity at the full actuator disk. Ellington [26] calculated the induced power, that was modified to consider a partial actuator disk and stroke plane incline. Momentum theory (actuator disk) simplified models have their limits; momentum theory doesn't provide time-dependence of the lift and doesn't account for change in wing shape, size, morphology and kinematics. Therefore, although acceptable for rough sizing and required power of a flapping wing, it is not suitable for detailed design.

A vortex based simplified model presented by Rayner [55, 56] suggested modeling small-core coaxial vortex rings for each half flapping wing. Lift and drag coefficients can be determined from this model, but the effects of stroke amplitude and stroke plane angle were not included. Later on, Ellington [27], developed a simplified model based on vortex sheets that can also account for the influence of forward speed.

While steady-state aerodynamic theory does not explain the lift enhancement sources (delayed stall, pitch-up and wake capture) in insect flight, a different approach was adapted and examined by many authors using a quasi-steady model. A quasi-steady aerodynamic model is a reduced

order model in which the instantaneous aerodynamic forces and moments are computed solely based on instantaneous velocity, wing geometry and effective angle of attack, i.e. there are no flowfield hysteresis effects such as shed wake. In the present work, the flight dynamics model utilizes an embedded quasi-steady model to represent the flapping wing aerodynamic forces. Though this model provides qualitative trends that describe the coupling between wing kinematics and associated loads, it does not capture unsteady aerodynamic effects due to shed vortices, a key phenomenon in flapping wing flight [5]. Therefore, a higher-fidelity aerodynamic model is necessary to obtain accurate airloads. By comparing the quasi-steady results against experimental data, Ellington et al. [27], demonstrated that a quasi-steady model is insufficient to predict wing force magnitudes accurately.

Later, semi-empirical corrections were proposed to augment the quasi-steady models with unsteady effects [27, 29, 52]. Though such modified quasi-steady models can be tuned to provide good agreement with the experimental measurements, such an approach represents "point calibrations" based on data fitting, and must be retuned for each geometry and flap frequency. Unsteady forces (added mass, wake capture) play a significant role in insect flight and are highly influenced by the wing kinematics and wing shape. Therefore, a quasi-steady model, while proving a good tool to obtain rapid estimations of the aerodynamic force-kinematics trends, is insufficient to capture unsteady force mechanisms from first principles. Therefore, using just a quasi-steady aerodynamic model may result in an over-designed or under-designed vehicle. A higher-fidelity model that captures the essential aspects of insect flight is required for accurate performance estimates.

2.4.2 CFD Modeling of a Flapping Wing

Reliable experimental measurements on millimeter-scale models that flap at high frequencies (i.e., 100 Hz) are challenging to obtain. This difficulty arises from the small magnitudes of the forces involved (resulting in low signal-to-noise ratio), very small length scales and the high sampling rates required to obtain time-resolved information within each flap cycle. Experimental work involves conducting experiments on living insects or scaled up mechanical wings such as robotic wings. Experiments using robotic wing [5, 27–29, 35, 38, 52] have proved to be efficient tools to investigate the aerodynamics mechanisms of flapping wings. The majority of these experiments considered an isolated wing using simplified kinematics to quantify the effects of wing rotation, wing-wake interaction and leading edge vortex formation.

Alternately, CFD simulation models can help provide a good understanding of the unsteady flow mechanisms and insight into the critical design parameters. The computational approach is to calculate the flow variables by solving the governing equations and associated boundary conditions with a flapping wing numerically. In the last decade, researchers have taken advantage of the advancements in computing facilities and developments in computational techniques to develop solvers that can address the insect flights with different degrees of success.

The use of computational tools poses two major challenges. The first of these is the computational cost. Simulations needed to resolve insect flight require extensive computational resources to handle viscous flows, accurately capture vortical structure and allow for the complexity of moving grids. The second issue is that CFD studies rely on experimental results for both validation and for the relevant kinematic inputs. Currently, high fidelity solvers can be executed in parallel

on high performance computing clusters to shorten the wall time needed to obtain well resolved solutions.

To address the second concern, collaboration between empirical and computational studies critical for both approaches. Once the CFD solver is verified by the experimental results, it can be used to provide insight about more complicated kinematics and trends that experiments find challenging to capture. There are a variety of mathematical algorithms in the literature that can resolve the insect flight governing equations, including DNS (direct numerical simulations), Navier-Stokes (N-S) solvers, Reynolds-averaged Navier-Stokes (RANS) and panel method.

Panel methods have been used to model flapping-wing flight, where the wake geometry is prescribed as a series of vortex rings [26, 55, 56]. 3D panel methods have been used to study the experimental flapping of the Hawkmoth, and vortex panel methods have been used to study the inviscid lift generation, i.e., Wagner effect in a pitching airfoil. However, prescribed-wake models are limited by their inability to capture evolution of the wake geometry over time. Navier-Stokes computations were used to simulate the flow around a flapping-wing by many authors [33, 37, 39, 58, 59]. While this approach calculates properties of the entire flowfield and the instantaneous forces, there are drawbacks in terms of computational cost, as mentioned previously. Also, a considerable effort is required to construct the sutiable mesh that discretizes the flowfield. In the case of a flapping wing, the simulations required moving boundaries, and the most popular grid methods used have been: 1) Immersed boundaries (IB), 2) conforming body mesh (overset) grids, or 3) unstructured mesh. Computational methods can also divided into large spectrum of methods, such as three-dimensional modeling, two-dimensional modeling, and quasi-steady analysis.

The governing equations used to describe flapping wings physics are the unsteady Navier-Stokes (N-S) equations. However, progress in computing facilities and new algorithmic capabilities in the last decade now allow for researchers to relatively efficiently use CFD tools to simulate flapping wings and to deal with their model complexity. Solving the NS equations provide time accurate flow-field variables (velocity field, density and pressure). Much computational work has been carried out on insect-wing related kinematics at low Reynolds number; among them are Liu and Kawachi [33] who performed the first 3D simulation of insect flapping to compare against the scaled Hawkmoth wing experimentally studied by Ellington [27]. Their model predicted the leading-edge vortical structure, and showed good qualitative agreement with smoke flow visualization. Sun and Tang [37], and Ramamurti and Sandberg [58] also performed 3D CFD simulations, that were validated against Dickinson's Robofly experiments. And they obtained reasonable agreements between the computational data and the experimental measurement. The Robofly experiments have provided a large amount of experimental data that CFD predictions can be compared to. Though this approach calculates properties of the entire flowfield and the time-resolved aerodynamic forces with high accuracy, it incurs significant computational cost.

2.5 Trim and Delta Coupling

Trim refers to a steady flight condition in which the translational and rotational accelerations are zero (also termed "equilibrium of forces and moments"). Trim flight modes include hover, steady level flight, steady climbing flight, steady level turn and steady climbing/descending turns of constant radii.

Trim for a fixed-wing aircraft is defined as a steady flight condition in which the control settings, orientations and velocity of the vehicle produce forces and moments (inertial and aerodynamic) that exactly cancel out external forces (gravity), allowing the aircraft to remain in its state of uniform motion "indefinitely". The force distributions on a fixed-wing aircraft are fairly steady in nature, and so the loads, during trim, at any two instants in time will be near-identical. In contrast, the loads generated by a flapping wing are not steady but rather periodic in time. Thus, presence of wing flapping motion requires a modification to the traditional definition of aircraft trim.

The identification of wing kinematics for trimmed (non-accelerating) flight has been addressed in the literature. Using CFD-based wing force predictions, Sun and Xiong [60] demonstrated a trial-and-error based approach to adjust the wing kinematics to achieve vertical force equilibrium in hover with a body assumed to be fixed in space. In hover, the number of kinematics parameters to adjust is one (flap stroke amplitude or flap frequency) to control the vertical thrust with a symmetric flap stroke. In forward flight, the number of wing kinematics parameters needed to trim the vehicle is 3 so as to balance vertical force, propulsive force and pitching moment simultaneously. Therefore, trial-and-error based approaches are computationally expensive. An efficient trim algorithm can reduce these runtimes significantly without compromising the accuracy of the solutions.

Approaches to achieve trimmed flight for flapping wing platforms are mentioned in the literature. For example, Stanford et. al. [61, 62] and Oppenheimer et. al. [63] adopted an approach based on time marching and periodic shooting to identify a steady-state hover solution. The trim

analysis was based on a quasi-steady blade element aerodynamic model, which the authors identified as being of insufficient fidelity compared to the wing structural model and flight dynamic model. To obtain accurate airloads and trim kinematics, a high-fidelity flowfield model is required, which must be coupled to the trim process. Till date, an efficient framework incorporating a trim process coupled to a CFD model for a flapping wing vehicle is not in the literature. The present work seeks to address this deficiency.

As noted by Sun [12], the nature of forces produced by flapping wings closely resemble those on a helicopter blade. While Sun refers to the aerodynamic and inertial loads in the context of stability analysis, this analogy; between a flapping wing vehicle and a helicopter; readily lends itself to the calculation of performance in steady flight for a flapping wing MAV. Therefore, the techniques developed for helicopter performance calculation [13, 14] are adapted in this work and applied to the flapping wing platform for obtaining CFD-coupled trim solutions.

2.6 Objectives of the Present Dissertation

The aim of this dissertation is to quantify flapping-wing MAV performance, where the approach is systematically to determine wing kinematics for a given steady (trim) flight conditions by: 1) incorporating high fidelity aerodynamic models into trim analysis and 2) applying computationally efficient procedures to combine both CFD and trim. A longer term goal is to better understand aspects of how the kinematics may affect the aerodynamic forces generation, while the whole insect configuration is considered. The specific objectives of this dissertation are:

1. Verify that OVERTURNS (CFD analysis code) will predict forces, moments and power of a

flapping wing for the very low Re numbers regime $O(10-10^2)$.

2. Conduct a parametric sweep to study the performance of various wing geometries and kinematics and determine appropriate measure of efficiency for performance comparisons.

3. Investigate how well a quasi-steady model can be used to predict the aerodynamics loads, either in a stand-alone mode or as a basis for trim with CFD coupling.

4. Formulate a computationally efficient and robust framework to obtain trim solutions in steady level forward flight by coupling a flight dynamic model with a high-fidelity CFD analysis. Such an analysis will provide the ability to incorporate the effects of detailed aerodynamic forces from CFD into the trim solution for flapping wing kinematics.

5. The CFD coupled trim model used to identify the variation of wing kinematics parameters with forward flight speed, and highlight the improvements introduced by CFD over the quasi-steady analysis.

6. Use the proposed numerical framework to study more complicated modes of flight such as a steady coordinated turn.

7. Study the detailed vortical flow field in trimmed flight, as well as the induced inflow, induced power and average forces.

2.7 Scope and Organization of the Dissertation

This work considers three main topics: 1) The application of the CFD solver, OVERTURNS, to resolve flapping-wing simulations, including validation and verification of the solver and a para-

metric study to investigate the effect of related parameters on the aerodynamics forces generation, 2) The development of a trim algorithm to obtain the required kinematics to achieve trim conditions in different flight modes with accompanying analysis of the results , and 3) Investigation of the flow features and wake structure of a flapping wing. The dissertation is divided into eight chapters.

The first and second chapter introduces the physical phenomena of insect flight along with a detailed literature survey related to the physical problem and the different approaches that have been used to study these phenomena and bring it to a level useful for design. Also the technical and physical challenges facing the development of such a design tool are reviewd. The models that were previously developed to study insect-flight aerodynamics principles are discussed.

Chapter 3 presents the computational models, the reduced model (Quasi-steady) and the first principle-based three dimensional Naiver-Stokes. The principles and the assumptions of the reduced models used are discussed. The baseline of the CFD solver is presented, along with the grids generation type and methodology. The set-up of the CFD simulations are discussed in details such as spatial and temporal schemes, kinematics, wings shape and grid sensitivity.

Chapter 4 presents the CFD solver validation and verification by comparing the predicted results from the NS CFD solver with data obtained from experiments that were performed by the facilities of the army lab (ARL) especially for this project. The experimental set-up and data analysis are introduced. Also the solver was validated with some representative simple 3D flow cases as baseline cases. CFD sensitivity is analysis also included in this chapter.

Chapter 5 discusses the parametric study of single wing conducted computationally. The

parametric study aims to introduce an efficiency matric to compare between different kinematics and geometrical parameters in hover. The parametric study is essential for the next step and is looking at the whole insect-flapper MAV as one system. Also the flow-field and wake structure around a single flapping wing is discussed and visualized.

Chapter 6 discusses in details the suggested trim algorithm, based on loose coupling. Flight dynamic model and trim Jacobian methods are presented and discussed. Following this Chapter, Chapter 7 presents the trim analysis results in hover, forward flight and coordinated turn. The insect-flapper as one flying system was studied by looking at trim conditions, which gives a significant insight and suggests a way to look at flapping-wing flying systems for design and performance purposes, and also contribute to the understanding of the flight principles that insects rely on. The complex flow-field created by the flapping wing is discussed as well.

The last chapter summarizes the important conclusions and contributions of the development of an efficient trim algorithm for incorporating high fidelity CFD analysis to flapping wingsAssociate application and offers suggestions for future work.

Chapter 3

Mathematical Modeling

This chapter presents the mathematical and computational models used in this study. The chapter is divided into two main sections. The first section describes the aerodynamic models used, the reduced aerodynamic model that will be referred to it as quasi-steady (QS) and a first principles, 3-dimensional, Navier-Stokes CFD solver and it will refer to as OVERTURNS. The solver baseline and the computational methods are outlined along with the improvements that added to the solver framework to carry out the insect kinematics simulations. The details of the mesh system and the connectivity approach are discussed. The second section describes the steady-flight trim model, where the coupling strategy used between the various codes will be laid out and the idea of a multi-fidelity framework introduced.

3.1 Aerodynamic Models

Two main aerodynamic models were used in this study:

1. Quasi-Steady (QS): This is a simplified model based partially on experimental data summarized in look-up tables for lift and drag coefficient as a function of the operating angle of attack. This model is used first to perform a parametric study, compare the obtained airloads against CFD airloads, and highlight the differences between both. The second use of quasi-steady aerodynamic is to incorporate this in the loose-coupling process to determine

trim variables for a given flight condition. More details will be discussed later in this chapter about the trim algorithm.

2. OVERTURNS (CFD): This first principles model is used to simulate the detailed flapping wing of the insect model, resolve the flow features and predict the airloads. It is a Naiver-Stokes (NS) solver. Insects operate at very low Reynolds numbers (viscous effects dominate) which results in the formation of vortical structure and flow separation. Reynolds numbers are between $10 - 10^2$, and low Mach number $O(10^{-3})$. The forces are highly unsteady. Therefore, to properly capture the physical phenomena, 3D, unsteady NS solver that accurately predicts the forces and moments is required as compared to an inviscid Euler solver.

3.1.1 Quasi-Steady Aerodynamic Model

The motivation behind using the aerodynamic reduced model (QS) is to predict flapping-wing MAV aerodynamic forces with a simple, fast and computationally inexpensive (in terms of computational time and resources) tool. The question to be asked is how well QS can predict these airloads compared to these that insects generate during their flight. It is difficult to properly answer this question, because a full understanding of all insect flight mechanisms is not fully achieved yet. But, QS results can be compared against experimental data or CFD predictions. This question is addressed in Chapter 4 and Chapter 5. As will be shown in the results, QS does not capture all of the physical phenomena, which leads to some inaccuracy in the forces. But, QS is efficient and can be used to obtain ”trim“ solution, an approach that will be discussed in the trim algorithm section.

The QS model used for the parametric survey was developed by the Army Lab (ARL) facilities. It is based on experimentally derived equations and it accounts for three aspects of aerodynamic load: instantaneous steady translational forces as well as unsteady circulatory and non-circulatory forces. Ignored are any forces associated with interactions between the wing and wake including induced forces or "wake capture" effects [6]. The translational force model was formulated empirically by Dickinson [5] for the experimental set-up shown in Fig. 3.1(a & b). Undergoing steady rotation at constant pitch angle, the translational lift and drag were measured on a dynamically-scaled wing. The measured force values were normalized to form coefficients based on the wing area and dynamic pressure at a spanwise location corresponding to a radius formed from the second moment of the wing area. These coefficients are utilized as sectional lift and drag coefficients described in the conventional sense:

$$f = qcC_f \tag{3.1}$$

where f is the force per unit span, q the local dynamic pressure, c the chord at a given spanwise location, and C_f the force (lift or drag) coefficient which in this case is a function only of the geometric angle of attack. The coefficient model found by Dickinson is not symmetric about zero angle of attack (Fig. 3.1(c)). The formulations have been modified from the original as follows to eliminate the asymmetry about zero angle of attack:

$$C_l = 1.58\sin(2.13\alpha) \tag{3.2}$$

$$C_d = 1.92 - 1.55\cos(2.04\alpha) \tag{3.3}$$

where α is in radians.

The applied model for the unsteady loads includes the circulatory forces taken from quasi-steady thin airfoil theory (Ref. [64]). This solution is formulated for a flat plate in an ideal flow, and therefore, the lift curve slope is 2π and it does not a model for stall. This classic solution treats a plunging and pitching flat plate airfoil as though it possesses a camber equivalent to the instantaneous curvature of the relative flow along its surface, a virtual camber. Treatment of the unsteady fluid inertial load applies a solution by Sedov [65] for a flat plate airfoil undergoing unsteady motion (including two orthogonal directions of translation as well as rotation about an arbitrary point). This is again a two-dimensional solution which assumes attached, inviscid flow.

Sectional loads are integrated down the wing-span to derive the forces and moments generated at the root of the wing. Finite span effects are ignored as are variations in Reynolds number, both spanwise and as they vary throughout the parameter set explored. For the trim coupling process, a similar aerodynamic reduced model is used where wing loading in the quasi steady model is estimated using the experimentally measured lift and drag curves based on the Dickinson Robofly experiments. But, it is relatively simpler as compared to the previous one; circulatory and non-circulatory lift are not included, and only the translational forces are considered. The look-up table provides the lift and drag coefficient for the whole wing (sectional forces are ignored).Thus, lift is calculated as :

$$L = \frac{1}{2}\rho V^2 S \hat{r}_2^2 C_L(\alpha) \tag{3.4}$$

where ρ is the density of air, V is the average velocity seen by the wing tip, S is the wing area, and $\hat{r}_2$ is the second moment of area of the wing. $C_L(\alpha)$ is the experimental lift coefficient at angle of

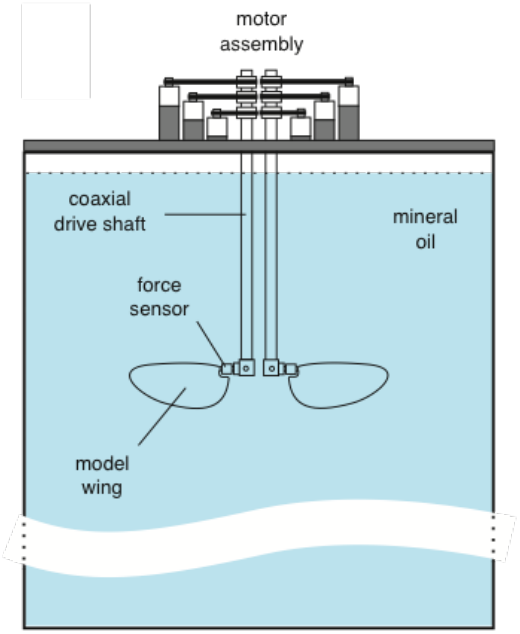

(a) Dickinson Robofly experiments:Robotic fly apparatus

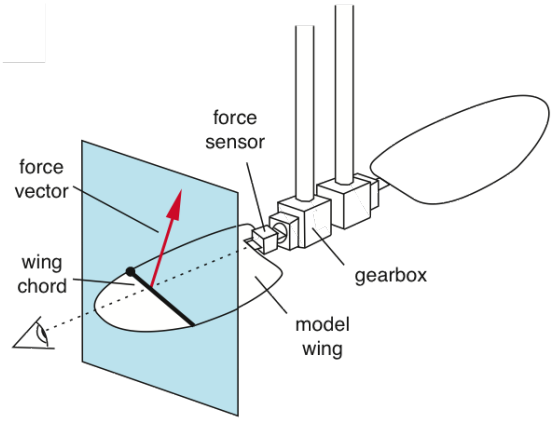

(b) Close-up view of robotic fly

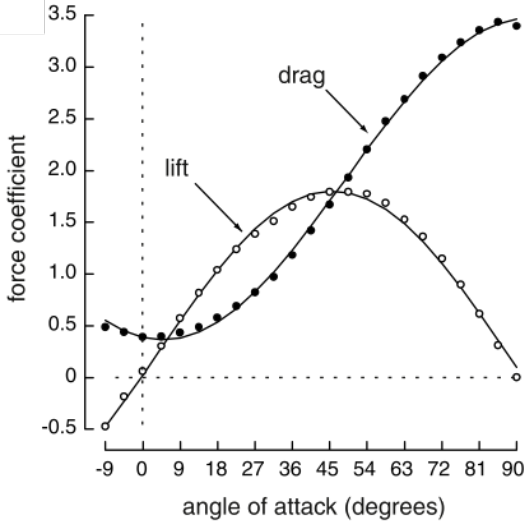

(c) Average translational force coefficients as a function of angle of attack

Figure 3.1: Dickinson Robofly experiments, as given is Ref. [5].

attack α given by Dickinson et al. (1999) [5] which is given in Equation 3.2. A similar equation is constructed for drag. The wing frame forces can be transformed to the inertial frame giving $\mathbf{F} = [X\ Y\ Z]^T$. Moments around the insect's center of gravity are dominated by the wing loading, so $\mathbf{M} = \mathbf{r_{MA}} \times \mathbf{F}$, where $\mathbf{r_{MA}}$ is the moment arm from the insect's center of gravity to the point of action of the forces on the wing, assumed to be at 75% span.

3.1.2 OVERTURNS: Navier-Stokes Solver

The acronym used to describe the solver is OVERTURNS (Overset Transonic Rotor Unsteady Navier-Stokes), and it is a structured, overset, compressible solver, that solves three dimensional Navier-Stokes equations [66, 67]. OVERTURNS was developed at the University of Maryland for rotorcraft applications, and was extended for this work to analyze flapping wing platforms. The solver was modified to simulate a three dimensional *diptera* type vehicle, consisting of two flapping wings and a rigid body in various flight modes (i.e. hover, forward flight, coordinated turn). The baseline solver with corresponding numerical schemes are described in the following section.

3.1.2.1 Flow Domain of Flapping Wing MAV

The focus of the current work is to simulate the flow-field of insect (diptera) configuration at low Reynolds numbers. The insect configuration consists of two moving (flapping and pitching) wings and fixed body, who's surface can be represented as a solid wall. The far-field of the simulated domain is extended, and limited to a few wing chord from the wall in any direction. The

computational domain is represented by grid points, where the flow solution can be represented only at finite locations. This is achieved by decomposing the flow domain into smaller cells. The flow variables represented at each of these grid points constitute the flow solution. The accuracy of the solution is determined by the quality of the grid.

The Reynolds numbers of flapping-wing MAV are low, which indicates that the flow is highly viscous such that a complex flow field is obtained: large shear boundary layer, vortical formation and flow separation may occur. Therefore, the computational domain should be fine enough in appropriate regions to capture all of these features on the wing surface and in the wake.

In addition, the grids are moving by prescribed, relatively complex kinematics. A common difficulty in simulating complex geometries is that a single, contiguous grid is not sufficient to represent all the flow features with adequate resolution. For a flapping wing, it is very difficult to obtain a single structured mesh which can represent the wing surface and also preserve important off-surface flow features, such as the shed vortices. In such cases, common approaches used are: unstructured meshes, multiblock structured meshes, or overlapping "Chimera" structured meshes. Unstructured meshes are generally considered to be easily adaptable to complex configurations, but they require more memory and are less efficient compared to structured meshes (limited accuracy). Using block structured grids, the grid interfaces have to be matched and this makes the grid generation process very complicated.

Overset structured grids have the advantage that different grids can be generated independent of each other and can be placed in the region of interest without any distortion. As well for relative motion between meshes, overset is required. Due to these advantages, the current work employs

overset meshes similar to previous studies performed using OVERTURNS [66–68]. The cost of using overset grids lies in the additional work required in identifying points of overlap between meshes and the solution connectivity (interpolation) in the overlap regions. Additionally, there is a possibility of a loss of the conservation property of the numerical scheme. However, the flow in the Reynolds numbers region of interest are assumed to be laminar such discontinuous features like shocks and thin shear layers are unlikely to occur.

3.1.2.2 Governing Equations

The governing equations solved in OVERTURNS are the three-dimensional Navier-Stokes equations [66]. NS equations are the mathematical representation of the three conservation laws of physics:

- Conservation of Mass
- Conservation of Momentum
- Conservation of Energy

Together, these laws are expressed as a system of partial differential equations that models an unsteady, compressible, viscous flowfield. Additional equations, such as the equation of state or a turbulence model, are required to ensure that the system is fully determined. The general formulation in Cartesian coordinates is given by:

$$\frac{\partial Q}{\partial t}+\frac{\partial F_i}{\partial x}+\frac{\partial G_i}{\partial y}+\frac{\partial H_i}{\partial z}=\frac{\partial F_v}{\partial x}+\frac{\partial G_v}{\partial y}+\frac{\partial H_v}{\partial z}+S \tag{3.5}$$

where Q is the vector of conserved variables, F_i, G_i, and H_i are the inviscid convective flux vectors, F_v, G_v and H_v are the viscous flux vectors and S is the body-force source term. The vectors in the above equations are further developed below. The non-conservative variables are: ρ, density, (u,v,w), the velocity components in Cartesian coordinates, e, the total energy, and p, the pressure.

The conserved variables are expressed as:

$$Q=\begin{bmatrix}\rho\\ \rho u\\ \rho v\\ \rho w\\ e\end{bmatrix} \tag{3.6}$$

The inviscid fluxes are expressed as:

$$F_i=\begin{bmatrix}\rho u\\ \rho u^2+p\\ \rho uv\\ \rho uw\\ (e+p)u\end{bmatrix}\quad G_i=\begin{bmatrix}\rho v\\ \rho uv\\ \rho v^2+p\\ \rho vw\\ (e+p)v\end{bmatrix}\quad H_i=\begin{bmatrix}\rho w\\ \rho uw\\ \rho vw\\ \rho w^2+p\\ (e+p)w\end{bmatrix} \tag{3.7}$$

The viscous fluxes are expressed as:

$$F_v = \begin{bmatrix} 0 \\ \tau_{xx} \\ \tau_{yx} \\ \tau_{zx} \\ u\tau_{xx} + v\tau_{yx} + w\tau_{zx} - q_x \end{bmatrix} \quad G_v = \begin{bmatrix} 0 \\ \tau_{xy} \\ \tau_{yy} \\ \tau_{zy} \\ u\tau_{xy} + v\tau_{yy} + w\tau_{zy} - q_y \end{bmatrix} \quad H_v = \begin{bmatrix} 0 \\ \tau_{xz} \\ \tau_{yz} \\ \tau_{zz} \\ u\tau_{xz} + v\tau_{yz} + w\tau_{zz} - q_z \end{bmatrix} \tag{3.8}$$

where q_x, q_y, q_z are the thermal conduction terms and can be expressed as a function of temperature, following Fourier's law:

$$q_i = -k\frac{\partial T}{\partial x_i} \tag{3.9}$$

with k as the thermal conductivity and T as the temperature. The equation of state for a perfect gas can be used to derive the pressure p from the other flow quantities:

$$p = (\gamma - 1)(e - \frac{1}{2}\rho(u^2 + v^2 + w^2)) \tag{3.10}$$

with γ, the ratio of specific heats (ratio of C_p: specific heat at constant pressure, and C_v: specific heat at constant volume). In all simulations carried out in this work, γ is set to 1.4, i.e. the working fluid is air. The temperature can be obtained from density and pressure:

$$T = \frac{p}{\rho R} \tag{3.11}$$

where R is the gas constant. Finally, the mean stresses are expressed following Stokes' hypothesis, :

$$\tau_{ij} = \mu \left[\left(\frac{\partial u_i}{\partial x_j} + \frac{\partial u_j}{\partial x_i} \right) - \frac{2}{3} \frac{\partial u_k}{\partial x_k} \delta_{ij} \right] \tag{3.12}$$

in which μ is the laminar viscosity obtained from Sutherland's law ($\mu = f(T)$) [69].

3.1.2.3 Overset Grids System

Two rigid wings and a rigid insect body are modeled in this study. The farfield extent of the modeled domain is limited to a few wing chords from the wing in x, y, z directions, sufficient for capturing far field flow features, as shown in Fig. 6.6.

A single structured mesh can not preserve the complexities in the flow-field such as tip vortices, trailing edge vortices and far field wake features. In this case, the two wings and the body meshes are overset onto a coarser nested background mesh. The overset grid system has five grids as shown in Fig. 6.6(a). The grids are divided into two types: body-fitted curvilinear grids and Cartesian background meshes.

Body-fitted, curvilinear grids are used for the wings and the insect body. These grids are important for the near-field flow, near the wings and body surface. The wing surface is treated as a solid wall. The body-fitted wing grids are moving according to the prescribed kinematics, and the insect body is fixed (Fig. 6.6(b)). A 3D algebraic mesh generator [67] for structured, curvilinear, body-fitted CFD grids is used for the wings and insect body grids. The insect body and wing meshes are finely spaced near the surface to resolve the boundary layer features and associated viscous effects [67],

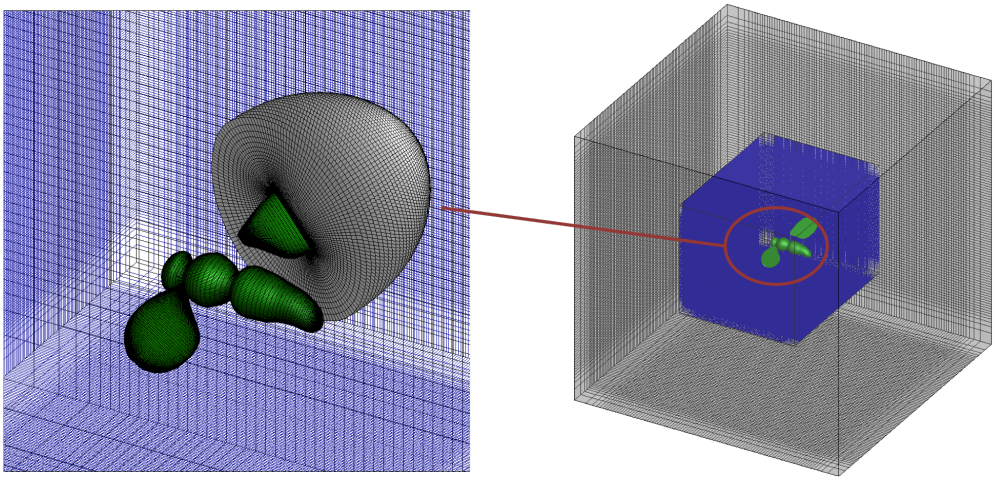

(a) Nested overset grids

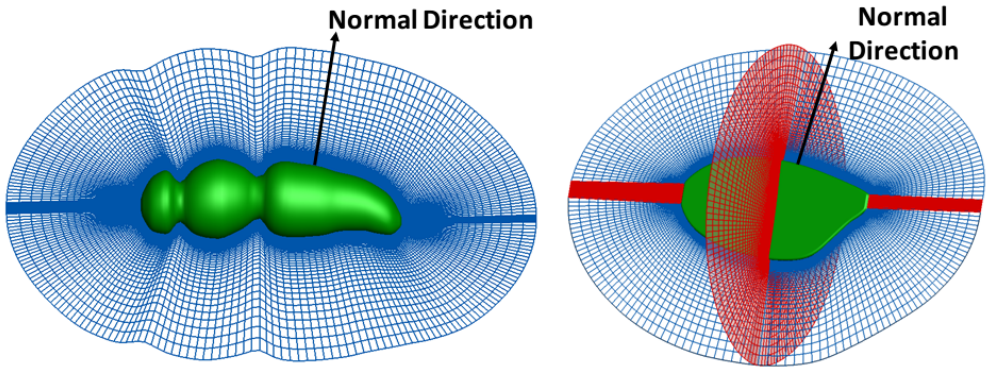

(b) OO body-fitted grid for insect body and wing shape

Figure 3.2: Nested overset grid system.

as shown in Figs. 6.6(b), and 3.3. The resulting body-fitted meshes have an O-O topology.

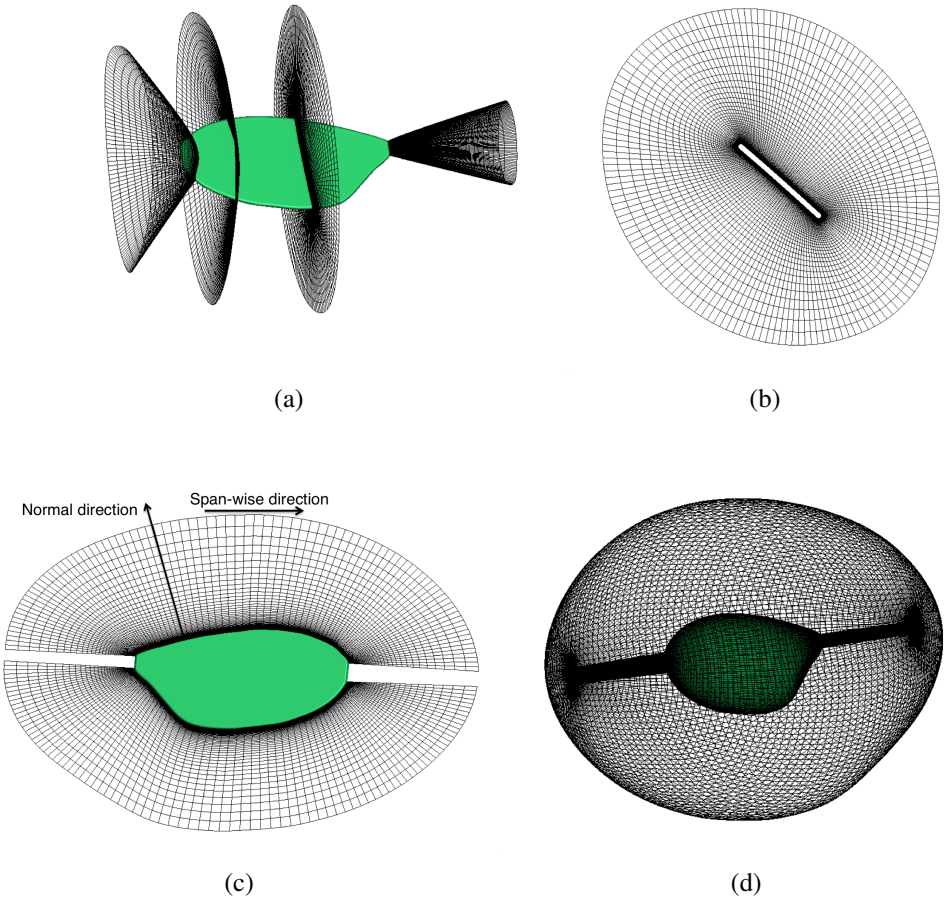

Figure 3.3: OVERTURNS: (a) Near-body O-O mesh at various span-wise sections; (b) O-O mesh at a spanwise 2D section; (c) The mesh in the normal direction near the leading edge and the trailing edge; (d) Volume near-body O-O mesh.

Nested Cartesian background meshes are used to capture the far-field effects. For the background grids a simple Cartesian mesh generator is used for this purpose. Two levels of Cartesian background, nested grids are used, finer and coarser. The coarser mesh extends up to 5 wing chords on each side. The nested background meshes are stationary, and extended to allow for the motion

of the wings. The wing grids translate and rotate according to user-prescribed kinematics while the body mesh is fixed for hover and forward flight modes. Such a setup minimizes the total mesh points required to obtain a detailed resolution of the flowfield, and allows for selectively refining flow domains of interest. The overall overset grid system has five grids for *diptera* configuration, as shown in Fig. 6.6(a), and it consist of roughly of 10 million mesh points (depending on the simulation type). Between the meshes (wings, body and backgrounds) there are overlap regions; connectivity and information transfer across the overlapping areas is handled by implicit hole cutting (IHC) [66]. The computations are performed by high performance computing platforms using parallel computing approach. More details about the simulations set-up and grid sensitivity will be discussed in Chapter 4, Section 4.4.

3.1.2.4 Initial and Boundary Conditions

The governing equations require initial and boundary conditions in order to obtain a unique solution. Initial conditions are specified by prescribing the density, flow velocities and pressure everywhere in the solution region at the beginning of the solution procedure. Typically for a flapping wing MAV in hover and forward flight, the initial conditions are set such that the density, pressure and flow velocities are freestream values.

There are two common types of physical boundary conditions for external flow, the wall boundary condition and the farfield boundary condition. Wall boundary in the physical domain arises from the wall surfaces being exposed to the flow. For a viscous fluid which passes a solid wall, the no-slip condition is applied such that the relative velocity between the surface and the fluid

directly at the surface is zero. At the solid wall, the density (ρ) is extrapolated from the interior of the domain. The pressure (p) is then obtained from the normal momentum equation [66].

The truncation of the physical domain or system for the purpose of numerical simulation leads to artificial farfield boundaries, where certain physical quantities have to be prescribed. The farfield boundary condition has to fulfill two basic requirements. First, the truncation of the domain should have no notable effects on the flow solution as compared to the infinite domain. Second, any outgoing disturbances must not be reflected back into the flow-field. The farfield boundary on the background mesh is placed as far away in the radial direction from the body surfaces as computationally practical such that the conditions at these mesh points are very close to freestream.

Additional boundaries are numerical in nature rather than physical.These additional numerical boundaries are determined due to the mesh system and grid topology, namely: periodic boundary conditions due to the overlap of the O-O grid type; wake-averaging boundary condition, which is interface boundary condition at the root and the tip of the wing; and overset boundary which are determined by the Implicit Hole-Cutting code, and are used to provide connectivity information between the blade and background meshes.

3.1.2.5 Non-Dimensionalization

The Navier-Stokes equations are solved in their non-dimensional form using the following variables. Velocity is non-dimensionalized by speed of sound, a_∞. The length by characteristic length, L, for flapping-wing it is a mean chord. Density by free-stream density, ρ_∞. Time by L/a_∞. Similarly for kinematic viscosity and temperature. As a result the pressure is non-dimensionalized

by ρa_∞^2. The non-dimensional variables are summarized below:

$$
\begin{aligned}
t^* &= \frac{t a_\infty}{L} \qquad (x^*, y^*, z^*) = \frac{(x, y, z)}{L} \qquad (u^*, v^*, w^*) = \frac{(u, v, w)}{a_\infty} \\
\rho^* &= \frac{\rho}{\rho_\infty} \qquad T^* = \frac{T}{T_\infty} \qquad p^* = \frac{p}{\rho a_\infty^2} \quad e^* = \frac{e}{\rho a_\infty^2} \qquad \mu^* = \frac{\mu}{\mu_\infty}
\end{aligned}
\tag{3.13}
$$

where the superscript $*$ is used for the non-dimensionalized quantities, the subscript ∞ represents free-stream variables, $a = \sqrt{\gamma p/\rho}$ is the speed of sound, and L is a reference length scale of the flow. Additional non-dimensional parameters are defined as:

$$\text{Reynolds number :} \qquad Re_\infty = \frac{\rho_\infty U_{ref} L}{\mu_\infty}$$

$$\text{Mach number :} \qquad M_\infty = \frac{U_{ref}}{a_\infty}$$

$$\text{Reduced frequency :} \qquad r_f = \frac{2\pi f \bar{c}}{2U_{ref}}$$

For the hover case, Reynolds number is defined as the following:

$$\mathrm{Re} = \frac{\mathrm{U_{ref} L_{ref}}}{\nu} \tag{3.14}$$

where ν is the kinematic viscosity, and ν is equal to the value of air at standard sea level atmospheric conditions ($1.46 \times 10^{-5}\ m^2/s$). For insect/avian based flight, it is common to choose the mean chord as a reference length, which is $\bar{c}$ is equal to wing length divided by aspect ratio ($\bar{c} = b/AR$). The reference velocity in hovering is chosen to be equal to mean wing-flap velocity

($U_{ref} = \omega R$) during a flap-cycle, R is the distance from the rotation axis to the wing tip and ω is the rotational velocity ($\omega = 2\Phi f$, Φ is a flapping amplitude). Therefore, Reynolds number in hover can be written as:

$$\mathrm{Re} = \frac{2\Phi f R \bar{c}}{\nu} \tag{3.15}$$

and in case such $R = b$ (root cut-out is equal to zero), Reynolds number can be reduced to

$$\mathrm{Re} = \frac{2\Phi f R^2}{\nu(AR)} \tag{3.16}$$

For low Reynolds numbers (10-100), no turbulence treatment is needed and so all the simulations are laminar.

When non-dimensionalized, the mean stresses term can be expressed as:

$$\tau_{ij} = \frac{\mu M_\infty}{Re_\infty}\left[\left(\frac{\partial u_i}{\partial x_j} + \frac{\partial u_j}{\partial x_i} - \frac{2}{3}\frac{\partial u_k}{\partial x_k}\right)\delta_{ij}\right] \tag{3.17}$$

It should be noted that the superscript $*$ is omitted here to simplify the notation.

3.1.2.6 Spatial Reconstruction

For spatial reconstruction, a third order MUSCL scheme utilizing Koren's limiter [70] was used, with an option to use higher order schemes such as the Compact-Reconstruction Weighted Essentially Non-Oscillatory (CRWENO) schemes [71]. The inviscid terms were computed using Roe-Turkel flux difference-splitting [72–74] and the viscous terms were computed using a second order central scheme.

3.1.2.7 Time Marching

Implicit dual-time stepping with ten sub-iterations per time step were used to remove the factorization and linearization errors and recover time accuracy for unsteady computations. Convergence of sub-iterations between time steps was ensured by monitoring the density residual for a decrease by at least two orders of magnitude. To complete the flapping cycle, 2880 time steps were used per flapping cycle. To get a converged periodic flow field solution, four flapping cycles are performed. The airloads obtained from the insect kinematics are periodic, therefore the differences between the airloads from the 4^{th} and the 5^{th} are minor. For averaged forces and moments the 4^{th} cycle is considered. Typical run time for the CFD simulation is one week, with an option to restart the solution. In this case the computations require 38 hours on 20 cores per flap cycle.

3.1.2.8 Low Mach Preconditioning

Since a flapping wing MAV operates in low-Mach and low-Reynolds Number flow regime, it is necessary to employ a low-Mach preconditioner to help maintain accuracy and convergence of the compressible Navier-Stokes flow solver near the incompressible limit. The use of the preconditioner achieves several specific goals, among which two are listed below:

1. System stiffness: since there is a large difference between eigenvalues in low Mach flows, the solution is computationally stiff and therefore requires more time to reach a steady-state solution. The preconditioner accelerates convergence by bringing the magnitude of the acoustic eigenvalues closer to the convective eigenvalues, thereby reducing stiffness.

2. Accuracy: A low-Mach preconditioner removes scaling inaccuracies between dissipation terms. This is most beneficial near the stagnation term and near surface boundary layers, since the preconditioner makes the pressure terms and convective terms more consistent to each other [139].

In this work, time accurate low Mach preconditioning in dual-time schemedescribed by Buelow et al. [121] and Pandya et al. [122] is used.

Chapter 4

OVERTURNS: Verification and Validation

This chapter focuses on the validation and verification of the CFD solver, OVERTURNS, in-order to establish confidence in the high-fidelity flowfield model used to predict the aerodynamic loads i.e., forces and moments. Insects operate in a highly viscous flow (low Reynolds numbers), and the characteristic length is small (order of millimeters) compared to existing air vehicles, fixed and rotary wing. Therefore, all validation cases are related to laminar viscous flows, in the range of low Reynolds numbers for which insects (i.e. *drospphila*) operate at (Re$\leq 10^4$).

OVERTURNS was developed primarily for helicopter rotor blade applications, where the operating Reynolds number is of the order of millions (10^6), and the flow is compressible with possibly turbulent conditions. OVERTURNS was previously adapted to simulate aviation flapping kinematics at Reynolds numbers of $10^3 - 10^4$ [68] successfully. In this study, OVERTURNS was further extended to simulate nearly incompressible flow at very low Mach number (i.e., mean tip velocity around 2 – 4 m/s) and Reynolds numbers of the order of magnitude of $10 - 10^2$. The flapping wing simulations require:

- Insect flapping kinematics routine
- Mesh system for insect *diptera* configuration
- Appropriate numerical parameters

To obtain converged, time-accurate solution, mesh spacing and time step were studied as part of a CFD sensitivity study to attain time-accurate simulations, more details are discussed in Section 4.4. Low Mach preconditioning is another parameter that effects the convergence, and it was applied for these low-Mach conditions. The validation study considered a range of flow conditions from steady state flow around stationary objects to unsteady flapping wing cases.

The specific cases are discussed in the following sections:

- Sphere at Reynolds numbers range of 10 – 100.
- Impulsive translated wing at low Reynolds number, Re=300 .
- Unsteady isolated flapping wing at low Reynolds numbers range of 100 – 370.

4.1 Sphere at Low Reynolds Number

This problem of flow around a sphere is encountered in multiple flow regimes; however, the present validation focuses on the flow around a sphere at low Reynolds numbers. The goal is to verify OVERTURNS computational set-up (i.e. grid spacing; time step; boundary conditions) by quantitatively and qualitatively comparing the predicted flowfield with expected results in the steady axisymmetric flow regime at Re less than 120.

Reynolds number is defined as :

$$\mathrm{Re} = \frac{\mathrm{U_{ref}} \mathrm{L_{ref}}}{\nu} \tag{4.1}$$

where $\mathrm{U_{ref}}$ and $\mathrm{L_{ref}}$ are the characteristic speed and length. For the sphere case, $\mathrm{U_{ref}}$ is

equal to the free-stream velocity and the characteristic length is the sphere diameter, which is set as 1 mm. The flow conditions were assumed to be at standard atmospheric conditions; thus, the kinematic viscosity was $\nu = 1.46 \times 10^{-5}\ m^2/s$.

4.1.1 Computational Set-up

Steady flow was computed in a domain that extended two diameters ($4R$) in each direction with $115 \times 121 \times 82$ points in the streamwise, cross-stream and wall normal directions, respectively. The simulations were performed with a single, structured, curvilinear, body-fitted grid that has an O-O topology as shown in Fig. 4.1(a). A spacing of 0.01% of the sphere diameter is used for the first point from the wall in the normal direction, allowing for a fine clustering near the wall (the sphere surface) to capture the flow separation point and vortical structure. As the mesh extends outward this becomes larger, allowing for a coarse mesh spacing where far away from the surface, where a fine spacing is not required, as shown in Fig. 4.1(b). This is demonstrated in that the cell volume becomes larger in the normal direction due to an applied mesh stretching.

Although the sphere cases are steady, the unsteady solver option was still used to ensure that the steady solution is obtained. Also, a constant dual time step is used with 7 sub-iterations. Overall, 6480 steps with constant time step were performed to obtain the forces that reach a steady state with time. The simulations were performed on the University of Maryland high performance computing Deepthought2 (UMD HPC) facilities [75], using 4 processors in parallel (64 CPU hours). The flow around the sphere was investigated for variouse Reynolds numbers:10, 40, 75 and 100. The flow at these Reynolds numbers is laminar, therefore the N-S equations were solved using the

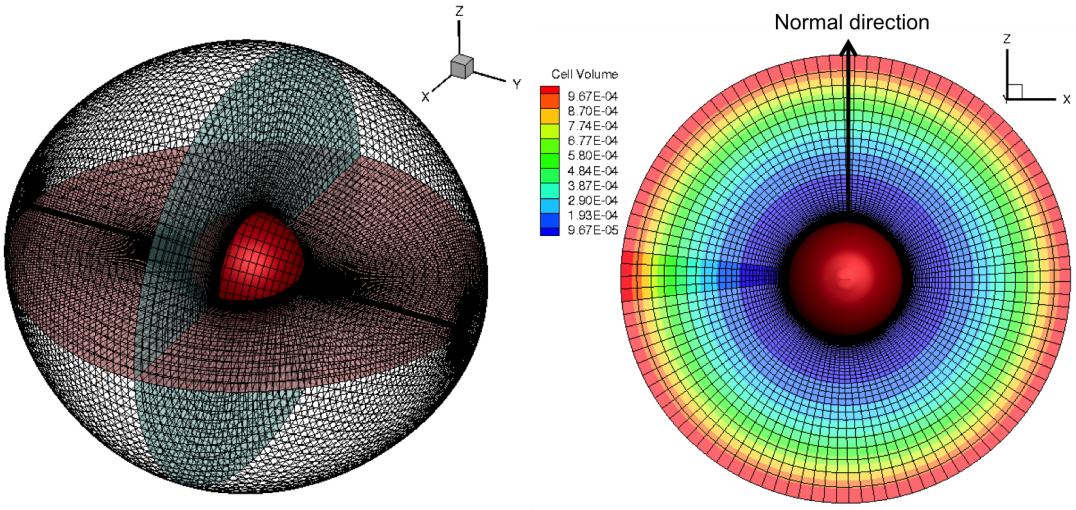

(a) Body-fitted volume sphere grid (b) Sphere grid section in streamwise direction

Figure 4.1: Volume sphere grid, with O-O topology type.

third order MUSCL scheme for spacial discretization of the inviscid terms, second order central differencing for the viscous terms, and a second order implicit scheme for time using backward differencing. Tables 4.1 and 4.2 summarize the relevant computational set-up parameters and grid details.

Table 4.1: Sphere simulation computational parameters

OVERTURNS Solver Options	
Number of grids	1
Total timesteps	6480
Flow	Laminar (viscous)
Newton sub-iterations	7
Pseduo time step	0.1
Spatial scheme - inviscid terms	MUSCL 3rd order
Spatial scheme - viscous terms	2nd order central differencing
Temporal scheme	2nd order backward differencing
Number of processors (Parallel execution)	4 (64 CPU hours)

Table 4.2: OVERSET grid system - Sphere

Mesh	Type	Dimensions	Mesh points (in millions)
Sphere	Structured Body-fitted O-O	$115 \times 121 \times 82$	1.14

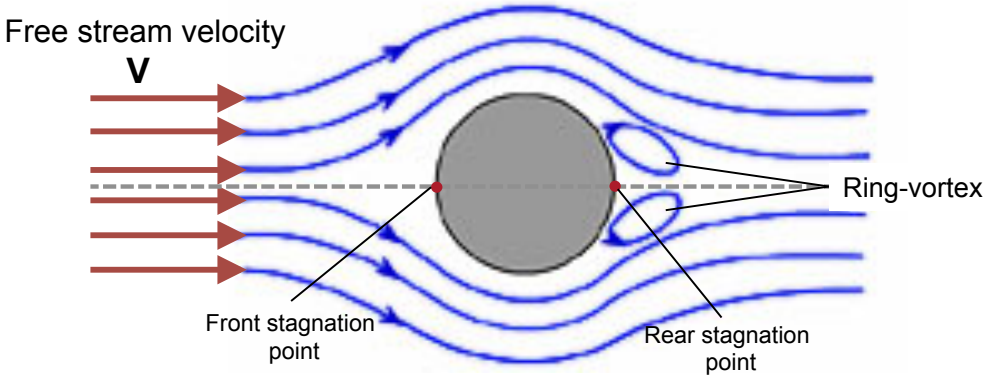

Figure 4.2: Characteristics of flow over Sphere subject to Reynolds numbers $10 < Re < 120$

4.1.2 Results

The flow over a sphere for Reynolds numbers $10 < Re < 120$ was characterized by formation of two permanent vortex-rings symmetric with respect to the rear stagnation point as shown in Fig. 4.2. For Reynolds number less than 10, the flow is perfectly attached (Stokes flow) with no formation of a vortex-ring in the rear side of the sphere and the streamlines are attached to the sphere surface; with increasing Reynolds numbers, the flow starts to separate from the rear side, forming two similar vortices behind the sphere. The laminar separation vortex is referred to by Taneda [7] as a vortex-ring. This vortex-ring is stable and thus permanent at this range of Reynolds numbers.

The streamlines over a sphere from the computational simulations are plotted to compare with streamlines observed in the experiments by Taneda [7], shown in Fig. 4.3. As can be seen

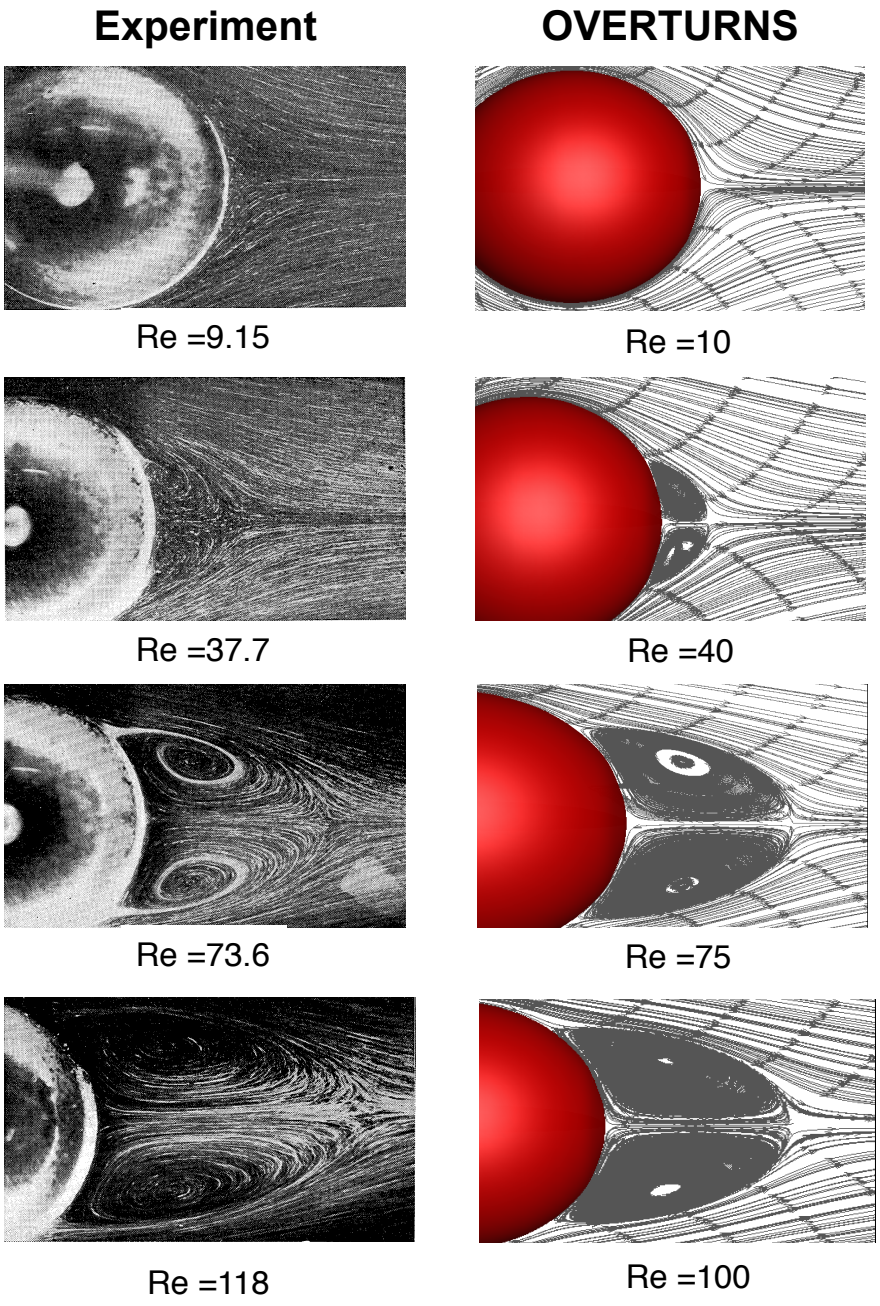

Figure 4.3: Streamlines over a sphere at low Reynolds numbers, on the right side OVERTURNS computational results compared against experimental data obtained by Taneda [7].

from Figure 4.3 the size of the vortex-ring grows as the Reynolds number increases. Considered visually, the flow around a sphere from CFD agrees with the images of the streamlines obtained from experiments, although the vortex-ring size is slightly under-predicted by CFD in comparison to that seen in the experiments.

The size of the vortex-ring and the position at which the flow separation occurs are a function of Reynolds number. These values experimentally were determined by examining the images of the flow around the sphere; similarly these values for the CFD results were determined visually. Figure 4.4 plots the nondimensional vortex length and nondimensional vortex position as compared with the experimental findings of Taneda [7] and the body-fitted computations of Johnson and Patel [76]. The computed vortex locations shown in Figure 4.4(b) are in good agreement with the experimental and prior computational results. Also the computed drag coefficients of the present cases are compared with the results obtained by Hoerner [8] for the drag coefficient of a sphere versus Reynolds number. Reasonable agreement is obtained, as shown in Fig. 4.5.

The simulations results provide confidence that OVERTURNS is able to accurately capture steady separated flow at low Reynolds numbers around spherical geometrics; similar in shape to insect bodies.

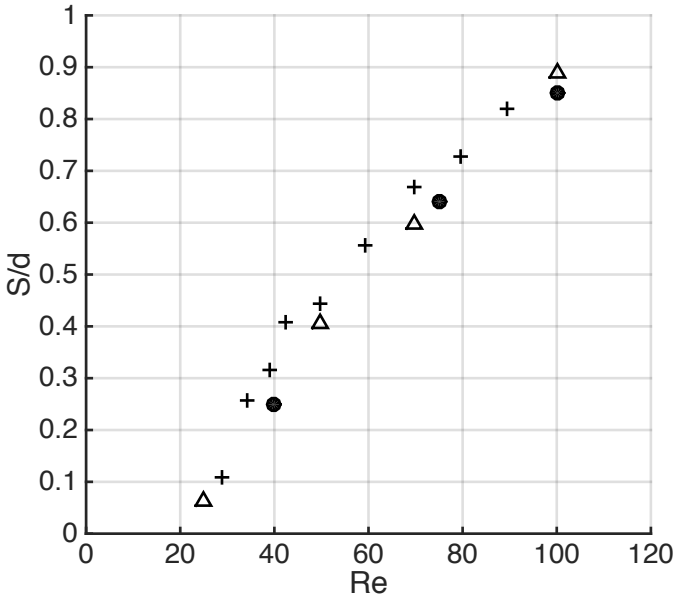

(a) Steady separation vortex length

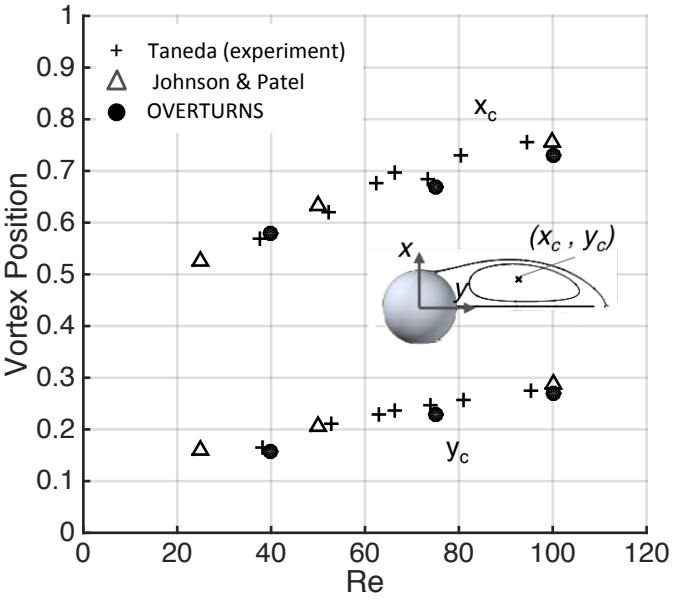

(b) Steady separation vortex position

Figure 4.4: Computed 3D sphere flowfield parameter at various Reynolds numbers.

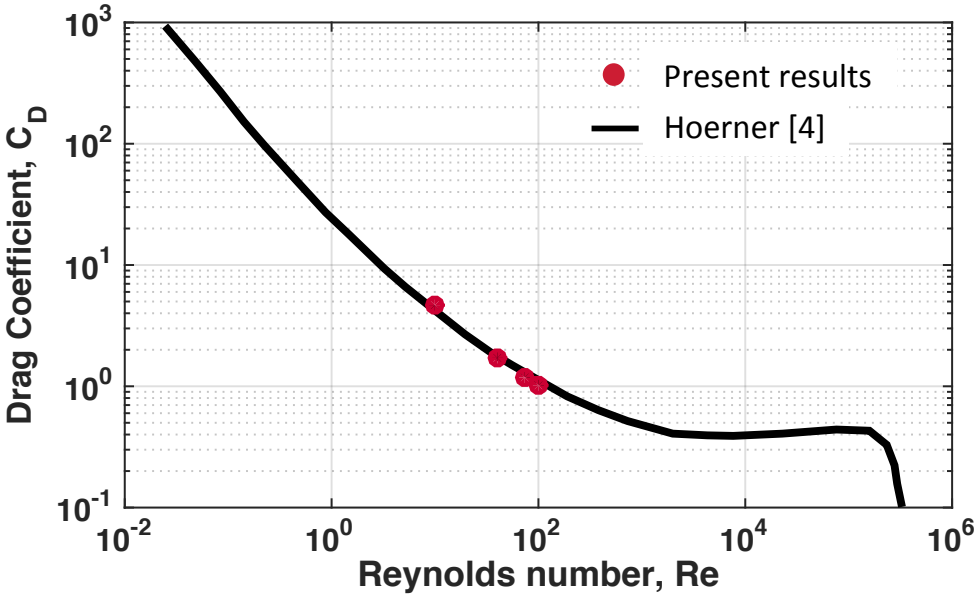

Figure 4.5: Drag coefficient of a sphere versus Reynolds number [8].

4.2 Translational Wing at Low Reynolds Number - Re = 300

In three-dimensions, flow over an impulsively started wing at a fixed angle of attack is computed and compared against a previous study performed by Taira and Colonius [9] on low aspect ratio (AR) flat-plate with various planform geometries. The studied cases in the reference were investigated numerically using a three dimensional immersed boundary (IB) solver. The flat plate was impulsively translated at low Reynolds numbers of 300 and 500. This section presents a verification case, where a bio-inspired wing (with AR of 2.8 at Reynolds number 300 and angle of attack 30°) is compared with different flat planform geometries at the same angle of attack and Reynolds number from the Taira and Colonius study [9]. The time history forces and wake structure were considered for this verification. The planform geometries are rectangular (AR $= 2$), elliptic (AR $= 2$), semicircular (AR $= 4/\pi$), and delta-shaped flat plates (AR $= 4$).

The wing in the present study has a fruitfly *Drosophila* shape, similar to the Robofly wing used by Dickinson et. al., as shown in Fig. 4.6(a). The studied wing has a different planform; however, the wing aspect ratio is in the range of the reference study cases. Therefore, the purpose of the comparison is to highlight the differences and the similarities between the fruitfly wing shape and the other planform geometries, and to investigate if similar force magnitudes and trends are also obtained for the bio-inspired wing shape.

4.2.1 Computational Set-Up

An overset mesh system consisting of a body conforming O-O type wing mesh and two Cartesian background grids (nested) was set-up. Initially, the flapping wing simulations were

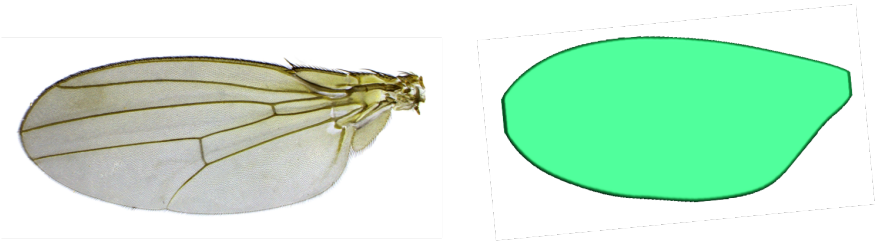

(a) Bio-inspired wing shape

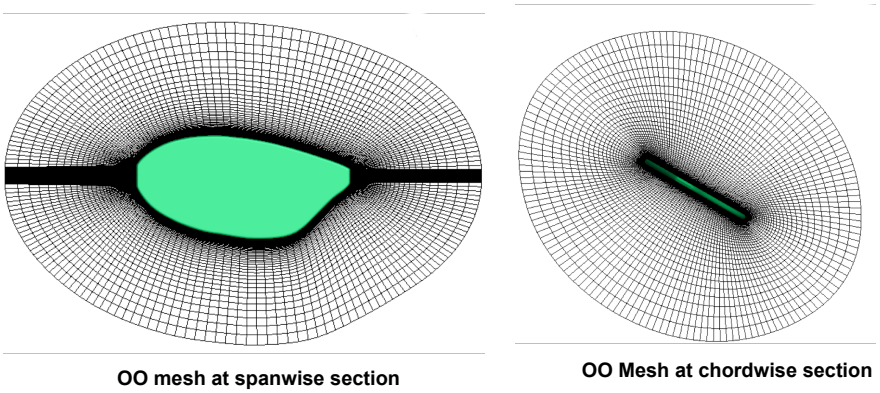

(b) Body-fitted wing mesh

Figure 4.6: The bio-inspired wing computational model, (a) The bio-inspired shape similar to fruit-fly wing shape (b) Body-fitted wing mesh with O-O topology.

performed with one main background mesh; later the one background mesh was replaced by two nested grids that lower the computational cost by reducing one third of the total number of points used in the background. The wing body-fitted O-O mesh is shown in Fig. 4.6(b). The wing body-fitted O-O mesh consists of $155 \times 91 \times 82$ points in the wraparound, spanwise and wall normal directions. A spacing of $1 \times 10^{-4}\bar{c}$ is used in the wall normal direction, and the mesh expands for $1\bar{c}$ in each direction, to resolve the flow in the boundary layer and surrounding region. The wing grid system is shown in Fig. 4.7.

A system of two nested cartesian grids was used as background grids to capture the wake flow-field features; the first background (inner) has finer spacing than the second background mesh (outer). The inner background mesh has a grid spacing of 0.05 chords and the outer background a spacing of 0.2 in each direction in their regions of finest spacing. Such a set of meshes saves many mesh points by refining the spacing in the area of interest. The nested backgrounds meshes are highlighted in Fig. 4.7. The inner background extends approximately $5\bar{c}$ (5 chords) in the x, y, z directions, and the outer background extends approximately $11\bar{c}$ in the x, y, z directions. This distance is chosen to be far enough to prevent any reflections from the farfield boundary. The data connectivity between the overlap regions is handled by using implicit hole cutting [66]. The simulations were performed on UMD HPC facilities, using 16 processors in parallel. Table 4.3 summarizes all computational set-up parameters, and Table 4.4 describes the nested overset grids system.

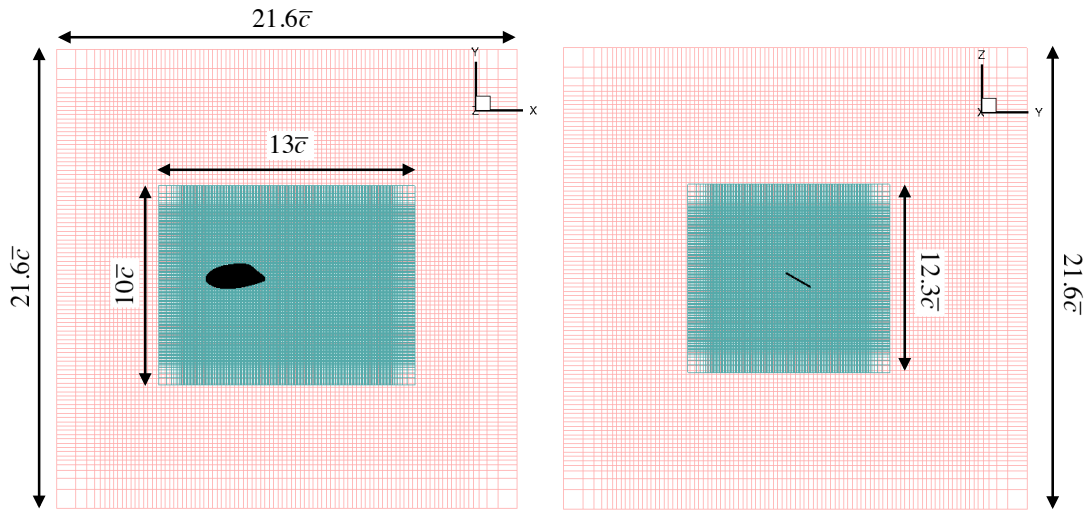

(a) Top view (b) Side view

Figure 4.7: Overset grid system with two background nested meshes.

4.2.2 Results and Discussion

The bio-inspired wing has an aspect ratio of 2.8 and a thickness of 4% of the mean chord, such that it is considered a flat plate. The wing is in the range of low aspect ratio that the cases in the reference study considers ($AR = 2-4$). During insect flight, it has been observed that the stable leading edge vortex of a rotating wing leads to lift enhancement. During the flapping stroke, the shedding of these vortices is prevented by draining the excess vorticity, which is enabled by the wing rotation effect that induces the convective transport of the created vorticity from root to tip. This effect is absent in pure translation. Therefore, the LE vortex detaches from the wing in a manner similar to that of more traditional dynamic stall that very temporarily leads to lift enhancement. But after detachment, the forces reach a steady state value without the effect of the delayed LEV. Figure 4.8 shows the lift and drag coefficients as a function of non-dimensional convective time. Non-dimensional time is defined as $U_\infty t/\bar{c}$, where U_∞ is the free-stream velocity, and $\bar{c}$ is the

Table 4.3: Impulsive translated wing simulation computational parameters

OVERTURNS Solver Options	
Number of grids	3
Total timesteps	8000
Flow	Laminar (viscous)
Newton sub-iterations	10
Pseduo time step	0.1
Spatial scheme	MUSCL 3rd order
Temporal scheme	2nd order backward in time
Processors (Parallel execution)	16

Table 4.4: OVERSET grid system - Impulsive translated wing

Mesh	Type	Dimensions	Mesh points (in millions)
Wing	Structured Body-fitted O-O	$155 \times 91 \times 82$	1.15
Background 1	Structured Cartesian	$212 \times 160 \times 148$	5
Background 2	Structured Cartesian	$95 \times 95 \times 95$	0.85
Total mesh points - 7 M			

mean chord. Maximum lift was achieved after the impulsive start and decreased slowly afterwards to approximately half of the earlier maximum value at large time. It was concluded from the reference study cases that for most of the cases, maximum lift was achieved at a non-dimensional time around $t \approx 1.7$ regardless of the aspect ratio, angle of attack and planform geometry [9]. From the comparison of the present wing the maximum lift was obtained at $t \approx 2$. In the reference study it was found that a curved or angled LE led to a slight delay in the LEV, but it wasn't sufficient to induce a transport of a spanwise vorticity. The bio-inspired wing in impulsive translation follows the observed trend for the lift and drag coefficients. The drop in the forces occur as a results of the leading-edge vortex detachment and convection downstream. The overall trend for the lift and

drag histories was found to be similar to those of the flat plate with various geometries.

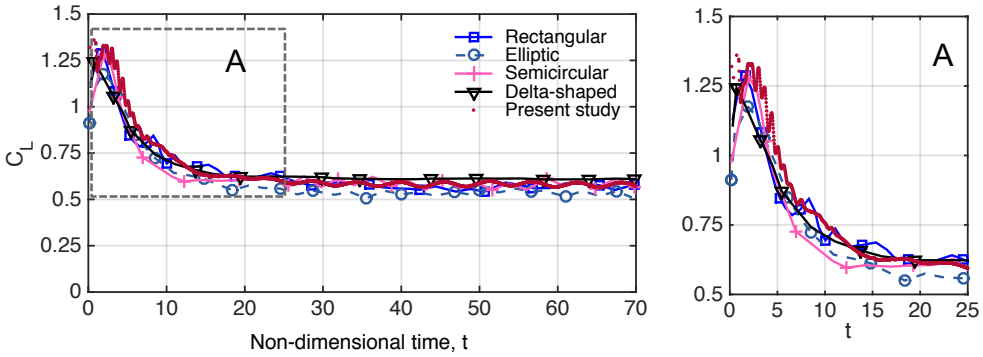

(a) Lift coefficient

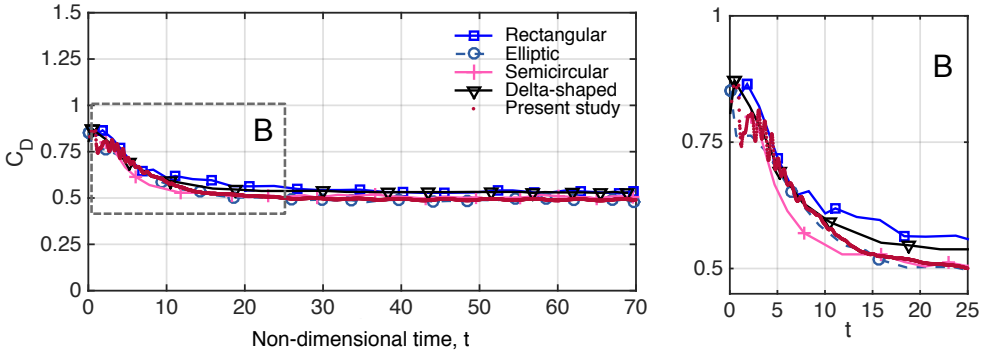

(b) Drag coefficient

Figure 4.8: Time trace of lift and drag coefficients for 4 planforms (rectangular, elliptic, semi-circular and delta-shaped) [9] compared with present study wing (bio-inspired) at Re $= 300$ and $\alpha_g = 30^\circ$. The figures on the right side magnify the corresponding transient behaviour at early time shown in the left-side figures. The wing planforms are elliptic, semicircular and delta-shaped with AR of 2, 2, $4/\pi$ and 4, respectively. The present study wing has a bio-inspired shape, and AR $= 2.8$.

The wakes behind non-rectangular wings are shown along with the present study wing in Fig. 4.9. For the elliptic and semicircular cases, there are no discontinuities in the vortex sheet that emanates from tip to tip, therefore the vortices detach from the tips. For delta wing the vortex shedding occurs in a different fashion, with discontinuity in the LEV at mid-wing. The bio inspired wing developes a conical shape of leading edge vortex (LEV), such that it's strength increases from

tip to tip. Among the different planform geometries, the wake structure behind the bio-inspired wing is most similar to the elliptic wing.

The main conclusion made by Tairan and Colonius was that at large time (t$>$ 20), depending on the aspect ratio, angles of attack and Reynolds number, the wakes reached one of the three states: (1) a steady state, (2) a periodic unsteady state or (3) an aperiodic unsteady state. For a wing with aspect ratio of 2.8 and angle of attack of 30° (bio-inspired wing), at large time the wake reaches a periodic unsteady state. These states are concerned with the natural shedding of the leading and trailing edge vortices, which in this case will be in a periodic fashion. While the vortical flows are different for the various planform geometries, the lift and drag exerted on the wings do not show significant variations as shown in Fig. 4.8. This results from the viscous nature of the flows at this low Reynolds number, even thought the wake structure (vortical shedding) changes as a function of planform geometries.

In conclusion, an impulsively translated flat wing with bio-inspired shape at low Reynolds, will experience unsteady vortex dynamics due to the formation of leading edge vortex that shed. After a large time, the forces will reach either a steady value or a slightly oscillatory value for both lift and drag. The lift and drag exerted on the present study wing was similar to the magnitude and trend of the forces that flat plates with low aspect ratio and various planform geometries (i.e. elliptic, rectangular) experience. The wake structure and the vortical shedding is affected by the wing shape and in this case, the structure and the vortical behavior of the bio-inspired wing is similar to the elliptic shape (curved LE).

This study provides confidence in OVERTURNS to be able to predict the unsteady flow

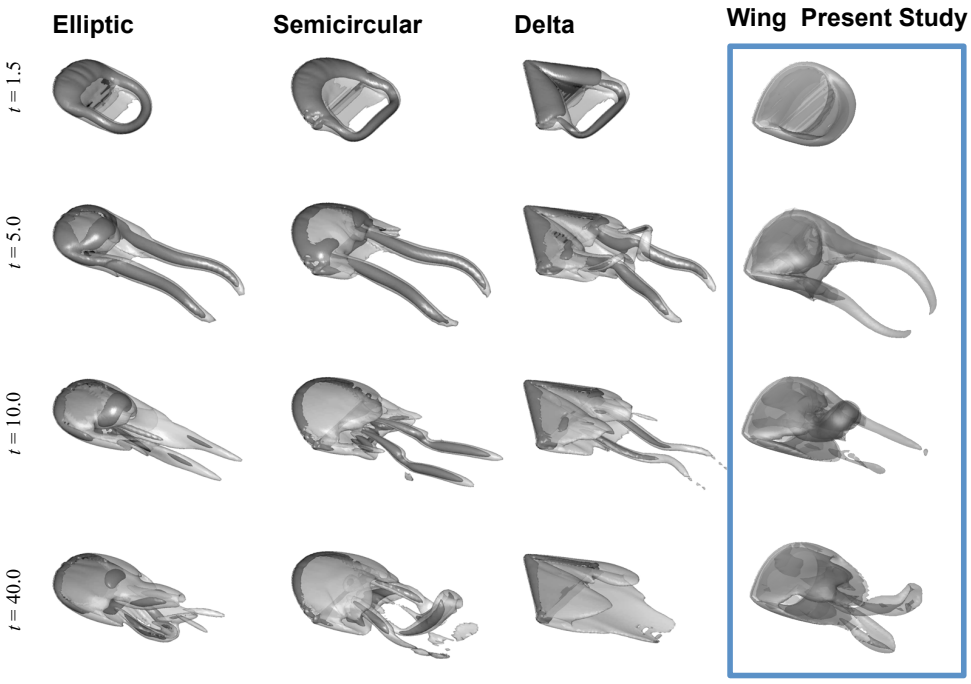

Figure 4.9: Isometric views of the wake vortices behind different planform geometries at $\alpha_g = 30$ degrees and Re $= 300$ with iso-surface vortex obtained from the reference study [9], compared with the present study (OVERTURNS). The wings have elliptic, semicircular and delta-shaped planforms are chosen with AR of 2, 2, $4/\pi$ and 4, respectively. The present study wing has a bio-inspired shape, and AR $= 2.8$.

around insect wing-like shapes at low Reynolds number.

4.3 Unsteady Wing at Low Reynolds Number in Hover

This section contains the validation of OVERTURNS prediction of a flapping wing against experimental data at low Reynolds number. Basic uncertainty and repeatability tests were performed as part of the experiments and are detailed in this section.

4.3.1 Computational Model

The computational wing model planform approximates the geometry of the blowfly wing. This geometry is based on a scaled model of a blowfly used by the US Army Research Laboratory (ARL Low Reynolds Number Oil Tank [10]), as shown in Fig. 4.10. The wing is located with a 0.75 mm offset from the rotation axis for the wing-span of 3 mm. The aspect ratio (AR) of the wing is defined as root-to-tip divided by average chord, and is equal to 2.7.

The mesh system for the flapping wing consisted of a body-conforming O-O wing mesh and a cartesian background mesh as shown in Fig. 4.11. An overset mesh system was used to capture all the features of the flow field. Those features include the vortices and the interactions between the wing and the wake produced during the reverse stroke. The wing has 121 points in the wraparound direction, 101 points in the spanwise direction and 67 in the normal direction. The mesh near the wing surface is refined, with a spacing of 1×10^{-4} of mean chord in the wall normal direction. The Cartesian background mesh has $22.4\bar{c}$ length in the y direction, $17.6\bar{c}$ in the x direction and $15\bar{c}$ in the z direction, with $286 \times 322 \times 95$ points respectively. The overset set-up is summarized

(a) Blowfly *Calliphoridae* wing shape

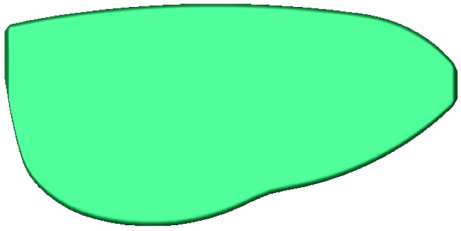

(b) Blowfly computational model

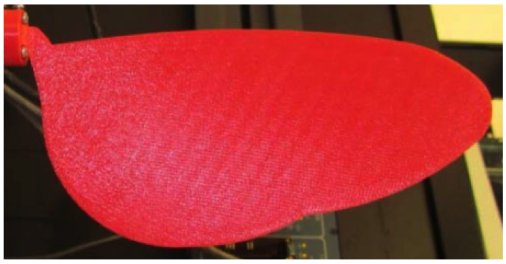

(c) Blowfly experimental model

Figure 4.10: The bio-inspired blowfly wing shape. Aspect ratio of the computational and experimental model is equal to 2.7.

in Table 4.5; the total mesh points is 9.8 million.The spacing in the finer region of the background is $0.05\bar{c}$. For the flapping wing simulation, the time step is given in terms of azimuth size, which is the same time definition used by rotor blades simulations. In these simulations time-step of 0.125 degree is used, such that 2880 steps are required to complete one flapping cycle (upstroke and downstroke). Up to 10 Newton sub-iterations were used to remove the factorization error and obtain time accuracy for unsteady computations. The computational set-up for the isolated wing is summarized in Table 4.5. The computations were performed using 32 processors.

All of the computational results shown in this study were obtained after the solution had converged to a periodic flow. The convergence of the solution was determined by two factors: 1) The drop in the density residual during the Newton sub-iterations; which was required to be reduce by at least two magnitude to ensure that the solution is temporally converged, and 2) A constant or

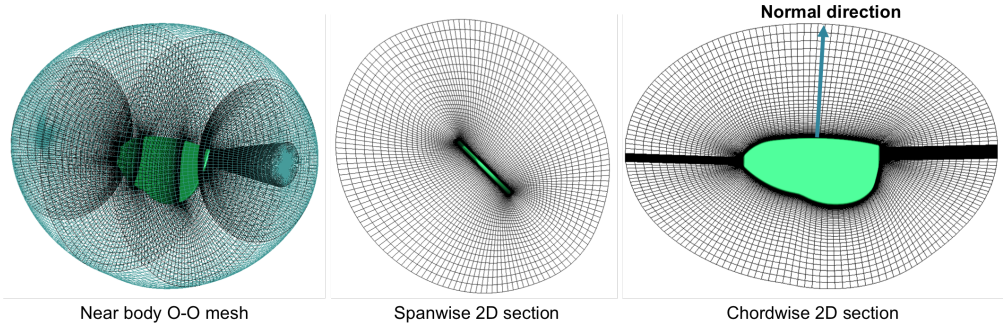

(a) Body-fitted O-O wing mesh

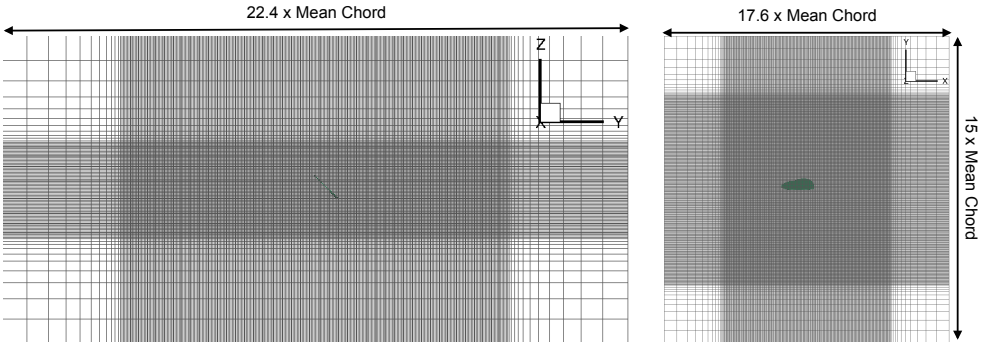

(b) OVERSET grid

Figure 4.11: Computational domain of an isolated hovering wing. (a) Blowfly wing volume mesh (b) OVERSET grid system contains wing and background.

Table 4.5: Flapping wing simulation computational parameters

OVERTURNS Solver options	
Number of grids	2
Total timesteps	12240 (2880 steps/cycle)
Flow	Laminar (viscous)
Time-step size	0.125 degrees
Newton sub-iterations	10
Pseduo time step	0.1
Spatial scheme	MUSCL 3rd order
Temporal scheme	2nd order backward
Processors (Parallel execution)	32

Table 4.6: OVERSET grid system - Unsteady wing

Mesh	Type	Dimensions	Mesh points (in millions)
Wing	Structured Body-fitted O-O	$155 \times 91 \times 82$	1.15
Background 1	Structured Cartesian	$286 \times 322 \times 95$	8.7
Total mesh points - 9.85M			

periodic trend in the force and moment history across the flapping cycles.

4.3.2 Wing Kinematics

The prescribed kinematics for these simulations describe a normal-flapping mode where the pitch angle is 90° at the end of each half stroke as in Fig. 4.12. The wing motion is an idealized fruit fly wing motion with a flapping stroke angle rotating through a 120° arc. The rotational velocity is sinusoidal, and the maximum velocity occurs at midstroke. The geometric angle of attack (pitch angle) remains nearly constant except near the stroke reversal during supination and pronation. The kinematics are described by the following equations:

$$\alpha_g(t) = 90 - \alpha_{max} \tanh(2.7 \sin(2\pi f t)) \tag{4.2}$$

$$\phi(t) = -\phi_{max} \cos(2\pi f t) \tag{4.3}$$

where ϕ is the flapping stroke angle (the rotational position angle), ϕ_{max} is the amplitude of the stroke, f is the wing stroke frequency, α_g is the pitch angle (also can be referred as geometric angle of attack), and α_{max} is the amplitude of the pitch angle at one quarter of the flap stroke. For this study, ϕ_{max} is defined as 60°. The kinematics angles are described in Fig. 4.12(a), along with

the flap stroke description in Fig. 4.12(b).

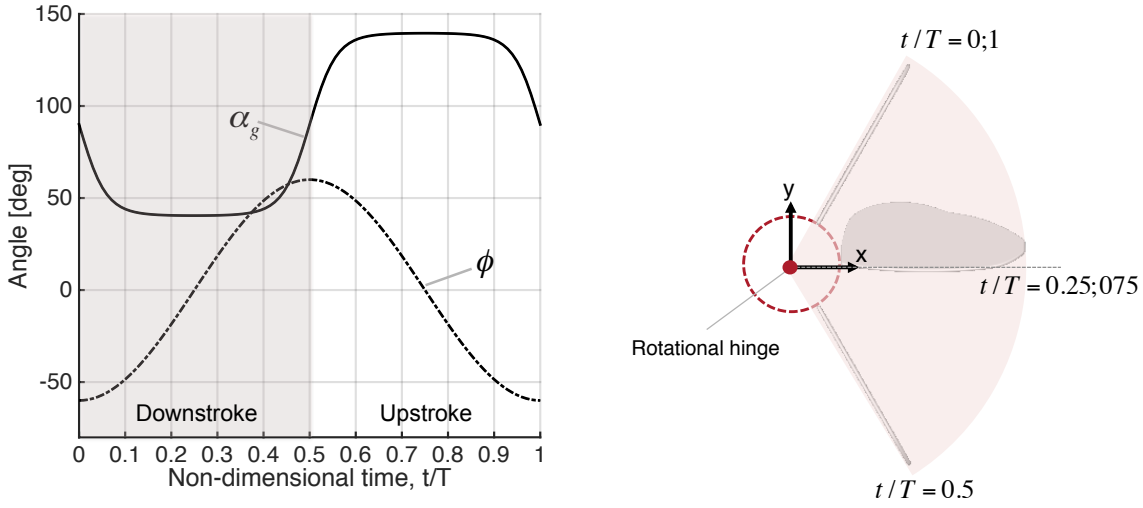

(a) Positional angles (b) Flapping stroke

Figure 4.12: Description of the flap angle ϕ with $\phi_{max} = 60^\circ$ and the pitch angle α_g with $\alpha_{max} = 45^\circ$.

The wing is assumed to be a rigid body, with a 3 mm span with root-cut of 0.75 mm. The kinematic parameters investigated were (1) flapping frequency f ranging from $100 - 300$ Hz with steps of 50 Hz and (2) geometric AoA (pitch angle) which was parameterized to include 30°, 40°, 45°, and 60° as observed at the middle of each half stroke where the pitch axis is at the leading edge, (Fig. 4.12). The pattern of this idealized kinematics will be consistent for all the studies presented in this dissertation, with only the magnitude of the pitch angle and maximum flap angle varying.

4.3.3 Experimental Set-Up

The facility used to conduct the flapping wing experiments is an oil tank, which is depicted in Fig. 4.13(a-b). The tank's cross section is hexagonal, spanning 63.5 cm from opposite walls,

and is 76 cm tall. The working fluid is mineral oil with a density of 850 kg/m^3 and a viscosity of 16.8 $mPa \cdot s$ at room temperature. The tank, filled to a height of 71 cm, contains a volume of 248 liters of oil. The ARL wings are designed to match the kinematics and shape of a fruit fly. In the simulations, only the wing was modeled and not the rest of the structure.

The wing studied was supported at the wing root by a six-component balance (ATI Nano-17 titanium [77]) with the axis of rotation for the wing in the center of the tank. The motion of the wing and balance was controlled through an apparatus which has two degrees of freedom, wing rotation (flapping axis) and pitch. The wing rotation is controlled by a stepper motor on the top of the tank with the motion transmitted down the larger of two concentric shafts. The mechanics for the wing pitching motion were mounted in the rotating frame of reference with a second stepper motor controlling the wing pitch through the center shaft and bevel gears. Analog balance outputs were routed through a slip ring out of the rotational frame to a signal conditioning unit and ultimately to an analog to digital converter (ADC).

The wing models themselves, one of which is depicted in Fig. 4.13c, conformed to the planform used in the numerical modeling but were scaled isometrically to a larger size, so that Reynolds number obtained in oil would be consistent with that in air. The span from the axis of rotation to wing tip was 17.5 cm with a root cutout of 20% of that span. The wing thickness did not scale with the computational model but was 3.7 mm.

Commanded angular positions were achieved utilizing a stepper motor with a resolution of 2,000 steps per revolution. The rotation and pitch axes were geared down by factors of five and two, respectively, from the motor to the axis of rotation of the wing. This results in positioning

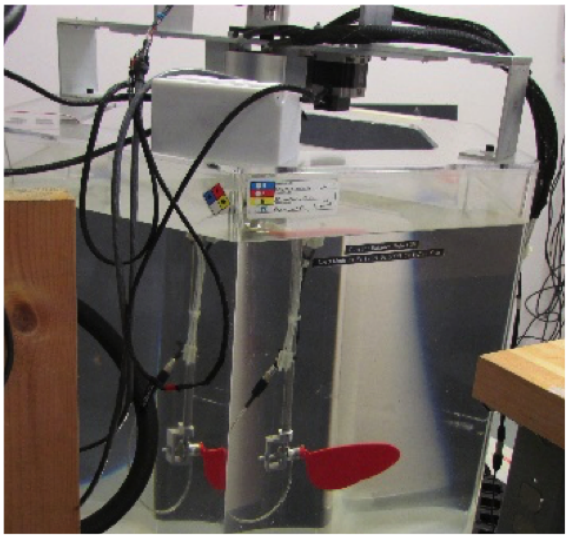

(a) Hexagonal tank

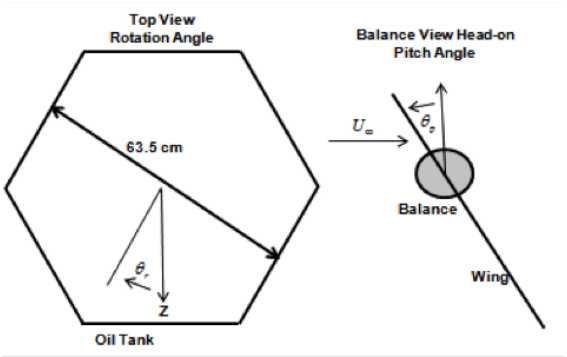

(b) Motion coordinate system

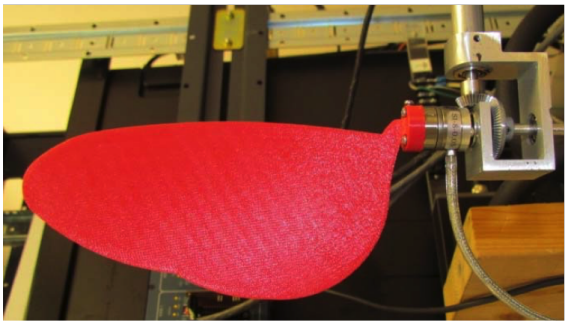

(c) Mounted wing model

Figure 4.13: The oil tank facility: a) The hexagonal tank with supporting infrastructure, b) the definition of the motion coordinate systems for the rotation and pitch degrees of freedom and c) the wing model mounted to the balance [10].

resolutions of 10,000 and 4,000 steps per revolution. The angular motions of the rotational and pitch axes were each monitored with motor-mounted encoders capable of resolving 2,000 steps per revolution, matching the resolution of the motors.

Wing alignment is performed with an alignment tool whenever a new experiment is initiated. This alignment device was mounted to the rotational drive shaft and the wing pitch angle was adjusted to ensure it was vertically aligned with the drive shaft by positioning it flat along an aluminum edge on the alignment device, Fig. 4.14. This alignment position was then referenced to the once-per-revolution index position of the relative pitch encoder. With this index, the wing was then realigned to vertical once submersed in oil.

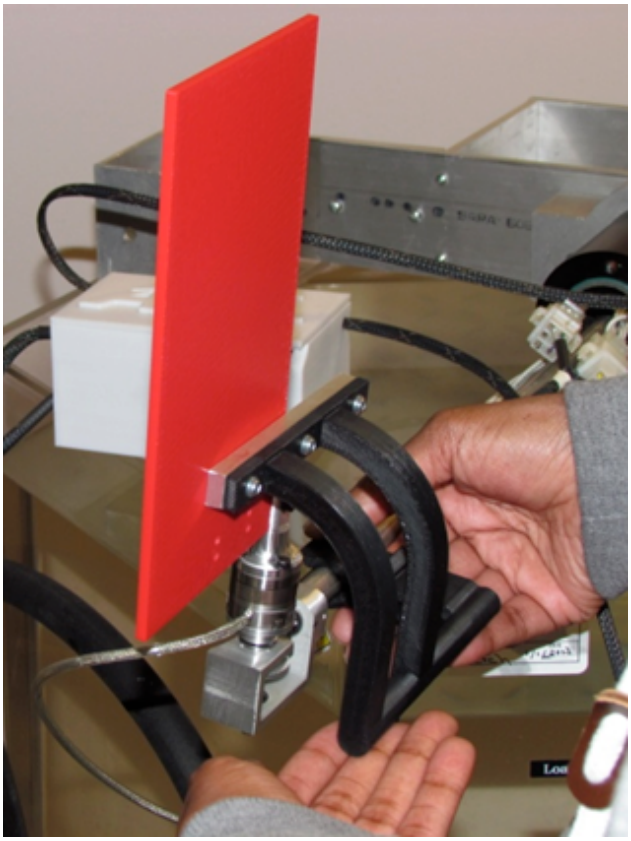

Figure 4.14: Aligning the wing with the rotational shaft. The depicted wing is not the subject of this study.

Figure 4.15 depicts the motion executed by the wings during the flapping experiments. These kinematics conform to those of the numerical simulations. The computational frequencies modeled at insect scale were 150 and 300 Hz. The corresponding Reynolds number matched frequencies in oil were 0.094 and 0.187 Hz respectively. Figure 4.15(a) reflects the measured rotational position through five flapping stokes for each of the flapping frequencies. The corresponding pitching profiles appear in Fig. 4.15(b) reflecting the three pitch angles tested.

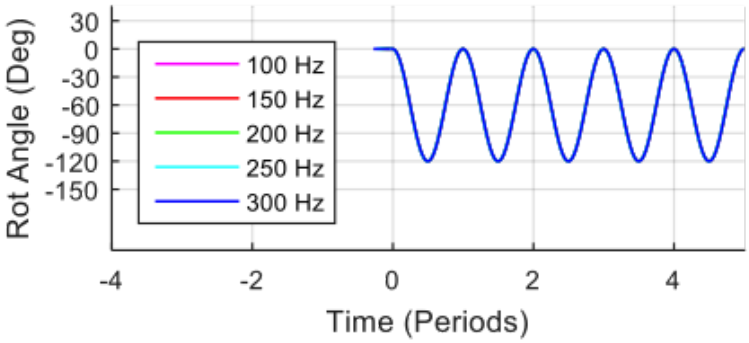

(a) rotational angle

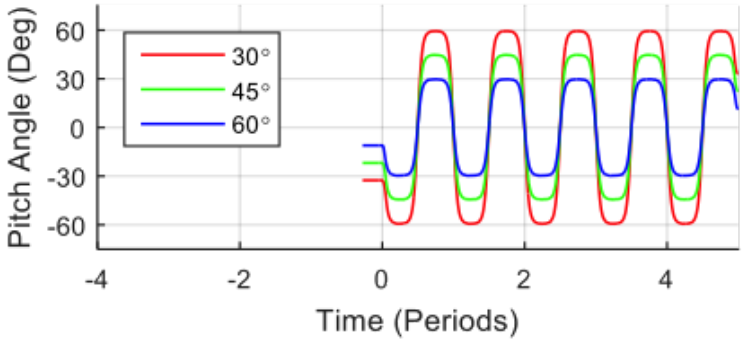

(b) Pitch angle

Figure 4.15: The kinematics of all trials were measured in the a) rotational and b) pitch axes over time.

The balance and encoder signals were all measured simultaneously with an ADC. Doing so ensured that all the data measurements were temporally synchronized. To ensure proper measurement of the encoder pulses, a sampling frequency was selected to ensure no pulses went undetected.

This resulted in sampling frequencies of 6400 Hz and 12,800 Hz for the slower and faster rotation rates respectively. The ADC applied analog filtering to prevent aliasing, and while processing the data the force time histories were further filtered with a sinc low pass filter, using a 0.75 period wide Hann window, with a cut-off frequency at 10 times the flapping frequency of the wing.

The zero force measurement of the balance is prone to drift over time, being a strong function of the local temperature. To negate this possible drift between runs, a zeroing procedure was performed prior to every run. This involved rotating the balance mounted wing through eight angular positions and measuring the voltage response of the six balance channels at each position. These eight positions started at -90° from vertical and stepped through 30° increments. With this data the effects of wing weight as a function of angle of attack, and any zero force offsets, could be calculated and subtracted from the balance measurement. Balance voltages could then be converted to units of force using a factory provided calibration.

4.3.3.1 Force Conversion

The forces reported from the experiments were converted from the actual force measurements to that which would be measured at the insect scale. The matched kinematics share the same pitch and flapping amplitudes and otherwise satisfy the equation:

$$\frac{\rho_a \omega_a {R_a}^2}{\mu_a} = \frac{\rho_o \omega_o {R_o}^2}{\mu_o} \tag{4.4}$$

where ω is the flapping frequency, R is the wing span, μ is the viscosity of the fluid, and ρ is the density. The subscripts "a" and "o" refer respectively to "air" and "oil" where oil are

the characteristics of the experiment and air those of the insect scale. With the Reynolds number matched, the forces, F, scale according to only the fluid properties:

$$\frac{F_a}{F_o} = \frac{\rho_o {\mu_a}^2}{\rho_a {\mu_o}^2} \tag{4.5}$$

For an air density of 1.225 $\mathrm{kg/m^3}$ and viscosity of 17.89 $\mu\mathrm{Pa-s}$, the resulting scaling factor from the experiment to insect-scale is 7.87×10^{-4}.

4.3.3.2 Analysis of Measurement Uncertainty and Repeatability

There were several sources of measurement uncertainty and noise in these experiments. These sources include uncertainty associated with the accuracy of the measurement systems (force balance, ADCs and encoders) and undesired wing kinematics (motion introduced by the stepper motors through unsteady forcing).

All data was digitized using one of two National Instruments PXI-4472b cards. Force measurements were made using an ATI nano-17 titanium six-component balance. These were all calibrated by the manufacturer within the last year as recommended. The measurement resolutions were 24 bits for each analog to digital conversion and ± 4.7 μN (± 0.006 N in unscaled units) in each force axis. The measurement of the commanded positions is within $\pm 0.036^\circ$ for the rotation axis and $\pm 0.09^\circ$ for the pitch axis. For the rotational axis, there is no need to achieve alignment with an absolute position but this is required for the pitch degree of freedom. The uncertainty of the wing root position is dominated by this initial alignment of the wing, which proceeds as described above. Based on the length of the wing positioned along the alignment gage and the estimate that

a gap of 0.5 mm can be easily perceived, the initial alignment is within $\pm 0.6^{\circ}$.

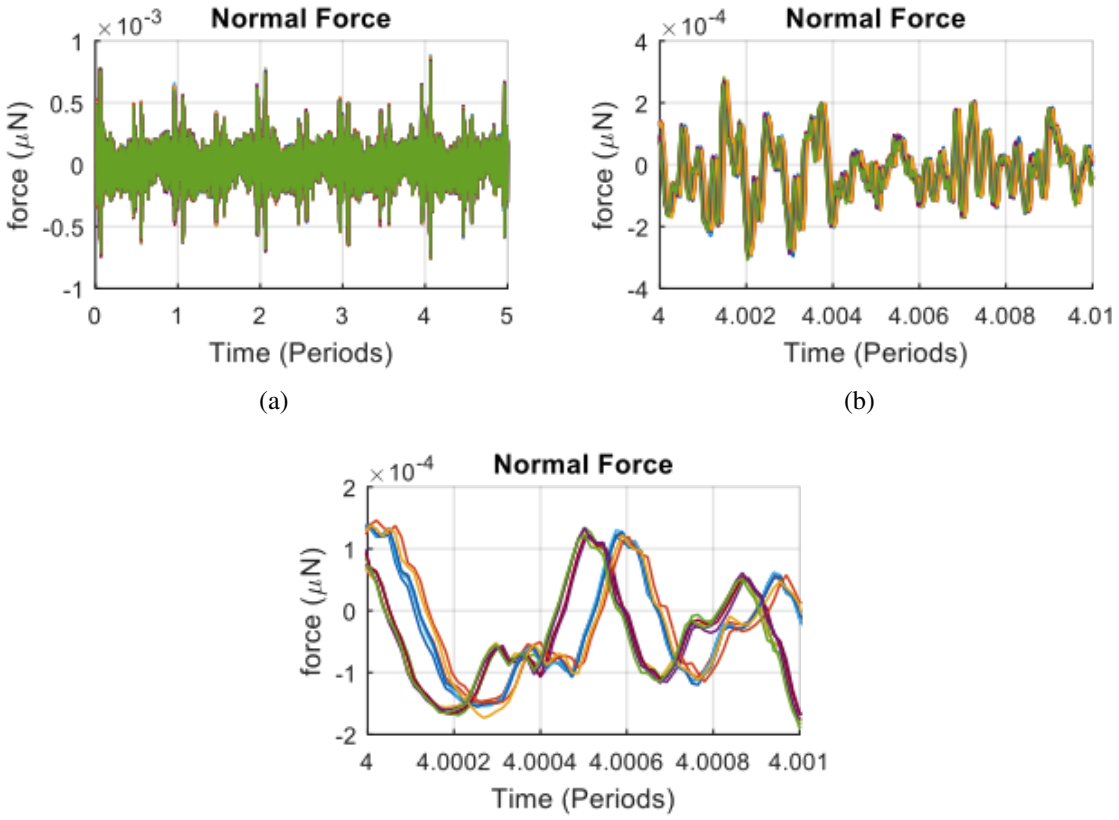

Figure 4.16: Increasingly magnified view of the force measured perpendicular to the plane of the wing throughout five flap strokes of 12 different runs (simulating 150 Hz with at 30 degrees angle of attack). At the highest resolution, it becomes clear that the high frequency oscillation from several trials are quit repeatable with minimal undeterministic noise overlaid. There is some temporal misalignment between the multiple curves, with two pairs of clustered results.

Beyond these measures of uncertainty, there is unsteady motion exhibited in the wing which introduces large amounts of noise. These take the form of oscillations, with high frequencies introduced by the tank's drive system. The stepper motors move the wing through a series of discrete positions (with step sizes noted in the previous section). The stepper motors, relative to the common servo-motor alternative, are well designed to following precision motion profiles.

However, while appearing like smooth motion, each step is a rapid high torque input and these impulsive loads are apparent and deterministic in this system (see figure 4.16).

Twelve trials were repeated for each of the six kinematic profiles presented. Each was filtered as described above and the 12 trials were averaged. Calculating the temporally varying standard deviation from the multiple runs gives some measure of the repeatability of each measurement. The plotted region of uncertainty depicted in Fig. 4.17 represent the sum of the ± 4.7 μN balance measurement uncertainty and three standard deviations of measurement variability (achieving the 99.6% confidence interval assuming the noise profile represents a normative distribution).

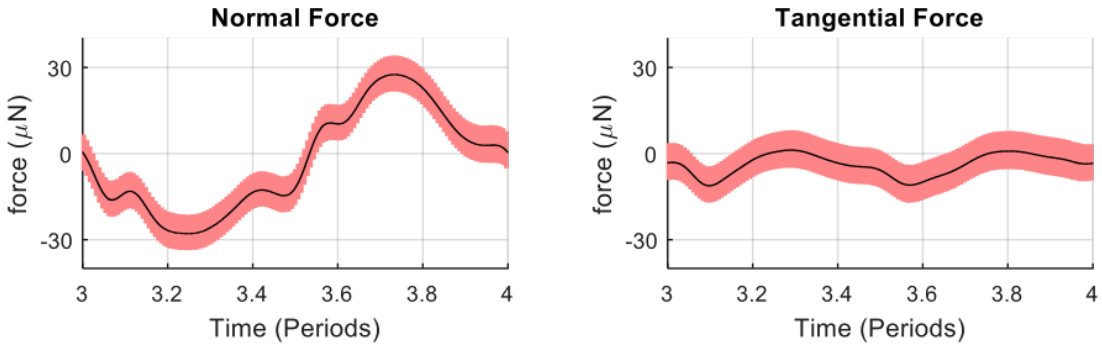

(a) (b)

Figure 4.17: The measured forces a) normal and b) tangential to the wing surface plotted with uncertainty representing the sum of ± 4.7 μN and 3 standard deviations of the filtered noise for the 150 Hz, 60 degrees angle of attack case.

It should be noted that the experiments used a scaled wing with similar shape and pitch angle as in the simulations. Care was taken to ensure that the resulting Reynolds number was the same.

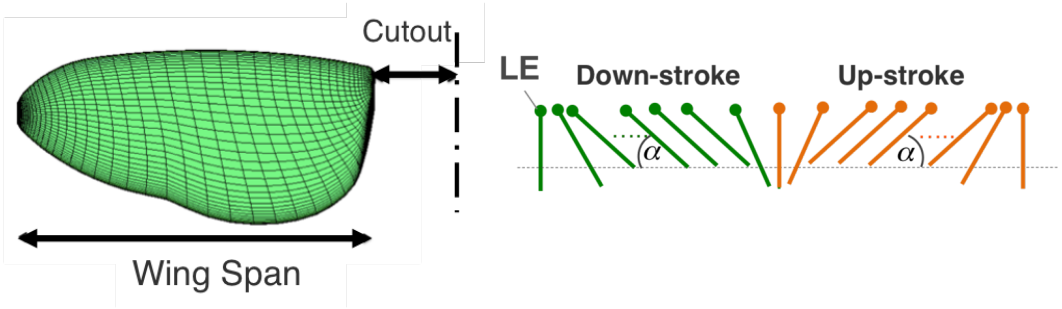

(a) Computational wing base-line

(b) Flapping stroke

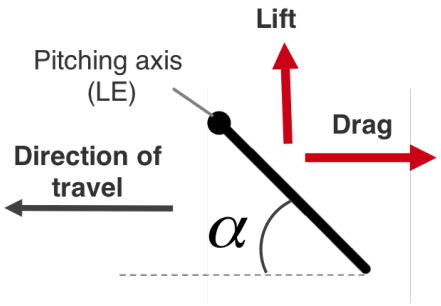

(c) Flapping wing forces

Figure 4.18: (a) Computional wing base-line, wing span of 3 mm and root-cut of 0.75 mm (from the flap rotation axis), the wing pitch around the leading edge axis, (b) The flap stroke consists of up-stroke and downstroke, the demonstration shows the chord section evolved in time during the flap cycle, (c) Schematic aerodynamic forces lift and drag.

4.3.4 Results and Discussion

4.3.4.1 Physical Understanding

It is known that the flowfield around a flapping wing at low Reynolds numbers, in hover or otherwise, is highly vortical in nature. The primary source of lift enhancement in flapping wings with insect-like kinematics are the unsteady sources. This phenomenon is especially true for low-Reynolds number flows. Sane and Dickinson [6] investigated lift enhancement mechanisms in hovering insect flight and they defined three major aerodynamic sources: (a) Delayed stall, (b) Rotational circulation, and (c) Wake capture, (which were described in the background (Chapter 2, Section 2.3). In the present study the wing (see Fig. 4.18(a)) was designed for the experiments and the numerical simulations to undergo a prescribed harmonic motion.

A representative simulation is chosen to explain the vortical structure and the airloads the wing experiences during a flapping cycle in hover, Fig. 4.18(b). The kinematics of the wing consisted of a 45 degrees pitch angle with a flapping frequency of 300 Hz, which corresponds to a Reynolds number of approximately 346. Details of the time-dependent lift and drag (as defined in Fig. 4.18(c)) from both experimental measurements and computational simulations along with the flow field at key instances during the flapping cycle are shown in Fig. 4.19. The presented case demonstrates a hovering environment in which there is no free-stream velocity imposed on the wing and the flapping cycle is symmetric, and the downstroke and upstroke are similar.

It can be seen from Fig. 4.19 that during each stroke there are three positive peaks in the lift and drag denoted by times A, B, and C in the down-stroke and D, E, and F in the up-stroke. By definition, lift is the component of the total aerodynamic force along the wing-span perpendicular

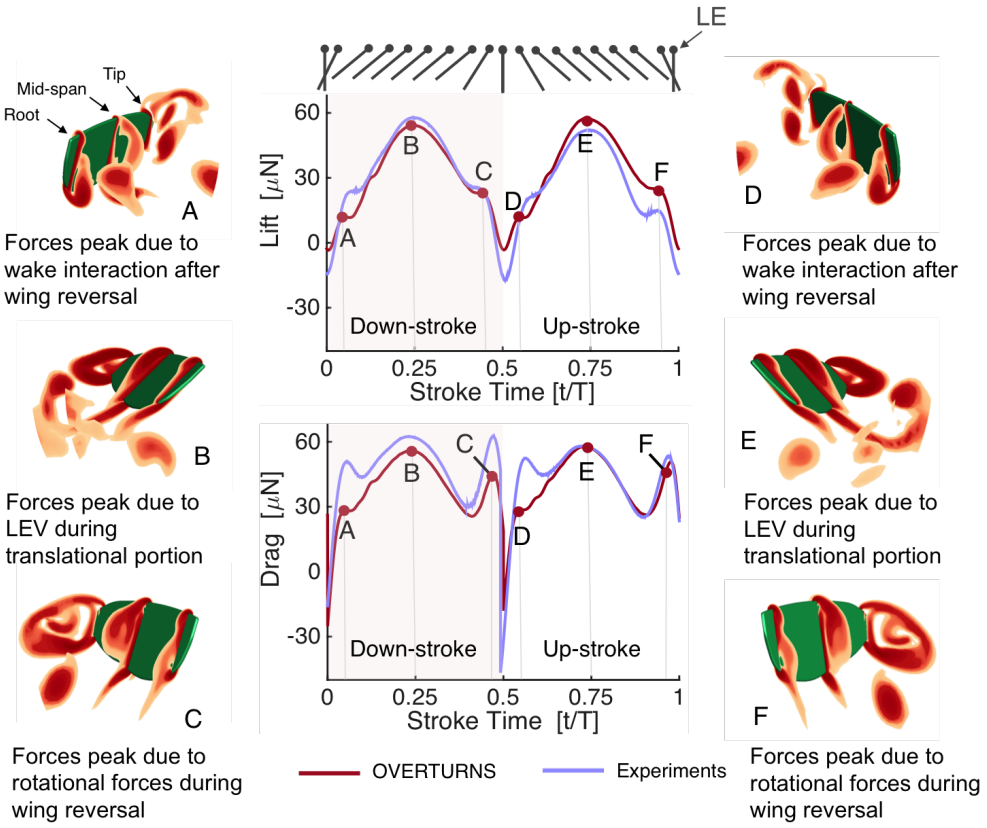

Figure 4.19: Experimental and computational lift and drag forces at Reynolds number 346, where the peaks A, B, C, D, E and F are described by the vortex magnitude at three chord-wise sections; root, mid-span and tip during the flapping cycle.

to the translational velocity and drag is the component of the total aerodynamic force parallel to the translational velocity. Therefore, drag is positive when the vector points in the opposite direction of the translation velocity, as shown in Fig. 4.18(c). At the beginning of each stroke the local peak in forces was obtained from the wake capture mechanism (peaks A and D), where the wing encounters the vortices shed/trailed from the previous stroke in the cycle. The local peak toward the end of each up or down stroke (C and F) was attributed to the rapid acceleration of the wing, as a result of the pitch-up motion.

Alternatively, the earlier conclusions can be arrived at by studying the flow field around the hovering wing. Aligned along the edges in Fig. 4.19 are instantaneous snapshots of the vortical structure in the wake (corresponding to points annotated in the lift and drag curves), at three locations along the span in the chord-wise direction, i.e., wing-tip, mid-span and wing-root. At points A and D, where the first peak of each stroke was observed, the wake structure behind the wing is comprised of shedding vorticity from the tip and root, and in the mid span from the leading-edge (LE) and trailing-edge (TE). This interaction of the wing with the vortical wake corresponds to the local peak in the aerodynamic forces. At points C and F, the wing flips at the end of the stroke, it can be seen that vortices are most prominent on the upper surface as they shed from the wing, which will now correspond to the lower surface of the wing after the wing flips. This local peak in forces corresponds to the rapid pitch-up motion as described by the wing kinematics.

4.3.4.2 Validation against Experiments

To validate the results predicted by OVERTURNS simulations against experimental measurements, three different pitch angles (30°, 45° and 60°) were simulated at Reynolds numbers ranging from 75 – 360. Reynolds number in this case is defined as:

$$\mathrm{Re} = \frac{\mathrm{U_{ref}}\bar{\mathrm{c}}}{\mu} \tag{4.6}$$

where $\mathrm{U_{ref}} = 2\Phi fR$ is the mean wingtip velocity, R is the span of the wing and the root-cut , $\bar{c}$ the mean chord length, μ is the kinematic viscosity of the fluid, and ρ is the fluid density. Note that the Reynolds number was altered by modifying the flapping frequency, which changes the mean wingtip velocity. The flapping angle magnitude (peak-to-peak), Φ, was set to 120° and remains constant for the studied cases.

As part of the validation effort, OVERTURNS unsteady lift and drag forces were compared against experimental data. Also the QS reduced model lift and drag predictions are plotted along the presented results to show the differences, more discussion about the quasi-steady (QS) results will be discussed in the next chapter. Figures 4.21 and 4.20 show the time history of the unsteady aerodynamic forces lift and drag, for three different mid-stroke pitch angles at two different Reynolds numbers, 180 and 360 respectively. Wing dimensions for both cases are equivalent to 3 mm span with root-cut of 0.75 mm from the rotation axis. Reynolds number 173 is corresponds to flapping frequency of 150 Hz and 346 to flapping frequency of 300 Hz. The reason behind testing at different frequencies and pitch angles was to observe changes in the magnitude and trend of the forces predicted by the CFD simulations and if they are correlate well against those obtained in the

experiments. The differences between the forces trends (as it shown in Fig. 4.20) for the different pitch angles can be expressed in terms of the magnitude of the peaks and the amount of force produced during the translation portions. For example, on one hand, the peaks attributed to wake capture and rapid pitch-up for pitch angles (α_g) of 45° and 60° are much smaller as compared with the lift developed during the translational portions of the cycles. On the other hand, as in the case of a pitch angle of 30°, the peak because of rapid pitch-up is higher than the maximum lift during the translational portions. The obtained aerodynamic forces during a flapping cycle are function of the kinematics.

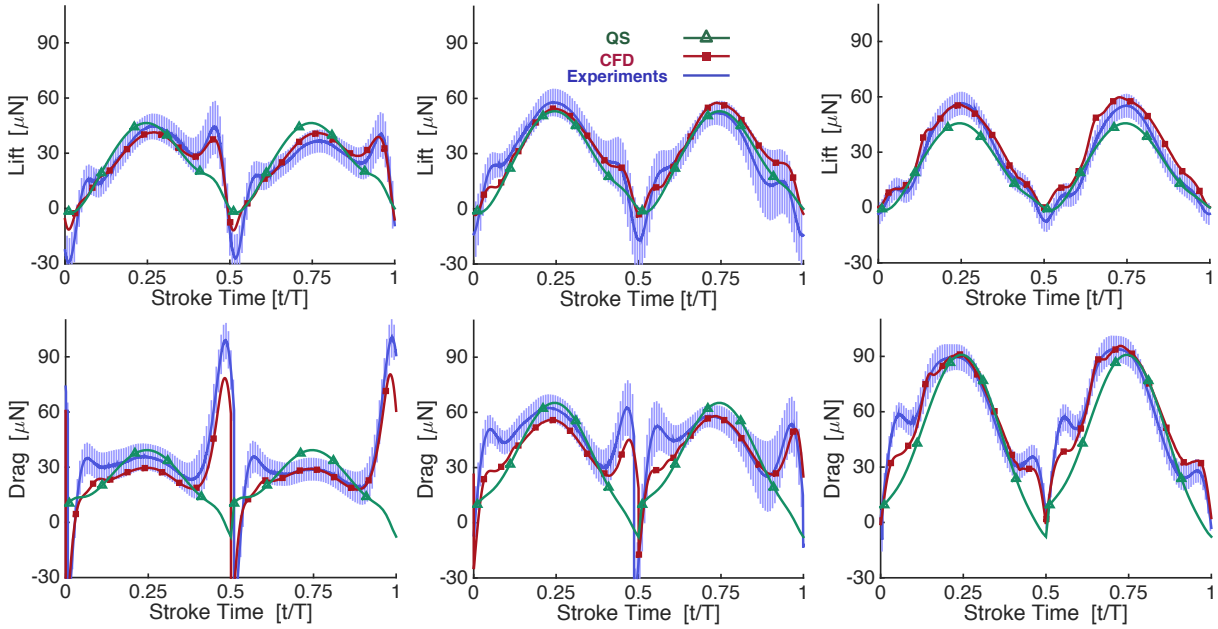

(a) Mid-stroke pitch angle 30 degrees (b) Mid-stroke pitch angle 45 degrees (c) Mid-stroke pitch angle 60 degrees

Figure 4.20: Time history lift force during a flapping cycle of isolated wing in hover.The comparison is among experimental measurements and computational predictions of QS and CFD . Wing span 3 mm and 0.75 mm cut-off and flapping frequency is 300 Hz, with equivalent Reynolds number 360. The bars (shaded area) represent the experiments uncertainty, and it is equal to $\pm(4.7+2\sigma)\mu N$, σ : standard deviation.

In case of the 30° pitch angle, the rotation effects are more dominant relative to the translation

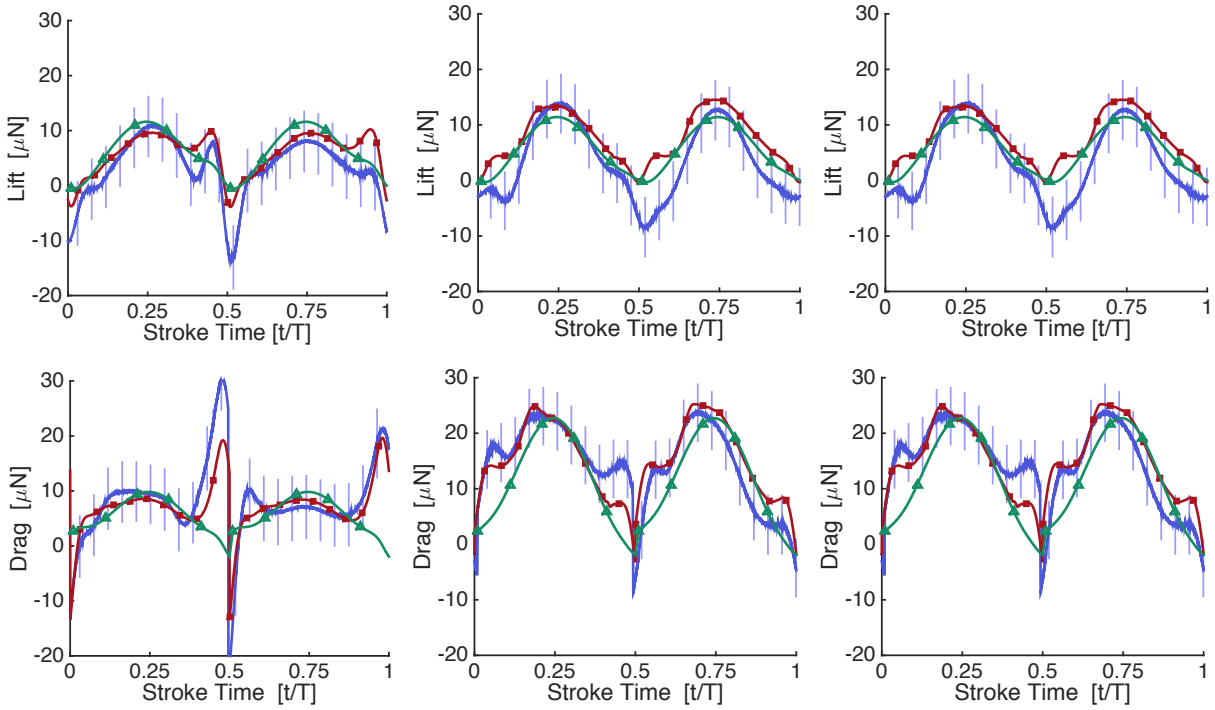

(a) Mid-stroke pitch angle 30 degrees (b) Mid-stroke pitch angle 45 degrees (c) Mid-stroke pitch angle 60 degrees

Figure 4.21: Time history lift force during a flapping cycle of isolated wing in hover.The comparison is among experimental measurements and computational predictions of QS and CFD . Wing span 3 mm and 0.75 mm cut-off and flapping frequency is 150 Hz, with equivalent Reynolds number 180. The bars represent the experiments uncertainty, and it is equal to $\pm(4.7+2\sigma)\mu N$, σ : standard deviation

produced forces and wake-capture effects as the wing at mid-stroke will flip 120° (more than the wing with 45° or 60°), which enhances the lift peak as well the drag. The first peak, dominated by the effect of wake capture, is weaker for 30° pitch angle when compared to the other angles of attack, which is reasonable when it is taken into account that the flow is less complex compared to those with higher angles of attack in terms of the vortical structures shed into the wake. In the cases of 45° and 60° the difference between the first and the third peak is smaller, with the second peak only slightly elevated. The transitional forces are dominant and it develops to reach the maximum at the middle of each down- and up-stroke, which is proportional to the angular velocity of the flap stroke, and is maximum at the middle of each stroke.

The predictions from CFD agree reasonably well with the measurements from experiments. However, for the lower Reynolds number of 180, the noise content is more significant and as noted previously, the resolution of the balance is limited to 4.7μN, as shown in Fig. 4.21. Therefore, the peak forces are of the same order of magnitude as the noise from the balance. Consequently, the results from experiments and CFD do not agree well with a discrepancy noticeable between the force histories. This discrepancy is seen primarily as an asymmetry in the forces (which is not expected) between the up- and down-stroke for the lower frequency case, particularly for pitch angles of 30° and 60°. Despite the noise caused by the modal vibratory response (an experimental limitation that could be improved upon in the future) and the asymmetry for the lower Reynolds numbers, the trends and average peak magnitudes (between the up- and down-stokes) are captured well by CFD.

4.4 Spatial and Temporal Sensitivity Studies

This section presents a CFD spatial and temporal sensitivity analysis that aims to show that OVERTURNS simulations set-up parameters are adequate to obtain a physical solution. This section concerns with one example set-up of a single wing in nested background grid system. Initially for flapping wing simulations the overset set-up was used similar to the presented in section 4.3 for the unsteady flapping wings validation. This set-up consisted of one background mesh with overall mesh points of approximately 10 million mesh points, and performed on the 32 processors, later a nested grid set-up similar to the one used in the impulsive translational wing (section 4.2) was used to reduce the number of the mesh points used in the background without affecting the solution resolution. Nested grids set-up reduced the background mesh-pints from 8.7 Millions to 5 Millions, and therefore less computational resources were required (i.e. numbers of processors).This set-up was used later in the "trim analysis" cases that will be presents in Chapter 7, where 2 wings and a body were simulated. The same procedure was performed for running cases produced previously.

4.4.1 The Spatial Reconstruction

For spatial reconstruction, a third order MUSCL scheme utilizing Korens limiter was compared with higher order schemes with fifth order accuracy, Compact-Reconstruction Weighted Essentially Non-Oscillatory (CRWENO) schemes [71]. Such a comparison is shown in Fig. 4.22, the lift and drag are compared between the two schemes. The third order scheme results are very close to the ones obtained with the fifth order, which provide that the CFD set-up accuracy is acceptable

in this case.

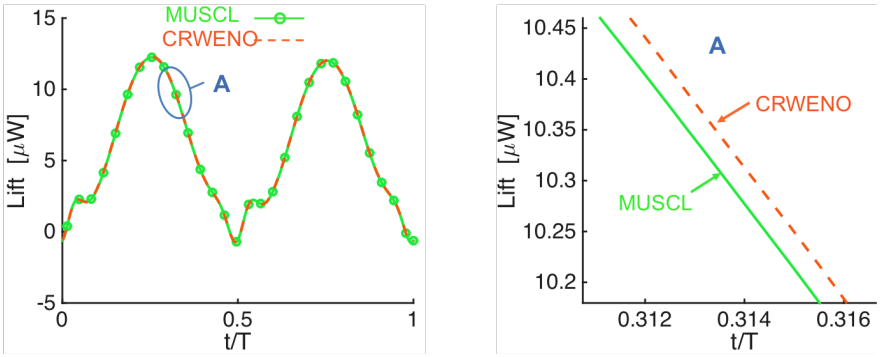

(a) Time history lift

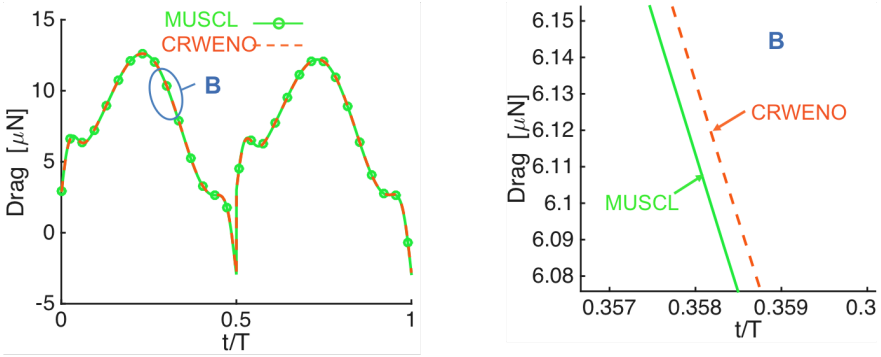

(b) [Time history drag

Figure 4.22: Time history lift force during a flapping cycle of a single wing in hover.The comparison is among 3rd order scheme MUSCL and 5th order CR-WENO. Wing span 3 mm, flapping frequency is 200 Hz.

Therefore, most of the flapping-wing simulations were chosen to be computed with MUSCL scheme.

4.4.2 Grid Size

Several grids were used to test the CFD grid sensitivity, and at the end of the procedure, meshes that guaranteed solution accuracy are used in the study. The important grid parameters are the following: a) spacing near the wall (wing surface) is 0.01% of the mean chord in the

normal direction, and the wings grid is extended in the normal direction over 82 planes to resolve the near-wake and boundary layer features b) Wing thickness is 4% of the averaged chord c) The inner nested background mesh has equal spacing in all direction and equal to 5% of the mean chord, where the outer background has length scale of approximately 4 times the inner background cell length. More details of the computational domain and it borders are described in Fig. 4.23. Overall approximately 9 million mesh points are in the computational domain, and computations are performed on 20 processors in parallel, on high performance computing platforms.

4.4.3 Time Step

For temporal analysis, three different time steps sizes were compared, the time steps in terms of degrees are 0.25, 0.125 and 0.0625. Where the baseline time step is 0.125 degrees, and twice larger and twice smaller time step were investigated. The time history forces components are shown in Fig. 4.24, it can be seen that for twice finer time step 0.0625 the results are not close enough to the 0.125 degrees time step case. Taking a courser time step results in discrepancy in the forces peaks especially at the mid strokes (t/T$= 0.25; 0.75$) and the peak that results from wake interaction (t/T$\approx 0.05; 0.55$). Therefore, time step size of 0.125 degrees was chosen to simulate the flapping wings. For steady cases larger time step can be used, and Newton sub-iteration are not required.

Newton sub-iterations were used to remove the factorization error and contribute to time accuracy for unsteady computations. Overall, 2880 steps (0.125°) are used to complete one flapping cycle. The airloads obtained from the insect kinematics are periodic, therefore when the

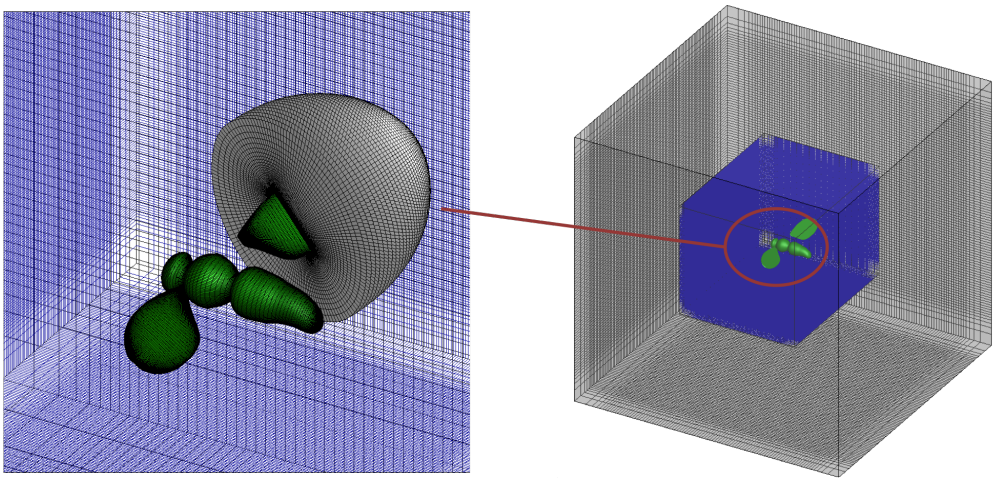

(a) Nested overset grids

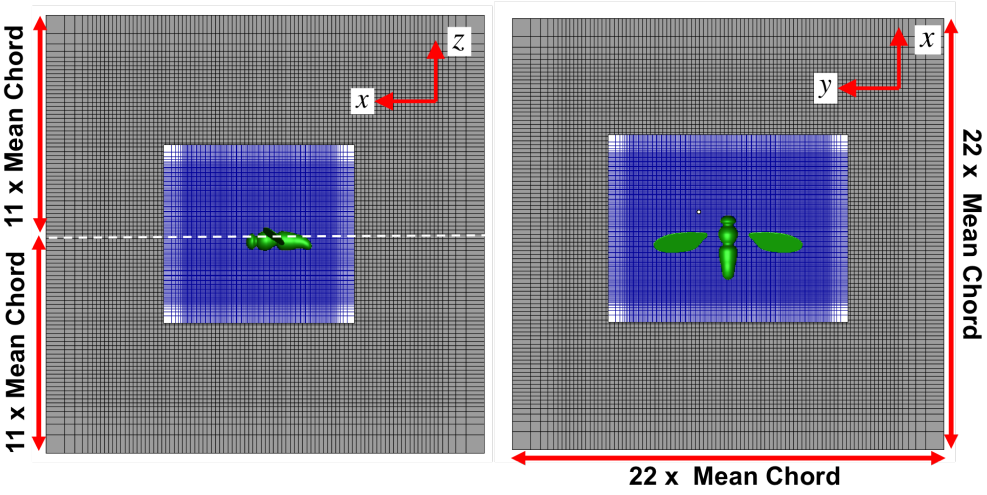

(b) Insect body OO body-fitted grid

Figure 4.23: Nested overset grid system

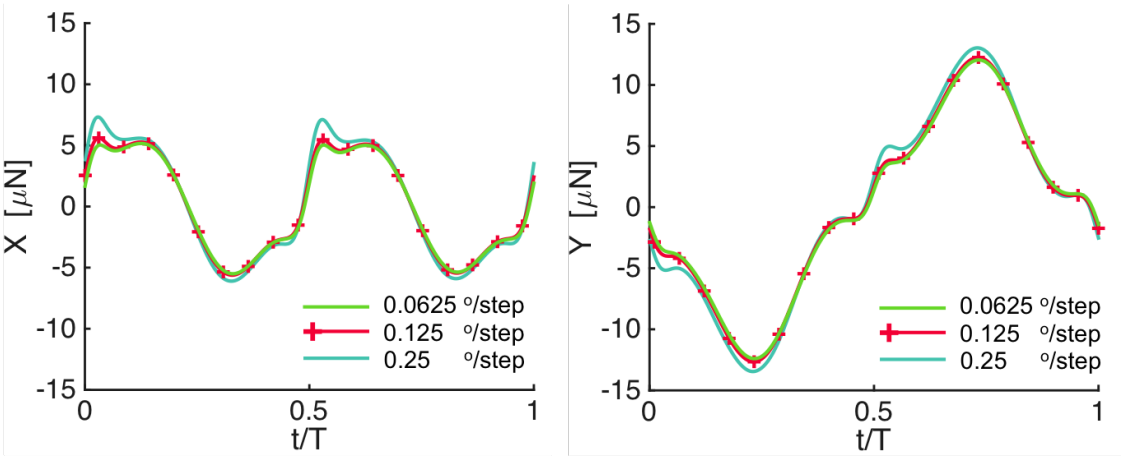

(a) X force

(b) [Y force

(c) Z force

Figure 4.24: Time history force in x,y,z directions during a flapping cycle of a single wing in hover.The comparison is among three time steps, 0.0625, 0.125 and 0.25 deg/step. Wing span 3 mm, flapping frequency is 200 Hz.

solution is converged in the terms of time-history forces periodicity. Seven flapping cycles were performed, and as it can be shown in Fig. 4.25 that the differences between the Z force from the 4^{th}, 5^{th}, 6^{th} and 7^{th} are minor. Therefore, for computational efficiency reasons, averaged forces and moments at the 4^{th} cycle was considered.

4.5 Summary: OVERTURNS Validation

In this chapter, validation and verification of the capability of the CFD solver "OVERTURNS" to predict aerodynamic forces and wake structure at low Reynolds number flows were shown. Three bluff bodies were investigated, a sphere and two shapes of bio-inspired wings (one wing has a fruit-fly shape the other one a blow-fly shape). The summary and the conclusions are:

- Sphere at low Reynolds Number Flow: Good agreement drag coefficient obtained between experimental measurements and numerical predictions

- Impulsive translated wing at Re=300: The forces lift and drag magnitude and trend is similar to the flat plates with low AR at low Reynolds number. The wake structure and vortical shedding of bio-inspired wing relatively similar to the one obtained with the elliptic wing.

- Numerical simulations were performed to examine the aerodynamics of impulsively started low-aspect-ratio flat-plate wings under pure translation at Reynolds numbers of 300. This Reynolds number region is high enough to induce flow separation and unsteadiness in the wake but low enough for the flow field to remain laminar.

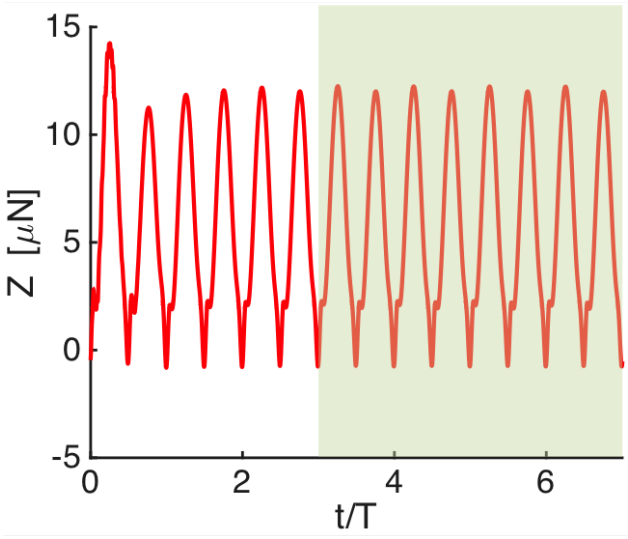

(a) 7 flapping cycle

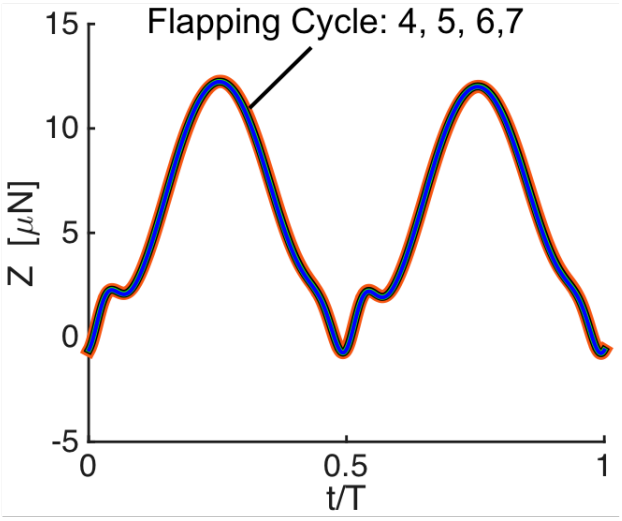

(b) 4th, 5th, 6th and 7th flapping cycle

Figure 4.25: Time history Z force during seven flapping cycles of a single wing in hover. The last 4 cycles are plotted on the top of each other. Wing span 3 mm, flapping frequency is 200 Hz.

- Isolated wing: Correlated OVERTURNS predicted forces with experiments using a single isolated wing in oil tank. Good agreement in lift and drag obtained between experimental measurements and numerical predictions.

Chapter 5

Parametric Study

This chapter presents the results of a parametric sweep of a single wing in hover, performed using the 3D, unsteady Navier-Stokes solver OVERTURNS. The CFD outputs (lift, drag and aerodynamic power) are compared against data obtained using an aerodynamic reduced model quasi-steady (QS). The primary benefit of the CFD solver (OVERTURNS) is that it is a high fidelity numerical solver that accurately captures the physics and detailed the aerodynamic loads; but, using CFD is also computationally expensive in terms of resources and computing time. In comparison, the QS model is simplified, computationally fast and cheap but its drawback can be lack of accuracy. The goals of this parametric study are to: (a) Study the effect of varying kinematics on the resulting forces, (b) Formulate efficiency metrics to compare between varying kinematics and to optimize the design of a flapper based insect's kinematics, and finally (c) Determine how well the QS model predicts the aerodynamics loads.

5.1 Isolated Flapping Wing

The wing planform used in the parametric study cases is a bio-inspired wing that has a shape of a blowfly wing, similar to the wing described in Chapter 4, Chapter 4, Section 4.3. All the run cases simulate a hover condition for flapping frequencies ranging from $100 - 300$ Hz with 50 Hz increments. Varying pitching angles (mid-stroke angle of attack) were considered, i.e. $\pm\ 30^{\circ}$;

$\pm$ 40°; $\pm$ 45°; $\pm$ 60°. The studied wing spans were 2, 3 and 4 mm. The kinematics motion and the computational set-up are identical to those described in Section 4.3. The same overset grid system and computational parameters were used in all the study cases. The parametric study is an extension of the validation of isolated wing cases described in Chapter 4, Section 4.3.

5.1.1 Flapping-Wing Motion

The wing kinematics is a simplified kinematics, similar to the kinematics described in the experimental validation Chapter 4, Section 4.3. The kinematics represented by three positional angles (Fig. 5.1) are:

- Flap angle ϕ: The wing position in the flap stroke.
- Stroke plane angle β: The incline of the stroke plane with respect to x axis.
- Pitch angle α_g: The angle between the wing chordwise direction and the flap-plane; also referred to as "geometrical angle of attack".

The coordinate system and the kinematics parameters are shown in Fig. 5.1, defining the pitch axis and the flap (rotation) axis. Pitch axis is the axis around which the wing pitches and it is located close the leading edge, at the wing root level ($z = 0$). The rotation axis around which the wing flaps is aligned with the z direction.

The flap angle and the pitch angle are defined using harmonic motions. The flap angle (ϕ) is defined as sinusoidal, and described as:

$$\phi(t) = -\phi_{max}\cos(2\pi ft) \tag{5.1}$$

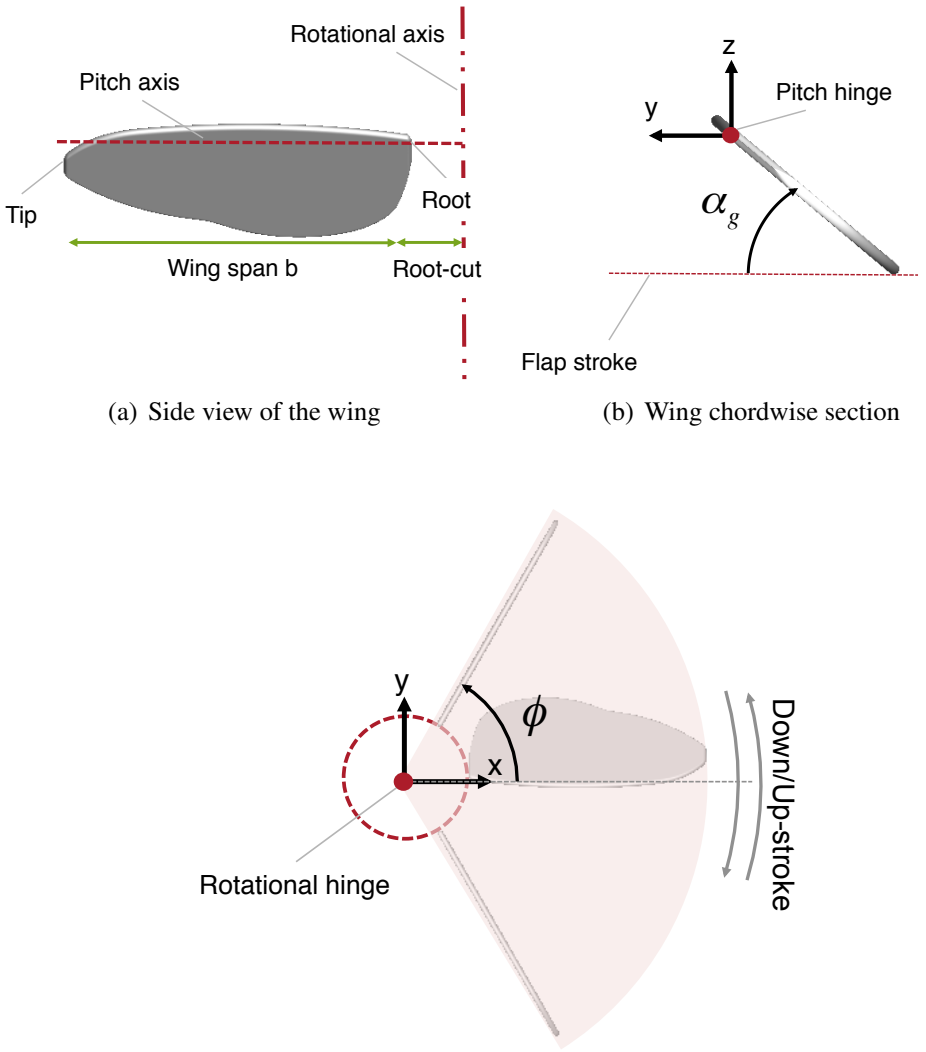

(a) Side view of the wing

(b) Wing chordwise section

(c) Top view

Figure 5.1: Schematic diagram of the coordinate system and wing kinematics, the fixed axis system (x,y,z) is located at the center of the flap rotation. Pitch axis is located at the leading edge of the wing. The wing has a 20% root cut-out from the wing rotational axis. The shaded area represents the flap-stroke, the flap amplitude $\Phi = 120^{\circ}$, peak-to-peak amplitude. The flap stroke in hover is parallel to x,y plane which implies that the stroke angle (β) equal to zero.

where $\phi_{max} = 60^{\circ}$ (half peak-to-peak of the stroke amplitude). The pitch angle α_g roughly resembles a modified square wave, which results in a constant pitch angle during the translations portions:

$$\alpha_g(t) = 90 - \alpha_{max} \tanh(2.7 \sin(2\pi f t)) \tag{5.2}$$

In hover, β, the stroke plane inclination angle, is zero; i.e., the flap-stroke is horizontal.

The peak-to-peak amplitude is 120 degrees, and it remained constant for all run cases. Pitch angle was investigated in this study, and four different angles were considered. Flapping frequency (f) was also investigated and varied from 100 – 300 Hz. The wing aspect ratio (AR) is defined as wing span squared (b^2) divided by the wing area ($S = \bar{c}b$), therefore AR is equivalent to $b/\bar{c}$. In this study, wing AR was constant and equal to 2.7. The geometrical and kinematics parameters used in the parametric study are summarized in Table 5.1.

Table 5.1: Geometric and kinematic parameters

Parametric study	
Wing span - b	2, 3 and 4 mm
Root cut-out	0.5, 0.75, and 1 mm
Wing aspect ratio - AR	2.7
Flapping frequency - f	100-300, 50 Hz step
Mid-stroke pitch angle - α_{max}	30, 40, 45 and 60 deg
Max flap angle - ϕ_{max}	60 deg
Flap amplitude - $\Phi = 2\phi_{max}$	120 degrees

5.1.2 Reynolds Number

The Reynolds number is proportional to flapping frequency f, the wing length squared and inversely proportional to the wing aspect ratio. For the studied cases, the aspect ratio and flap

amplitude are set to remain constant. Therefore the change in the flapping frequency and wing span resulted in changes to the Reynolds numbers. The range of Reynolds numbers for wing span of 3 mm and flapping frequencies from 100 – 300 Hz varied from 100 – 370. Reynolds numbers regime, flapping frequencies and geometrical size are similar to those of tiny insects observed in nature, such as the fruitfly.

5.2 Results and Discussion

This section presents the main results and outputs from the parametric study. First the QS model is considered, following by comparisons between CFD and QS predictions. Suggestions for an efficiency metric of flapping wings are discussed as well. The flow features are considered from two aspects by analyzing first the wake vortical structure and second the induced inflow.

5.2.1 Quasi-Steady (QS) Forces

At the transition from an up-stroke to a down-stroke, the wing pitch reversal is called pronation, and at the transition from a down-stroke to an up-stroke, it is called supination, and in between the flap portions are called translational portions. The non-dimensional time and wing locations during a one flapping cycle are described in Fig. 5.2. Middle of downstroke occurs at t/T= 0.25, and middle of upstroke occurs at t/T= 0.75 during the translational portions. The transition from down to upstroke (supination) occurs at t/T= 0.5, and the transition from up to downstroke happens at t/T= 1.

As discussed in the background (Chapter 2, Section 2.3), lift enhancement mechanisms in

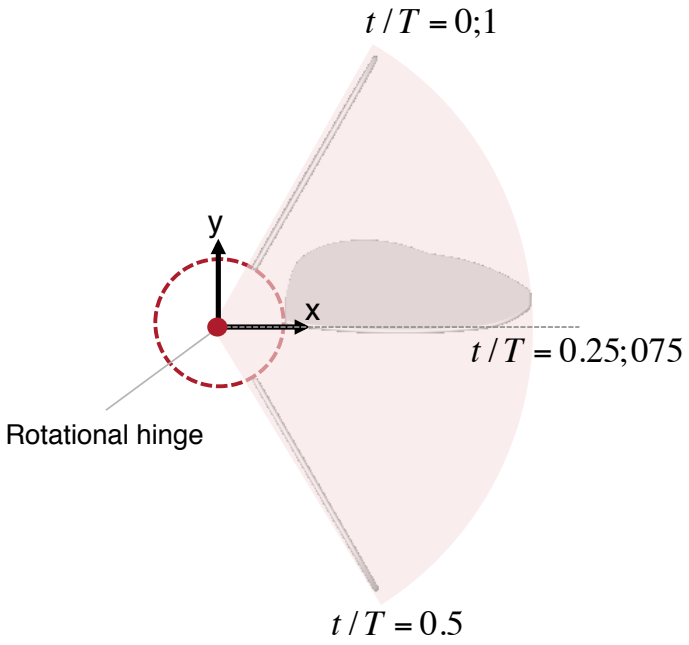

Figure 5.2: Non-dimensional time (t/T), at t/T= 0.25 the middle of the downstroke; t/T= 0.75 the middle of the upstroke; t/T= 0 supination; t/T= 0.5 pronation

hovering insect flight are determined by three major sources: (1) Delayed stall, (2) Rotational circulation and (3) Wake capture. The effect of these mechanisms on lift enhancement can be depicted by peaks in the forces, which occur during the transitions between downstroke to upstroke, and from upstroke to downstroke (the beginning and end of each up/down stroke). Also, the inertial forces affect the magnitude of the peaks [29]. The majority of produced lift is obtained during the translational periods (while the wing pitch is nearly stationary), which is due to the delayed stall mechanism (formation of the LEV).

The time-dependent lift and drag along a flapping cycle in hover are shown in Figs. 5.3 and 5.4 accordingly. Total forces and their components are shown. These components are labeled by rotational due to circulatory forces, added mass due to non-circulatory and translational forces. The time-history forces obtained are plotted as a function of the non-dimensional time. The lift

is the component of the total aerodynamic force along the wing-span perpendicular to the translational velocity. Drag is the component of the total aerodynamic force parallel to the translational velocity and it is positive when it points in the opposite direction of the translation velocity. The presented results considered cases of 3 mm wing span with flapping frequency of 200 Hz, comparing between three different mid-stroke pitch angles (α_g = 30, 45 and 60 deg); the equivalent Reynolds number for these cases is 240.

Examining the lift curve, the total force is mostly contributed by the translational forces. Added mass effect contributes mostly during the stroke reversal (transition from up to down-stroke - supination, or from down to up-stroke - pronation) and less during the translational portions (as shown in Fig. 5.3). The peaks in the lift due to added mass are not equal in magnitude during the supination and pronation. For example, during the supination there are two peaks due to added mass, one at t/T= 0.45 and one at 0.55. The first peak is less in magnitude as can be seen from Fig. 5.3.

The rotational effects are emphasized during reversal strokes. During the transition from downstroke to upstroke, the wing starts to pitch up rapidly and results in a positive lift (t/T= 0.45). When the wing flips (t/T= 0.5) there is a drop in the rotational force, and when the wing starts the upstroke and pitches down, that results in a negative lift (as shown in Fig. 5.3). The upstroke and downstroke are symmetric in hover, therefore the same pattern in forces due to added mass and rotational forces is obtained during the transition from up-to-down stroke. The negative peak of the rotational force is in the opposite direction to the added mass contribution, and they eliminate each others effect in the total force (t/T= 0.05, 0.55). The positive peak of the rotational force enhances

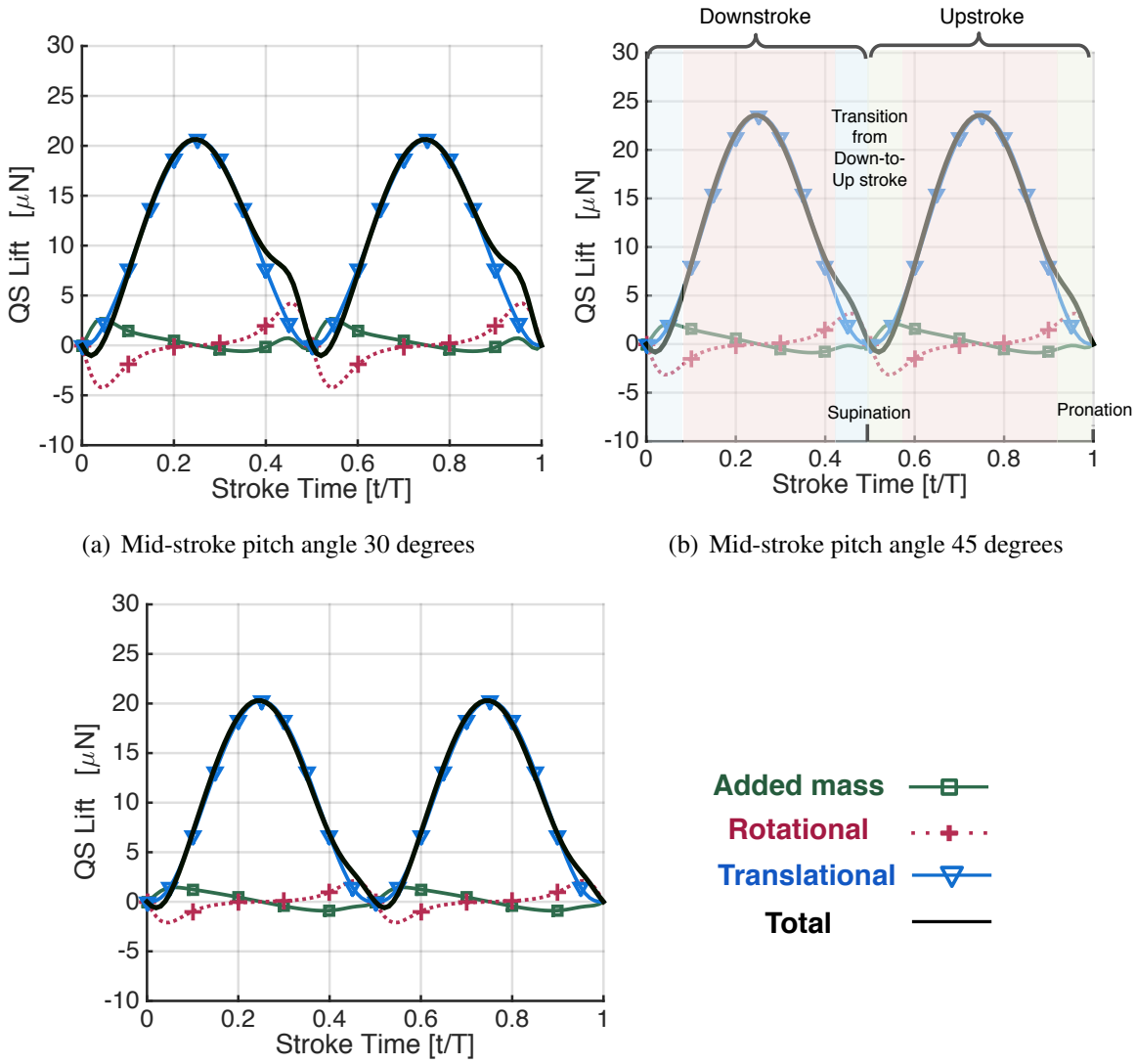

(a) Mid-stroke pitch angle 30 degrees

(b) Mid-stroke pitch angle 45 degrees

(c) Mid-stroke pitch angle 60 degrees

Figure 5.3: QS time history lift force and its components: added mass, rotational, translational along with the total. Wing span 3 mm and 0.75 mm, root cut-out (20%) and flapping frequency 200 Hz, equivalent to Re = 240.

the added mass peak (t/T= 0.55, 0.95) in the total force. Added mass and rotational forces have a minor contribution during the translational portions. The QS prediction for total drag is shown in Fig. 5.4. The total drag force consists of just added mass contribution and the translational forces.

From QS lift and drag forces, it can be seen that the forces magnitude are affected by the pitch angles, where more lift is obtained for the 45° and 60° pitch cases; however the greater the pitch angle, the greater the resulting drag. The question raised here is how well QS predicts lift and drag when including the unsteady circulatory and non-circulatory forces contribution; this requires a comparison to experimental measurements and CFD results. In comparison with experimental results, QS underpredicts the peaks magnitude (Chapter 4, Section 4.3), while the force during the translational portion are reasonably close to those obtained by experiments. In the following section, QS results are examined by looking at time history and averaged aerodynamic loads compared against those from CFD (OVERTURNS) predictions.

5.2.2 Forces: QS vs. CFD

Flapping-cycle averaged aerodynamic loads are important because they help quantify the forces and aerodynamic power needed to keep the insect aloft while also demonstrating the sensitivity of the instantaneous forces to the kinematic parameters. In bio-inspired flapping flight and under the assumption that the aerodynamic timescales are an order faster than the body dynamics, averaged aerodynamic loads are a valid approximation. The forces obtained from CFD are non-dimensional; the dimensional aerodynamic forces, lift (L) and drag (D) are described by the

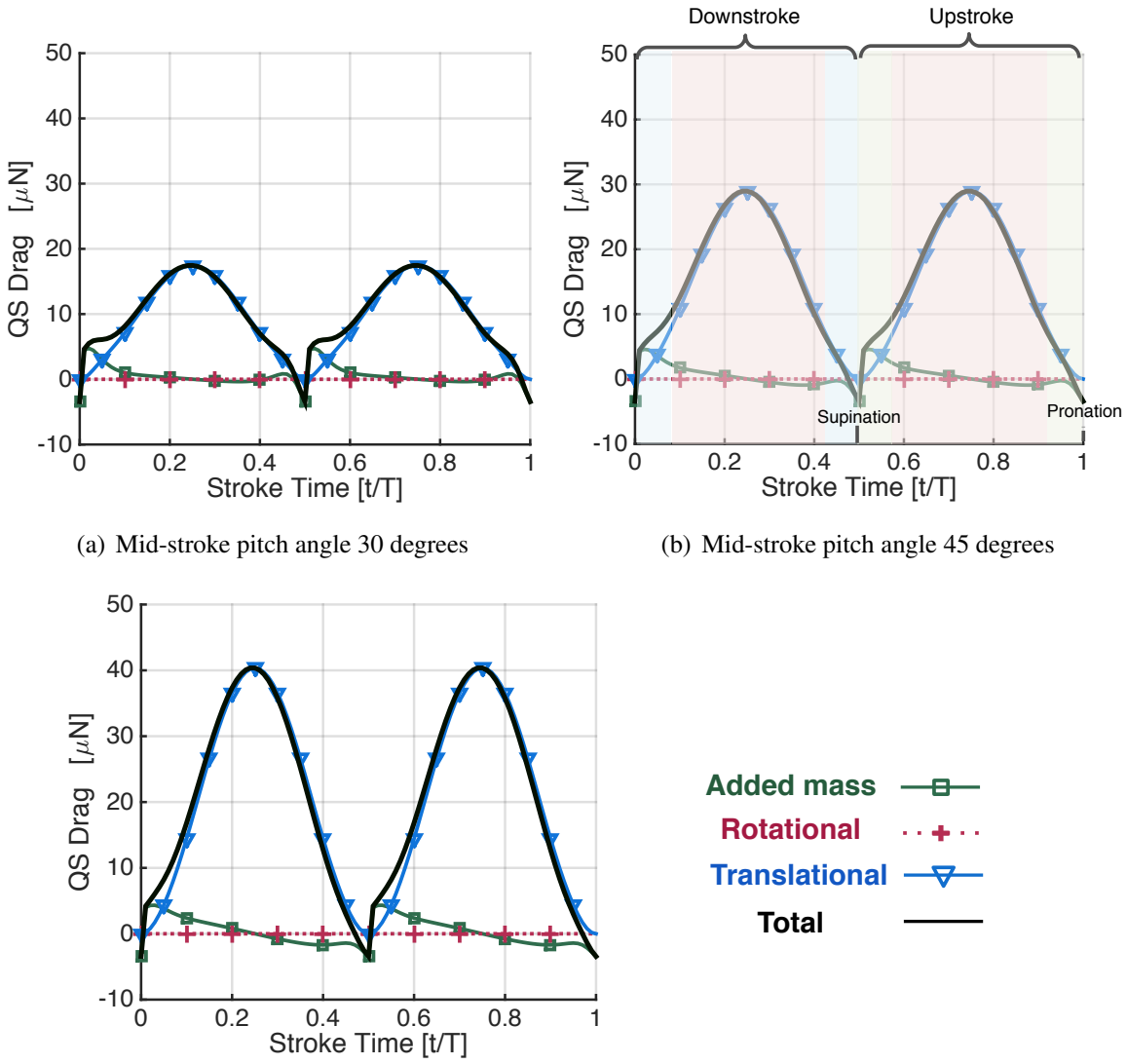

(a) Mid-stroke pitch angle 30 degrees

(b) Mid-stroke pitch angle 45 degrees

(c) Mid-stroke pitch angle 60 degrees

Figure 5.4: QS time history drag force and its components: added mass, rotational, translational along with the total. Wing span 3 mm and 0.75 mm root cut-out (20%) and flapping frequency 200 Hz, equivalent to Re = 240.

following equations:

$$L = 0.5\rho U_{ref}^2 S C_l \tag{5.3}$$

$$D = 0.5\rho U_{ref}^2 S C_d \tag{5.4}$$

where U_{ref} is the mean tip velocity as described previously, S is the wing area. The area is determined by the mean chord ($\bar{c}$) multiplied by the wing-length (b). The density of air at sea level is represented by ρ and is 1.225 kg/m^3. It is expected that the magnitude of the averaged forces increases with increasing frequency. For example, for the pitch angle of a 45° case, the lift obtained at 300 Hz is eight times more than the lift obtained at 100 Hz, slightly below being proportional with the square of velocity.

First, a comparison in time history lift and drag between QS and CFD is shown in Fig. 5.5 for a pitch angle 45° and flapping frequency of 200 Hz (Re= 240). During the translational portions, lift obtained from a QS model is in good agreement with the CFD results; while for drag prediction, QS model is overpredicted relative to CFD. The QS model doesn't include an adequate mathematical model for induced inflow that can lead to a reduction in the drag. The significant difference between QS and CFD drag predictions is greatest in the stroke transition partitions (Up-to-Downstroke and Down-to-Upstroke), represented by the shaded areas in Fig. 5.5 marked by A and B. CFD has dominant peaks, especially the peak in (A) portion which results from the rapid pitch-up effect. The relatively smaller peak in (B) is due to wake interaction. With the added mass and rotational forces effect modeling in QS, QS still underpredicts these peaks in comparison to CFD. This is a similar to the one observed when comparing QS predictions and experimental

measurements.

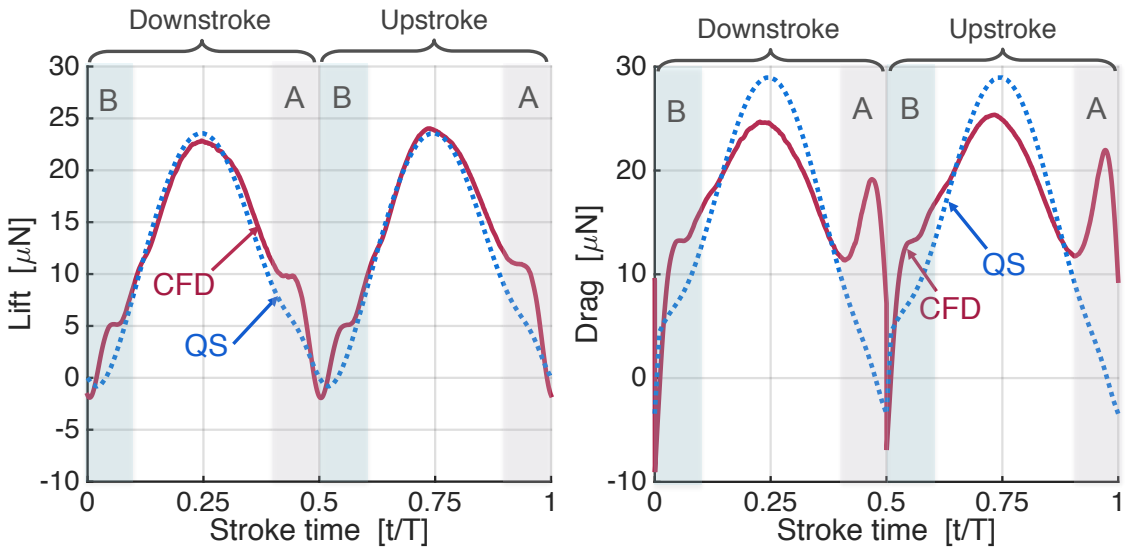

(a) Time-history lift

(b) Time-history drag

Figure 5.5: Comparison between CFD and QS time history lift and drag during a flapping cycle. Wing span is 3 mm with root cut-off 0.75 mm (20%). Mid-stroke pitch angle is 45 deg, Reynolds numbers is 240.

The wing aerodynamic forces obtained from QS and CFD (OVERTURNS) are averaged over one flap-stroke (flap-cycle). Averaged over a flapping cycle, lift, drag and power are plotted against flapping frequency (100–300 Hz) for a wing with 3 mm wing length and 45° pitch angle at the mid stroke. The CFD results obtained from OVERTURNS are compared against the QS results in Figure 5.6, and shows that QS model underpredicts the average lift and drag, and the discrepancy between QS and OVERTURNS increases with increasing flapping frequency. The reasons for this discrepancy can be: (1) Reynolds number is larger for larger flapping frequency and QS lift and drag coefficients are based on results obtained for a specific Reynolds number (Re= 120), so the model is insensitive to Reynolds number effects; or (2) The QS model does not includes the unsteady mechanism of the wake interaction during the stroke reversal, and the unsteady circula-

tory and non-circulatory forces represented in the model do not accurately capture the unsteadiness effect in flapping wings. This is highlighted in terms of underpredicted average lift and drag by QS. Despite the discrepancy between CFD and QS predicted forces, the resulting trends are similar. For the CFD and QS predictions of power magnitudes, the trends and magnitudes are similar. The underpredicted drag force using QS model seems to be compensated by an moment arm used ($0.75R$) that is greater than that captured by CFD.

5.2.3 Wake Structure

To analyze the flapping wing wake, a fifth order spatial accuracy scheme CRWENO was used instead of the MUSCL scheme. Both schemes give the same forces magnitude, but more details in the wake are captured by using the higher accuracy scheme (CRWENO). Simulations of insect kinematics for different pitch angles (30°, 40°, 45° and 60°) were carried out, with wing-span of 3 mm, flapping frequency $f = 200$ Hz, and equivalent Reynolds number equals to 240. The purpose of these simulations is to show the wake structure, evolution, augmentation of the LEV, and shed vortices as a function of angle of attack, α_g, and the rotational angle, ϕ, during the flapping cycle. To get a clear picture of the flow wake structure, one can examine the Q-Criteria [78] of the vortices (Appendix E). The up and down strokes are symmetrical and, therefore, only the downstroke wake structure and forces are shown. As mentioned and discussed previously three positive peaks are observed during each stroke. These three peaks occur at approximately t/T= 0.05; 0.25; 0.45. The figures (Figs. 5.7–5.9) show the time-history lift obtained during the downstroke (half of the flap cycle) as a function of pitch angle (three are considered: 30°, 45° and 60°), and the iso-surfaces

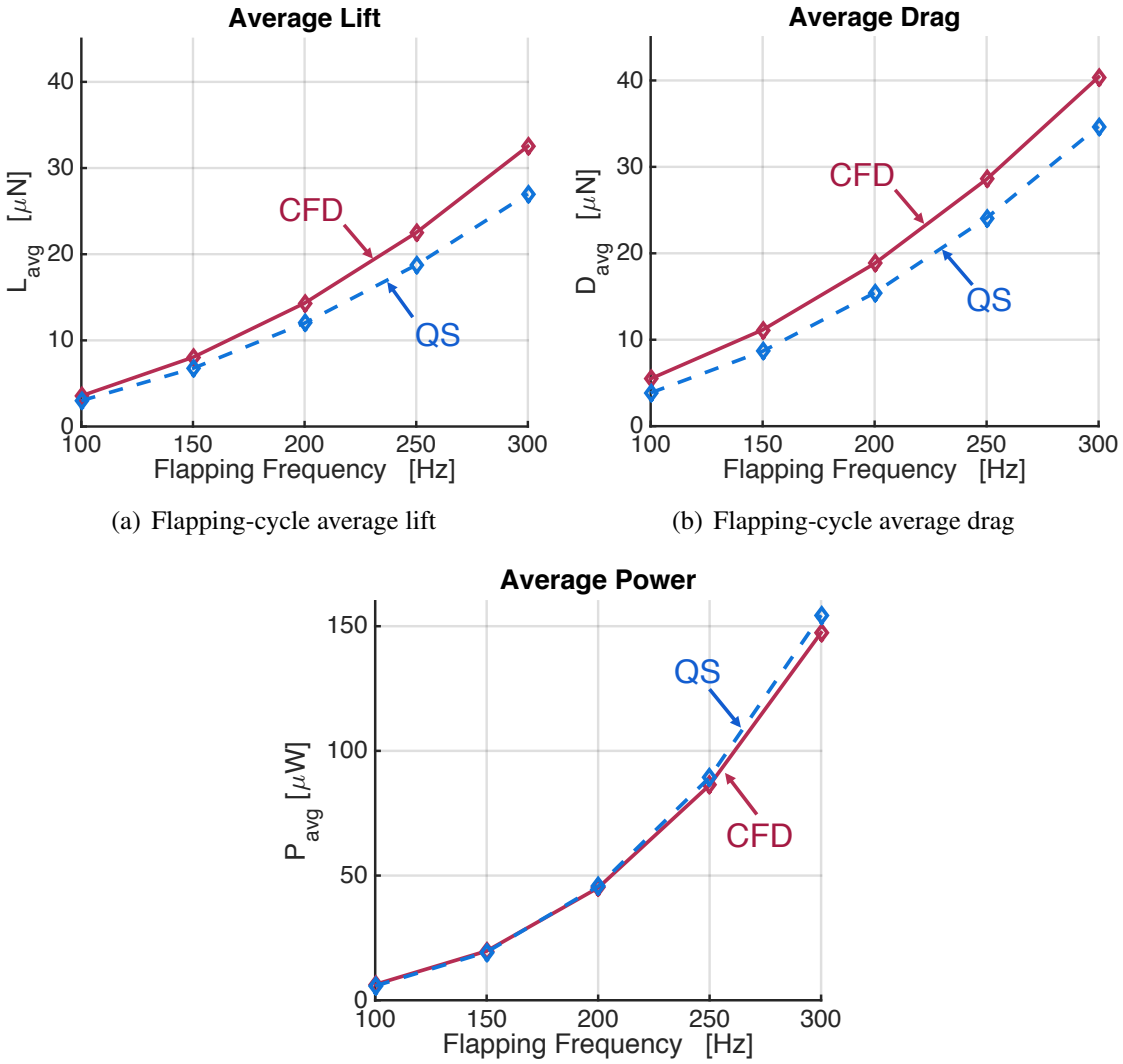

(a) Flapping-cycle average lift

(b) Flapping-cycle average drag

(c) Flapping-cycle average required aerodynamic power

Figure 5.6: Comparison between CFD and QS flapping-cycle average airloads as function of flapping frequency, for wing span 3mm with cut-off 0.75 mm. Mid-stroke pitch angle is 45 deg. Reynolds numbers range from 115 ($f = 100$) to 345 ($f = 300$).

of Q-criteria of the wake around the wing is plotted at the three time stations where the lift peaks occur. The presented cases are for same Reynolds number (Re = 239) and rotational velocity.

The up and down strokes start with a 90° pitch that will decrease until the desired mid-stroke pitch angle is obtained. The pitch remains constant more than 70% of the stroke period (translational period) and it only changes during stroke reversal. The LEV created in the early stage of the down/up-stroke is stable during the entire downstroke. This LEV is shown in Fig. 5.7 at the middle of the down-stroke. The presence of the LEV is responsible of the generated lift and drag during the translational portions, by generating a low pressure area on the upper surface of the wing, and high pressure in the lower surface.

From looking at the corresponding iso-surface of Q-criteria, a wing with pitch angle of 30° develops a less intense LEV than the wing at pitch angle of 45° and 60°, which is also reflected in the produced lift. The LEV has a conical shape starting from the root and expanding to the tip. Toward the tip the vortex starts trailing creating a dominant tip vortex. The wings with the various pitch angles show the same LEV structure during the translational portions, but what is changing is the separation or the trailing point. Across a larger pitch angle at the middle of each half stroke the separation point of the LEV along the wing span displays a trend of moving inward in the spanwise direction. For example the separation point for pitch of 60° case occurs at 75% of the wing span, while the separation point for the pitch of 30° case occurs further toward the wing tip. Figure 5.7 illustrates the formation and size of the LEV as a function of the pitch angle. The LEV size increases with an increase in the translational portion pitch angle. This demonstrates that the LEV size is a function of pitch angle. Also, from Fig. 5.9, the wake produced by the convected,

shed and trailed vortices is shown, and obviously for the larger pitch angle, the vortical structure is more complex. The tip and trailing vortices are more dominant for the larger pitch angle.

The pressure coefficient contours are plotted in Fig. 5.10. The pressure coefficient contours are plotted at mid-stroke (t/T= 0.25). In hover the free-stream velocity is zero; therefore, in this case the pressure coefficient is defined as a pressure gradient normalized by the dynamic pressure calculated using the mean tip velocity Uref as defined earlier. With increasing pitch angle the low pressure is more dominant on the upper surface, forming an expanding area from root to tip. The pressure on both sides is not distributed uniformly, indicating that during the translational portions more lift is produced toward the tip, which will be referred to later as "tip dominated lift".

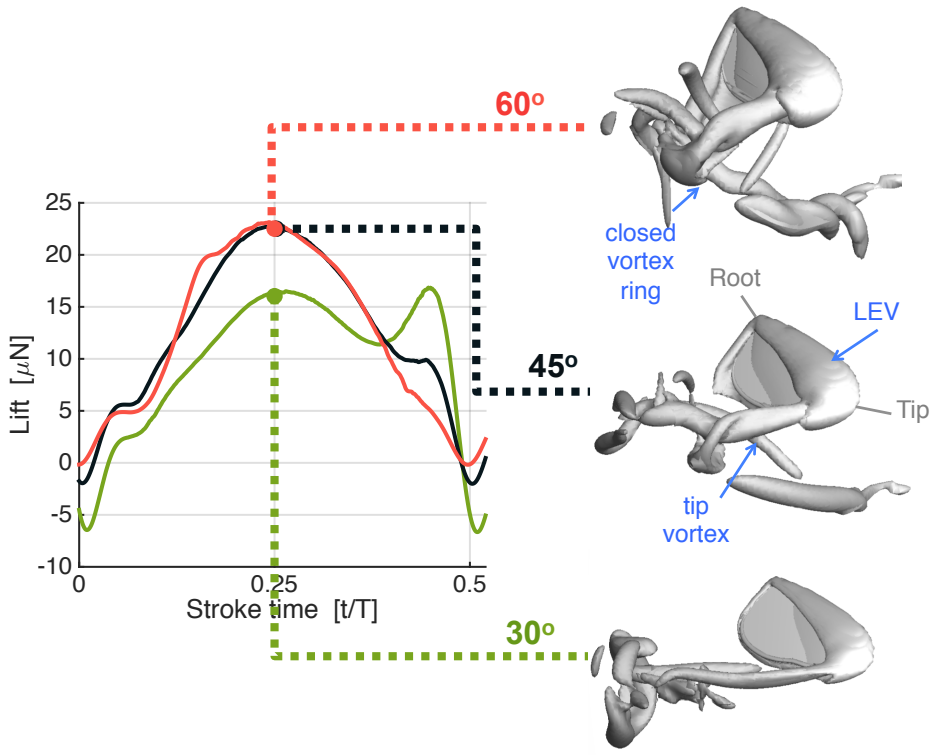

Figure 5.7: Detail of lift time history during downstroke. Isosurfaces of Q-criterion for each case are plotted at t/T=25% "peak 2" to highlight factors affecting the formation of the LEV and the wing surrounding wake structure for the 30°, 45° and 60° cases.

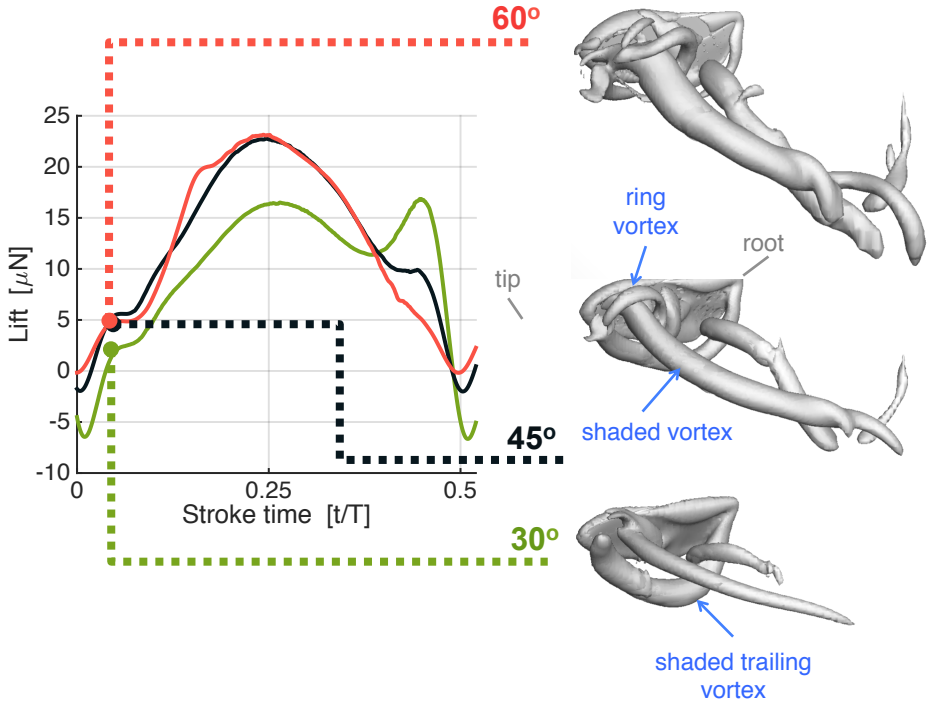

Figure 5.8: Detail of lift time history during downstroke. Isosurfaces of Q-criterion for each case are plotted at t/T=5% "peak 1" to highlight factors affecting the differential behavior of the lift curve during pronation (stroke reversal from upstroke to downstroke.) for 30°, 45° and 60° cases

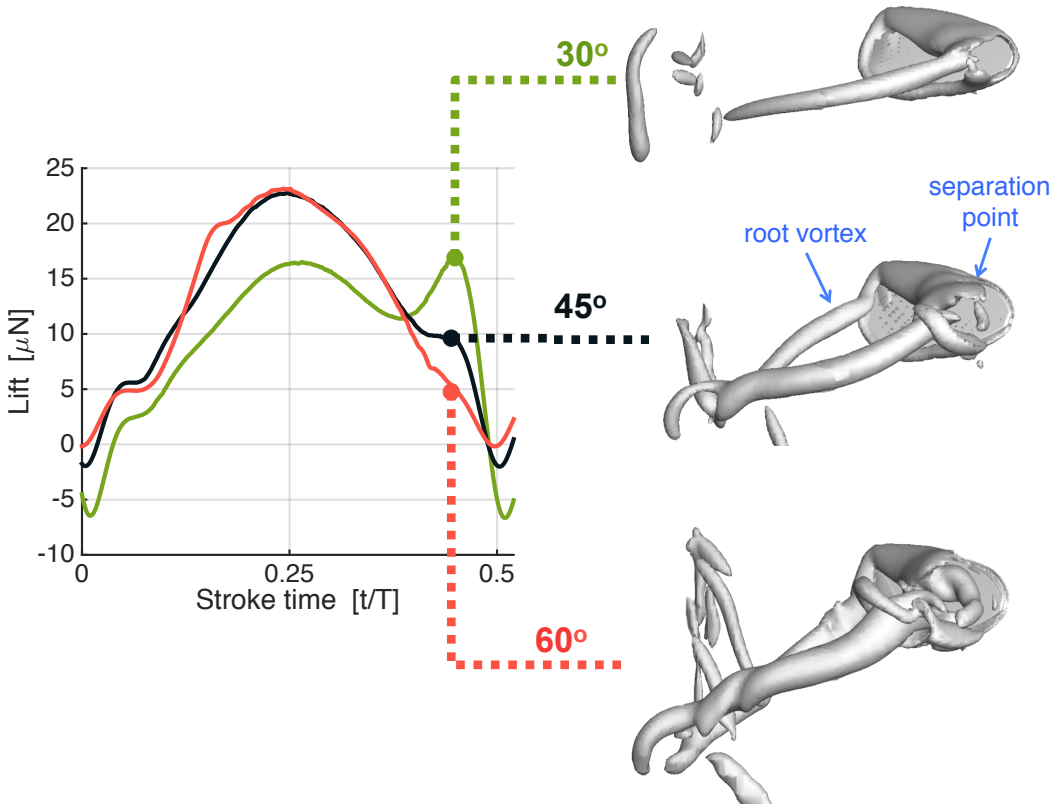

Figure 5.9: Detail of lift time history during downstroke. Isosurfaces of Q-criterion for each case are plotted at t/T=45% "peak 3" to highlight factors affecting the differential behavior of the lift curve during supination (stroke reversal from downstroke to upstroke.) for 30°, 45° and 60° cases

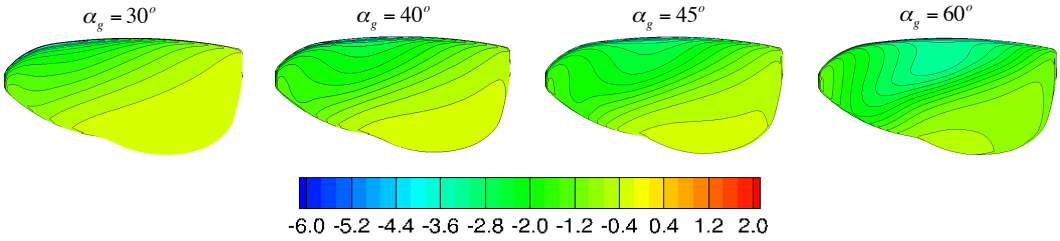

(a) Pressure coefficient (Cp) contours on the wing upper surface

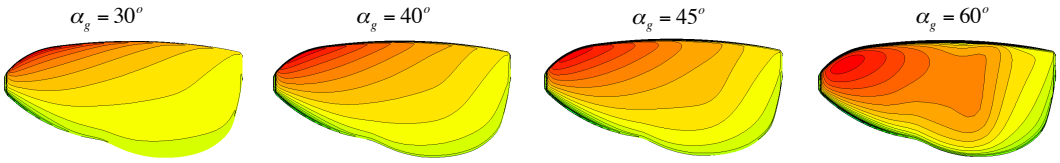

(b) Pressure coefficient (Cp) contours on the wing lower surface

Figure 5.10: Pressure coefficient contours on the lower and upper surface at mid-stroke (t/T= 25%) for the variouse pitch angles (30°, 40°, 45° and 60°).

In general the wake is more complex for larger changes in angle of attack, so when the wing starts the upstroke, the one with the larger midstroke pitch angle will produce a more complex wake. The wing also will extract more energy from the wake as can be seen in first peak of the time force histories. The first peak in each half stroke (Fig. 5.8) is related to the capability of the wing to extract energy from the wake. In the case of a pitch angle of 60° the wake is more complex, contains more energy and the corresponded first peak of the forces enhancement is more emphasized. In the case of a pitch angle of 30° the wake is relatively weak, and the first peak is relatively small.

Figure 5.9 concentrates on the third peak, which is due to the fast rotation of the wing around its pitch axis ("rotational forces" effect). The largest peak belongs to the mid-stroke pitch angle of 30° case and the smallest to the 60° mid-stroke case. This results from the wing with the lower pitch angle (30°) needing to perform a larger rotation and therefore force peak magnitude for this pitch angle is larger.

5.2.4 Efficiency Metrics - Average Forces and Power

The question to answer is how to best quantify efficiency metrics in insect flight, where kinematics and aerodynamic loads are coupled. Efficiency metrics are an essential tool to compare various kinematics and geometrical parameters for design.

For conventional airplanes and rotary-wing vehicles in forward flight, flight efficiency can be defined by looking at Lift-to-Drag (L/D) ratio. Whether L/D ratio for a flapping wing is the best efficiency metric is discussed next.

Lift-to-Drag ratio (L/D): For insect flight, most of the lift is obtained during the translational portion due to the leading edge vortex (LEV) formation. The resultant force from the LEV is perpendicular to the wing and has both lift and drag components. These components are a function of the pitch angle. In Figure 5.11(a), the averaged lift during a flapping cycle is shown as function of flapping frequency, for various pitch angles (30°, 40°, 45°, 60°). For flapping frequency 100 Hz (Re= 115), the averaged produced lift for the various pitch are close in magnitude. With increasing in flapping frequency (larger Reynolds number), the discrepancy between the produced lift of various pitch angles increases. Average lift vs. frequency of wing with pitch angle of 40° and 60° are very close, wing with pitch angle of 30° produces less lift as discussed in the previous section. Wing with 45° has a slightly small advantage over the 40° and 60° pitch angle cases. The flapping cycle averaged drag is shown in Fig. 5.11(b), and here the differences between the various pitch angles is more emphasized. For the lowest flapping frequency, 100 Hz, the resulted drag force magnitude is similar for the various pitch angles cases. However with increasing in flapping frequency the discrepancy between the curves increases. No surprise, that the wing with pitch angle of a 60°, produces the largest drag at every flapping frequency relatively to the other pitch angles cases. The wing with pitch angle angle of a 30°, and pitch angle of 45° has slightly larger drag than the 40° pitch angle case. The produced lift and drag are a function of Reynolds number, LEV size and pitch angle (that determine the resultant suction force direction).

Now, as can be seen in Figure 5.11(d), the lift-to-drag ratio (L/D) in insect-like flapping wing is less than 1. One reason for this low L/D value is the prescribed kinematics. The wing starts the rotational stroke with a pitch angle of 90° which leads to high drag and decreases until it reaches

the required mid-stroke pitch angle (geometrical angle of attack). For the pitch angle larger than 45°, the drag component is larger than the lift. This is reflected in the average values of L/D. The lowest L/D is obtained for the 60° pitch angle case (Fig. 5.11(d)). The maximum L/D is obtained for the wing with pitch angle of 30° at a 300 Hz. Although, Fig. 5.11(a) shows that 45° pitch angle case has the largest magnitude of average lift during the flapping cycle. The magnitude of the lift for the 40° and 60° cases shows similar quantities but the 40° case produces much less drag. Here one can see the advantage of the kinematics with pitch of 45° as compared to the pitch of 60°. While an pitch angle of 30° produces higher values of L/D, the lift produced by pitch angle of 30° is less than that produced by the 45° or 40° cases. Therefore L/D ratio in case of flapping wing flight provides only a limited understanding about the vehicle performance. Other quantities can be investigated to examine efficiency metric of flapping wing.

For fixed wing, where velocity is uniform and power is the product of integrated drag and velocity, L/D is equivalent to L/P. However, this relation does not hold for flapping or rotating wings where the velocity is time-varying and non-uniform along the wing span. It can therefore be concluded that to compare between flapping wings with different kinematics or geometrical parameters as well as to other micro-air vehicles.

Power Loading (L/P) : To investigate the efficiency of the kinematics, one can look at the lift-to-power ratio (L/P power loading) for the four mid-stroke pitch angles. Aerodynamic power is computed by summing the dot product of the local aerodynamic force and local wing velocity along the wing-span. The inertial power incurred in biological and mechanical flight was not investigated in this study. The resultant aerodynamic power varies for the given pitch angles,

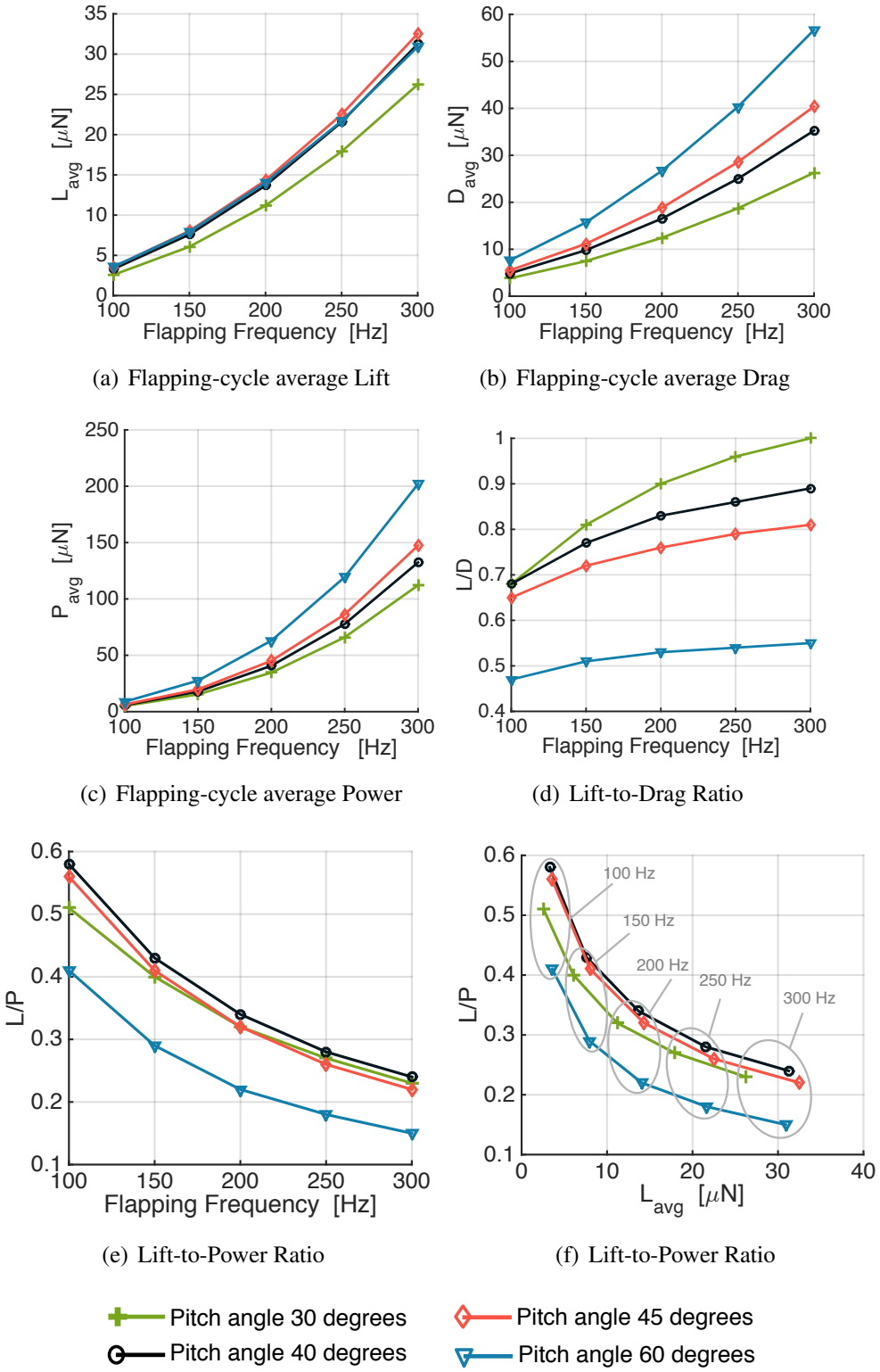

(a) Flapping-cycle average Lift

(b) Flapping-cycle average Drag

(c) Flapping-cycle average Power

(d) Lift-to-Drag Ratio

(e) Lift-to-Power Ratio

(f) Lift-to-Power Ratio

Figure 5.11: CFD flapping-cycle average lift, drag and required aerodynamic power of wing with 3 mm span and 20% root cut-off (0.75 mm). The results are shown for different mid-stroke pitch angles: 30,40, 45 and 60 degrees, Reynolds numbers range from 115 ($f = 100$) to 345 ($f = 300$)

wing-length and flapping frequency. The power requirements increase as the mid stroke pitch angle increases at the same Reynolds number and increases with an increase in Reynolds number as well (increasing frequency or wing-length) as shown in Fig. 5.11(c). (For each frequency all the points corresponding with it have the same Reynolds number). The difference between the mean aerodynamic power curve for the various pitch angles increases with increasing flapping frequency, more power is required for larger Reynolds number. Also, more power required to flap the wing at larger pitch angles, which is expected.

Now considering L/P as a function of flapping frequency (f) as shown in Fig. 5.11(e), the case of the pitch angle of 60° has the lowest L/P ratio when compared to pitch angles of 30°, 40° and 45°. The ratio L/P decreases with increasing frequency for each pitch angle. The power coefficient increases as the Reynolds decreases and this is the result of increasing drag for lower Reynolds number. Power loading values for 40° and 45° are almost identical with a small advantage to pitch angle 40°. The pitch angle 30° and 45° cases are similar for frequencies greater than 150 Hz. This caused by the non-identical force distribution along the span for each pitch angle, and also the differences in the rotational power between the two cases. It appears that the 40° pitch case is best across the entire frequency range. However, if one plots the L/P for the mid-stroke pitch angles versus the corresponding average lift, as in Fig. 5.11(f), then one can clearly see the superiority of the 40° pitch though it is not far from the efficiency of 45°. There are many aspects to include when talking about flapping wing efficiency metric (i.e. maximum lift, minimum drag, minimum required power, flapping frequency and pitch angle) and by considering flapping-cycle averaged L/P versus flapping-cycle averaged lift, all these aspects are represented. Power loading

as a function of averaged lift (L/P vs. L_{avg}) is more appropriate as an efficiency metric than is the L/D ratio. The proposed metric properly accounts for the required aerodynamic power and vertical thrust as a function of prescribed kinematics. The ratio L/P versus lift can be used to determine the performance. Power and vertical thrust are the key parameters for design and performance.

To highlight what was discussed earlier about the difference between CFD and QS, L/D and L/P ratio are plotted against flapping frequency in Fig. 5.12. QS values for L/D ratio remains constant with increasing flapping frequency, and that is because the QS model lacks wake interaction effect and appropriate unsteady mechanisms (unsteady circulatory and non circulatory forces). Considering L/P instead L/D ratio can give more insight even in the case of QS analysis. This insight can not be obtained from L/D ratio that it is insensitive to the change in Reynolds number. QS averaged L/P versus flapping frequency curve has a similar trend as the CFD obtained results, but it underpredicts the values, and that is mainly because the QS underpredicted lift and the inaccurate power estimation.

5.2.5 Induced Flow

The induced inflow ratio is a nondimensional quantity that is used in rotorcraft and defined for helicopters as (Ref. [64]) $\lambda_i = v_i/(\Omega R)$, v_i, where is the inflow velocity at the rotor disk normalized by the blade tip speed in hovering flight (ΩR). In rotorcraft, using momentum theory assumptions, analytical relation between the thrust and the induced velocity in hover can be derived, and it is:

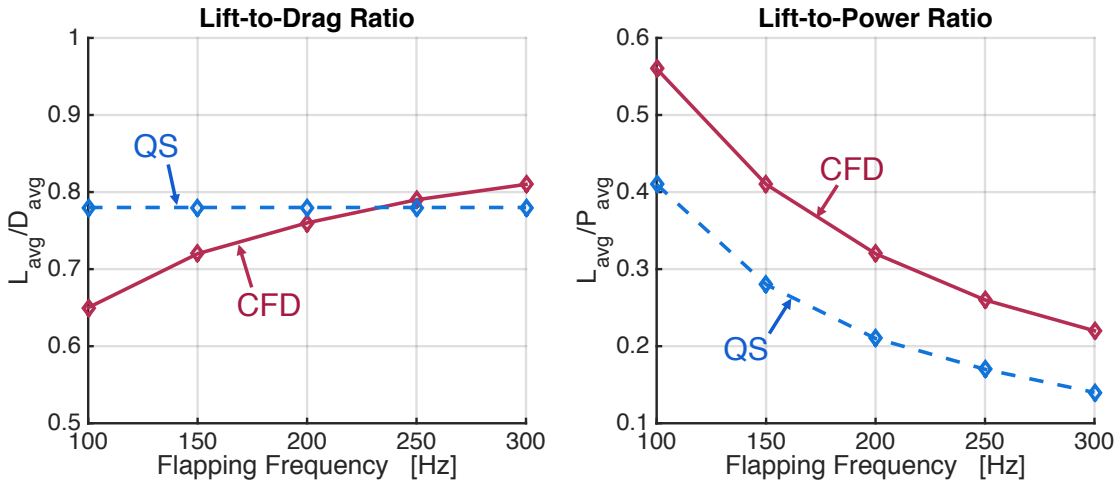

(a) Average lift-to-drag ratio versus flapping frequency

(b) Average lift-to-power ratio versus flapping frequency

Figure 5.12: Comparison between CFD and QS efficiency parameters for wing span of 3 mm and 20% root cut-out equal to 0.75 mm. Mid-stroke pitch angle is 45°.

$$\lambda_h \equiv \lambda_i = \sqrt{\frac{C_T}{2}} \tag{5.5}$$

where C_T is the rotor thrust coefficient, and equal to $T/\rho A(\Omega R)^2$.

Momentum theory assumes a 1-D flow of an ideal actuator disk, where the rotor is modeled as an infinitely thin disc, with a time-averaged induced constant velocity across the disk. These assumptions do not necessarily hold for flapping-wing insect flight, therefore the relation derived for rotorcraft may not apply here. Despite that, looking at the induced inflow can provide insights about the wake involved with the flapping kinematics; for example; showing which portions of the stroke are most affected by induced flow from previous wake, comparing between different pitch angles and their effect on the wake and induced inflow, and estimating the obtained effective angle of attack.

For a flapping wing the induced inflow ratio is defined as the vertical velocity component $v_i = w$ normalized by the mean tip velocity in hover. The first case to examine is the induced inflow ratio at the wing stroke plane for the various pitch angles. The wing stroke plane is defined as the plane normal to z direction that cuts through the middle the of wing during the flapping cycle at ($Z = -0.5\bar{c}$) as shown in Fig. 5.13.

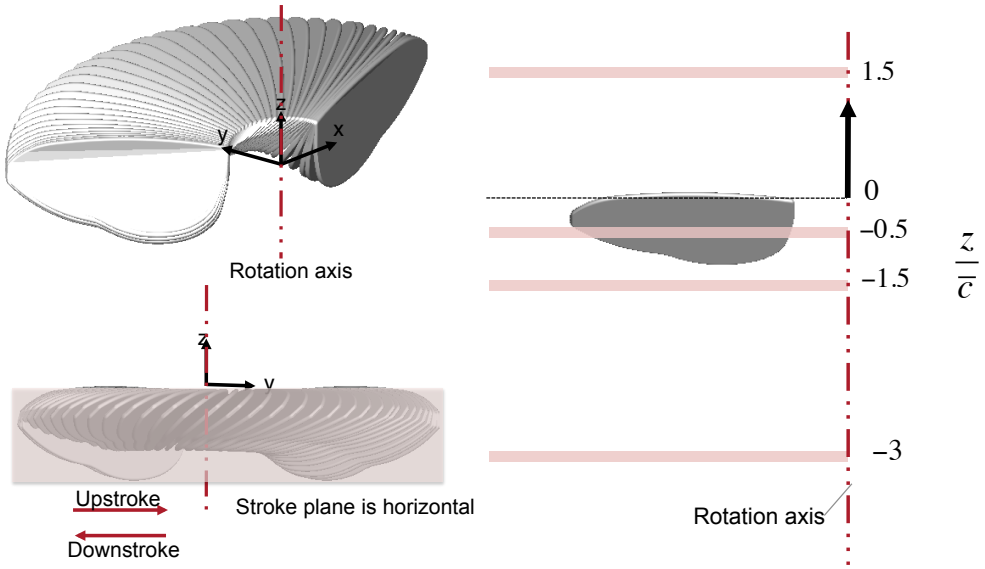

(a) Hovering flap stroke

(b) Section parallel to the flap-stroke plane in the Z direction

Figure 5.13: Schematic diagram of the hovering flap-stroke. Flap-stroke is horizontal.The shed lines describe the planes parallel to flap-stroke at different location in the Z direction below and above the wing. The location is given in non-dimensional quantity (normalized Z by R).

A map of the time-averaged (along upstroke and downstroke) inflow distribution normal to the stroke plane is plotted in Figure 5.14. Inflow at mid-stroke as a function of radial position is also plotted below each map for the various pitch angles (Figure 5.14). The contours of the averaged inflow along the flap cycle shows that the intensity of the inflow ratio increases with increasing pitch angle (although the intensity decreases slightly for the 60° case toward the end of

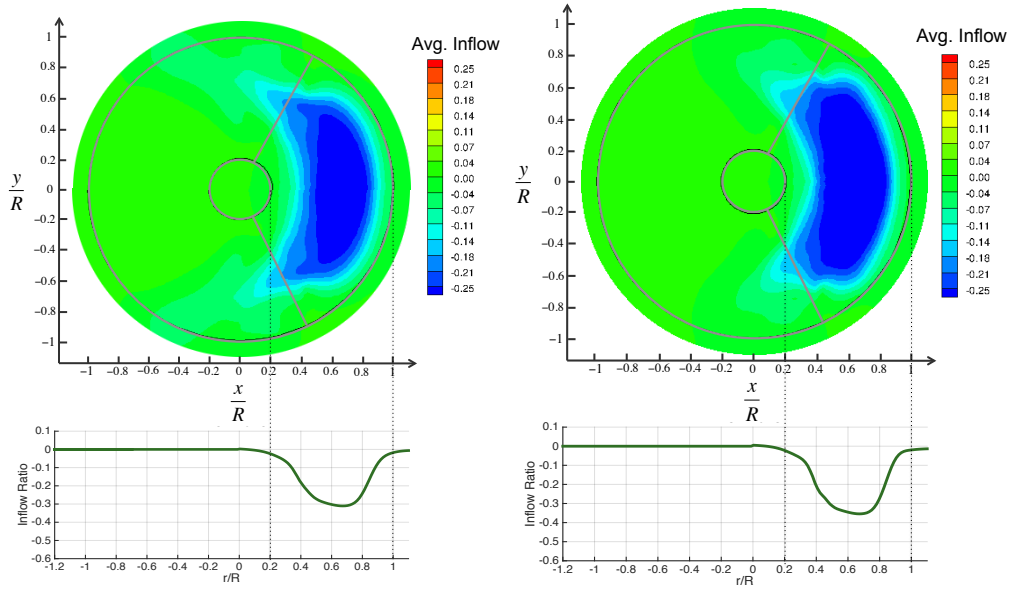

(a) Pitch angle 30 deg

(b) Pitch angle 40 deg

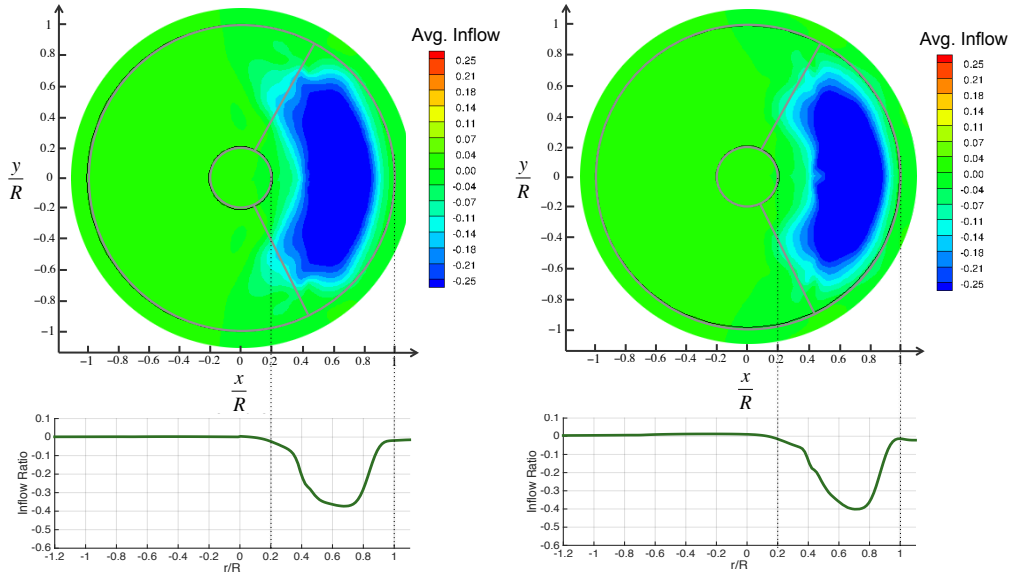

(c) Pitch angle 45 deg

(d) Pitch angle 60 deg

Figure 5.14: Inflow ratio.

the strokes). At mid-stroke, it shows a roughly linear increase in inflow magnitude radially up to a peak in induced inflow ratio at approximately $r/R = 0.7$. The maximum peak location at mid-stroke is approximately the same for all of the considered pitch angles, but the peak magnitude varies with the pitch angle, where a larger peak is obtained for the pitch angle of 60° case with value of 0.4 (downward) and a peak of 0.3 for 30° case; for 40° and 45° cases the induced inflow ratio reaches a peak of around 0.35.

The effective angle of attack can be approximated as:

$$\alpha_{eff} = \alpha_g - \tan^{-1}\left(\frac{v_i}{\omega(t)r}\right) \tag{5.6}$$

The local velocity $\omega(t)r$ also increases linearly with r, thus the induced angle of attack change is nearly constant for the inboard 70% of the wing, before sharply decreasing outboard. Also, this induced angle of attack change continues during the translational portions (before the reversal portions). Figure 5.15 shows the variation of the effective angle distribution along the wing span at mid-stroke for the cases with various geometrical pitch angles. The reduction in the pitch angle is nonuniform along the span due to varying rotational velocity and induced velocity along the span. The minimum effective pitch angle occurs in the wing inboard portion, between r/R$= 0.4 - -0.8$. The maximum reduction magnitude is about 20 to 25 degrees.

The inflow distribution for the case of mid-stroke pitch angle of 40° is investigated further by plotting at different planes parallel to the stroke plane, one above the wing and two below in the inflow direction, as shown in Figure 5.16. As can be expected, the flow further below the wing convected downstream in hover from the trailed and shed vortices; as a result the inflow

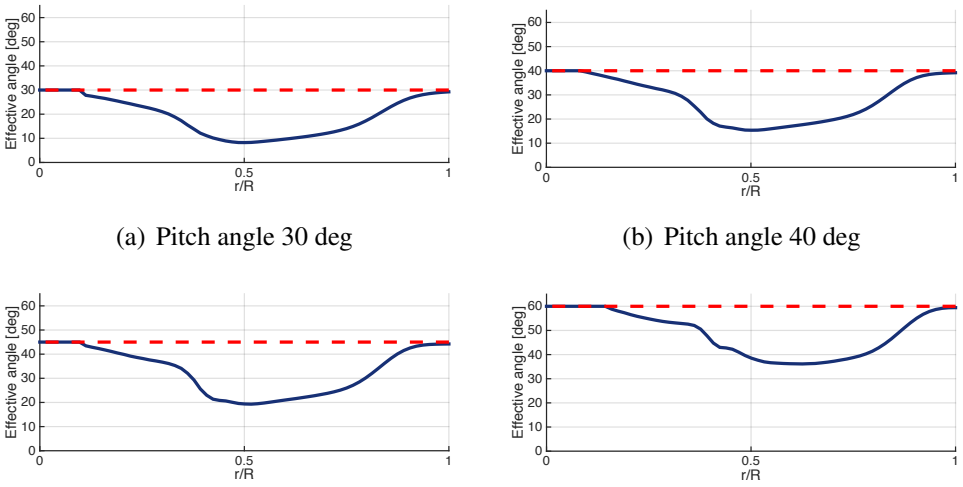

(a) Pitch angle 30 deg

(b) Pitch angle 40 deg

(c) Pitch angle 45 deg

(d) Pitch angle 60 deg

Figure 5.15: Effective angle distribution as a function of wing span at midstroke. The dashed red line indicates the geometric pitch angle.

ratio increases. For example at the mid-stroke station the inflow peak increases from 0.35 (at $r/R = 70\%$) at the stroke plane to approximately 0.5 at a plane that is located 3 mean chords below the wing ($Z = -3\bar{c}$). Further, the distribution of the inflow changes where at the stroke plane it is narrowed to the wing stroke, with the inflow becoming weaker towards the reversal stations. In the down stream the inflow expands further demonstrating the convecting tip vortices that convect downstream and far from the wing. Below the stroke plane, the highest inflow velocities shift more towards the stroke endpoints. Above the stroke plane ($Z = 1.5\bar{c}$) very little inflow is observed.

5.3 Summary and Conclusions

A parametric study of a flapping wing was presented in this chapter in order to determine the most appropriate efficiency metric for a flapping wing case and to investigate the effect of kinematic parameters, along with some features of the flowfield. The efficiency metric was deter-

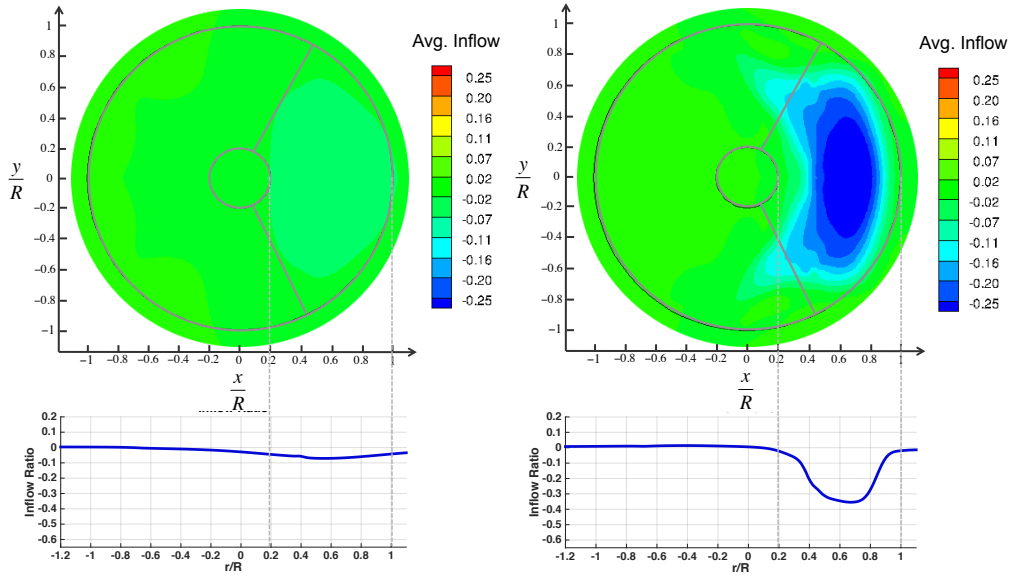

(a) Z=1.5$\bar{c}$ (b) Stroke plane (Z=-0.5$\bar{c}$)

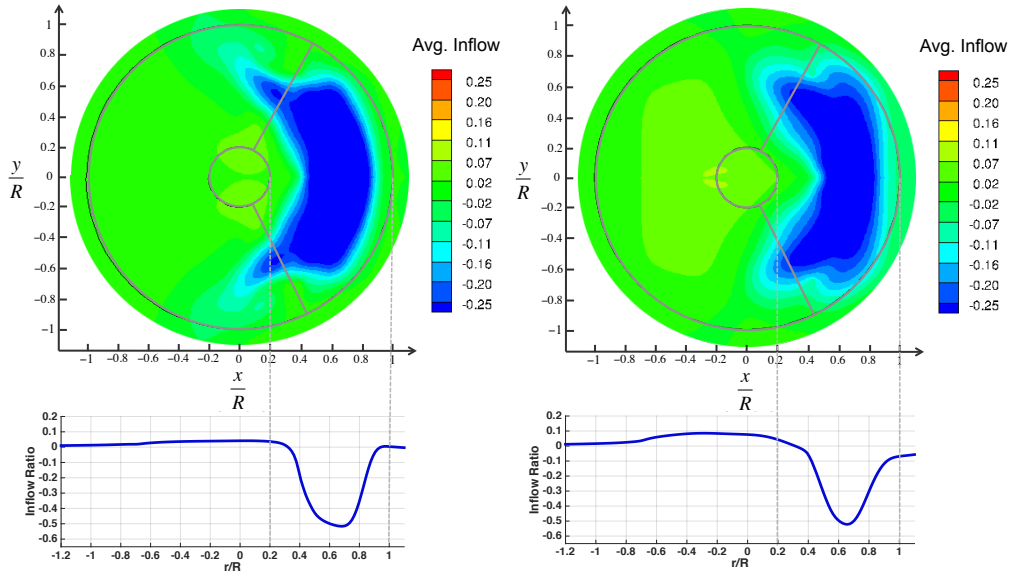

(c) Z=-1.5$\bar{c}$ (d) Z=-3$\bar{c}$

Figure 5.16: Inflow ratio.

mined by studying the averaged forces and power for various pitch angles and range of Reynolds numbers. Also, CFD results were compared against the QS results. The main outcomes from this chapter are the following:

- **Effiiency metrics**
  - It was conclude the power loading as a function of averaged lift (L/P vs. L_{avg}) is more appropriate as an efficiency metric than is the L/D ratio. The proposed metric properly accounts for the required aerodynamic power and vertical thrust as a function of prescribed kinematics. The ratio L/P versus lift can be used to determine the performance. Power and vertical thrust are the key parameters for design and performance.
  - In terms of efficiency metrics, the QS model fails to predict the values obtained by CFD, especially when L/D is considered. This results from the inadequate modeling of the unsteady mechanisms in the QS model.
  - One specific outcome of the analysis is the conclusion that for the given flapping frequencies ranging from 100-300 Hz, a pitch angle of 40 degrees has a clear advantage over pitch angles of 30 and 60 degrees in terms of L/P versus lift.
- **QS model**
  - Quasi-steady model performed quite well at lower Reynolds number; with increasing Reynolds number the discrepancy between the mean lift and drag as compared to CFD were larger.

- In terms of an efficiency metric, QS model fails to predict the values obtained by CFD. This results from inappropriate modeling in QS of the unsteady mechanisms.
- the trend of L/P predicted by QS is similar to those predicted by CFD, but with lower magnitudes predicted overall.

- **Wake and induced inflow**
  - It was found that the flowfield dynamics were affected by pitch angle as well as Reynolds number. LEV size and the shed and trailed tip and root vortices are more dominant for large mid-stroke pitch angles for the same Reynolds number. This resulted in a benefit in the lift force but this advantage was limited to a pitch angle up to 45°. For pitch angles larger than 45°, the drag component of the LEV becomes more significant in comparison to the lift component, which leads to low L/P ratio as well low L/D ratio.
  - Significant amounts of force are produced in the peaks resulting from wake capture and rotational circulation. The increase in the required power can be approximately 30% of the total power.
  - It was shown that the vortical wake around the wing that results from the shed and trailed tip and root vortices has a significant effect on the forces through the induced inflow. The induced inflow impacts the effective angle of attack experienced by the wing; this impact is a reduction in effective angle of attack, which might partially explain the 3D stability of the LEV during the translational portions.The effective angle of attack the wing experience are at least 15 degrees less than the geometrical angles.

Chapter 6

Trim Algorithm

This chapter discusses in details the trim algorithm used to analyze the performance of a flapping wing MAV in steady flight (i.e.: hover, steady level flight, steady coordinated turn). By coupling a flight dynamic model of the insect with a simplified quasi-steady wing aerodynamics to a high-fidelity CFD analysis. The objectives of the trim algorithm are:

- Generalize the flapping-wing trim framework and CFD solver to analyze steady flight including hover, forward flight and coordinated turn.
- Determine kinematics-driven limitations for the flight envelope in level turns.
- Apply CFD coupling to characterize the flight limits (i.e.: maximum forward speed) for a particular platform.

This tool would be useful for quickly evaluating different combinations of design parameters, and for performing detailed loads analysis for vehicle component sizing.

Trim refers to a steady flight condition in which the translational and rotational accelerations are zero (sometimes termed “equilibrium of forces and moments”). Therefore, trim includes hover, steady level flight, steady climbing forward flight, steady level turn and steady climbing/descending turns of constant radii.

Trim for a fixed-wing aircraft is defined as a steady flight condition in which the control

settings, orientations and velocity of the vehicle produce forces and moments (inertial and aerodynamic) that exactly cancel out external forces (gravity), allowing the aircraft to remain in its state of uniform motion "indefinitely". The force distributions on a fixed-wing aircraft are fairly steady in nature, and so the loads, during trim, at any two instants in time will be near-identical. In contrast, the loads generated by a flapping wing are not steady. The presence of wing flapping motion requires a modification to the traditional definition of aircraft trim.

When the chosen wing kinematics parameters are held constant, the flapping-wing MAV is said to be trimmed if the steady-state forces and moments are periodic, and do not change over successive periods. The time period is assumed to be that required for one complete flap cycle, due to the cyclic variation of the free-stream velocities experienced by the wings as driven by flap kinematics. Thus, the loads at the center of gravity of a flapping wing MAV are oscillatory in nature, fluctuating about a non-zero mean.

While trim solutions are obtained using a simplified aerodynamic model with very low computational cost, three-dimensional CFD simulations are key to capturing all associated unsteady phenomena and providing fundamental insight into the nature of the flow-field. This section provides the details of the flight dynamic model, trim condition, trim variables and the loose-coupling algorithm.

6.1 Flight Dynamics Model

The flight dynamics model is obtained by expressing the fundamental equations of force and moment equilibrium along the inertial coordinate system, shown in Fig. 6.2(a). The body of the

insect is assumed to be rigid and the dynamics are given as:

$$\mathbf{F} = \left(\frac{\partial}{\partial t} + \omega\times\right) m\mathbf{V} + m\mathbf{g} \tag{6.1}$$

$$\mathbf{M} = \left(\frac{\partial}{\partial t} + \omega\times\right) \mathbf{I}\,\omega \tag{6.2}$$

where **F** and **M** represent, respectively, the external forces and moments acting at the CG due to body drag, and wing aerodynamic and inertial loads. m is the total mass of the insect. At these length scales, the body mass is the dominant contribution to vehicle mass, and the mass of the wings is negligible in comparison. **g** is the acceleration due to gravity and ω is the body angular velocity vector. **I** represents the inertia tensor with body-fixed axes as reference. Wing inertial loads are ignored for trim since they are guaranteed to have a mean value of zero for periodic flapping. The quasi-steady aerodynamic loads are computed based on the dynamic pressure and local flow orientation at 75% span. Lift and drag coefficients are obtained using a table look-up process, provided by experimental data from Dickinson [5] as described in section 3.1.1.

The governing rigid-body ODEs are assembled numerically in a nonlinear implicit state-space representation as

$$\mathbf{f}(\dot{x}, x, u; t) = \mathbf{0} \tag{6.3}$$

x represents the vector of system rigid-body states and u represents the vector of controls; and will be referred to in this study as trim variables that determine the kinematics of the insect configura-

tion wings.

6.2 Wing Kinematics

Actual insect kinematics are complex, involving joint flexure, wing deformation, and a variety of stroke characteristics including asymmetric fore and aft and out-of-plane deviations. These three-dimensional motions are challenging to describe using sequential joint rotations. However, these complex motions can be simplified by imposition of two conditions

1. Wing translation motions are contained on a single plane (the stroke plane)

2. Wing motions for up-stroke and down-stroke are symmetric

The wing motion used in this study is a simplified representation of that exhibited by the fruit fly (drosophila). The insect wing stroke can be conceptualized as four distinct sequences that blend into each other smoothly: downstroke translation, supination, upstroke translation and pronation. Supination and pronation are the pitch reversals at the end of each translation stage and serve to keep the angle of attack positive. Figure. 6.1(a) shows the downstroke motion and supination. The geometric pitch angle with respect to the flapping stroke plane remains constant except near the stroke reversal during supination and pronation, as shown in Fig. 6.1(b).

In this study, flapping wing motions are parameterized using three sequential rotations (Fig. 6.2(a)):

- Stroke plane elevation angle (β), which determines the plane in which the wing flaps.

- Flap stroke angle (ϕ), which represents the azimuthal position of the wing in the flap cycle.

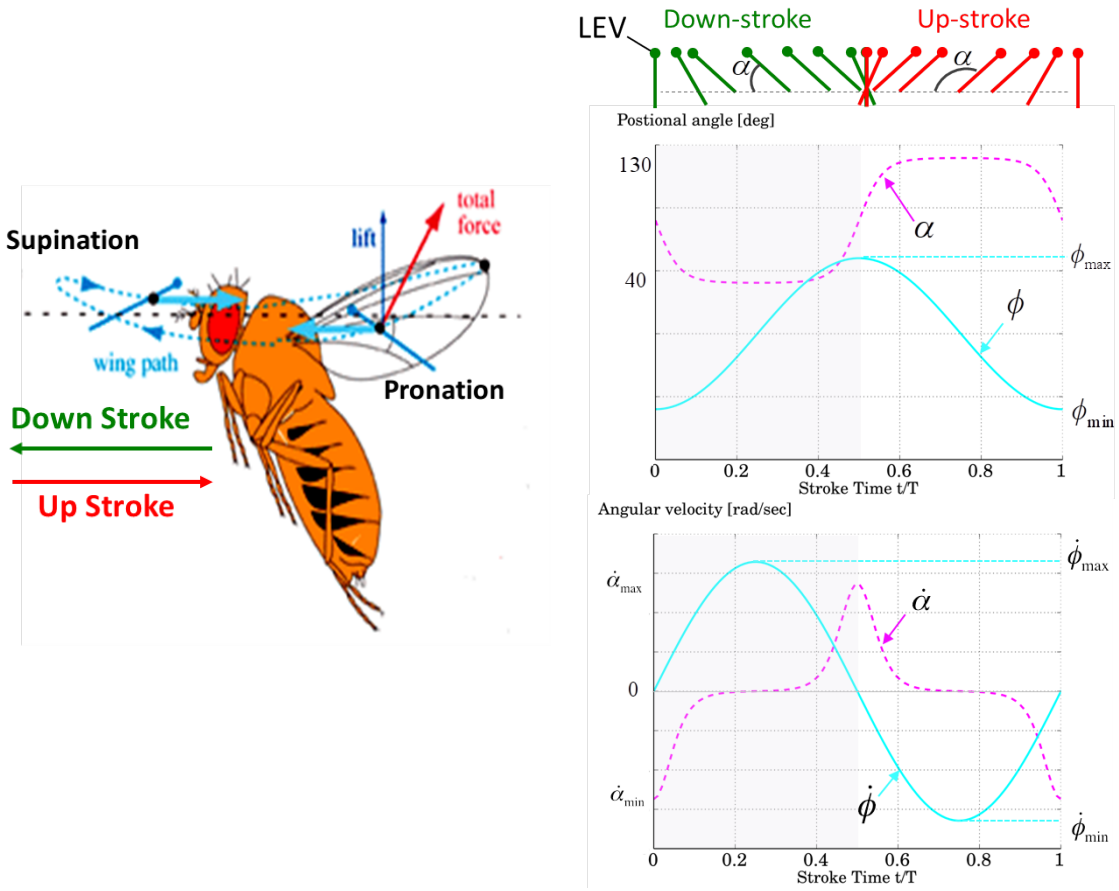

(a) Isometric view of wing kinematics [4]

(b) Wing positions and angular velocities

Figure 6.1: Schematic representation of insect wing kinematics and time histories of positional angles during a flap cycle.

- Pitch incidence of the wing (α_g) is the geometric incidence angle of the wing chord relative to the stroke plane.

Wing kinematics used in this study are qualitatively similar to the those used by Faruque and Humbert [79] for *Dipteran* insect flight dynamics, and by MacFarlane and Humbert [80] for *Drosophila* type platforms. Figure 6.1 shows the downstroke motion and supination.

The flap stroke velocity increases at constant rate and the maximum velocity occurs at mid-stroke. The azimuthal position of the wing in the flap cycle is given by

$$\phi(t) = -\phi_{\max}\cos(2\pi f t) + \phi_{\text{off}} \quad [deg] \tag{6.4}$$

The geometric pitch angle with respect to the flapping stroke plane remains constant except near the stroke reversal during supination and pronation, and is given by

$$\alpha_g(t) = 90 - \alpha_{\max}\tanh(2.7\sin(2\pi f t)) \quad [deg] \tag{6.5}$$

α_{max} (equal to 40 deg for baseline simulations) is the complimentary angle of the maximum geometric pitch at the mid-stroke with respect to flapping stroke plane. This angle remains constant during the translation periods and increases as the wing approaches stroke reversal, as shown in Fig. 6.1.

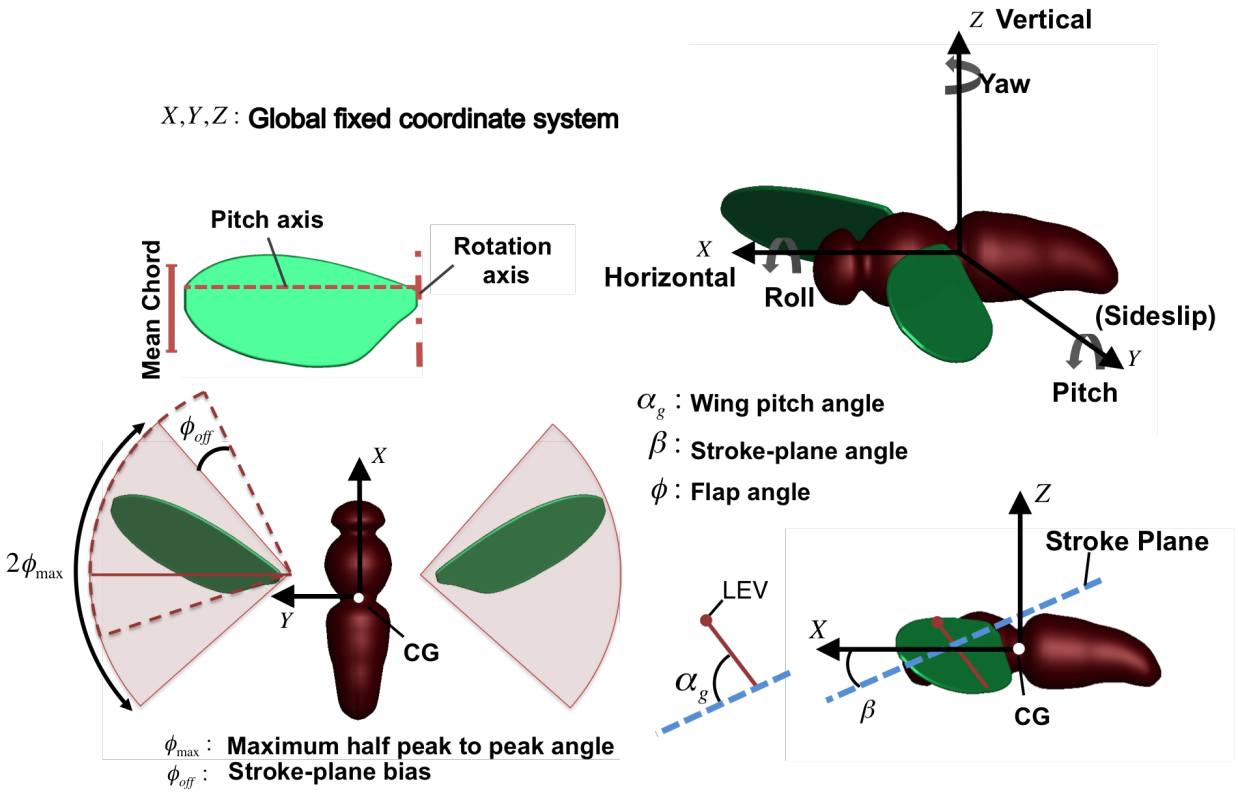

(a) Inertia coordinate systems and wing kinematic parameters ϕ, α and β

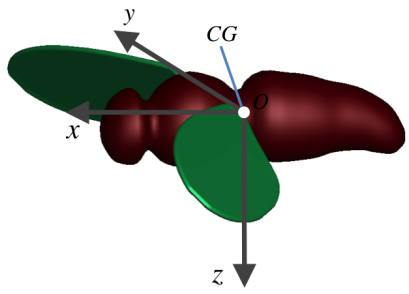

x, y, z : **Body fixed coordinate system**

(b) Body coordinate systems

Figure 6.2: Insect coordinated systems and wings kinematics.

6.3 Steady Trim Flight

Steady flight trim represents the condition where the insect center of gravity experiences zero translational and rotational accelerations as measured along the body-fixed axes. Mathematically, this condition is represented using the following equations:

$$\dot{u} = \dot{v} = \dot{w} = 0 \tag{6.6}$$

$$\dot{p} = \dot{q} = \dot{r} = 0 \tag{6.7}$$

Three flapping kinematics parameters for each wing are allowed to vary in this study to achieve the forces and moments required to maintain steady flight. These parameters are identical between the port and starboard wings in steady level forward flight, and are referred to as "trim variables". The trim variables in this study are:

1. Half peak-to-peak stroke amplitude ϕ_{max}: dominantly affects the vertical thrust
2. Stroke flapping bias ϕ_{off}: primarily affects the center of lift during the flapping stroke, and hence the body pitching moment
3. Stroke plane angle β: produces a forward tilt of the resultant thrust vector, used to eliminate drag by generating positive propulsive force

The trim variables, moments, and forces with respect to the global inertial (space-fixed) coordinate system are depicted in Fig. 6.2. Within each flap cycle, the aerodynamic forces on the wing are time-varying, thus the insect body experiences non-zero accelerations when flying at constant

speed. To obtain engineering solutions for this platform, insect trim is defined, using an analog of rotary-wing vehicle trim, as the condition where the time-averaged wing loads over one flap cycle exactly balance the forces and moments due to external loads (gravity and body drag). Steady non-accelerating flight is obtained in an *average* sense over one flap cycle. Schematic illustration showing the analogy between flapping wing and rotary-wing is shown in Fig. 7.2. For the study cases the insect body forces are neglected due to their small magnitude (see Appendix C).

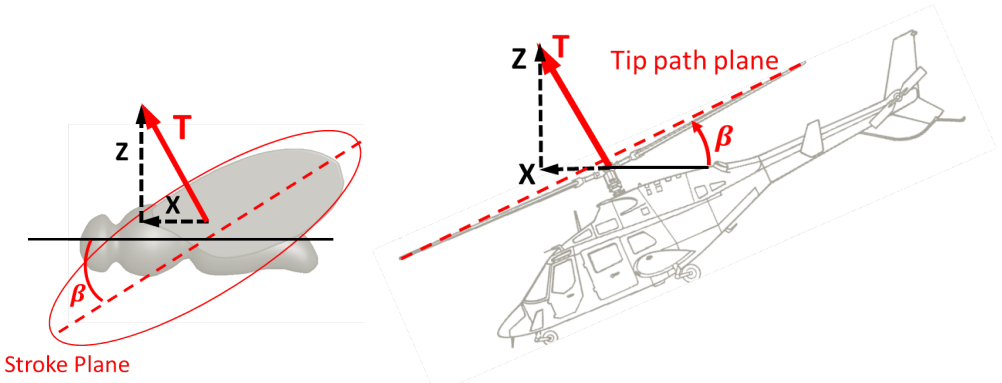

(a) Flapping wing stroke plane (b) Helicopter tip-path-plane

Figure 6.3: Free-body diagram showing analogy between flapping wing and rotary-wing: resultant thrust, time-averaged over one cycle, is nominally perpendicular to the stroke plane (insect) or tip-path-plane (rotor).

For trim analysis, the ODEs in Eqn. 6.3 are numerically reduced to algebraic equations, using a procedure similar to that adopted for rotorcraft trim. In steady turning flight, the heading Euler angle (ψ_B) is allowed to change at a constant rate, while the body pitch (θ_B) and body roll (ϕ_B) attitudes must be steady. Further, the body aerodynamics are neglected and the longitudinal position of the vehicle center of gravity is near the wing mount location. Therefore, the body pitch attitude θ_B is prescribed as zero. The kinematic consistency equations for rigid-body dynamics yield the following expressions for the translational and angular velocity components:

$$u = V_\infty \tag{6.8}$$

$$v = 0 \tag{6.9}$$

$$w = 0 \tag{6.10}$$

$$p = 0 \tag{6.11}$$

$$q = \dot{\psi}_B \sin\phi_B \tag{6.12}$$

$$r = \dot{\psi}_B \cos\phi_B \tag{6.13}$$

where $\dot{\psi}_B$ is the rate of turn, ϕ_B is the body pitch as described in Fig. 6.4. V_∞ is aligned with the body longitudinal axis, i.e. the MAV flies with zero sideslip. Substituting the translational and angular velocity in Eqns. 6.1 and 6.2 yields the following trim equations for force and moment balance:

$$\overline{F}_x = 0 \tag{6.14}$$

$$\overline{F}_y = mV_\infty \dot{\psi}_B \cos\phi_B - mg\sin\phi_B \tag{6.15}$$

$$\overline{F}_z = -mV_\infty \dot{\psi}_B \sin\phi_B - mg\cos\phi_B \tag{6.16}$$

$$\overline{M}_x = -(I_{yy} - I_{zz})\dot{\psi}_B^2 \sin\phi_B \cos\phi_B \tag{6.17}$$

$$\overline{M}_y = 0 \tag{6.18}$$

$$\overline{M}_z = 0 \tag{6.19}$$

In obtaining the moment balance equations, the cross-products of inertia were assumed to be zero. Here, $\overline{F}_x$ represents the component of stroke-averaged wing aerodynamic force along the body longitudinal axis. A similar notation has been followed for the other loads. In a coordinated turn, the body roll attitude is prescribed so that the lateral component of the stroke-averaged wing aerodynamic force (in the inertial reference) counters the centrifugal force, i.e. the aerodynamic force along the body lateral direction vanishes ($\overline{F}_y = 0$). This condition can be used to solve for the roll attitude as

$$\phi_B = \tan^{-1} \frac{V_\infty \dot{\psi}_B}{g} \tag{6.20}$$

Aerodynamic forces and moments, as well the body angles are described in Figure 6.4.

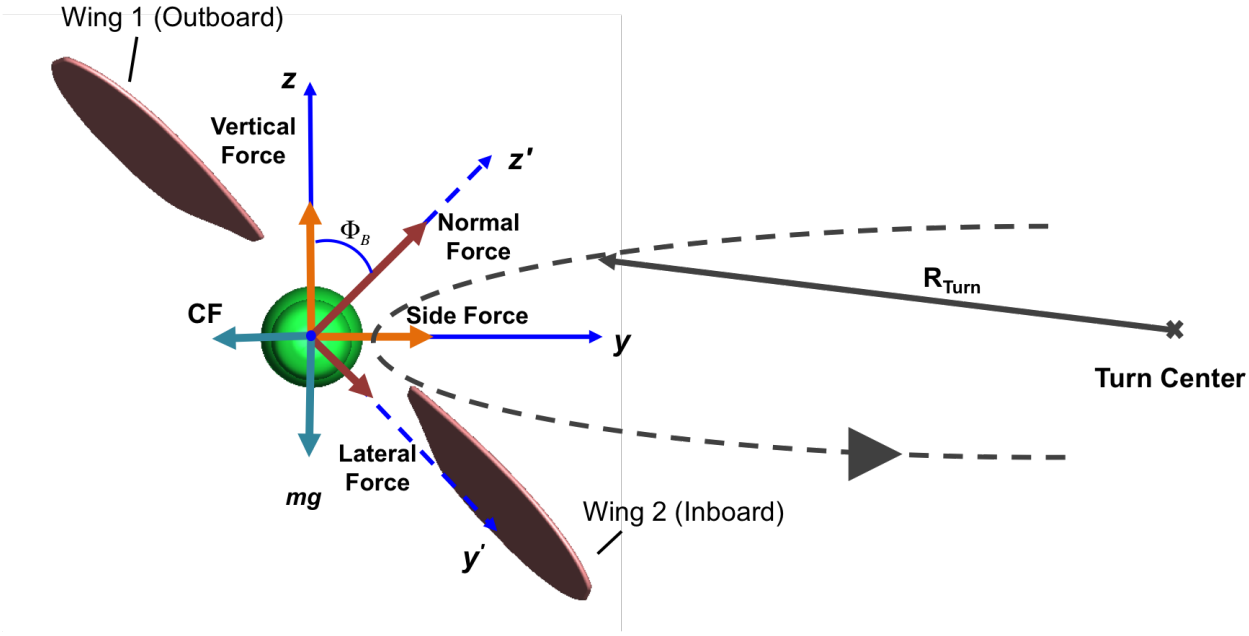

Figure 6.4: Forces and moments in coordinated steady turn.

Therefore, the trim equations for force balance reduce further to

$$\overline{F}_x = 0 \tag{6.21}$$

$$\overline{F}_y = 0 \tag{6.22}$$

$$\overline{F}_z = -\sqrt{(mg)^2 + (mV_\infty \dot{\psi}_B)^2} = -mg \sec \phi_B \tag{6.23}$$

Where $\sec \phi_B$ is the normal load factor produced by the wings in the vertical direction. The negative sign indicates that the wing force component is upwards, since the coordinate direction for body Z-axis points downwards.

In steady forward flight and hover, symmetry can be assumed with respect to the body X-Z plane. Turn rate and body roll angle is zero, and average side force is zero (no centrifugal force). Further, wing inertial loads are ignored because the inertial loads vanish when time-averaged over one flap cycle for periodic kinematics. Therefore, the flight dynamics reduce to the following longitudinal trim equations:

$$\overline{F}_x = 0 \tag{6.24}$$

$$\overline{F}_z = -mg \tag{6.25}$$

$$\overline{M}_y = 0 \tag{6.26}$$

Here, $\overline{F}_x$ represents the component of stroke-averaged wing aerodynamic force along the body longitudinal axis, $\overline{F}_z$ represents the component of stroke-averaged wing aerodynamic force in z direction and $\overline{M}_y$ represents the aerodynamic pitching moment about CG.

As stated earlier, the corresponding trim variables are the parameterized wing kinematics (ϕ_{max}, ϕ_{off}, β). The trim equations are solved using a gradient descent technique starting from an initial guess. The trim process relies on gradient descent to drive the system towards longitudinal force and moment balance, for which a trim Jacobian matrix is required. The quasi steady aerodynamic model is used to obtain the Jacobian, similar to the technique adopted by MacFarlane and Humbert [80]. In forward flight and hover the trim Jacobian is represented by a 3×3 matrix, that indicates the sensitivity of the time-averaged aerodynamic loads in the longitudinal plane to the wing kinematics:

$$J = \begin{bmatrix} \frac{\partial X}{\partial \phi_{max}} & \frac{\partial X}{\partial \phi_{off}} & \frac{\partial X}{\partial \beta} \\ \frac{\partial Z}{\partial \phi_{max}} & \frac{\partial Z}{\partial \phi_{off}} & \frac{\partial Z}{\partial \beta} \\ \frac{\partial M}{\partial \phi_{max}} & \frac{\partial M}{\partial \phi_{off}} & \frac{\partial M}{\partial \beta} \end{bmatrix} \tag{6.27}$$

While trim solutions are obtained using a simplified aerodynamic model with very low computational cost, three-dimensional CFD simulations are key to capturing all associated unsteady phenomena and providing fundamental insight into the nature of the flow-field. The next section provides details on the CFD methodology used in this study.

6.4 CFD- QS Coupling Procedure (Loose Coupling)

While CFD can provide detailed numerical representations of the flow-field around the insect body and flapping wings, the time taken for CFD analysis is several orders of magnitude larger

than the quasi-steady aerodynamic model. Using CFD directly in the trim process is therefore infeasible because of the associated computational cost. The approach adopted for this work uses CFD to *correct* the quasi-steady model at select stages in the trim process, instead of replacing it entirely. For this work, the *delta air-loads approach* used commonly in rotorcraft analysis [81, 82] is adopted. Using this approach, the spatial and temporal resolution of the unsteady air-loads generated by CFD can be judiciously introduced into the trim framework without incurring a large computational cost. The delta coupling approach is shown schematically in Fig. 6.5, and can be broken down into six distinct steps:

1. **Obtain initial trim variables**: The iterative convergence process begins with the calculation of wing kinematics in trimmed flight using the quasi-steady aerodynamic model to predict the wing forces. This process is relatively inexpensive, requiring approximately 5 – 10 seconds depending on the initial guess. This step is performed once to start the convergence process.

2. **Obtain quasi-steady wing forces**: Using the trimmed wing kinematics obtained from step 1, the quasi-steady model is used to predict the time history of airloads over one flap cycle. These forces and moments are stored for use in step 4.

3. **Compute CFD wing forces**: The trimmed wing kinematics are fed as prescribed motions to the CFD solver. CFD simulations of the flapping wing are performed using time marching for several flap cycles, until the wing loads and flow-field characteristics exhibit periodicity over successive flap cycles. Subsequently, the time history of wing forces and moments over one flap cycle are stored for use in step 4.

4. **Compute delta airloads**: For identical motions, the difference between the time histories over one flap cycle of the CFD-generated airloads and corresponding values from the quasi-steady model, are computed and stored as *delta* air-loads in coefficient form. These loads represent the airloads that, when added to the reduced-order model, *corrects* the quasi-steady aerodynamics to match the CFD predictions. This *delta* represents a point calibration for a particular combination of kinematics.

5. **Retrim using QS model with delta corrections**: The trim algorithm is used to compute the updated wing kinematics to match the chosen flight condition. During the calculation of wing forces, the quasi-steady model is augmented with the corrections generated in step 4, corresponding to the previous trim kinematics. The delta airloads are prescribed as a constant correction to the reduced-order quasi-steady model during the trim process (inner loop).

6. **Repeat steps 2 –5**: using alternate updates of wing kinematics and CFD airloads, the trim solver and delta airloads are computed until the trim variables converge. When convergence is achieved between two successive coupling iterations, the delta airloads (CFD - QS) generated using the previous set of wing kinematics exactly calibrates the simplified aerodynamic model to match the loads generated by the high-fidelity analysis, thus resulting in a consistent trimmed solution.

Steps 1 and 5 constitute the "inner" trim loop for this coupled analysis, while step 6 can be thought of as the "outer" convergence loop between trim and CFD.

The flight dynamic model with built-in quasi-steady wing aerodynamics is used to obtain

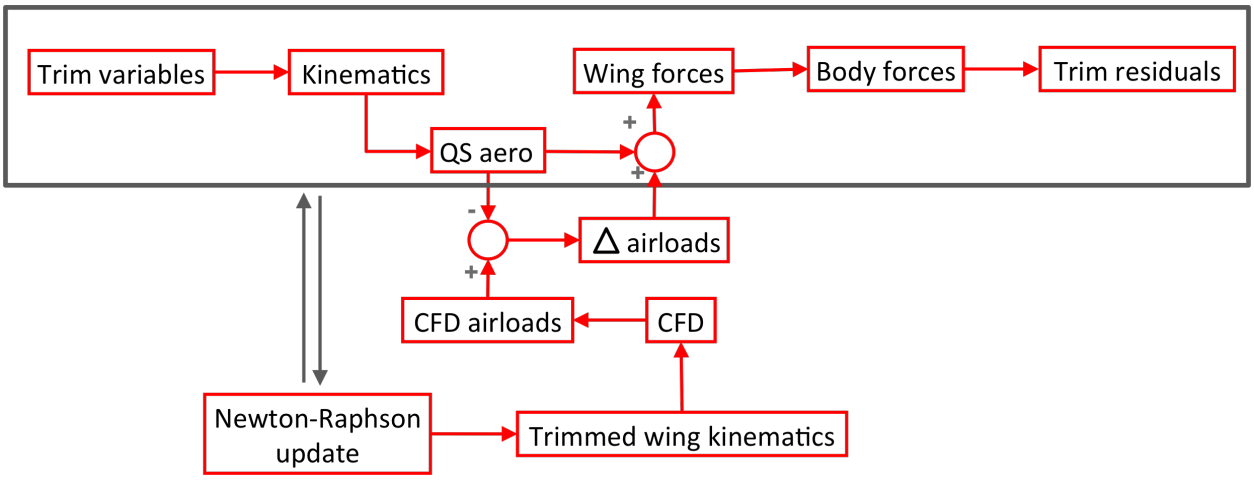

Figure 6.5: Loose coupling algorithm

the trimmed wing kinematics using Newton-Raphson iterations. For each iteration, the Jacobian (sensitivity of cycle-averaged force and moments to perturbations in the individual trim variables) is recalculated using forward differences about the current trim guess. For the vehicle parameters considered, 5 – 10 iterations are required until trim is achieved. The quasi-steady aerodynamic model is very inexpensive, and requires a few seconds to achieve trim.

6.5 Simulations Overview

The computational wing model is based on the scaled model of a fruit-fly (drosophila) wing used by Dickinson et al. for the robofly [28]. Wing kinematics, size and flapping frequency match those of the drosophila. The wing span and geometric angle of attack were chosen based on the parametric study presented in Chapter 5 :

- Wing geometric incidence angle α_g with respect to stroke angle: to maximize the hover power loading (lift/power), this parameter is set to 40 degrees.

- Wing span b: to generate sufficient vertical and propulsive force at a flap frequency of 200 Hz, a wing span of $3mm$ is required.

- The body mass m is 1.11mg, and the wing mass is negligible in comparison to the body mass (wing mass less than 0.5% of the body mass [4]).

The moments are calculated about the center of gravity, **CG**. The center of flapping for each wing is offset 1 mm to the side of the body centerline. Furthermore, this flapping axis is located 0.3 mm ahead and 0.4 mm above the **CG**. The key geometric and kinematic parameters are given in Table 6.1

Table 6.1: Geometric and kinematic parameters of insect simulations

Diptera Simulations Parameters	
Wing Span R	3 mm
Aspect ratio of each wing AR	2.8
Body length L_b	3.2 mm
Insect mass m	1.11 mg
Flapping frequency f	200 Hz
Pitch angle α_g	40 deg
Forward speed $\mathbf{V}_\infty$	0 (hover), 0.3, 0.5, 1, 1.2, 1.5 m/s

For the hover case, Re is approximately 140, and the Mach number is 0.0056. For the forward flight cases, U_{ref} is equal to the flight speed. The Reynolds number in 1 m/s forward flight is approximately 73, and the Mach number is 0.003. For low Reynolds numbers $O(10-100)$, no turbulence treatment is needed, and so all of the simulations are laminar.

For a complete flapping cycle (downstroke and upstroke), 2880 time steps are used. To achieve a converged flow field solution, four flapping cycles are performed. The airloads obtained from the insect kinematics are periodic. For averaged forces and moments, the 4^{th} cycle is consid-

ered. For the wake structure analysis, a 5^{th} order CRWENO scheme is used instead of MUSCL. Using a higher order scheme does not affect the aerodynamic loads obtained with MUSCL, but allows for capturing more features of the wake in the computational domain. Table 6.2 summarizes the computational parameters for the *diptera* simulations. More details regarding the baseline solver are presented in Chapter 3, Section 3.1.2.

Table 6.2: Computational parameters of *diptera* configuration simulations

OVERTURNS Solver options	
Number of grids	5
Total timesteps	12,240 (2,880 steps/cycle)
Flow	Laminar
Time-step size	0.125°
Newton sub-iterations	10
Pseduo time step	0.1
Spatial scheme	MUSCL 3rd order
Temporal scheme	2nd order backward (BDF2)
Processors (Parallel execution)	20

Grids for hover and steady flight simulations: The overset grid system has five grids, as shown in Fig. 6.6. The nested background meshes are stationary, extend to allow for the wings' motion, and are built from two levels. The inner mesh has a finer spacing, and an the outer background mesh has coarser spacing. The overset nested mesh is shown in Figs. 6.6(a) & 6.6(b).

The important grid parameters are the following:

- Spacing near the wall (wing surface) is 0.01% of the mean chord, and the wing grid is extended in the normal direction over 82 planes to resolve the near-wake features

- The inner nested background mesh has equal spacing of 5% of the mean chord in all directions, while the outer background has length scale of approximately 4 times the inner

background cell length.

More details of the computational domain and it borders are described in Fig. 6.6.

In the background meshes, 5.85 million mesh points are used. Overall approximately 9 million mesh points are in the computational domain. The computations are performed on 20 processors in parallel, on high performance computing platforms (UMD HPC facilities, Deepthoughts [75]). The nested overset grid system is described in Table 6.3.

Table 6.3: OVERSET grid system -*Diptera* simulation

Mesh	Type	Dimensions	Mesh points (in millions)
2xWing	Structured Body-fitted O-O	$155 \times 91 \times 82$	2.30
Insect Body	Structured Body-fitted O-O	$155 \times 91 \times 82$	1.14
Background 1	Structured Cartesian	$286 \times 322 \times 95$	5.00
Background 2	Structured Cartesian	$286 \times 322 \times 95$	0.85
Total mesh points - 9.85M			

Grids for Trim - Coordinated Turning Flight: To simulate turning flight, OVERTURNS was extended to allow for independent kinematics for each wing. The body and wing grids are allowed to translate and rotate according to the turn rate and turn radius, as shown in Fig. 6.7 a. For turning flight the wings and the insect body are allowed to roll. Two degrees of freedom were added to the grids kinematics: grid rotation around the center of the turning circle, and the insect vehicle rolling around the body axis as part of coordinated turning.

The simulation parameters are similar to these presented for hover and steady forward flight.

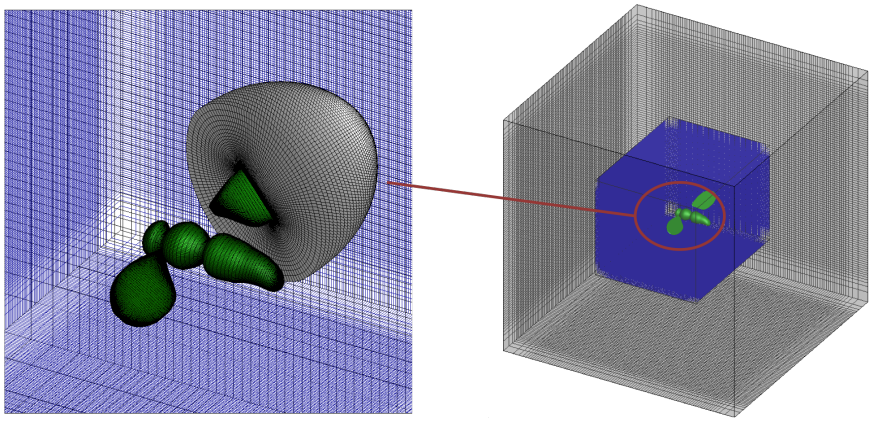

(a) Nested overset grids

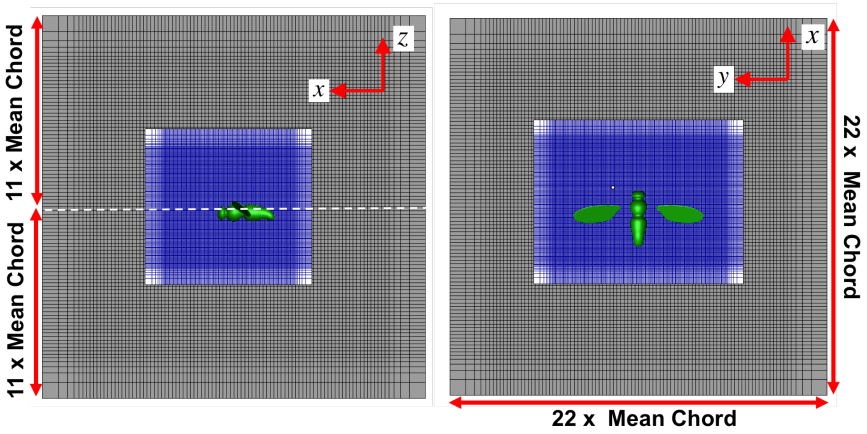

(b) Insect body OO body-fitted grid

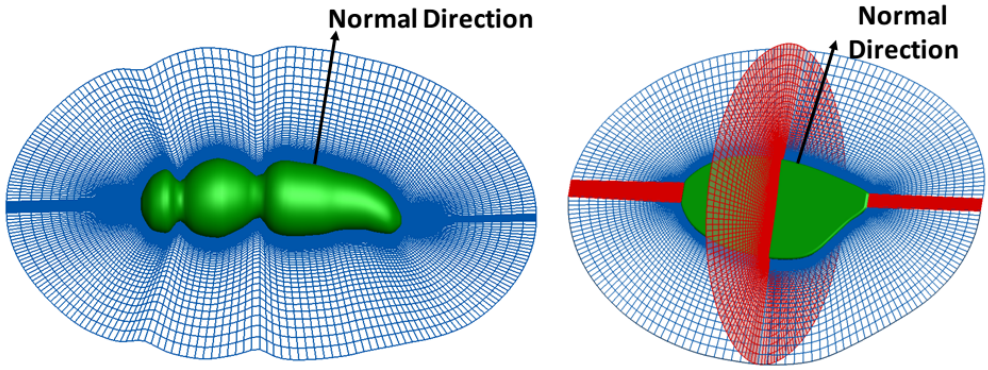

(c) Insect wing OO body-fitted grid

Figure 6.6: Nested overset grid system.

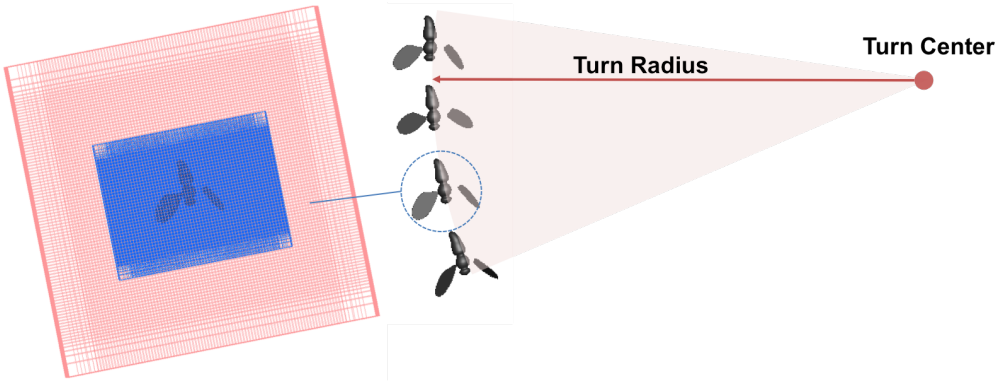

(a) Moving grids

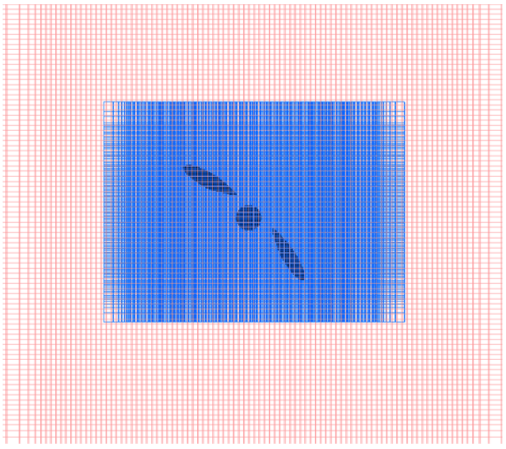

(b) OVERSET grids

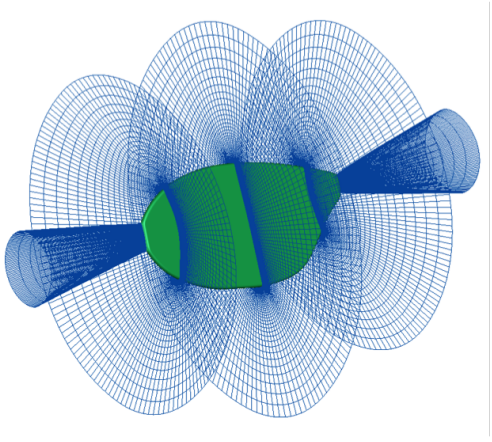

(c) Wing O-O grid

Figure 6.7: Moving overset grids.

Chapter 7

Trimmed Insect Flight Analysis

This study provides a methodology to analyze the performance of a flapping wing MAV in steady forward flight and hover and steady coordinated turning. By coupling a flight dynamic model of the insect with simplified quasi-steady wing aerodynamics to high-fidelity CFD analysis, trim solutions are obtained in realistic time frames. This procedure is analogous to rotorcraft periodic coupling for trim. This multi-fidelity approach, where many quasi-steady calculations are combined with a judicious number of CFD simulations, may be used in parametric sweeps and design studies to effectively study hover and cruise performance. The trim variables chosen in this study are the parameters used to describe the wing kinematics (stroke amplitude, ϕ_{max}, stroke flapping bias, ϕ_{off} and the stroke plane tilt, β). A flight dynamic model and an associated trim (equilibrium) framework are used to identify the wing kinematics required to achieve trimmed flight.

A CFD analysis is required to obtain accurate aerodynamic loads on the wings. Without an efficient trim algorithm, trial-and-error based identification of the trimmed wing kinematics is computationally expensive for forward flight using only CFD, because the number of kinematic parameters is tripled to simultaneously achieve longitudinal force and moment balance. Therefore, this analysis will provide the ability to incorporate the effects of detailed aerodynamic forces from CFD into the trim solution for flapping wing kinematics. The objective of this study is to

identify the variation of wing kinematics parameters with forward flight speed, and highlight the improvements from using CFD over quasi-steady analysis.

Flight conditions investigated in the first part are hover and range of forward flight speeds. A closer investigation of the flow field field features, forces, and power in hover and trimmed forward flight are performed in the second part. The third part presents an approach to use the trim algorithm to find the trim variables for the coordinated turning flight mode.

7.1 Hover and forward flight

7.1.1 Iterative Convergence and Trim

This section discusses the trim characteristics of the flapping wing kinematics, and compares the predictions obtained from using the CFD and quasi-steady analysis. Iterative convergence characteristics are also briefly discussed. The flight dynamic model with built-in quasi-steady wing aerodynamics is used to obtain the trimmed wing kinematics using Newton-Raphson iterations, in the following steps:

1. Set current guess for wing kinematics to initial guess, and reconstruct wing motions over one flap cycle

2. Compute aerodynamic wing forces at 100 equi-spaced instants in one flap cycle

3. Time-average longitudinal forces and pitching moment and substitute in Eqns. 6.26 to compute residuals of the trim equations (trim residuals)

4. Perturb wing kinematics about the current guess and compute corresponding trim residuals to populate the sensitivity matrix of trim residuals to wing kinematics (trim Jacobian)

5. Use the trim Jacobian and trim residuals to update the wing kinematics

6. Repeat steps 2 – 5 until the trim residuals decrease below a specified threshold (10^{-10})

A trim iteration is defined as the sequence of steps 2 through 5. For each trim iteration, the Jacobian (sensitivity of cycle-averaged force and moments to perturbations in the individual trim variables) is recalculated using forward differences about the current set of wing kinematics. For the vehicle parameters considered, 5 – 10 trim iterations are required until trim is achieved. The quasi-steady aerodynamic model is very inexpensive, and requires a few seconds to achieve trim. Though the periodic shooting method has been used in previous work [61], the technique employed in the present work does not rely on time integration of the governing equations. Instead, the ODEs governing flight dynamics are reduced to algebraic equations. Further, if the quasi-steady model is expanded to add further computational complexity, each instant of step 2 (sampling of loads over one flap cycle) may be parallelized to reduce run-times further. In the present case considered, such efforts were not necessary, but the algorithm lends itself readily for scaling if required in the future.

In comparison to the quasi-steady model, each CFD run is extremely expensive. Four full wing flap cycles are required to obtain a converged flowfield and steady-state airloads, and this process takes 4 days. Thus, it is about 30,000 times more expensive to use CFD instead of the quasi-steady model. The CFD loads are therefore introduced as "corrections" to the quasi-steady model. The key assumption in this process is that the trim Jacobian matrix is sufficiently accurate

to guide the CFD-corrected solution towards trim. The numerical values are provided in Appendix A, along with comparison between the QS and CFD trim Jacobian.

Given the non-linear nature of the aerodynamic forces with respect to each of the trim variables, several trim points may exist depending on the specific combination of flight condition and wing geometry. The present methodology obtains the trimmed wing kinematics in forward flight starting from a physically feasible hover solution, and incrementally increasing the forward speed. The trim solution for a lower flight speed is specified as the initial guess for the next speed. This process helps identify one continuously varying set of wing kinematics for various speeds. While other solutions may exist at various speeds, this set represents a physically realizable system (i.e. smooth vehicle acceleration using small increments to the stroke amplitude and plane tilt). Various initial conditions were also provided to the trim solver to identify whether several hover solutions exist. However, in hover, the stroke phase offset is driven by pitching moment balance, stroke amplitude is driven by thrust required to overcome gravity and stroke plane tilt must vanish to avoid producing forward thrust. Cross-couplings between the trim variables and longitudinal forces/moments are insignificant, and only one physically feasible hover solution exists for the chosen parameter set. Therefore, this identified family of solutions is termed "physically feasible", and is presented in this section. Qualitative trends obtained from the quasi-steady trim solutions at various airspeeds are discussed below.

7.1.2 Trim Characteristics

This section examines the variation of wing kinematics in steady forward flight as predicted by the quasi-steady model, for physical insight.

The variation of stroke amplitude with forward speed is shown in Fig. 7.1(a). As forward speed increases, vehicle drag increases primarily due to increased wing drag. The total force required from the flapping wing increases significantly beyond 0.5 m/s, and the stroke amplitude increases to match the thrust required. The variation of stroke phase offset is shown in Fig. 7.1(b). This parameter affects the longitudinal bias of the center of lift ahead of the vehicle CG ,shifting the mid-point of the flap cycle towards the tail for forward speed less than 1 m/s. For speeds higher than 1 m/s (1.2 and 1.5 m/s) an opposite trend is observed where the mid-point of the flap cycle starts to shift forward. The phase offset ϕ_{off} has a dominant effect on the pitching moment, and must be analyzed in conjunction with the stroke plane tilt β, shown in Fig. 7.1(c). The reason for the significant change in the bias angle is the increase in the stroke plane tilt for speed larger than 1 m/s . For a forward speed of 1.2 m/s the flapping plane tilt is almost 50°, and for a forward speed of 1.5 m/s it is approximately 55°.

The stroke plane is the flapping-wing analog of the rotor tip-path-plane, in that the resultant thrust produced by the wings over one cycle is nominally perpendicular to the plane containing the motion of the lifting surfaces. As vehicle speed increases, the stroke plane and hence the resultant thrust vector, time-averaged over one cycle, tilts forward to overcome air resistance, as shown in Fig. 7.2. Similar trends have been observed in the literature, notably by David el al. [51] and Willmott and Ellington [31]. In forward flight, stroke plane tilt was also observed to significantly

affects stall delay, as demonstrated by Nagai [53]. This observation emphasizes the following requirement for flapping wing analysis: the accurate prediction of trim kinematics is key to capturing the dominant flow phenomena. Utilizing either incorrect kinematics or an aerodynamic model of insufficient accuracy results in dominant flow characteristics being missed entirely. The present work, by incorporating high-fidelity CFD airloads into a trim process, addresses this requirement.

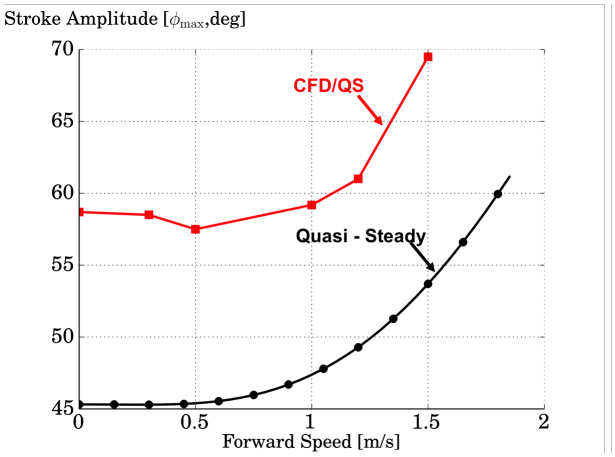

(a) Variation of stroke amplitude with forward speed

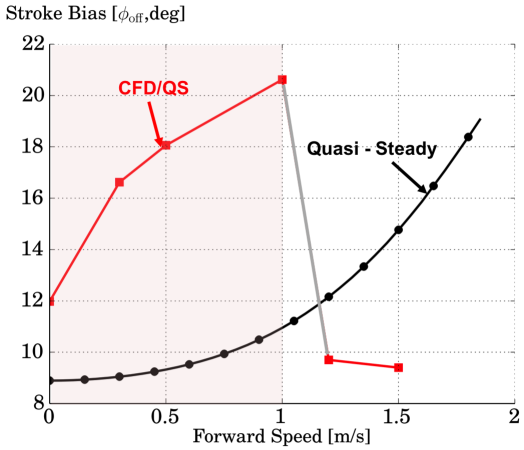

(b) Variation of stroke bias with forward speed

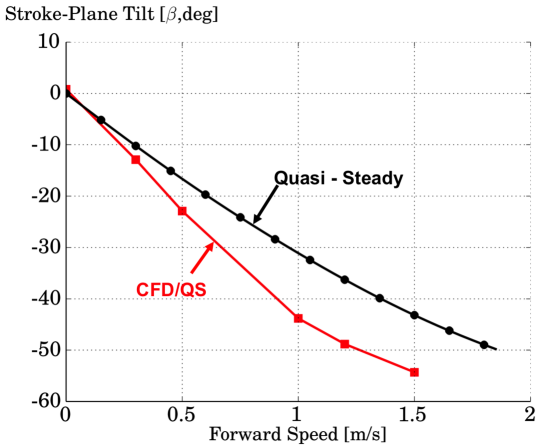

(c) Variation of stroke plane tilt (incline) with forward speed

Figure 7.1: Variation of trim variables with forward speed: quasi-steady aerodynamics vs. CFD.

The difference in dynamic pressure (and therefore lift) produced during the down-stroke

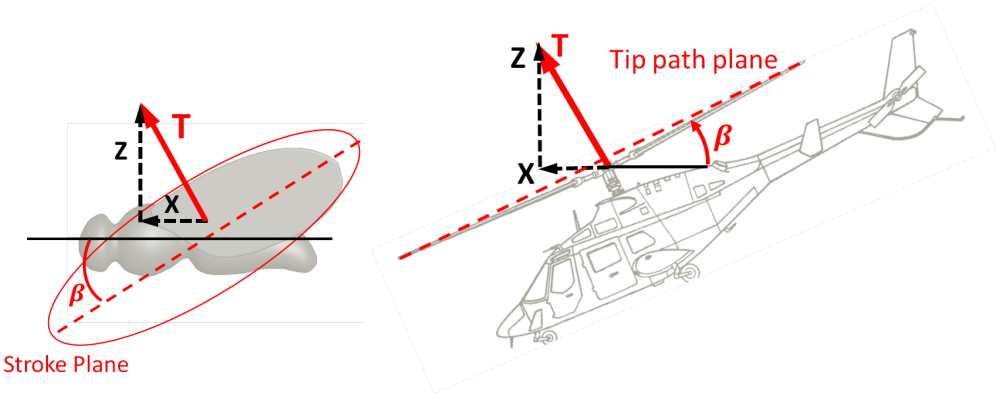

(a) Flapping wing stroke plane (b) Helicopter tip-path-plane

Figure 7.2: Free-body diagram showing analogy between flapping wing and rotary-wing: resultant thrust, time-averaged over one cycle, is nominally perpendicular to the stroke plane (insect) or tip-path-plane (rotor).

and up-stroke results in longitudinal shift of the center of resultant thrust towards the nose. To compensate for this pitching moment, the stroke phase offset increases (i.e. center of lift shifts back towards the tail) so that longitudinal trim is maintained. The maximum forward flight speed at which trim can be achieved is limited by practical aspects of the flapping wing mechanism, i.e.

- Wing stroke angle should not exceed 90 degrees (i.e. wings should not collide)
- Stroke plane tilt should not exceed 70 degrees to avoid complexities in the tilting mechanism

For the present set of parameters, the maximum flight speed is 1.8 m/s as limited by the physical constraints considered.

Figure 7.1 also shows the converged solution obtained using CFD coupling. The stroke amplitude, (Fig. 7.1(a)) is consistently larger than the quasi-steady model by approximately 10 degrees, indicating that the quasi-steady model over-estimates the lift produced. As speed increases, the stroke amplitude exhibits a slight increase at 0.3 m/s, followed by a decrease at 0.5 m/s. Again, the heli-

copter analogy may be used to gain some insight into the flow physics. In forward flight, the wings experience an increase in the total mass flow rate of air available for thrust production, decreasing the induced inflow (on average) and improving system efficiency. The stroke amplitude correspondingly decreases, similar to the reduction of rotor collective at moderate flight speeds. The corresponding effect on stroke-averaged power is shown in Fig. 7.1(d). The quasi-steady model does not include or capture the induced downwash effect, and so the decrease in power required with airspeed is imperceptible. In contrast, the CFD model does capture the downwash. Induced power (and therefore total power) initially decreases with airspeed. As speed increases beyond 0.5 m/s, aerodynamic drag increases and so total power again increases.

Figure 7.1(b) also shows the variation of stroke bias ϕ_{off} predicted by the CFD-coupled trim framework. The quasi-steady model under-estimates the bias by 3 degrees at hover, and exhibits a much gentler increase in stroke bias with airspeed as compared to CFD. However, stroke bias must be considered together with plane tilt with regard to pitching moment. Small changes in the stroke phase offset in forward flight are reflected in corresponding differences in the phase offset. Finally, Fig. 7.1(c) shows that the stroke plane tilt predictions obtained with CFD increase faster with airspeed compared to the quasi-steady trends. CFD predicts more wing drag and less lift than the quasi-steady model, resulting in consistently larger stroke amplitudes (to balance the weight) and greater forward stroke plane tilt (to overcome drag). The coupled CFD/QS framework is able to achieve iterative convergence in 4 CFD-trim cycles for the cases investigated. The following section describes convergence characteristics of the multi-fidelity approach.

7.1.3 CFD-quasi Steady Convergence

Figure 7.3 shows the convergence of the wing trim kinematics at four flight speeds ranging from hover to 1 m/s. All trim variables converge in six iterations with an initial overshoot following the first coupling cycle. The stroke bias ϕ_{off} varies between hover and forward flight by approximately 10 degrees as predicted by CFD. The quasi-steady model (iteration 1) predicts a smaller variation with airspeed for both stroke phase offset and stroke amplitude. At 1 m/s, the quasi-steady aerodynamic model under-predicts the stroke plane tilt angle significantly (more than 25% difference with respect to CFD). Similarly, the quasi-steady model also under-predicts the trim stroke amplitude for all airspeeds.

Figure 7.4(a) shows the time histories of the integrated wing force components resolved along the vertical direction at various stages in the convergence process for 1 m/s forward flight. After the initial CFD predictions, the vertical force component during the down-stroke is insufficient to maintain trim. Most of the imbalance is compensated for by the first wing kinematics update. Iterations 4 through 6 are near-identical, corresponding to the convergence of trim kinematics shown in Fig. 7.3. The time histories for horizontal force are shown in Fig. 7.4(b). Except for small differences during the down-stroke, iterations 4 through 6 exhibit almost identical time histories for this force component.

The time histories of converged longitudinal force and moment components for hover, along with power, are shown in Fig. 7.5. The initial kinematics obtained from the quasi-steady analysis result in significantly reduced vertical force for both hover and forward flight. As coupling iterations proceed, the wing stroke amplitude increases to compensate for this deficiency and the

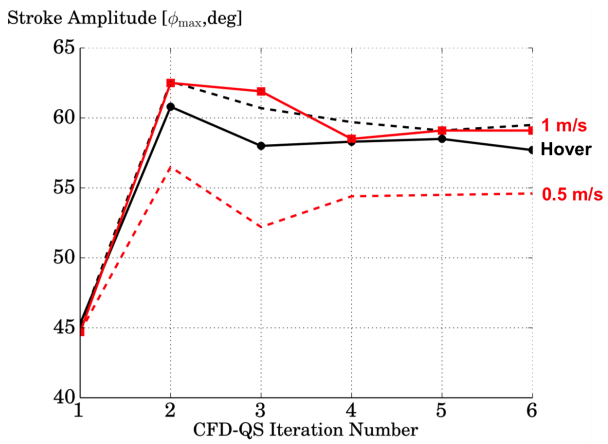

(a) Stroke Amplitude ϕ_{max}

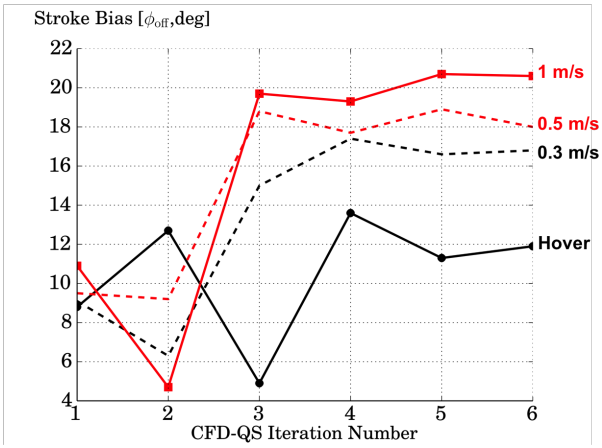

(b) Stroke Phase Offset ϕ_{off}

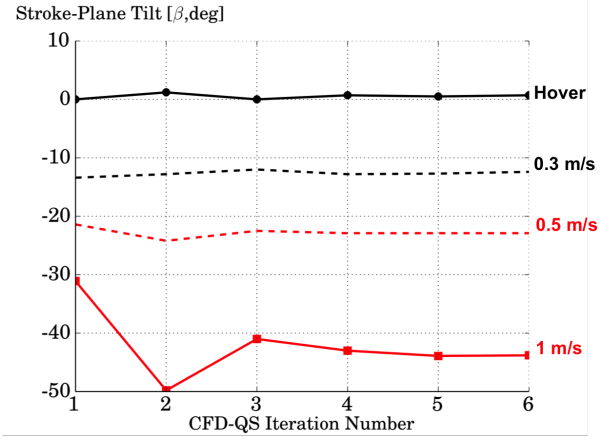

(c) Stroke Plane Tilt β

Figure 7.3: Convergence of trim variables at various forward flight speeds over coupling iterations between CFD and trim model with quasi-steady aerodynamics.

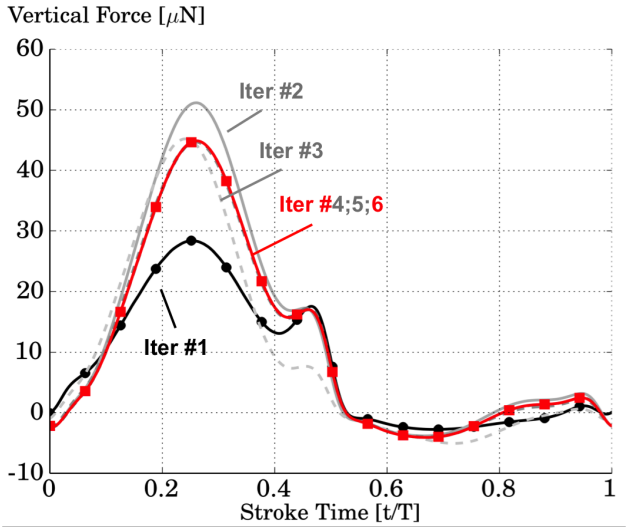

(a) Vertical force convergence

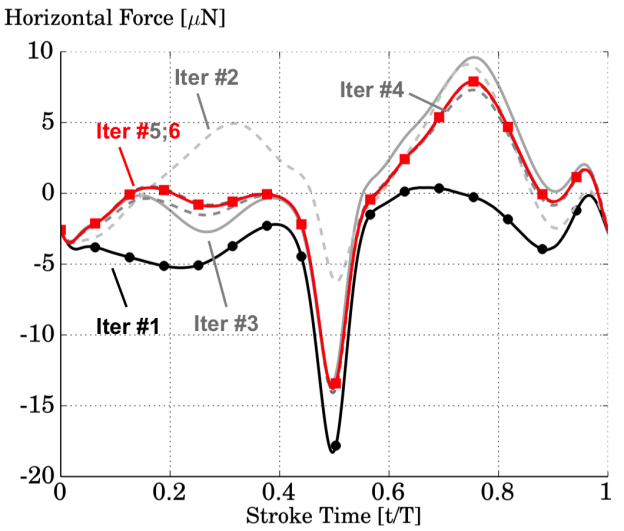

(b) Horizontal force convergence

Figure 7.4: Convergence of trim forces for forward flight speed of 1 m/s.

vertical component of thrust increases to nearly 200% of the initial guess. In forward flight, most of the vertical force is produced during the down-stroke, i.e. the portion of the flap cycle with largest dynamic pressure. In hover, the vertical force is identical between the down-stroke and up-stroke, while the horizontal force is anti-symmetric. In forward flight, most of the propulsive thrust is produced during the up-stroke, to compensate for the drag encountered during pronation (wing flip between down-stroke and up-stroke). The time history of the pitching moment in forward flight reveals the presence of a canceling up-down pulse during the down-stroke as the wing center of lift moves from above the CG to below the CG (stroke plane is tilted forward). During the upstroke, a small nose-down contribution is produced just before wing supination (transition portion from downstroke to upstroke). While qualitative features of the converged CFD airloads are observed in the initial CFD predictions, the quantitative values are significantly different. The next subsection highlights the differences between CFD and the simplified aerodynamic model.

7.1.4 CFD vs. Quasi-steady Loads

Shown in Fig. 7.5 are the predictions of longitudinal loads and aerodynamic power required at hover as obtained from the quasi-steady model, the initial CFD solution (using wing kinematics from the quasi-steady trim solution) and the final CFD-coupled trim iteration. Figure 7.5(a) shows the time history of the vertical force over the wing flap cycle. The most prominent feature of this plot is that the vertical force predictions for the quasi-steady model and final CFD solution are almost identical. The quasi-steady model does not capture the unsteady effects during pronation and supination at the stroke reversal parts of the flap cycle. Thus, even though the trim kinematics

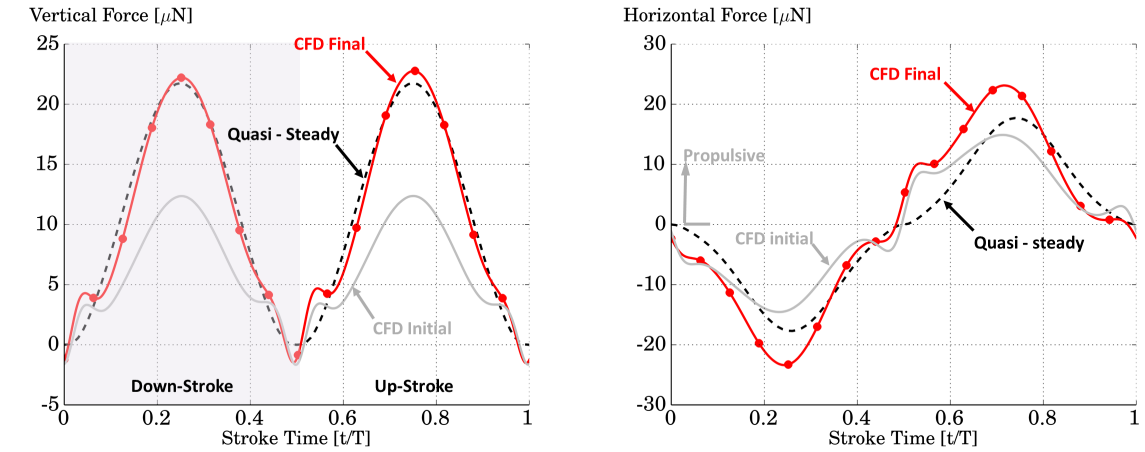

(a) Vertical force

(b) Horizontal force

(c) Pitching moment about CG

(d) Aerodynamic power required

Figure 7.5: Time histories of aerodynamic loads during a flapping cycle at hover: comparison of quasi-steady predictions with initial and final CFD.

are different, the airloads are very similar for the trimmed solutions obtained using quasi-steady aerodynamics and CFD. If the wing kinematics obtained from the quasi-steady trim solution are fed to the CFD model, the forces are severely underpredicted (almost 50% difference). Time histories of integrated airloads are identical between the up-stroke and down-stroke in hover since the kinematics are symmetric.

Figure 7.5(b) shows the time history over the flap cycle of the longitudinal propulsive force predicted by the quasi-steady trim solution, final CFD-coupled trim solution and initial CFD solution. All three predictions show similarities in the locations of peaks and phase. The time-averaged propulsive force is zero, as required for hover. However, the order of magnitude of the transient longitudinal force is similar to that of the vertical force. Thus, the flapping kinematics chosen expend energy in producing this transient longitudinal force that is ultimately dissipated without performing useful work. Figure 7.5(c) shows the time history over one flap cycle of body pitching moment. During the down-stroke, the effective center of lift is ahead of the CG as the wing moves forward, resulting in a nose-up pitching moment (negative according to the axes system chosen). During the up-stroke, the pitching moment is positive (nose-down) as the wing moves aft of the CG. Trim solutions obtained from the quasi-steady model and CFD demonstrate very similar pitching moment time histories – both in magnitude and phase – with the quasi-steady model having a slight under-prediction.

The time history over one flap cycle of aerodynamic power required to flap the wing is shown in Fig. 7.5(d). The key refinement introduced by CFD over the quasi-steady tables is the accurate prediction of viscous and pressure forces resolved over the entire wing surface. Using the “initial

CFD" as a reference, it is apparent that for the same kinematics, the quasi-steady model can capture qualitative trends in the power required, but severely under-predicts the magnitudes.

The corresponding time histories of aerodynamic loads and power required to flap the wings at 1 m/s level forward flight are shown in Fig. 7.6. The key difference between hover and forward flight is the loss of symmetry/anti-symmetry between the up-stroke and down-stroke. During the down-stroke, wing motion opposes the free-stream flow direction and the effective dynamic pressure increases, similar to the advancing side of a helicopter rotor disk. For the flapping wing configuration studied here, most of the vertical thrust needed to overcome gravity is produced during the down-stroke as shown in Fig. 7.6(a). During the up-stroke, the wing retreats from the flow and the effective dynamic pressure is low. Vertical force production is negligible in this part of the flap cycle. A significant contribution to wing drag in forward flight is encountered during pronation and supination, i.e. wing pitch rotation between the down-stroke and up-stroke phases. The corresponding propulsive force is produced during the up-stroke, as shown in Fig. 7.6(b). The quasi-steady trim solution and final CFD iteration exhibit differences in the propulsive forces produced during the down-stroke because of a difference in the stroke plane angle. With the same stroke plane angle, the CFD predictions agree better with the quasi-steady model.

Figure 7.6(c) shows the variation of pitching moment during the flap cycle. The up-down pulse during the down-stroke corresponds to when the wing crosses the body X-Y plane and force contributions to pitching moments reverse sign, shown in Fig. 7.7. The power required to flap the wings and overcome aerodynamic resistance is shown in Fig. 7.6(d). The area under the curve is the normalized battery energy required for one flap cycle. Most of the power is required to produce

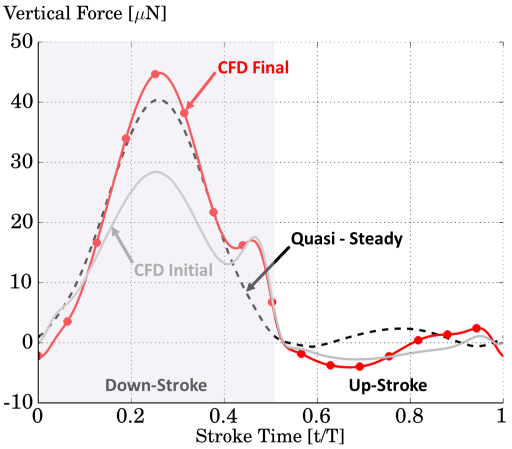

(a) Vertical force

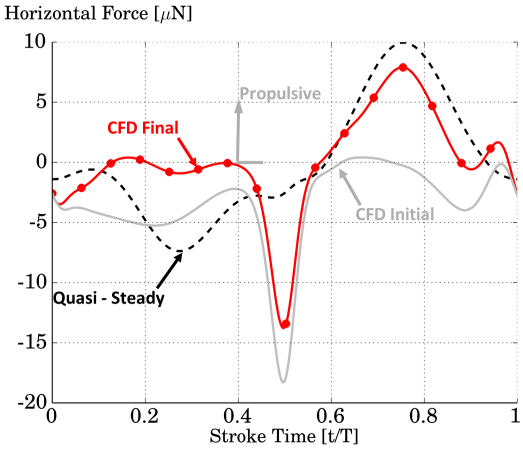

(b) Horizontal force

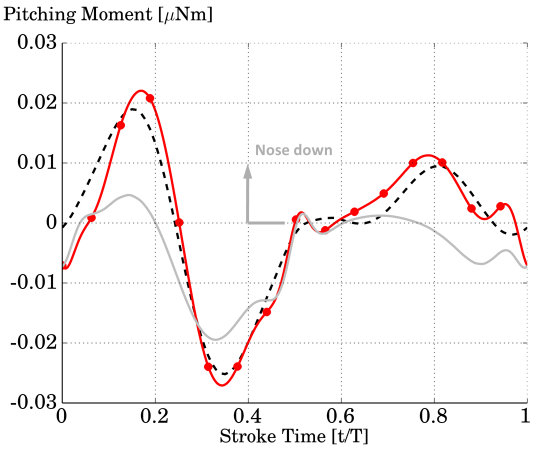

(c) Pitching moment about CG

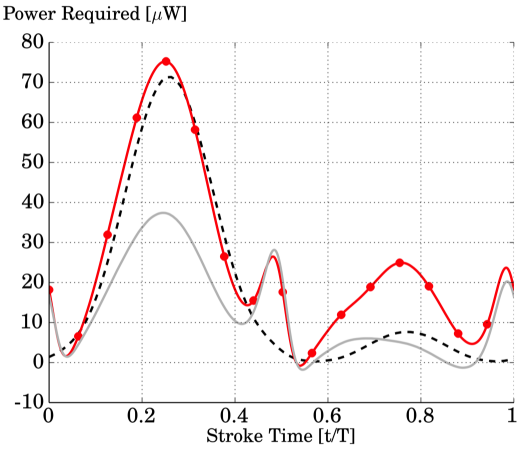

(d) Aerodynamic power required

Figure 7.6: Time histories of aerodynamic loads during a flapping cycle in trimmed forward flight at 1 m/s: comparison of quasi-steady predictions with initial and final CFD.

vertical thrust during the down-stroke. As the wing advances into the flow, the wake is swept away and the quasi-steady predictions agree excellently with the CFD model. The second peak during the up-stroke corresponds to the propulsive force produced.

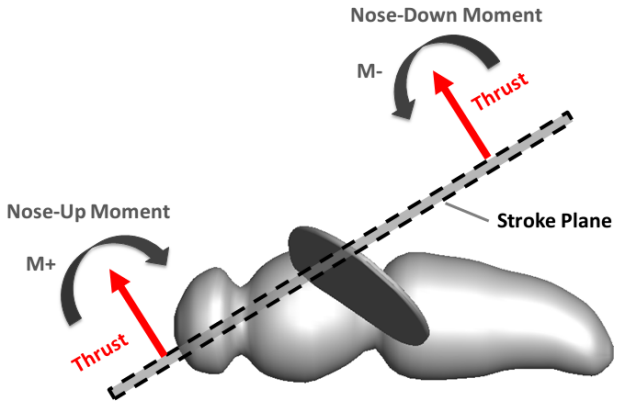

Figure 7.7: Schematic showing origin of up-down pulse in body pitching moment during down-stroke.

Predictions obtained using the quasi-steady model and final CFD solution are very similar, indicating that from a flight dynamics perspective, the quasi-steady model provides a qualitatively and somewhat quantitatively accurate picture of the global trends and integrated wing loads. However, these predictions are not exact for all force and moment components between the quasi-steady model and CFD. Though both models are trimmed to the same flight condition, the trim kinematics are different and fine details obtained from CFD are not captured in the quasi-steady model. Hence, the force predictions are similar but not identical. The key contribution of CFD is in accurate force and power estimates during the up-stroke, pronation and supination and at hover, i.e. when there is significant wing-wake interaction.

Figure 7.8 shows the time histories of the integrated wing loads and aerodynamic power required over the wing flap cycle for hover and three forward flight speeds: 0.3 m/s, 0.5 m/s and

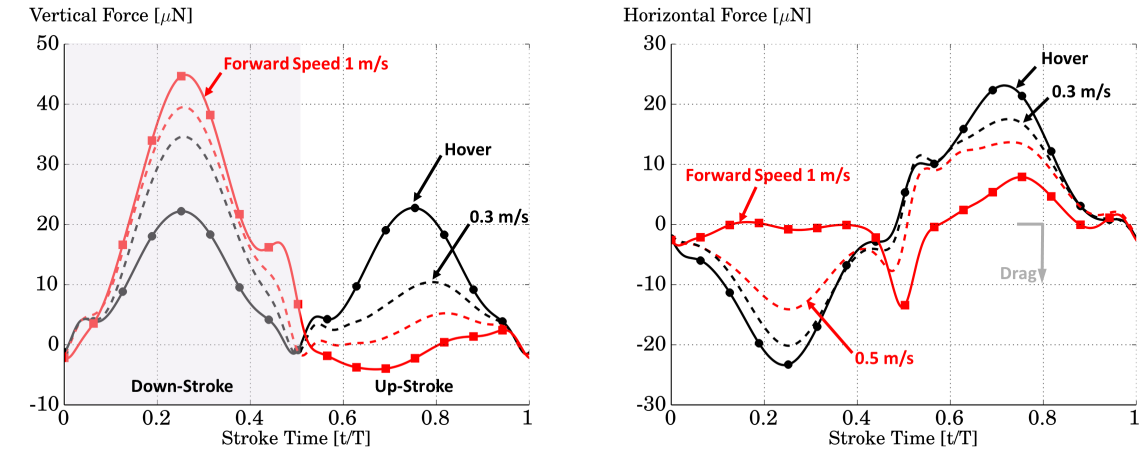

(a) Vertical force

(b) Horizontal force

(c) Pitching moment about CG

(d) Aerodynamic power required

Figure 7.8: Time histories of aerodynamic loads during a flapping cycle in trimmed level flight at various speeds from final CFD iteration.

1 m/s. These results represent the converged loads from the final CFD-coupled trim iteration. As forward speed increases, the production of vertical force shifts increasingly to the down-stroke part of the flap cycle, as shown in Fig. 7.8(a). With increasing forward flight speed, the transient drag and propulsive force produced during the down-stroke and up-stroke, respectively, diminish in magnitude. At 1 m/s, most of the wing drag is encountered during pronation, and the propulsive force is produced during the up-stroke resulting in reduced losses as the wake is swept away by the free-stream flow. Body pitching moments are shown in Fig. 7.8(c). With increasing forward speed, the transient peak at 0.2 t/T is more pronounced due to higher dynamic pressure during the down-stroke, while the peak at 0.8 t/T during the up-stroke is diminished. Most of the aerodynamic power requirements, shown in Fig. 7.8, are biased to the down-stroke portion of the flap cycle in forward flight, with a minor peak during the up-stroke that corresponds to propulsive force production.

7.2 Flapping Wings in Hover

In hover kinematics and aerodynamic forces are cross-coupled. The equilibrium in forces and moments in hover is obtained by the flapping wings only, unlike in helicopters where moment equilibrium can be obtained by taking advantage of the tail (anti torque). Unsteady forces and kinematics are involved in insect flapping wing MAV. To shed more light on Diptera configuration in hover the forces, moments, power and wake structure are discussed in the following sections.

7.2.1 Forces and Moments

Equilibrium in forces and moments in hover are obtained for the following trim variables: stroke amplitude (ϕ_{max}) of 58.7°, stroke bias (ϕ_{off}) of11.9° (shifting stroke midpoint toward the tail) and, stroke-plane tilt (β) equal to -0.7 (i.e. slightly backward). The reason that β is not zero, is that for the given CG, pitch moment balance must be obtained by the kinematics. Pitch moments are affected by stroke bias and stroke tilt. The hover stroke results in a roughly horizontal stroke that aligns with the observed conclusion that is made from watching insects in hover flight in nature (more detailed discussion about the cross coupling between airloads and trim variables is presented in Appendix A.

Figure 7.9 plots the total forces time histories over one stroke in hover. The total forces are contributed by the two wings, and computed in the inertial coordinate system. As in trimmed flight the average quantities must satisfy the trim conditions - vertical thrust (Z) equals the insect MAV weight and the average X and Y forces are zero. Figure 7.9 also shows the average quantities over a flapping cycle. The average forces satisfy the trim conditions, Z force is approximately (for $\beta = 0.7°$) similar between downstroke and upstroke (symmetric stroke), whereas in hover, vertical thrust (lift) is generated in both downstroke and upstroke. The force in the body axis direction (X) is asymmetric, where positive horizontal thrust is obtained during the downstroke and drag (negative horizontal force) during the upstroke. The averaged X force is approximately zero. The positive horizontal thrust and drag are obtained mainly from the LEV. The LEV roughly can be modeled with a suction force normal to the surface, that has two components, one vertical and one in the XY plane.

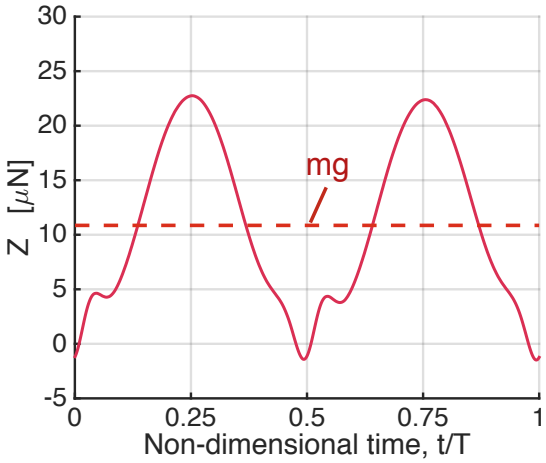

(a) Force in z direction

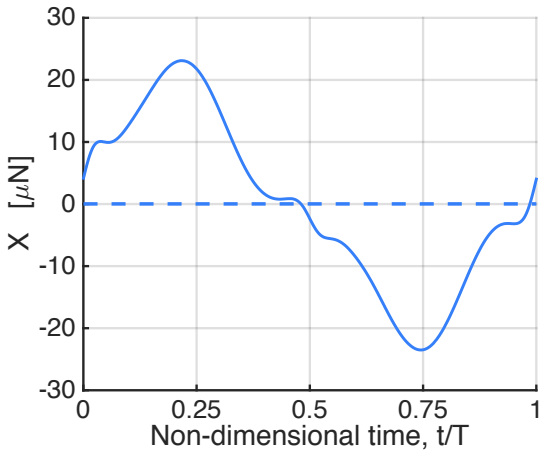

(b) Force in x direction

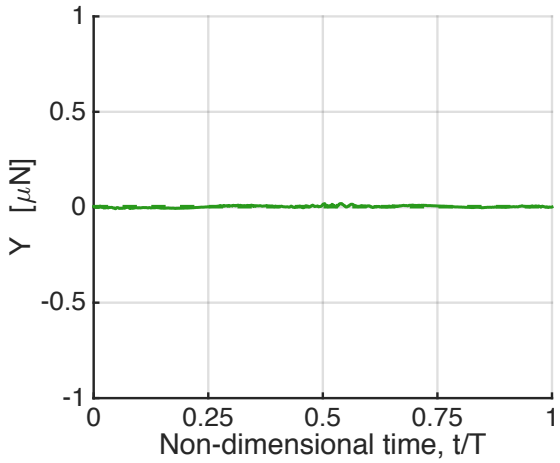

(c) Force in y direction

Figure 7.9: Time histories of forces in x,y and z direction during one flapping cycle in hover. The dashed lines represent the flapping-cycle averaged forces.

Side force (Y) is plotted in Fig. 7.9(c), this force in comparison to X and Z is insignificant. and it's averaged quantity is zero. The side force time history is minor because the side forces are cancelled out from the kinematics (as can be seen in Fig. 7.10), thus the assumption of symmetry with respect to the X-Z plane is valid (longitudinal symmetry). In terms of vertical force, the two wings produce identical force and each contribute half of the required vertical thrust.

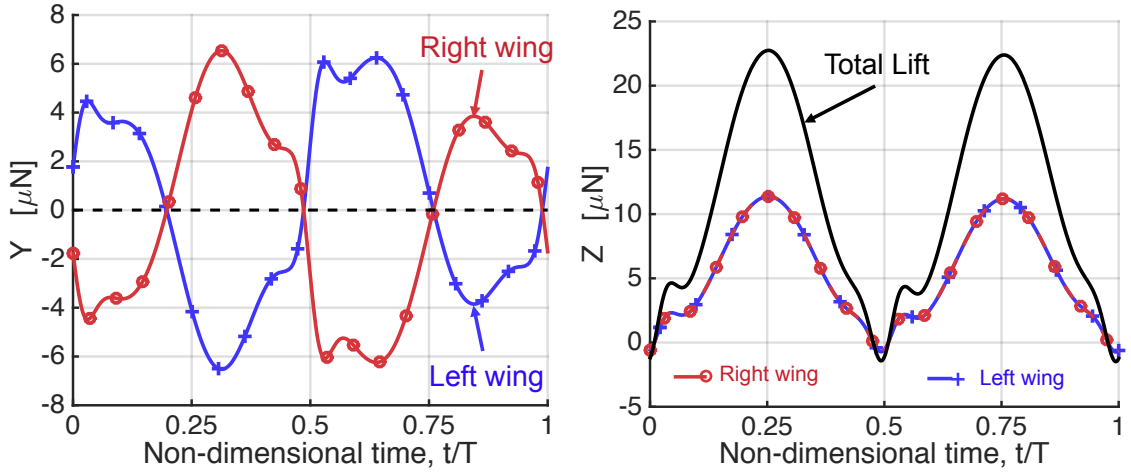

(a) Force in z direction

(b) Force in y direction

Figure 7.10: Time history vertical and side forces during a flapping cycle of each wing in hover.

Similarly to the forces, the time histories of the moments (roll, yaw and pitch) during a flapping cycle are plotted in Fig. 7.11. Moments are computed about the insect body CG. The CG is prescribed and assumed to be in the section between the thorax and abdomen of the insect. As can be seen from the figures, the magnitude of the yaw and roll moments is one order of magnitude smaller than the pitch moment. The stroke average roll and yaw moments are zero, as a result of the symmetric kinematics around X-Z plane. The dominant moment is the pitch moment, which is balanced by the trim variables. As mentioned earlier the pitch moment equilibrium in hover is

achieved by stroke bias and stroke tilt.

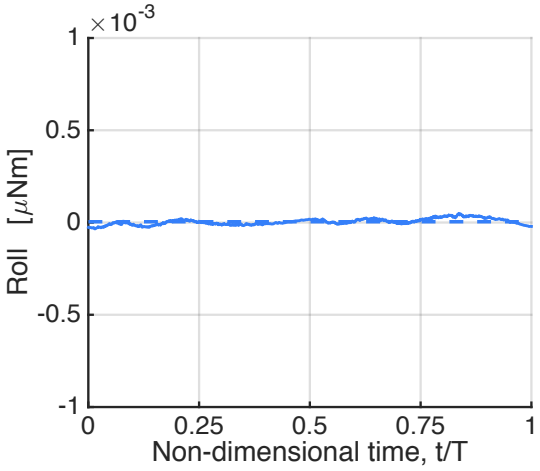

(a) Moment around x axis

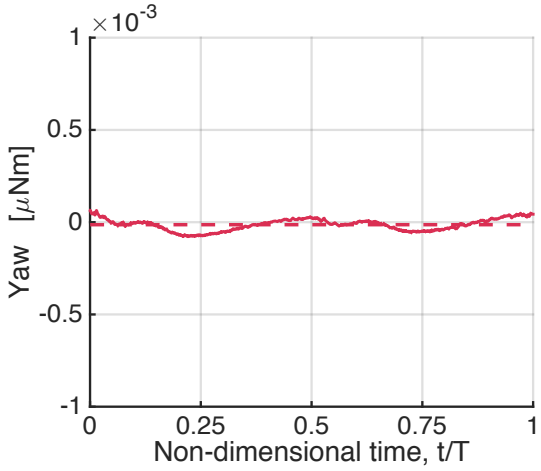

(b) Moment around z axis

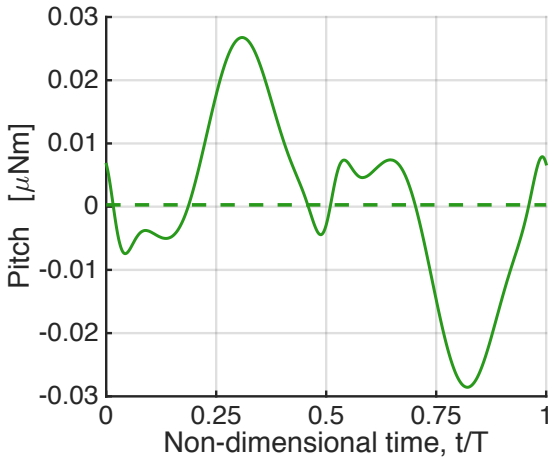

(c) Moment around y axis

Figure 7.11: Time histories of moments: roll, yaw and pitch, during one flapping cycle in hover. The dashed lines represent the flapping-cycle averaged moments.

7.2.2 Wake Structure

To study the wake system in hover, a case was run using similar parameters as the previous simulations, but with a higher order scheme (fifth order CRWENO) than MUSCL. The difference

in mean forces and peak force values between the two cases is insignificant (less than 0.5%), but with the higher accuracy scheme more details in the wake are captured. These results are used for the visualizations in the rest of this section. Wake visualizations are useful in identifying many phenomena, such as separation and reattachment regions, the trajectory of the tip vortex, and the strength of the surface flow. The hover case exhibits relatively simple flow patterns, where downstroke and upstroke are similar in this manner. The hover flapping cycle can be divided into four main portions :

- Translational downstroke - the wings move toward the insect head, and α_g remains constant
- Transition from downstroke to upstroke - Supination
- Translational upstroke - the wings move toward the insect tail, and α_g remains constant
- Transition from upstroke to downstroke - Pronation

A schematic chart of the hover stroke is represented in Fig. 7.12(a)

Figure 7.13 shows the vorticity normal to the $x = 0$ plane, in the middle of downstroke (t/T=0.25). The goal of plotting the x-direction vorticity is to identify the convecting vorticity in the X-Z plane. The red color represents clockwise vorticity and the blue color represents counter clockwise direction of the vorticity swirl. Top and side views with iso surfaces of positive (red) and negative value (blue) are plotted in part (a) of the figure, while part (b) shows the three different locations (a, b and c) as described in side view. The vorticity contours are plotted at these three locations. The computed vorticity is a normalized quantity.

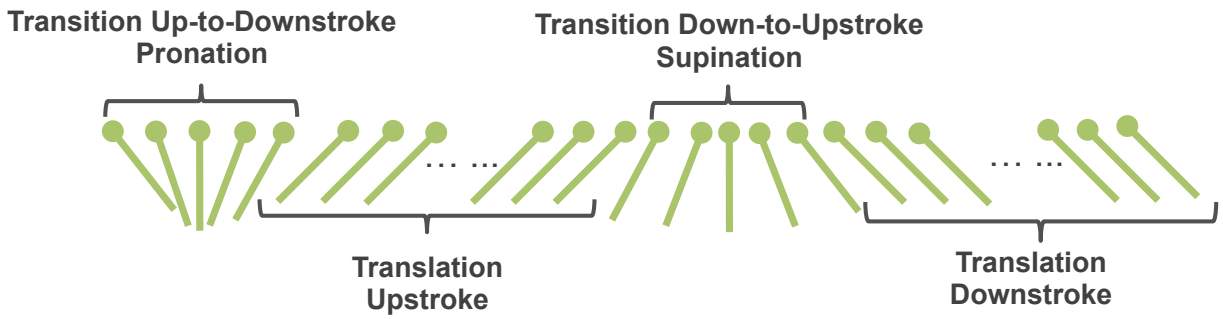

(a) Hover stroke

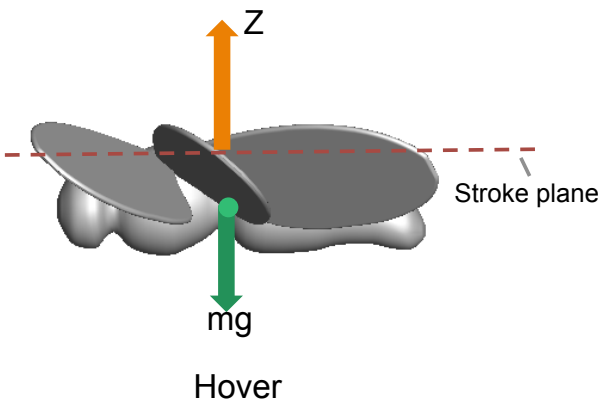

(b) Resultant vertical thrust

Figure 7.12: Schematic chart of the hover stroke - (a) The lines represent a chordwise section, the dots indicate the leading edge, (b) Side view of insect in hover, the wings location represent instant locations during downstroke.

The LEV that formed remains attached to the upper surface during the translational downstroke. The LEV grows from wing root to tip, indicating the rotational effect which results in a conical shape. This affects the vertical thrust (lift) distributions as will discussed later in this section. No new recirculation region is formed at the upper surface during the translational stroke, meaning that the behavior of this vortex is steady or quasi-steady. The LEV drains and separates from the wing through the wing tip, shaping a shed tip vortex trajectory. The vortices from each wing tip are identical in strength and have opposite circulation. Each vortex pair below the wings in Fig. 7.13(b) indicates the shed vorticity from previous stroke. The shed vorticity convects downstream below the wings flap stroke.

The wake structure during the transition from down-to-upstroke is shown in Fig. 7.14. During the transition the wing pitches up to flip and starts the reversal stroke (upstroke). During supination, the vortices detach from the wing surface, forming tip and root shed vortices, shed trailing vortices, and massive detach vortices from the wing upper surface forced by the kinematics (wing pitch-up). This separation of the vorticity is illustrated in Fig. 7.14(b), where the vorticity contours at three different locations are plotted showing the dynamics of the shed vorticity.

Similarly, the wake was plotted for upstroke at t/T= 0.75, and the same wake pattern is observed as in downstroke translation. The rotating wing develops and sheds a starting vortex at the trailing edge, at the early stages of the translational portion. When the wing starts the reversal stroke, it meets the previous wake, and the induced flow affects the generated aerodynamic forces as shown earlier.

The massive vortex shedding occurs during the transition portions, supination and prona-

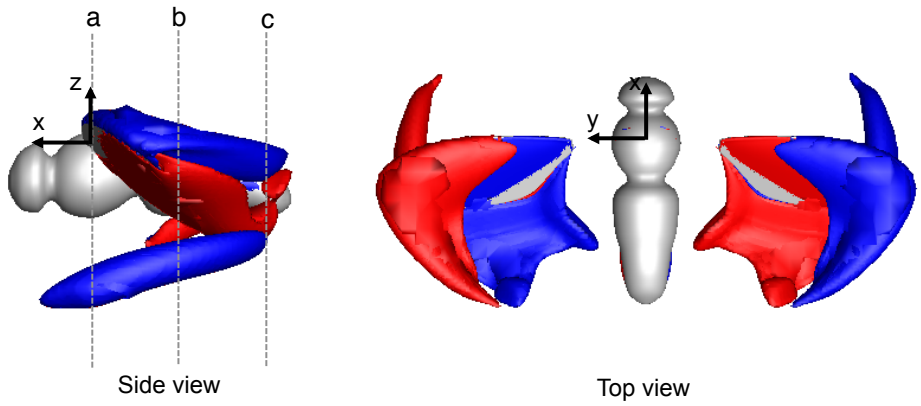

(a) Iso-surface vorticity

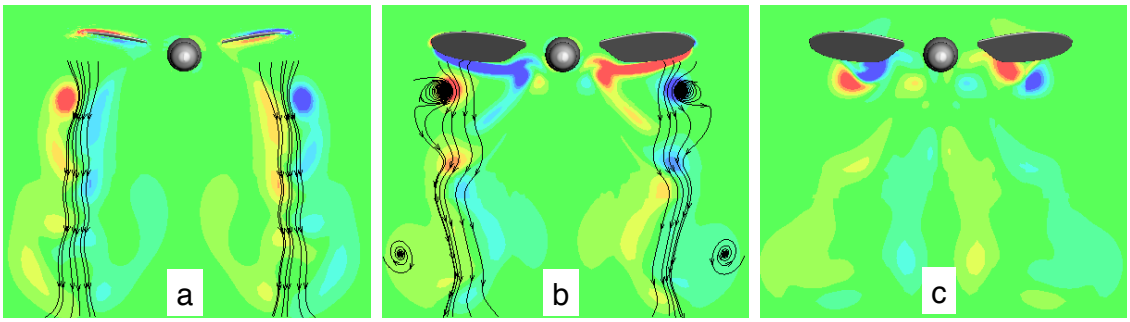

(b) Vorticity contours at a,b,c sections

Figure 7.13: The normalized vorticity normal to $x = 0$ plane during translational downstroke t/T=0.25, (a) Iso-surface positive vorticity (0.01) and negative vorticity (-0.01), red - clockwise and blue - counter clockwise directions.(b) The vorticity contours at three different locations in x direction (a,b,c) as demonstrated in the insect side view. The planes are normal to body axis (x). 2D streamlines are computed in the fixed inertial frame.

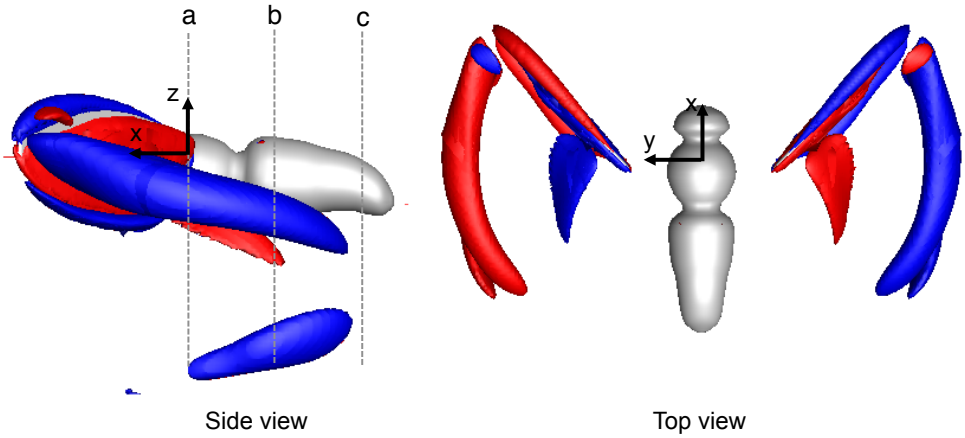

(a) Vertical force

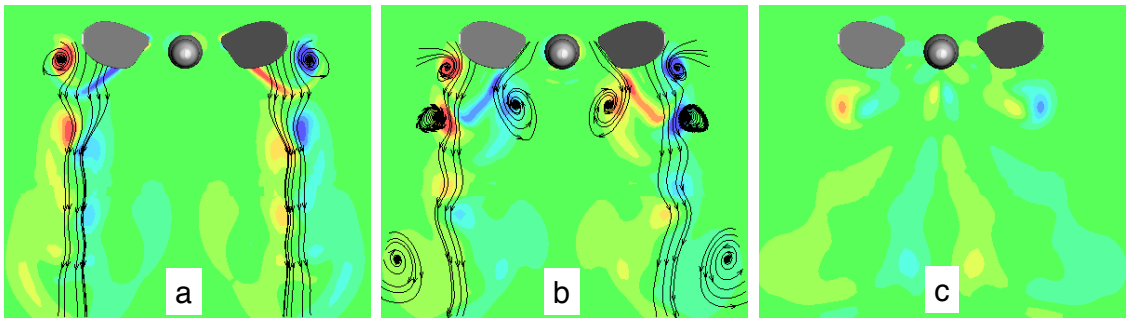

(b) Horizontal force

Figure 7.14: The normalized vorticity normal to $x = 0$ plane during the transition from downstroke to upstroke at (t/T= 0.5), (a) Iso-surface positive vorticity (0.01) and negative vorticity (-0.01), red - clockwise and blue - counter clockwise directions.(b) The vorticity contours at three different locations in x direction (a,b,c) as demonstrated in the insect side view. The planes are normal to body axis (x). 2D streamlines are computed in the fixed inertial frame.

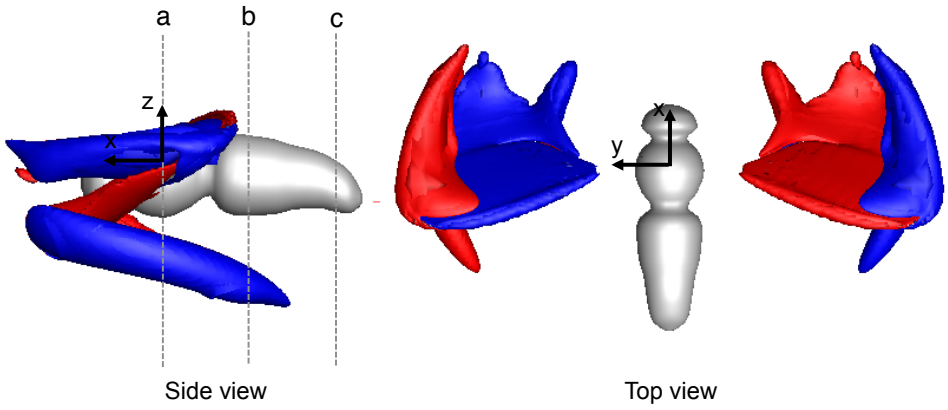

(a) Vertical force

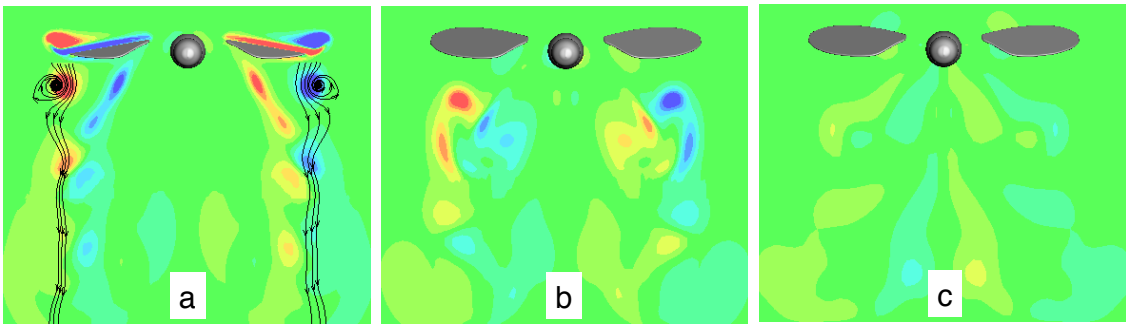

(b) Horizontal force

Figure 7.15: The non-dimensional vorticity normal to $x = 0$ plane during translational upstroke t/T=0.75, (a) Iso-surface positive vorticity (0.01) and negative vorticity (-0.01), red - clockwise and blue - counter clockwise directions.(b) The vorticity contours at three different locations in x direction (a,b,c) as demonstrated in the insect side view. The planes are normal to body axis (x). 2D streamlines are computed in the fixed inertial frame.

tion (Fig.7.16). The trajectory of the shed vorticty is below the wings. The wings generate induced inflow that contributes to the convection of the shed vorticity below the wing, similar to what is seen in a hovering rotor. Due to the unsteady kinematics in this case, more complicated unsteady mechanisms take place such as "wake interaction", the effect of the induced inflow of the LEV and its stability.

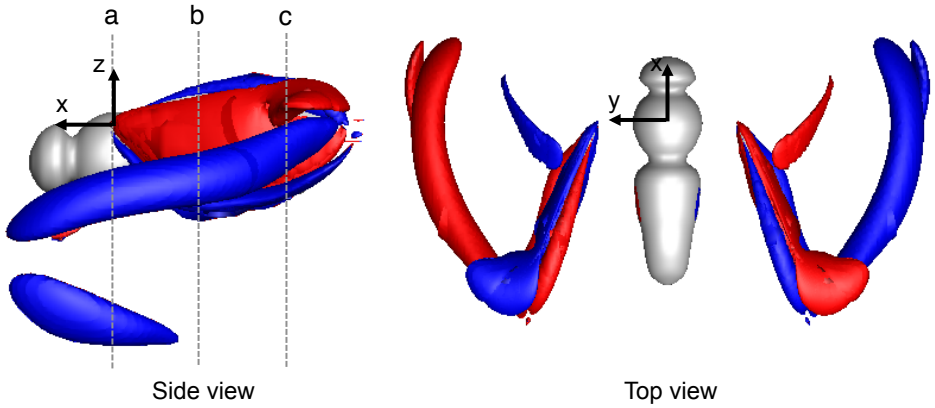

(a) Vertical force

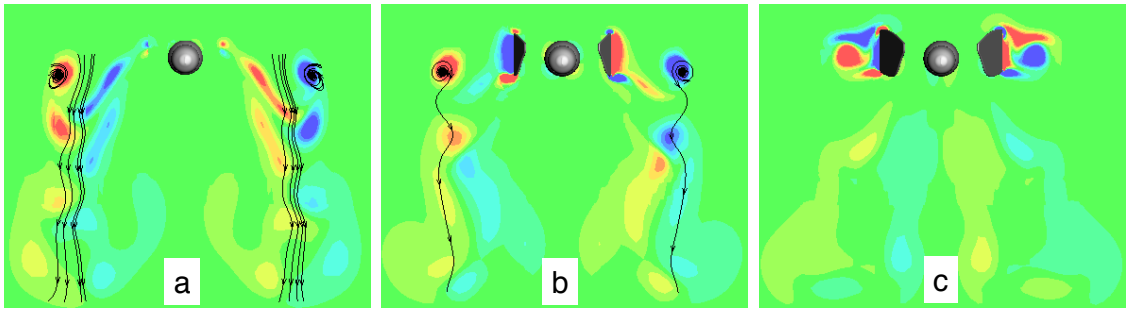

(b) Horizontal force

Figure 7.16: The normalized vorticity normal to y plane during the transition from downstroke to upstroke at (t/T= 0.5), (a) Iso-surface positive vorticity (0.01) and negative vorticity (-0.01), red - clockwise and blue - counter clockwise directions.(b) The vorticity contours at three different locations in x direction (a,b,c) as demonstrated in the insect side view. The planes are normal to body axis (x). 2D streamlines are computed in the fixed inertial frame.

7.2.3 Power and Vertical Thrust

This section presents the total power, local power distribution and local vertical thrust along the wing span during various times. The power analysis is based based on aerodynamic loads obtained from the CFD simulations. In real insect flight (mechanical or biological), there are losses due to inertial forces and mechanical losses in addition to the aerodynamic ones. The required aerodynamic power is divided into two sources: losses due to shear forces, and due to the pressure losses. The physical flow around the flapping wing is highly viscous (low Reynolds number), resulting in a large boundary layer and increased shear drag, which can be referred to as profile drag. Even for low Reynolds numbers, where shear forces can not be neglected, pressure forces still dominate shear forces. This can be seen in Fig.7.17. The power losses due to the pressure drag are much larger than the power losses due to the viscous profile drag through the hover stroke. The peak in pressure power losses occurs at the middle of the downstroke and upstroke. The viscous power losses increase at the beginning of the downstroke (and upstroke), reaching the peak around t/T$=0.2$ (upstroke t/T$=0.7$) and then there is a reduction until the end of the stroke, where there is a relatively small peak due to the rotational forces.

To learn more about the power losses the local distribution along the spanwise direction are plotted. The local power distribution at t/T equal to 0.25, 0.5, 0.75 and 1 are plotted in Fig. 7.18. Due to symmetry w.r.t body axis both wings have identical results, therefore only results obtained from one wing are presented. The profile loss (shear) is approximately zero at t/T=0.5 and 1 where the wings flip before it starts the stroke reversal. The power loss is contributed by the pressure, as illustrated in Fig. 7.18 (b&d), which results from the induced wake of the shed vorticity. The total

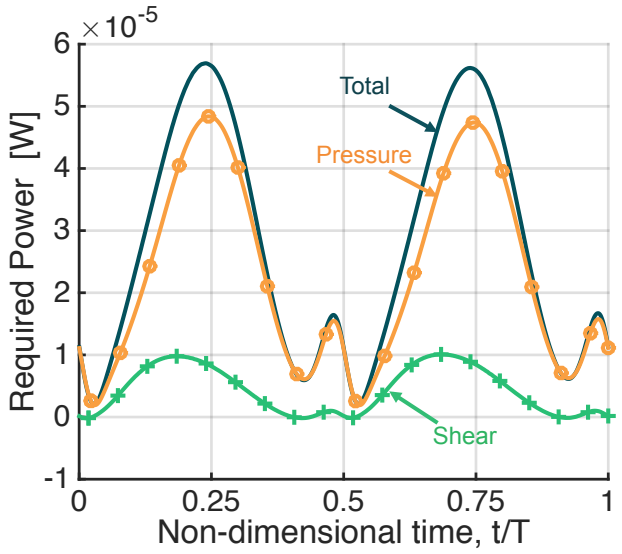

Figure 7.17: Time history of required aerodynamic power.

power during the translational portions is larger than the power during the transitional portions. This pressure power is caused by the formation of the LEV (drag from the suction force) and the induced wake. The shear losses are due to the viscous forces in the boundary layer. The viscous shear forces in the translational portions linearly increases toward the wing tip (r/R= 1), and the pressure curve also increases toward the tip, which are related to the LEV growth along the wing span. This behavior will be referred to as ”tip dominated” power (Fig. 7.18(a&c)). The peak in pressure power along the wing span occurs at r/R= 0.85.

The total integrated local distributed spanwise power and vertical thrust change during the hover stroke are also plotted (Fig. 7.19), with the hover stroke divided into the 4 portions that were mentioned earlier. The time instants considered during the translational portions (a, b and c) are the early stages of the translational portion, mid downstroke and the late stage of the translational portion. The total power (Fig. 7.19, curve a) increases until it reaches a maximum around mid-

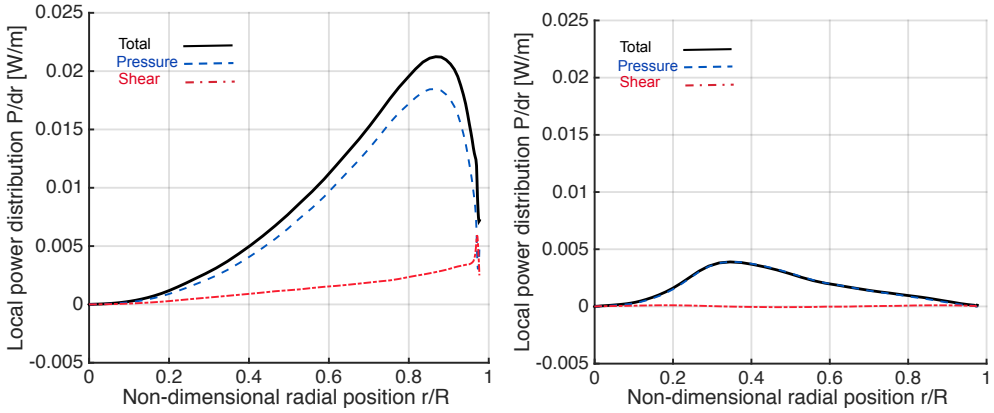

(a) Power distribution at t/T= 0.25

(b) Power distribution at t/T= 0.5

(c) Power distribution at t/T= 0.75

(d) Power distribution at t/T= 1

Figure 7.18: Power distributions along the wing span during 4 different time instants at downstroke (t/T= 0.25), supination (t/T= 0.5), upstroke (t/T= 0.75) and pronation (t/T= 1) in hover.

stroke, then the pressure power decreases. The linearly tip dominated behavior remains during the translational portion. At the early stages of the translational portion curve (a), the peak is located toward the tip; whereas for the other curves (b & c) the peak is at r/R= 0.85, which can be related to the early formation of the LEV, which keeps growing in time and along the span until midstroke. Then there is a reduction in its strength, due to the rotational velocity. In the second part of the Figure 7.19(b), the spanwise distributions of vertical thrust are plotted at the given time instants. The trend of the vertical thrust (lift) is similar to the "tip dominated" power, and is related to the same mechanism (the LEV). Maximum lift is achieved at mid-downstroke, and the peak occurs at r/R= 0.8. The drop in the vertical thrust toward the tip indicates the separation of the LEV from the wing tip.

Next, the transition period from down-to-upstroke (supination) is examined. Similar to the downstroke, three time instants are considered, t/T= 0.45, 0.5 and 0.55. As shown earlier, the total power during the transition is small relative to the power loss during downstroke. During supination, the wing pitches up, flips, and pitches down. Curve (d) in Fig. 7.20(b) shows how the wing pitches up (t/T= 0.45), the power peak is at r/R= 0.4, and is mostly due to the rotational forces, while at t/T= 0.5 the peak magnitude reduces and moves further inboard of the wing. After the wing flips and starts the reversal stroke, the power distribution along the span (curve (f)) is negative from r/R= 0.3–0.7, which might indicate that energy is extracted from the wake (Fig.7.20(b)). However, toward the tip, there is a positive power peak at r/R= 0.9. The spanwise vertical thrust, (curve (d)) is a positive until r/R= 0.6 (inboard of the wing), then the vertical force on the outboard of the wing is negative. At t/T= 0.5 (curve f) a negative vertical force is seen along the wing

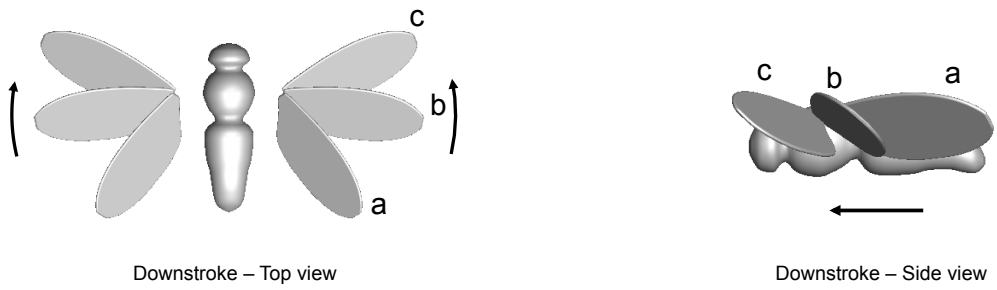

(a) Translation - Downstroke

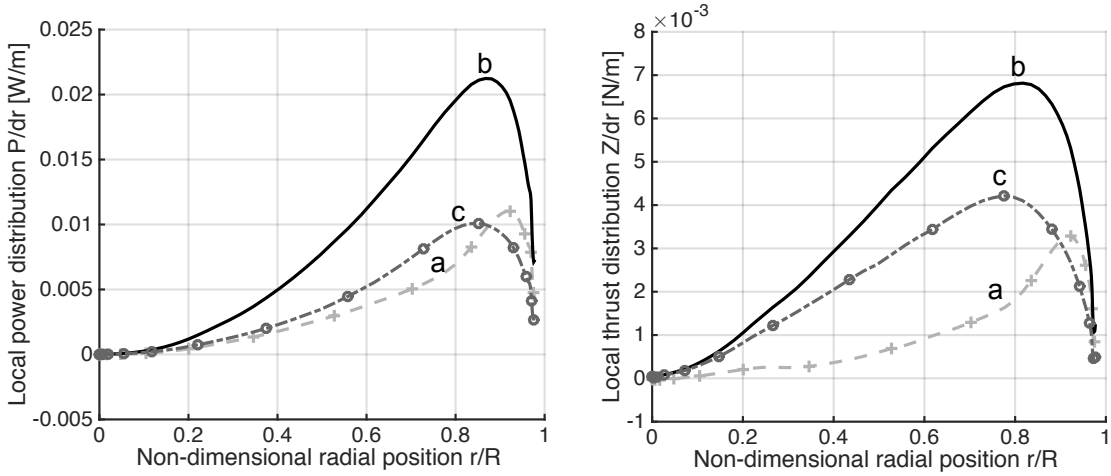

(b) Power and vertical thrust span distributions

Figure 7.19: Spanwise power and vertical thrust distributions along the wing span during translational downstroke, at three different time instants: (a) - t/T= 0.1, (b) - t/T= 0.25, (c) - t/T= 0.35.

span (untill r/R= 0.7) which explains the reduction (negative peak) in total vertical force at the mid-cycle (t/T= 0.5).

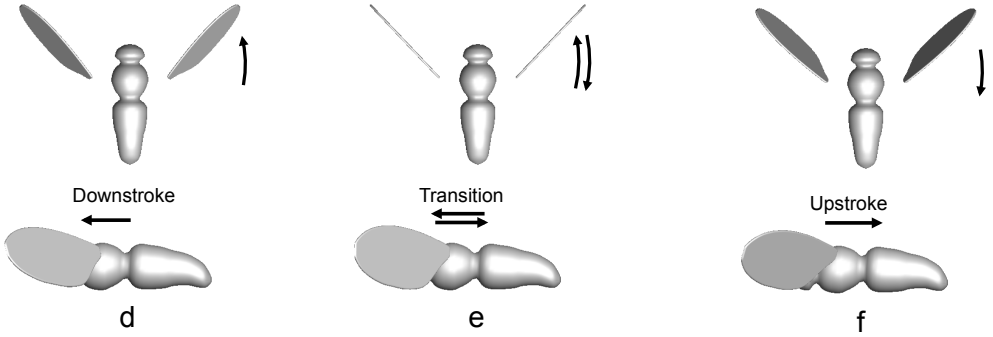

(a) Supination

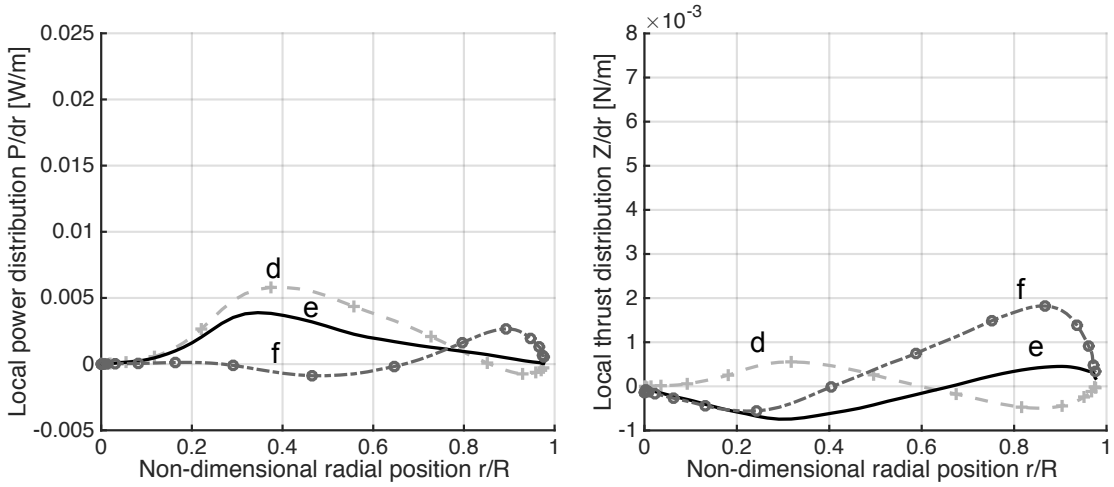

(b) Power and vertical thrust span distributions

Figure 7.20: Power and vertical thrust distributions along the wing span during the transition from downstroke to upstroke (supination), at three different location; (d) - t/T= 0.45, (e) - t/T= 0.5, (f) - t/T= 0.55.

In hover the flap cycle is roughly horizontal, therefore downstroke and upstroke are similar, with a slight change in the peak forces in the upstroke due to the backward tilt ($\beta = 0.7$ backward). Therefore the spanwise power and vertical thrust distribution during upstroke and pronation, are similar to those obtained during downstroke and supination. These results are plotted in

Figures 7.21 (upstroke) and 7.22 (pronation) for completeness.

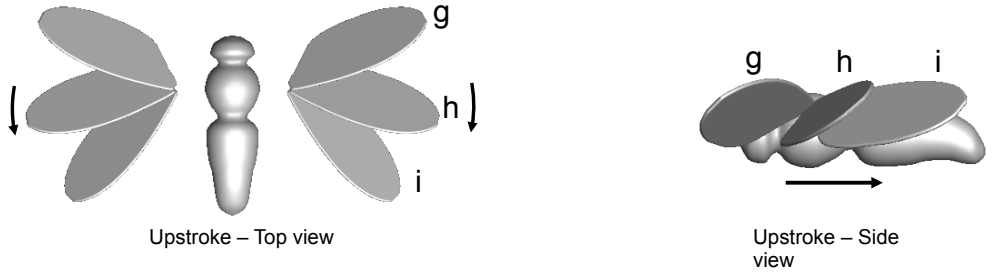

(a) Translation - Upstroke

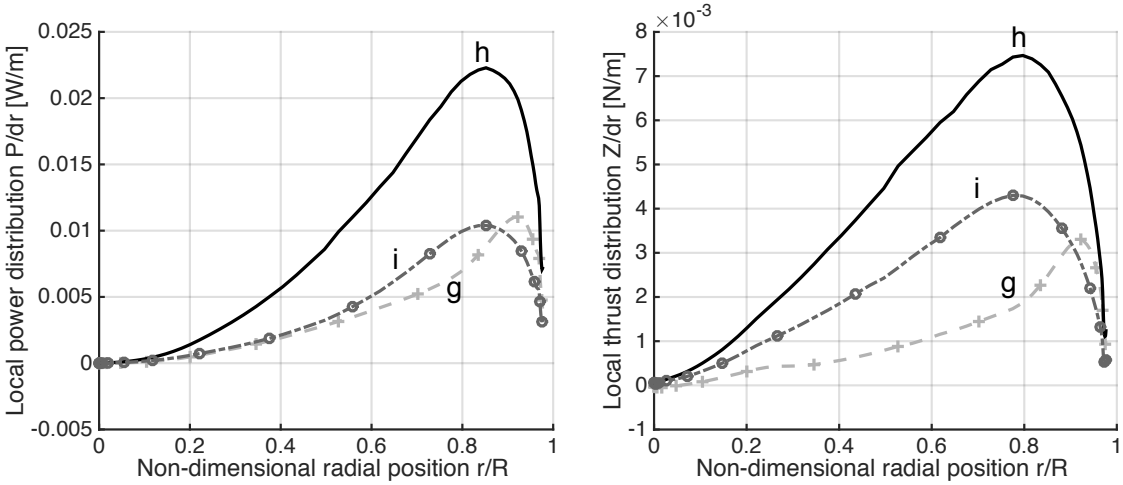

(b) Power and vertical thrust span distributions

Figure 7.21: Power and vertical thrust distributions along the wing span during translational upstroke, at three different location; (g) - t/T= 0.6, (h) - t/T= 0.75, (i) - t/T= 0.85.

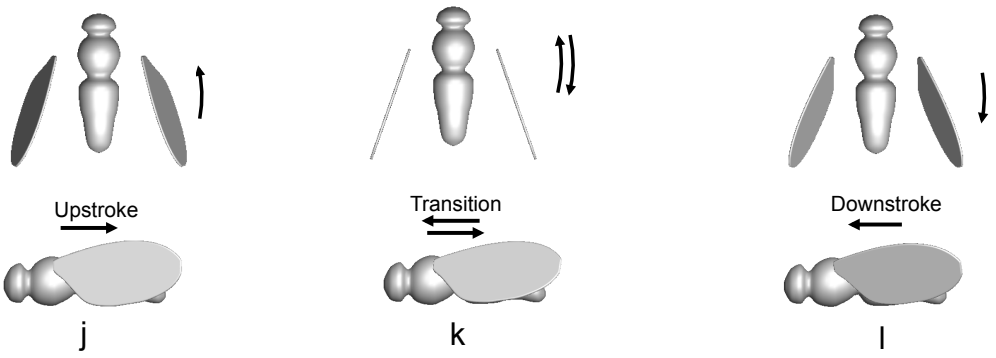

(a) Pronation

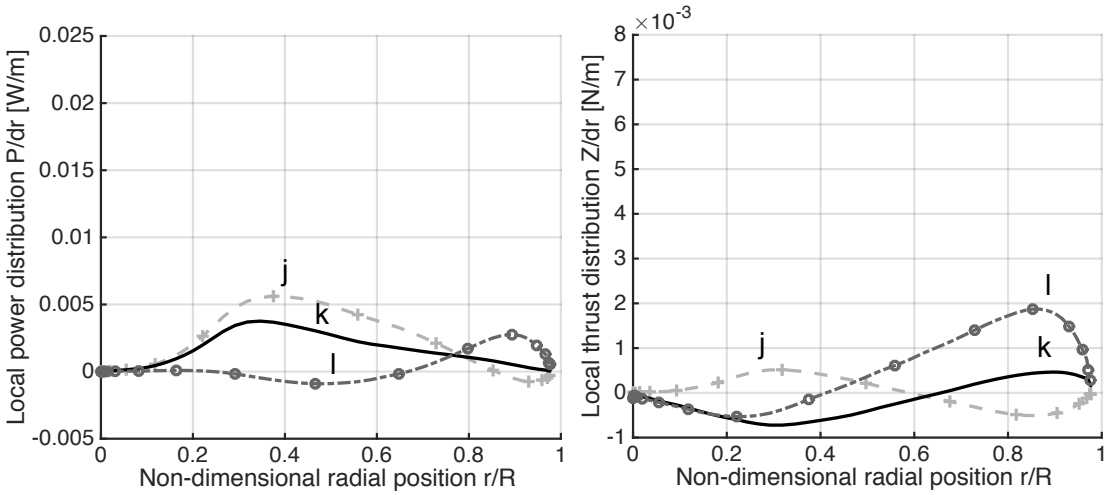

(b) Power and vertical thrust span distributions

Figure 7.22: Power and vertical thrust distributions along the wing span during the transition from upstroke to downstroke (pronation), at three different location; (j) - t/T= 0.95, (k) - t/T= 1, (l) - t/T= 0.15.

7.3 Flapping Wings in Forward Flight

The way insects (diptera configuration) move forward is by tilting the flapping stroke forward, such that the resultant force has a horizontal thrust. For a trim algorithm based on flap-cycle averaged forces and moments in forward flight, two components of thrust are required: vertical thrust and horizontal thrust. From the trim analysis described earlier it was found that there is a direct relationship between forward speed and the stroke plane tilt. With an increase in the forward speed the plane tilt increases. A similar trend is observed in rotary wing; when a helicopter moves forward, it tilts the rotor disk plane forward. The flow features in trimmed level (forward) flight is discussed in this section along with the forces, moments and power. The chosen case for trimmed flight was 1 m/s (see Appendix E for more details about trimmed forward flight at 0.3 m/s and 0.5 m/s).

7.3.1 Forces and Moments

Equilibrium in forces and moments in level forward flight for a speed of 1 m/s is obtained for the following trim variables, stroke amplitude (ϕ_{max}) of 59.2°, stroke bias (ϕ_{off}) of 20.6° what is shifted from midpoint towards the tail and a stroke-plane tilt (β) equal to 43.8° tilted forward. The schematic chart of the forward flight is described in Fig. 7.23(a), where the green lines describe the chordwise sections, and the circles are the leading-edge. Fig. 7.23(b) describes the level flight of the insect during downstroke and the resultant force.

In trimmed forward flight, the wings experience a local velocity from three sources: induced velocity, rotational velocity and freestream velocity. Due to the flapping-stroke kinematics,

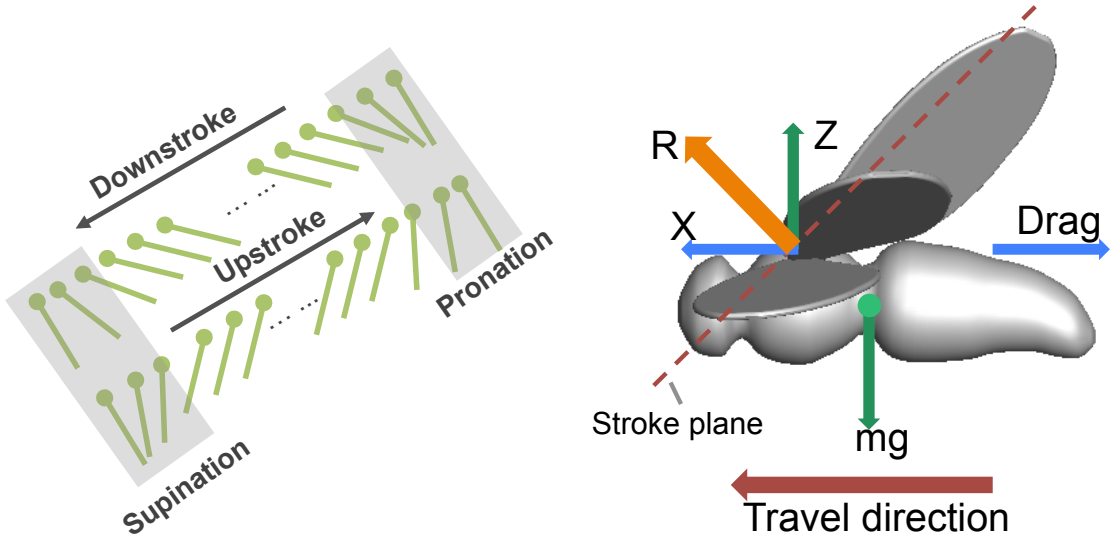

(a) Forward flight stroke

(b) Resultant force and its components

Figure 7.23: Schematic chart of forward flight stroke - The flapping stroke is tilted forward, the resultant force is roughly perpendicular to the flapping stroke, resembling in vertical and horizontal thrust, (a) The lines represent a chordwise section, the dots indicate the leading edge, (b) Side view of insect in trimmed forward flight, the wings location represent instant locations during downstroke.

the wings experience different resultant velocities during the downstroke and the upstroke. Figure 7.24 shows the resultant velocity U_R from the vector summation of U_T (the the perpendicular component of the rotational velocity) and V_{inf} (free stream velocity). The resultant LEV and circulatory force are a function of the effective angle of attack and the resultant velocity in the flapping plane. The wings have a larger resultant velocity in downstroke than in upstroke as is illustrated in Fig. 7.24. Therefore, the aerodynamic forces produced during the downstroke are larger than the forces during the upstroke.

(a) Resultant velocity - Downstroke (b) Resultant velocity - Upstroke

Figure 7.24: Incident velocities at a wing chordwise element during a flapping cycle in a trimmed level flight (1 m/s).U_T is the the perpendicular component of the rotational velocity, V_{inf} free stream velocity, U_R the resultant velocity (in-plane) the wings sees during the forward flapping stroke.

Next, time histories of forces during flapping stroke in forward flight are examined. Figure 7.25 plots the time histories of the total forces over one stroke in trimmed forward flight of 1 m/s. The total forces are contributed by the two wings, and computed in the inertial coordinate system. As in hover the average quantities must satisfy the trim conditions; that is, the vertical thrust (Z) is equal to the insect MAV weight and average X and Y forces are zero. Figure 7.25 also shows the average quantities over one flapping cycle. The average forces satisfy the trim condi-

tions. The majority of the vertical thrust is obtained during the downstroke. The downstroke and the upstroke are no longer similar due to the tilt of the plane forward and the different resulting velocity magnitude. The averaged X force is approximately zero. Most of the negative X force is obtained during the supination (with a negative peak), with a positive horizontal force obtained during the upstroke.

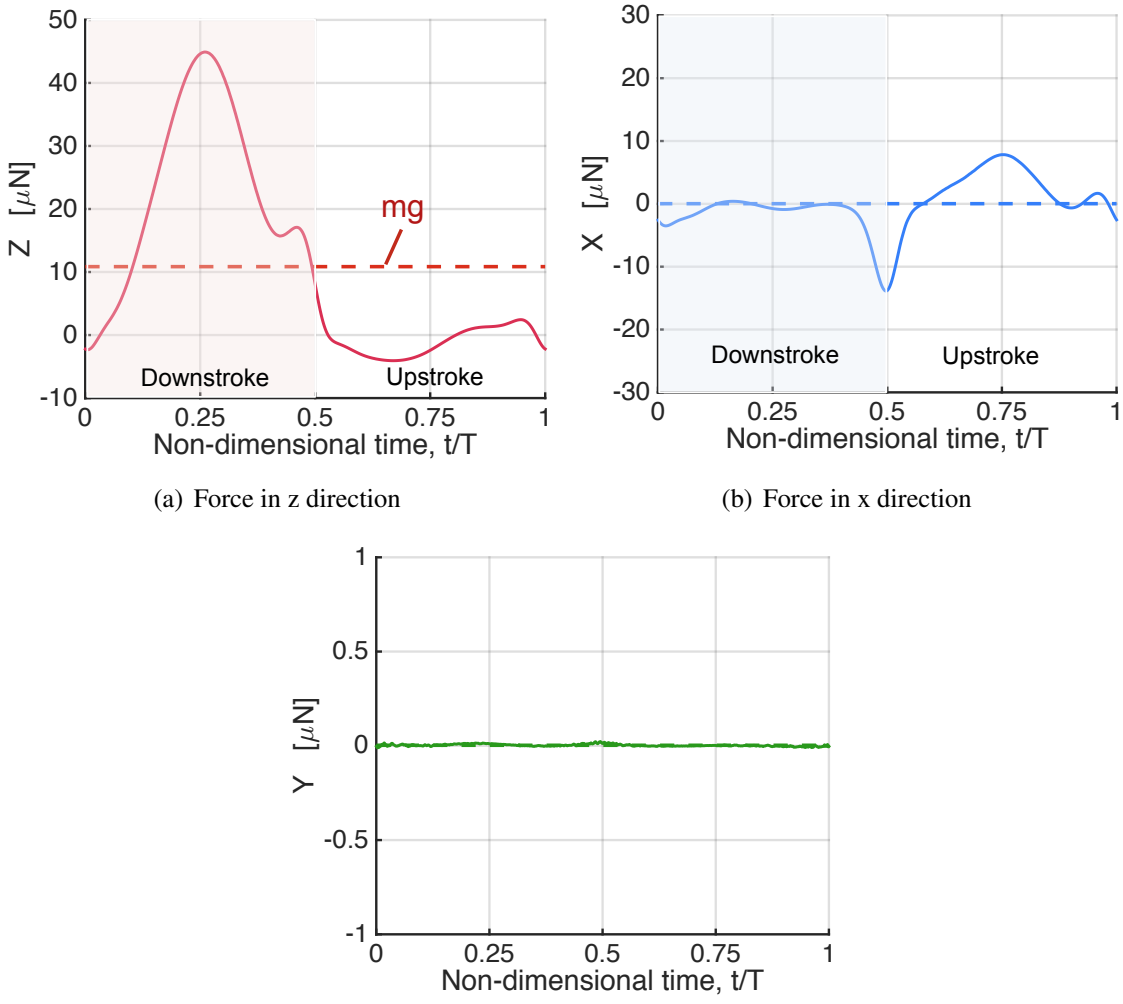

(a) Force in z direction

(b) Force in x direction

(c) Force in y direction

Figure 7.25: Time histories forces in x,y and z direction during a flapping cycle in trimmed level flight 1 m/s. The dashed lines represents the flapping-cycle averaged forces.

Side force Y is plotted in Fig. 7.25(c). The magnitude of this force is insignificant compared to that of the X and Z forces, and its averaged quantity is zero. The side force is minor because the side forces are cancelled out from the kinematics, as can seen in Fig. 7.26(a), where the side force of each wing has similar magnitude but opposite signs. The wing kinematics are symmetric with respect to the X-Z plane (longitudinal symmetry). In terms of vertical force (as shown in Fig. 7.26(b)), it is seen that each wing has equal contribution to the vertical thrust (Z force).

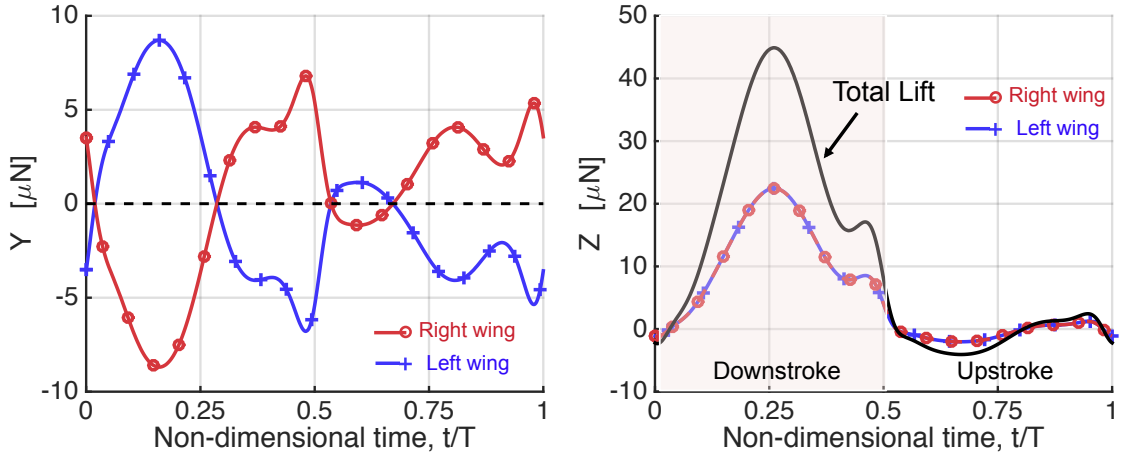

(a) Force in y direction

(b) Force in z direction

Figure 7.26: Time history vertical and side forces during a flapping cycle of each wing in trimmed level flight (1 m/s).

The time histories of moments (roll, yaw and pitch) during one flapping cycle in trimmed level flight are plotted in Fig. 7.27. Moments are computed around the insect body CG. As can be seen from the figures, the yaw and roll moments are one order of magnitude order smaller than the pitch moment. The flap-cycle averaged roll and yaw moments are zero, resulting from the symmetry around the X-Z plane. The dominant moment is the pitch moment, which is balanced by the trim variables. In hover, as mentioned earlier, the pitch moment equilibrium is achieved by

stroke bias and stroke tilt.

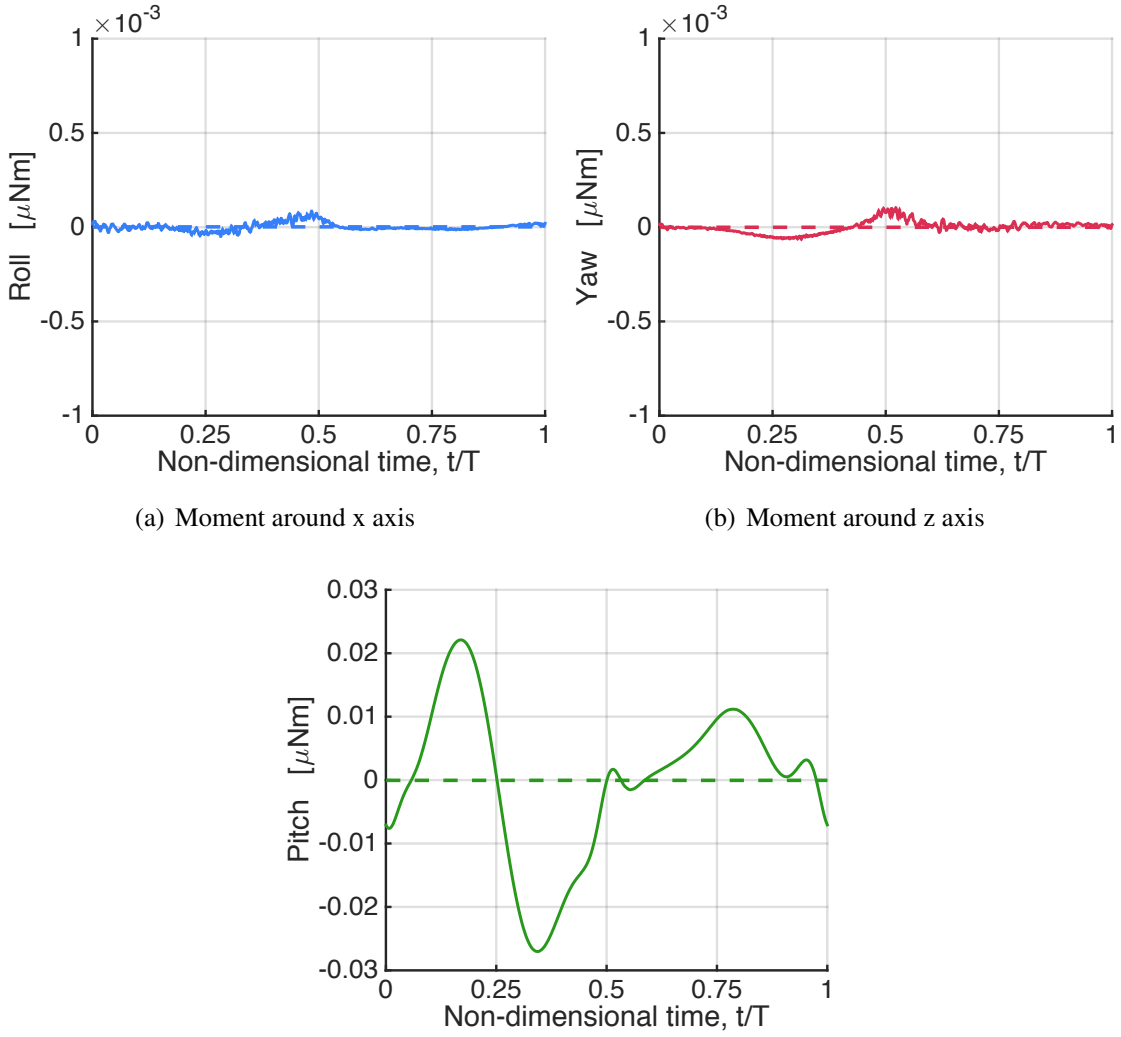

(a) Moment around x axis

(b) Moment around z axis

(c) Moment around y axis

Figure 7.27: Time histories of moments; roll, yaw and pitch; during a flapping cycle in trimmed level flight (1 m/s).The dashed lines represent the flapping-cycle averaged moments.

7.3.2 Wake Structure

The wake features in trimmed level flight are studied to identify the shed vortex and its trajectory and the flow field around the flapping wings. The main focus of this section is the LEV formation during upstroke and downstroke as well as the trajectory of the shed vorticity in forward flight at 1 m/s.

The leading edge vortex is one of the main mechanisms of lift enhancement in flapping wings. The dynamics of the LEV in forward flight are different from hover due to the kinematics. Figure 7.28 shows a comparison of the vortical structure during the translational downstroke and translational upstroke. The figure examines the vorticity magnitude contours. It is clear that during the downstroke (Fig. 7.28(a)) there is a permanent LEV on the upper surface of the wing. The LEV that forms remains attached to the upper surface during the translational downstroke. The LEV grows from wing root to tip, and indicating the rotational effect resulting in a conical shape. Unlike the strong vortex formation during the downstroke, in the upstroke the LEV is significantly weaker (Fig. 7.28(b)). Due to the high angle of attack the wing has during the upstroke, the dominant component of the suction force resulting from the weak LEV is in the XY plane. This results in the positive X force during the upstroke, where the nearly vertical force in the upstroke results in the negative force.

Another observation that can be made from the vortical structure around the wings is that during upstroke, the wing does not interact with the wake. This can also be seen in the time history of vertical force, where during the transition portions (supination an pronation) there is only an enhancement due to the rapid pitch-up (rotational forces) and there is no peak due to wake

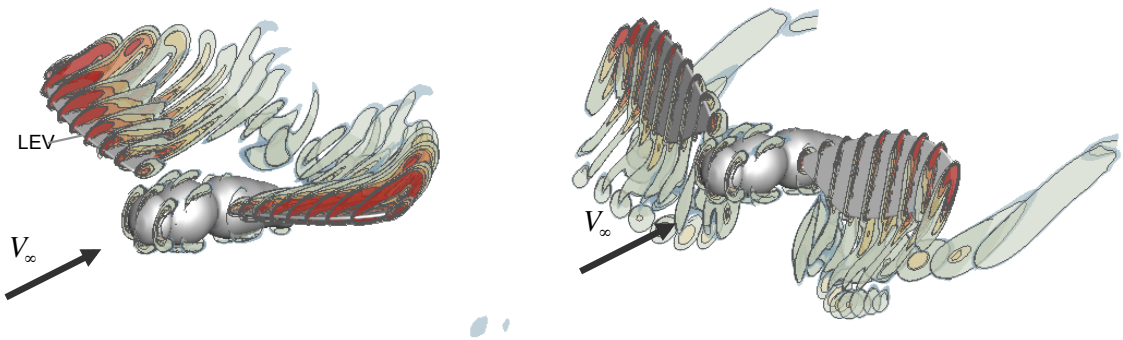

(a) LEV - Downstroke (b) LEV - Upstroke

Figure 7.28: The non-dimensional vorticity magnitude (0.009 - 0.045) during downstroke and upstroke at various planes parallel to XZ.

interaction.

To investigate the vortical wake and the flow in more detail, the vorticity in the x direction during different time instants is plotted as iso-surfaces of vorticiy and vorticity contours. Looking at the vorticity in the x direction allows the trajectory of the shed vorticity to be seen. Starting with the translational downstroke, Figure 7.29 shows the vorticity in the x direction at the middle of the downstroke (t/T=0.25). In the upper part of the figure, an iso-surface of vorticity (non-dimensional vorticity of 0.01) is plotted and shown in top and side views for the insect diptera configuration. In the second part of the figure, the vorticity contours are plotted at 4 different planes parallel to the YZ plane. The red color represents clockwise vorticity and the blue color represents counter clockwise direction of the vorticity swirl. The iso-vorticity indicates the formation of a strong LEV as discussed before. It can be seen that the plane tilt causes most of the shed vorticity is behind and above the wing (planes (c) and (d)). As a result of the free-stream the tip shed vortex goes further behind the body where as in hover the shed wake is mostly downward below the body.

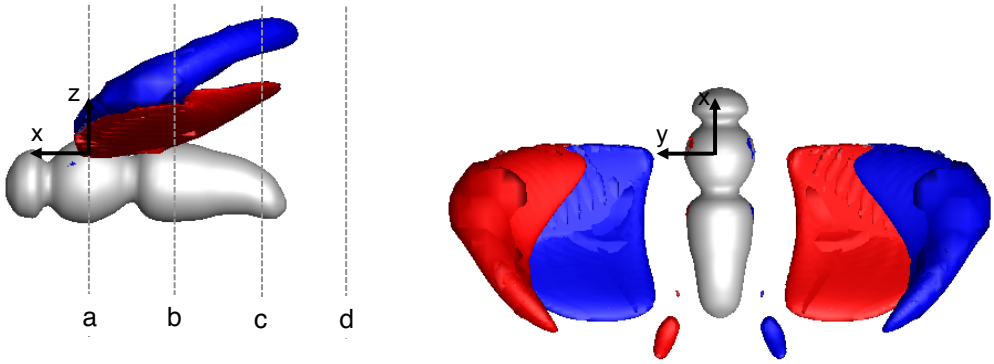

(a) Iso-surface of vorticity in x direction

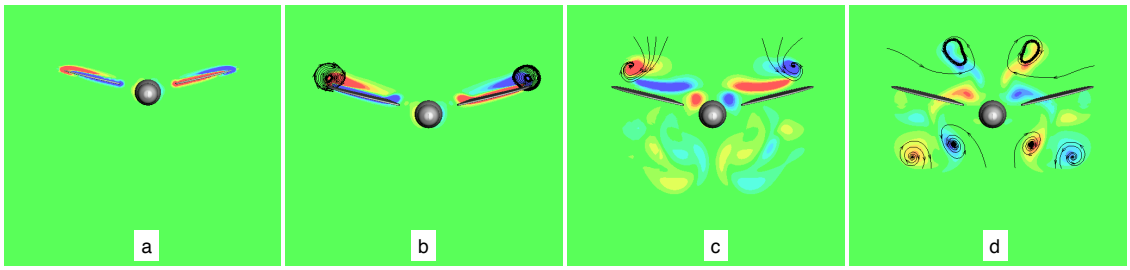

(b) 2d vorticity magnitude on section planes parallel to YZ

Figure 7.29: The normalized vorticity normal to $x = 0$ plane during translational downstroke t/T=0.25, (a) Iso-surface positive vorticity (0.01) and negative vorticity (-0.01), red - clockwise and blue - counter clockwise directions.(b) The vorticity contours at three different locations in x direction (a,b,c) as demonstrated in the insect side view. The planes are normal to body axis (x). 2D streamlines are computed in the fixed inertial frame.

The wake structure during the transition from down-to-upstroke (supination) is shown in Fig. 7.30. During the transition the wing is pitching up to flip and start the reversal stroke (up-stroke). During supination, the vortex detaches from the wing surface, forming both a tip and a root shed vortex. The massive detaching vortex is mostly from the tip. The wing is now located at the lowest point of the stroke. All of the shed vorticity is above the wing, and convects further downstream from the insect body due to the horizontal velocity component (planes (b), (c) and (d)).

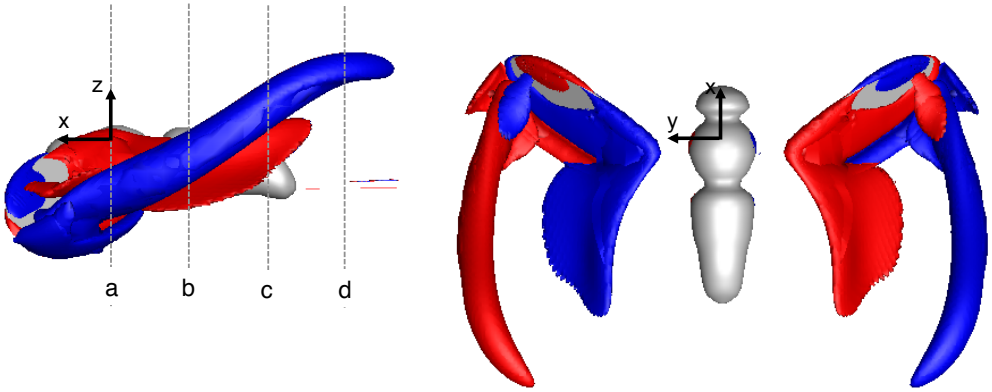

(a) Iso-surface of vorticity in x direction

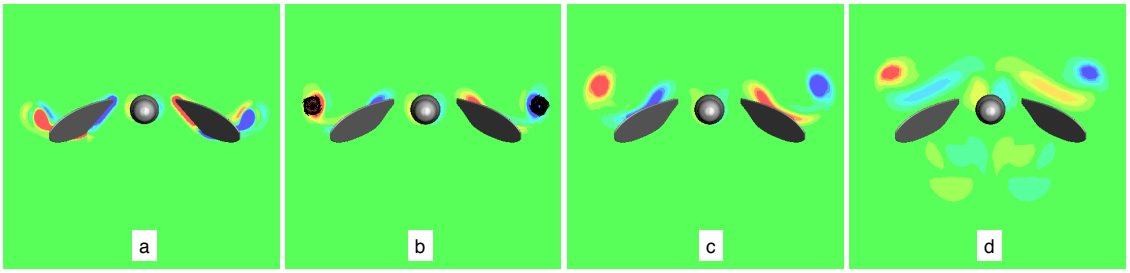

(b) 2d vorticity magnitude on section planes parallel to YZ

Figure 7.30: The normalized vorticity normal to $x = 0$ plane, during the transition from downstroke to upstroke (supination) t/T=0.5, (a) Iso-surface positive vorticity (0.01) and negative vorticity (-0.01), red - clockwise and blue - counter clockwise directions.(b) The vorticity contours at three different locations in x direction (a,b,c) as demonstrated in the insect side view. The planes are normal to body axis (x). 2D streamlines are computed in the fixed inertial frame.

During the translational upstroke, the vorticity formation on the leading edge is less strong than in downstroke as can be seen from Fig. 7.31. In the side view of the insect (Fig. 7.31(a)) the wing translates with a higher angle of attack, and the resultant speed also affects the LEV formation, strength and stability. From the wake snapshots (Fig. 7.31(b)) at different locations it is also clear that the wings do not interact with the previous wake, which has now convected downwards as well backward.

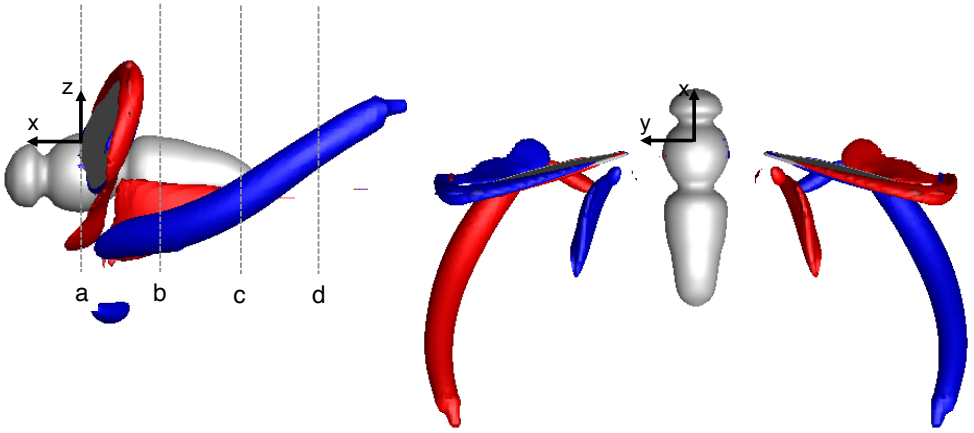

(a) Vertical force

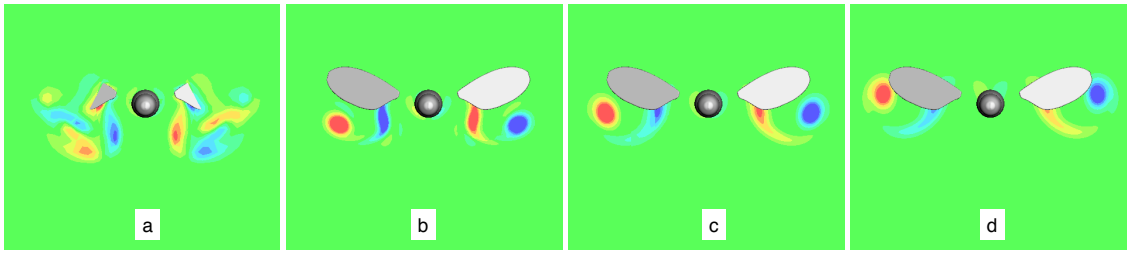

(b) Horizontal force

Figure 7.31: The normalized vorticity normal to $x = 0$ plane, during translational upstroke t/T=0.75, (a) Iso-surface positive vorticity (0.01) and negative vorticity (-0.01), red - clockwise and blue - counter clockwise directions.(b) The vorticity contours at three different locations in x direction (a,b,c) as demonstrated in the insect side view. The planes are normal to body axis (x).

At the end of the upstroke, the wing flips to start the downstroke, leaving relatively less

vortical wake, as can be seen in Fig. 7.32. The wing motion forces the LEV to shed from the upper surface, mostly at the tip and the trailing edge.

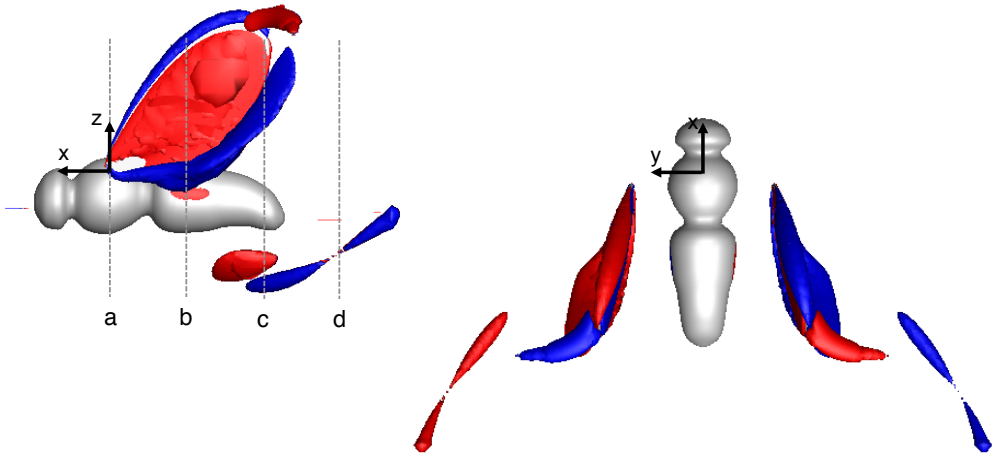

(a) Vertical force

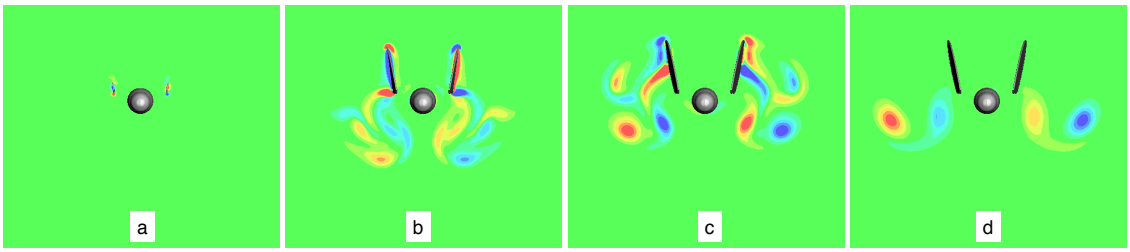

(b) Horizontal force

Figure 7.32: The normalized vorticity normal to $x = 0$ plane, during the transition from upstroke to downstroke (pronation) t/T=1, (a) Iso-surface positive vorticity (0.01) and negative vorticity (-0.01), red - clockwise and blue - counter clockwise directions.(b) The vorticity contours at three different locations in x direction (a,b,c) as demonstrated in the insect side view.

The freestream in forward flight thus affects the shed vortex trajectory. Furthermore, the induced velocity also affects the shed vorticity path. To compare the wake structure in forward flight and the wake in hover, iso-surfaces of vorticity magnitude are plotted in Fig. 7.33, where the vorticity is colored by the vertical velocity component. In hover, where there is no freestream velocity, the shed vorticity convects below the wings, creating distinguishable shed tip and root

vortices. In forward flight the shed vortices convect backward due to the free stream velocity and the plane tilt, and downwards due to the induced inflow. The vortical structure is more visible in hover than in forward flight. Also, the induced vertical velocity (blue regions) is stronger and more significant in hover than in forward flight.

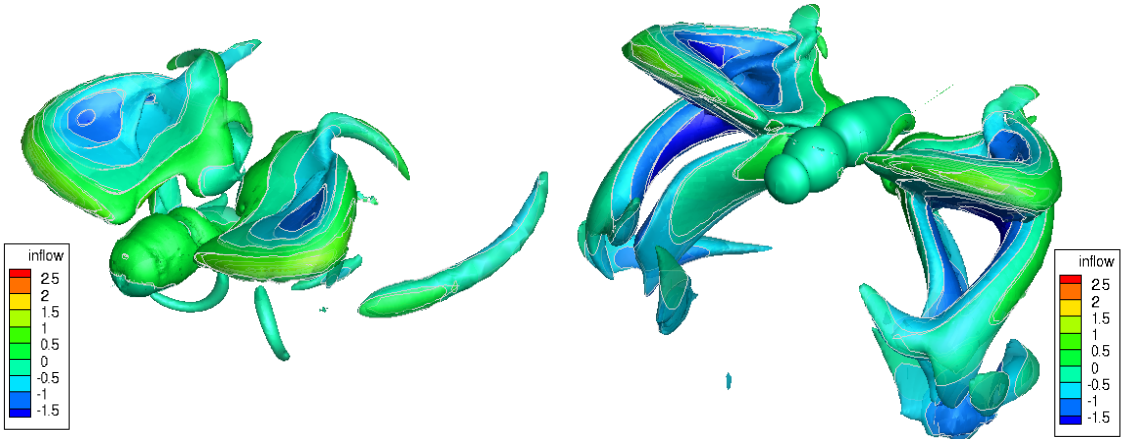

(a) Forward flight (b) Hover

Figure 7.33: Iso-surface vorticity magnitude colored by the vertical velocity component (induced velocity), in trimmed forward flight and hover in downstroke.

7.3.3 Power and Vertical Thrust

An analysis of the aerodynamic power required over a full stroke for the flapping wing MAV in trimmed level flight with a forward speed of 1 m/s is carried out in this section. This analysis considers only the aerodynamic power, extracted from the CFD simulations. Figure 7.34 shows the time history of required power during one flapping cycle in trimmed forward flight. The larger component of total power is due to the pressure, which can roughly be assumed to be ”induced power“. Therefore the power trend follows the vertical force trend, where a majority of the required

power is during the downstroke. The shear forces contribute less to the power, although during the upstroke the shear power magnitude is equally as significant as the pressure power.

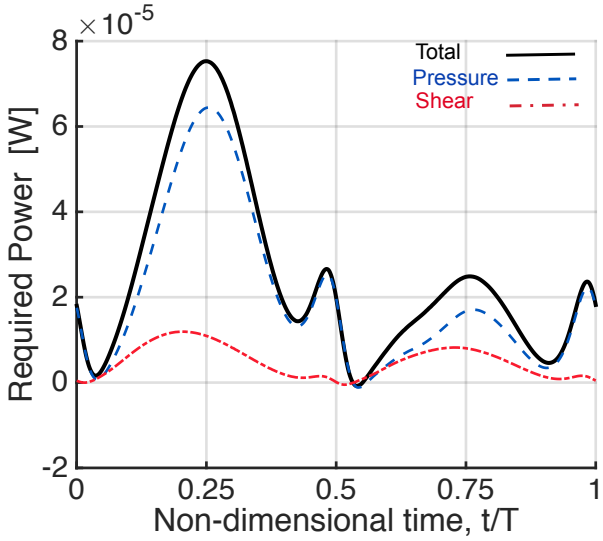

Figure 7.34: Time history of required power during a flapping cycle in trimmed forward flight. The total power divided into power due to shear (profile power) and power due to pressure (induced power).

To understand the power profile during the flapping stroke portions, the spanwise distribution of power is considered during downstroke, supination, upstroke and pronation in Figure 7.35. The trend of the power distribution along the wing span is different than that obtained in hover. In hover the power distribution was ”tip dominated“, where the maximum peak was achieved toward the wing tip. In trimmed forward flight the maximum peak occurs around r/R$=0.7$ in downstroke and upstroke (Fig. 7.35 (a),(c)). The total power trend is mostly affected by the pressure power trend. The total power in the inboard wing (r/R$=0--0.3$) is almost zero. This can be explained by the resultant velocity in this portion being small, due to the small perpendicular component of the rotational speed which is canceled by the freestream velocity (the rotational speed at R/r$=0.3$

is equal to 0.75 m/s) . The shear pressure increases linearly along the span (from r/R$= 0.3 - -0.9$) during the translation portions, but is negligible during the wing transition. During the supination and pronation (at t/T$= 0.5, 1$) the peak in the required power moves to the midspan.

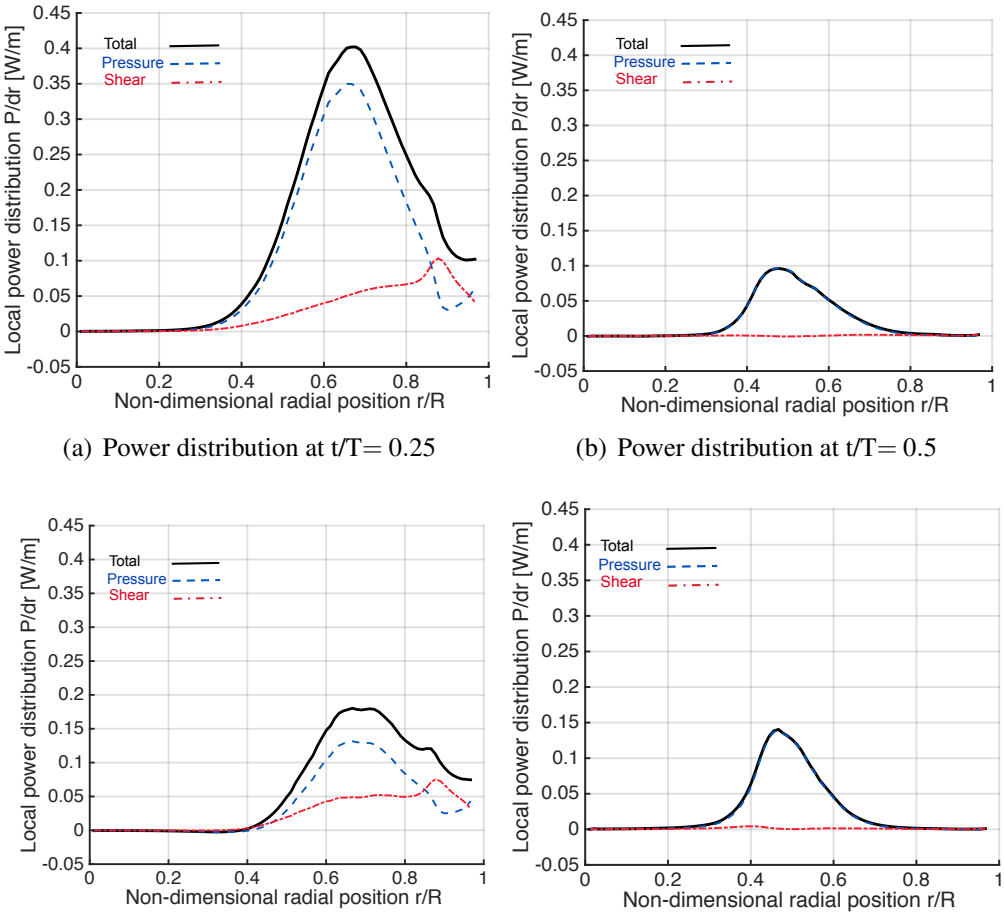

(a) Power distribution at t/T$= 0.25$

(b) Power distribution at t/T$= 0.5$

(c) Power distribution at t/T$= 0.75$

(d) Power distribution at t/T$= 1$

Figure 7.35: Power distributions along the wing span during 4 different time instants at downstroke (t/T$= 0.25$), supination (t/T$= 0.5$), upstroke (t/T$= 0.75$) and pronation (t/T$= 1$). The x axis represents the wing span normolized by the wing length. r/R$= 0$ the wing root, r/R$= 1$ the wing tip.

To shed more light the total required power, the distribution along the span is examined during the translational and the transitions at three time instants. Also the vertical thrust distribution

along the span is analyzed, to show how the vertical force and power are built-up during the flapping cycle. Figure 7.36 shows the power and vertical thrust distribution along the wing span. The three time instants: early stage of the translational downstroke, mid-downstroke and late stage of the downstroke, marked by a, b and c respectively. The wing locations at these times are shown in Fig. 7.36(a), for both top and side view. As expected the maximum peak in both power and vertical thrust occurs at mid-stroke where the resultant rotational velocity is maximum due to the maximum flapping velocity (sinusoidal function). After midstroke there is a reduction in the peak magnitude. The trends of the curves are similar.

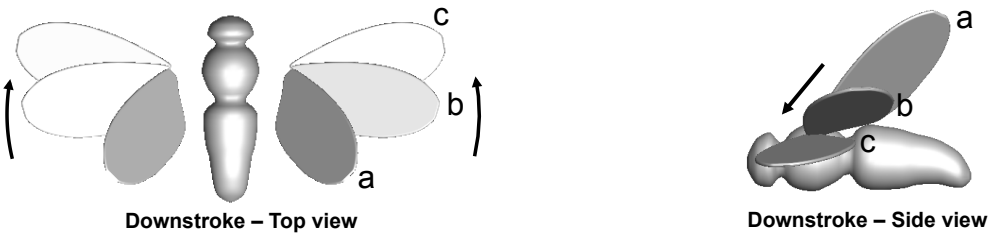

(a) Translation - Downstroke

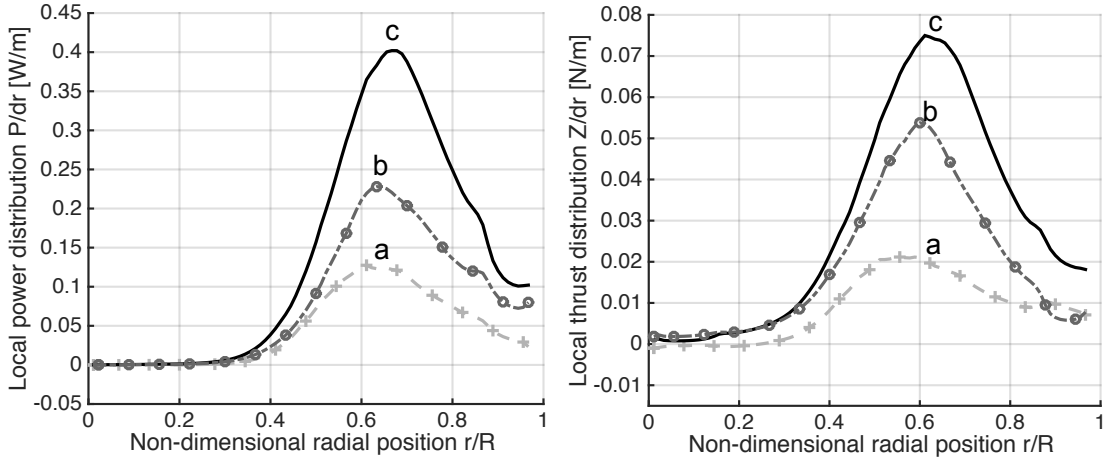

(b) Power and vertical thrust span distributions

Figure 7.36: Power and vertical thrust distributions along the wing span during translational downstroke in trimmed forward flight (1 m/s), at three different location; (a) - t/T= 0.1, (b) - t/T= 0.25, (c) - t/T= 0.35.

During the transition portions, the wing has different power and vertical thrust distributions from these obtained in downstroke, as shown in Fig. 7.37. Positive peaks in vertical force distribution during the supination portion (represented by d and e), result in a positive enhancement at t/T=0.45 and are associated with the positive peak due to the rapid pitch-up effect. At time instant f, it is seen that there is very little positive vertical thrust, and there is even a portion with negative thrust over the outboard section. And as shown in the previous section the wing does not interact with the previous wake.

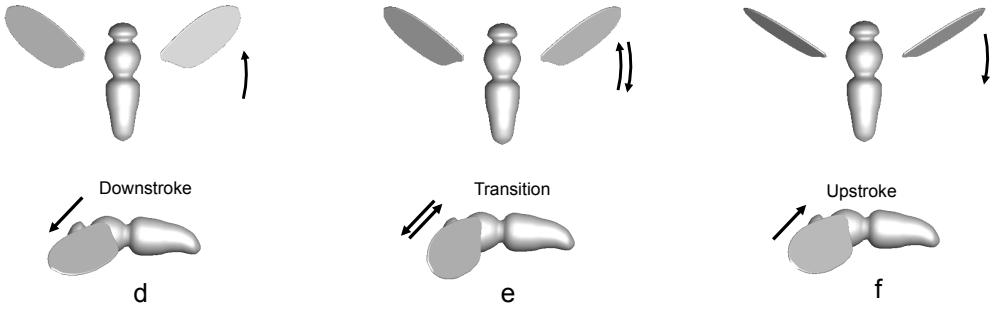

(a) Supination

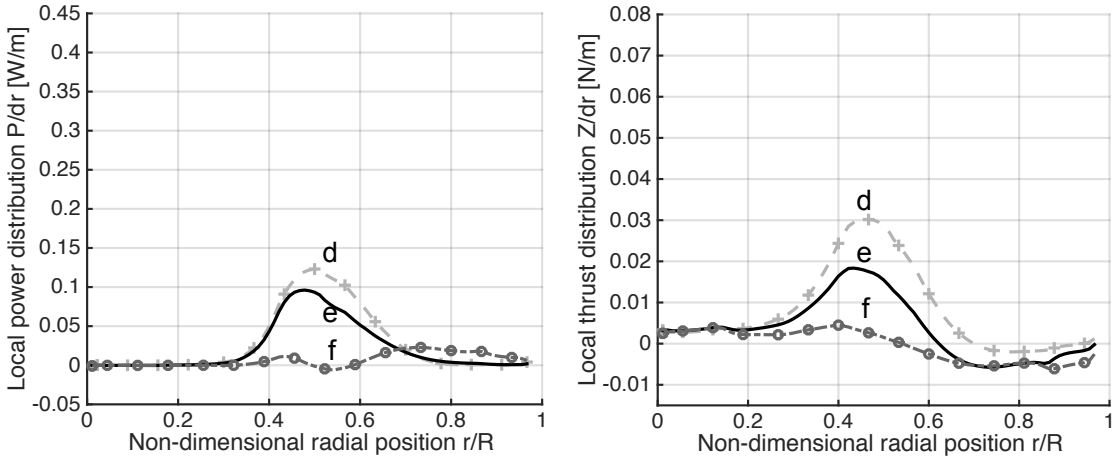

(b) Power and vertical thrust span distributions

Figure 7.37: Power and vertical thrust distributions along the wing span during the transition from downstroke to upstroke (supination) in trimmed forward flight (1 m/s), at three different location; (d) - t/T= 0.45, (e) - t/T= 0.5, (f) - t/T= 0.55.

During the upstroke, the wings translate from the lower point in the stroke toward the upper point as shown in Fig. 7.38(a). Following the previous discussion, the upstroke in forward flight does not contribute to the vertical thrust as shown in part (b) of the figure. The power distribution trend is similar to that observed in the downstroke, but the power magnitude is much less than that in downstroke.

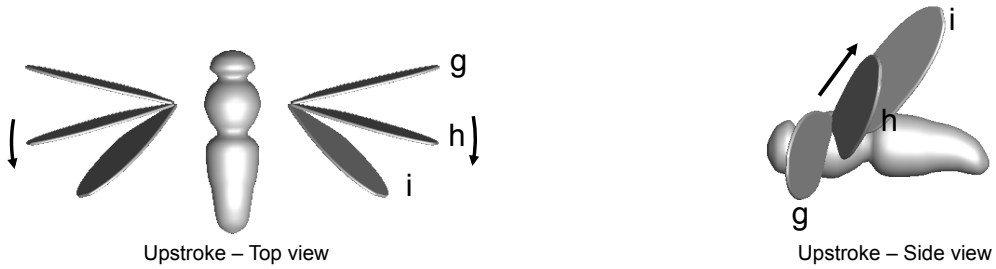

(a) Translation - Upstroke

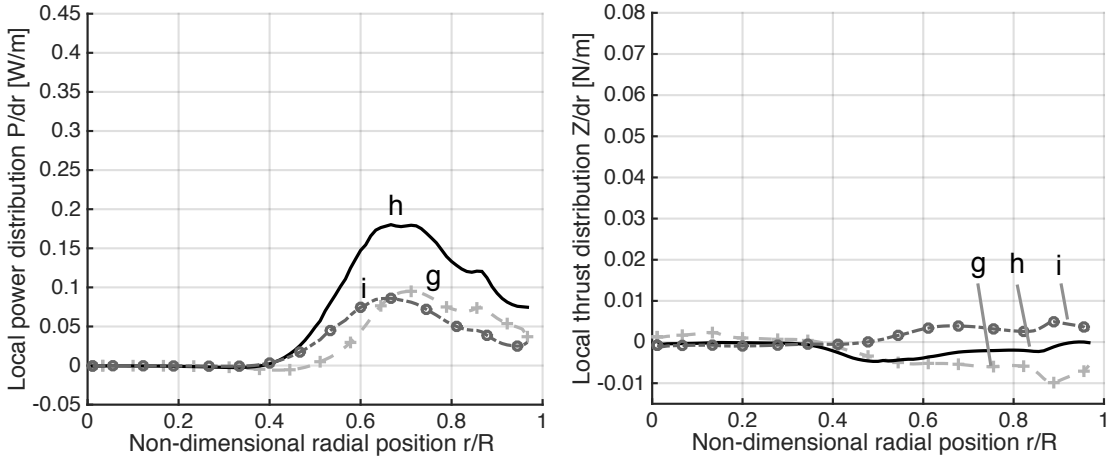

(b) Power and vertical thrust span distributions

Figure 7.38: Power and vertical thrust distributions along the wing span during translational upstroke in trimmed forward flight (1 m/s), at three different location; (g) - t/T= 0.6, (h) - t/T= 0.75, (i) - t/T= 0.85.

Figure 7.39 shows the spanwise distrbution of the power and vertical thrust during the transition from upstroke to downstroke. The vertical thrust has strong negative peaks along the wing

during the pronation at t/T= 1 and 1.15, but a small positive thrust is obtained at the beginning of the pronation (curve j). The magnitude is small, but results in a positive peak in the total vertical force at t/T= 0.95.

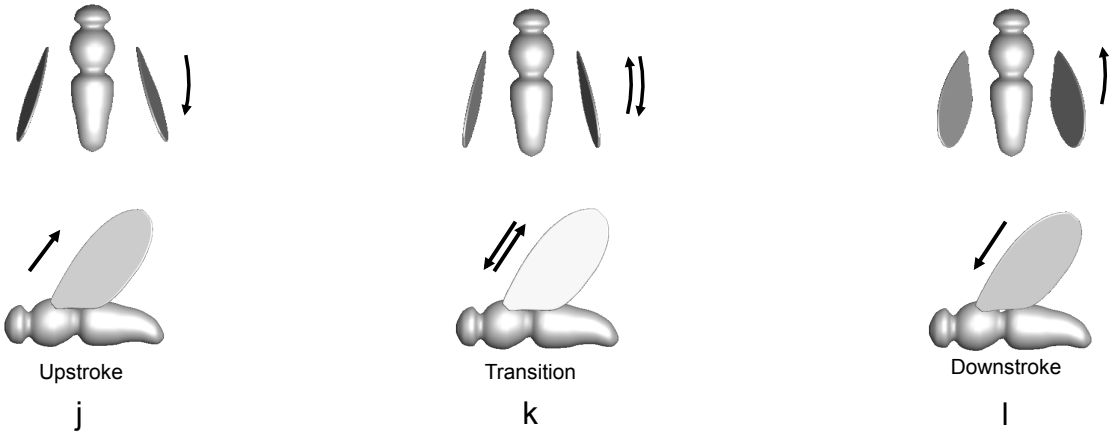

(a) Pronation

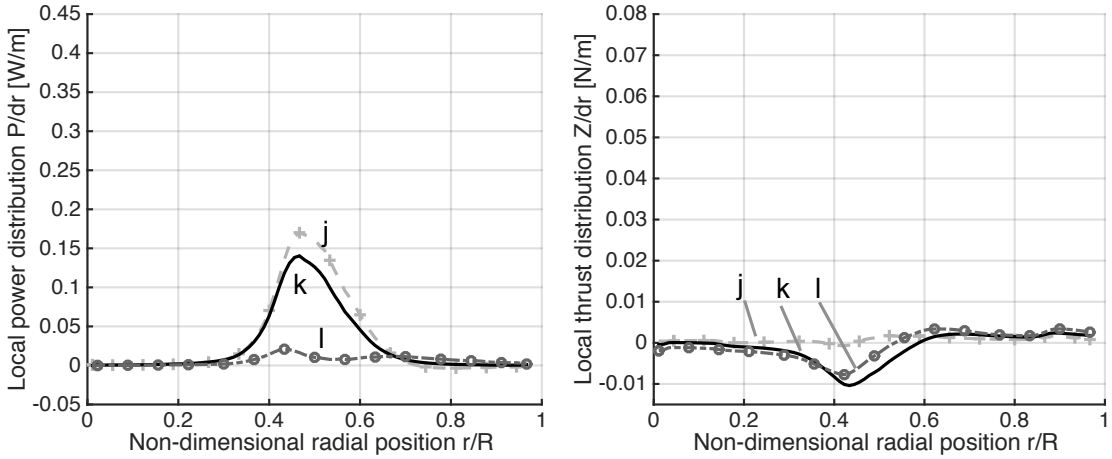

(b) Power and vertical thrust span distributions

Figure 7.39: Power and vertical thrust distributions along the wing span during the transition from upstroke to downstroke (pronation) in trimmed forward flight (1 m/s), at three different location; (j) - t/T= 0.95, (k) - t/T= 1, (l) - t/T= 1.15.

7.3.4 Mean Power Profile in Forward Flight

Figure 7.40 presents the CFD predictions of flapping cycle averaged aerodynamic power in trimmed forward flight as a function of forward speed. Note, that the aerodynamic power initially decreases with increasing forward speed; in this case minimum power is obtained at 0.5 m/s. However, it increases again with an increase in the flapping plane tilt for higher forward speeds. The aerodynamic power components are due to shear forces and pressure forces, as well as induced power. The profile of the mean power is similar to the main rotor power in forward flight in Fig. 7.41 (without considering the parasitic and tail power).

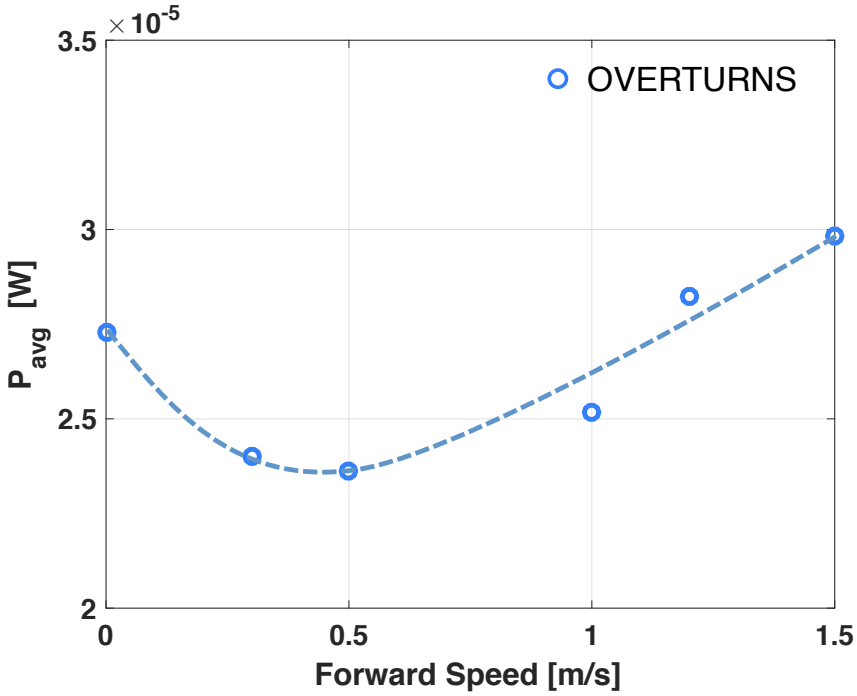

Figure 7.40: CFD predictions of flapping wings MAV aerodynamic mean power in trimmed forward flight.

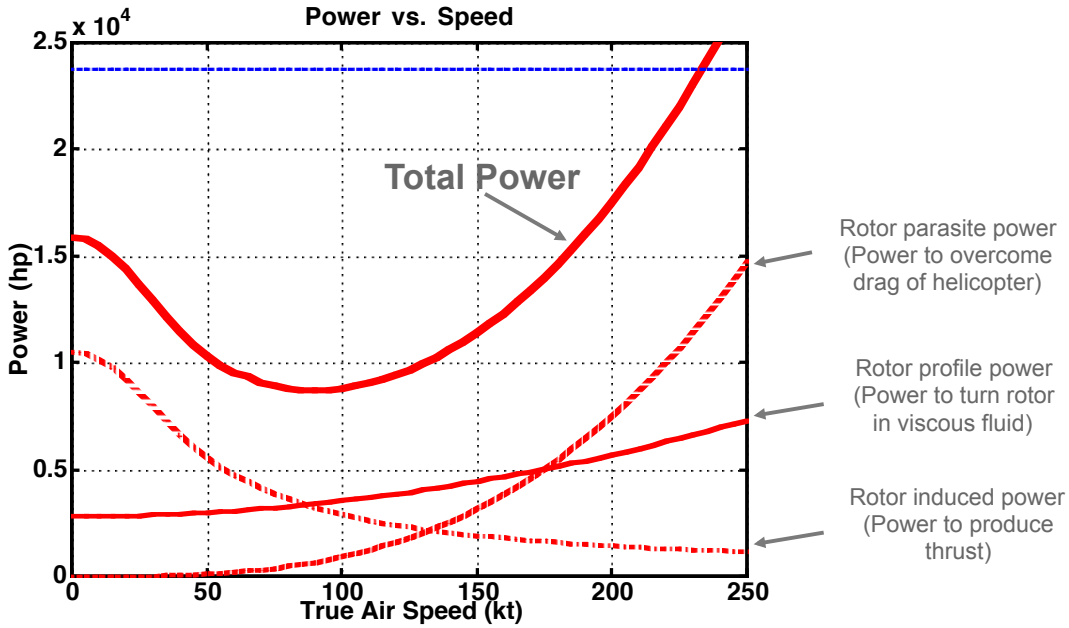

Figure 7.41: Main rotor power in forward flight [ref].

If the CFD predictions are compared with the QS, as can shown in Fig. 7.42, it can be clearly seen that QS can correctly not predict the induced power in forward flight.

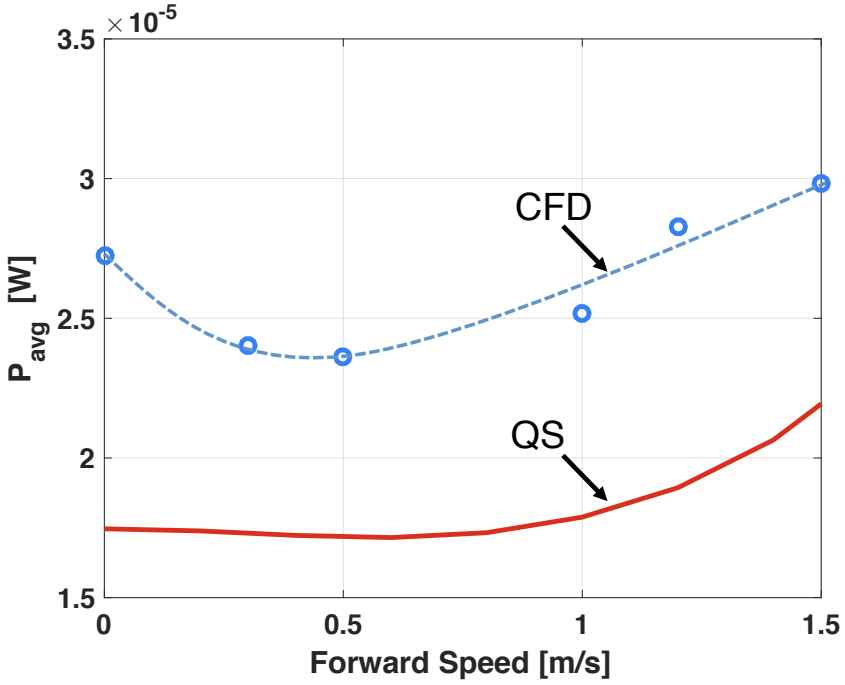

Figure 7.42: CFD and QS predictions of flapping wings MAV aerodynamic mean power in trimmed forward flight.

7.4 Steady Coordinated Turning Flight

This section presents steady coordinated turning analysis using the CFD-QS trim coupling model. The first part discusses trends in trim characteristics (flapping wing kinematics) in steady turning flight, using steady forward flight as a baseline condition. The analysis is performed using the reduced-order (quasi-steady) aerodynamic model. The second part compares the predictions obtained using the CFD and quasi-steady analysis for identical wing kinematics and trim conditions, and highlights the major differences between results simulated from CFD and quasi-steady aerodynamics.

An instantaneous snapshot of the insect in a steady level coordinated turn is shown in Fig. 7.43. Compared to steady level forward flight, turning flight requires the production of a side force to overcome centrifugal loads associated with the rate of turn. As in the case of fixed-wing and rotary-wing vehicles, introduction of body roll attitude into the turn ensures that a component of the lift vector is oriented towards the center of the turn to maintain the turn radius. With the chosen wing kinematics, the most efficient way to produce a lateral force to overcome centrifugal loads is to increase the total thrust (flap stroke amplitude) and roll the body into the turn. Presently, the wing stroke plane cannot be tilted laterally, therefore introduction of roll attitude is the only feasible means of overcoming centrifugal forces.

To expand the flight envelope of the flapping wing MAV, it is critical to regulate the body roll attitude exactly according to the coordinated turn condition. If this condition is not enforced exactly, then the maximum achievable turn rate for a given airspeed is significantly reduced. To illustrate this fact, the body roll attitude was prescribed as various fractions of the value from

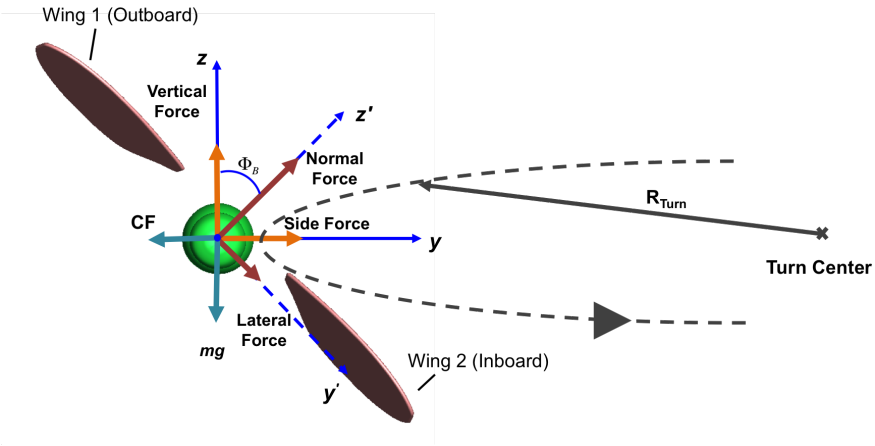

Figure 7.43: Forces in a Steady Level Coordinated Turn.

Eqn. 7.1.

$$\phi_B = \tan^{-1} \frac{V_\infty \dot{\psi}_B}{g} \tag{7.1}$$

These fractions were controlled by a parameter k less than one, which multiplies the prescribed roll attitude ϕ_B. Figure 7.44 shows the trim wing kinematics over a range of turn rates for various k, for both wings. As k approaches one, i.e. the turn is increasingly close to being coordinated, the maximum achievable turn rate increases from 250 deg/s, to 375 deg/s, to 1080 deg/s as k increases from 0.75, to 0.85, to 1.

Trim solutions were obtained with the forward flight speed set to 0.5 m/s, and the turn rate was varied from 0 to 1080 deg/s (i.e. three complete loops per second in a horizontal plane). The roll attitude was prescribed for each flight condition according to Eqn. 7.1 and is shown together with the aerodynamic power required in Fig. 7.45. Since the roll attitude is chosen to balance the lateral component of the wing force against centrifugal force, the roll attitude is unaffected by the

choice of body mass. However, the power required to execute the turn increases by almost 700% for the combination of higher insect and quickest turn rate studied.

By allowing the insect body to roll into the turn, the difference in force requirements between the left and right wings is minimized, while incremental differences in kinematics can still trim out small imbalances due to different dynamic pressures. Figures 7.46 (a)-(f) show the variation of wing stroke plane tilt, stroke amplitude and stroke phase offset with turn rate for the coordinated turn. Incremental differences in the stroke plane angle of the two wings, shown in Fig. 7.46(a) allow for the generation of a yawing moment. The yawing moment increases with airspeed, indicated by the growing differences between stroke plane angles for the two wings. For a heavier insect, the forward tilt of the stroke plane is smaller than for a lighter insect.

Figure 7.46(c) shows the variation of the stroke amplitude (of both wings) with turn rate for the baseline insect. For faster turns, the wing aerodynamic loads are correspondingly larger, being used to counter the centrifugal force in a turn. At the quickest turn rate (1080°/s) the turn radius is 5.3 cm, which is more than 8 times the lateral tip-to-tip span of the insect. The dynamic pressure between the two wings is not drastically different. Consequently, the stroke amplitude is near-identical for both wings at all turn rates considered. Heavier insects require a larger stroke amplitude to counter the larger centrifugal loads. Figure 7.46(e) shows the stroke phase offset for the two wings of the baseline insect. Incremental differences in this parameter allow for balancing the rolling moment at the body CG.

Figure 7.47 shows, respectively, the variation within a flap cycle of the aerodynamic power

required, vertical force, horizontal thrust and the side force produced by the wings at 0.5 m/s flight speed for various turn rates for the baseline insect mass. As the turn rate increases, the production of vertical thrust increases significantly during the first half-cycle of the flapping wing, and the power requirements increase correspondingly. This trend is qualitatively similar to that observed for increasing airspeed. When more thrust is required to turn faster, the wing downstroke provides most of the vertical force required and requires additional power, while the upstroke produces propulsive thrust. In the inertial frame (described in Fig. 7.43), the vertical force balances the vehicle weight. For the higher turn rate, the propulsive force in the downstroke and upstroke increase as a direct result of the increase in the flap stroke amplitude (ϕ_{max}). At higher turn rates, the increase of the flap amplitude with the body roll angle is used to generate side force to balance centrifugal force, as shown Fig. 7.47(c).

The trimmed wing kinematics at 0.5 m/s for turn rates ranging from 0 to 1080 deg/sec is shown in Fig. 7.46. The stroke amplitudes of the two wings are almost identical, but there are differences between the plane tilt and flap stroke bias. The forces in the inertial frame for a turn rate of 540 deg/sec and level flight, are plotted in Figs. 7.48 and 7.49. The time histories of forces from each wing are shown along with the total force. At 540 deg/sec, the vertical force and the propulsive force are similar, whereas in the side force there is a phase between the two wings.

In Fig. 7.50, the time histories of quasi-steady normal and lateral forces (body frame) are shown over one flap cycle. The lateral force is two orders of magnitude less than the normal force. The cycle-averaged lateral force is negligible in comparison to the normal force, demonstrating that turn coordination is effective in producing a dominantly normal resultant force as measured

along the body axes. Figure 7.50(a) shows that the normal force increases with increasing turn rate to produce additional lift to overcome the centrifugal forces.

From the trim analysis based on quasi-steady aerodynamics, the wing kinematics parameters for 0.5 m/s turning flight at 540 deg/s are obtained. The corresponding turn radius for this case is 0.05 m. The wing kinematics for this specific case are shown in Fig. 7.46; for wing1 (outboard wing) ϕ_{max1}, ϕ_{off1} and β_1 are 47.7, 8.5 and 16.7 (tilted forward) degrees respectively. For wing2 (inboard wing) ϕ_{max2}, ϕ_{off2} and β_2 are 47.8, 10 and 14.1 (tilted forward) degrees, respectively. The forces obtained in the inertia frame are plotted in Fig.7.51(a) – (c) where the CFD airloads are compared to those generated using the quasi-steady model with the same trim kinematics. As in the baseline case of level flight, the quasi-steady model overpredicts the airloads compared to CFD. The normal force generated by the insect, shown in Fig. 7.51(d), is insufficient to maintain the flight condition considered. The propulsive force from the QS and the initial CFD solution are similar in trend and magnitude, which indicates that rolling the whole vehicle with the body roll angle (ϕ_B) does not affect the forces in the longitudinal direction. The CFD vertical force trend the QS vertical force during the downstroke follows, but during the upstroke, it is almost flat with few small peaks and does not exhibit the force build up seen with the quasi-steady model. This difference might stem from unsteadiness in the flow such as vortical shedding and downwash. After the first CFD iteration, the new kinematics trim variables are achieved. The trim controls obtained are: 56.7, 25.0, -27.0 degrees (ϕ_{max1}, ϕ_{off1}, β_1) for wing1 and 58.9, 26.2, -23.0 degrees (ϕ_{max2}, ϕ_{off2}, β_2) for wing 2.

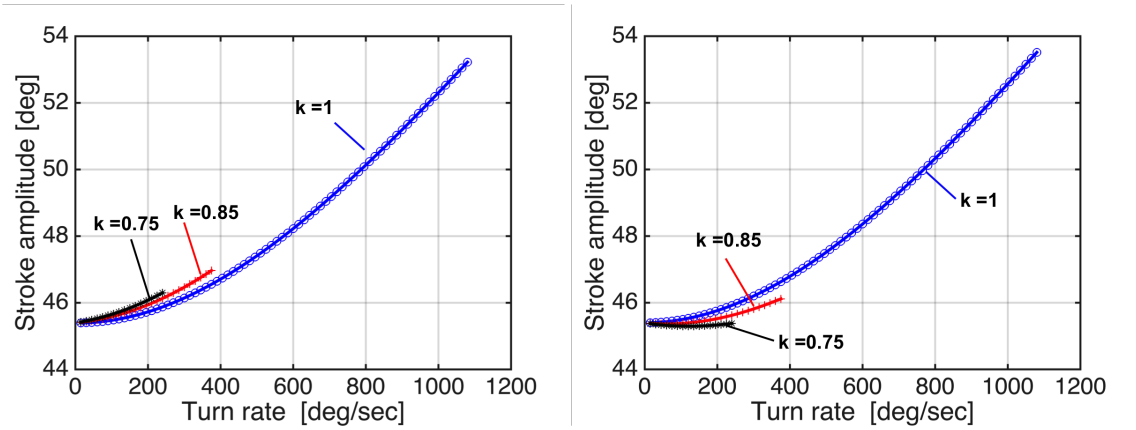

(a) Wing 1 stroke amplitude

(b) Wing 2 stroke amplitude

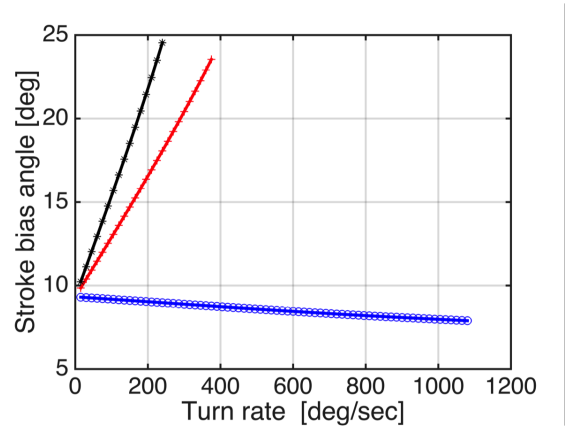

(c) Wing 1 flapping stroke bias

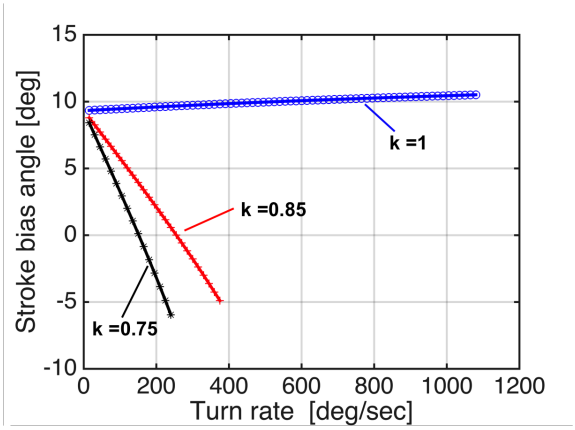

(d) Wing 2 flapping stroke bias

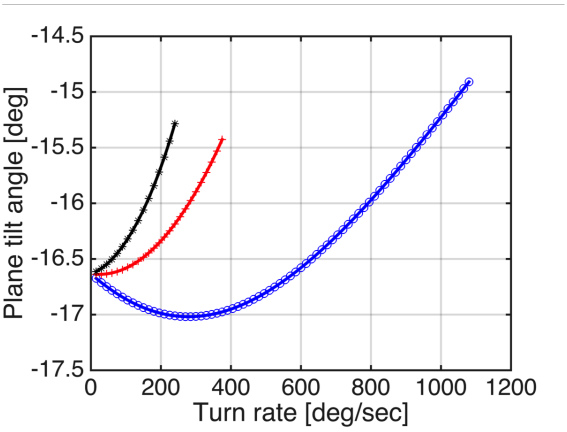

(e) Wing 1 plane tilt

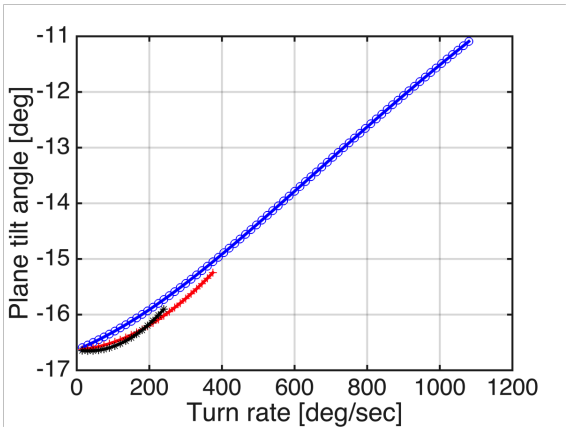

(f) Wing 2 plane tilt

Figure 7.44: Flight Envelope Limits in Level Turning Flight: Effect of Body Roll Attitude. $\phi_B = k\tan^{-1}(V_\infty \dot{\psi}_B / g)$. Flight Speed $V_\infty = 0.5$ m/s.

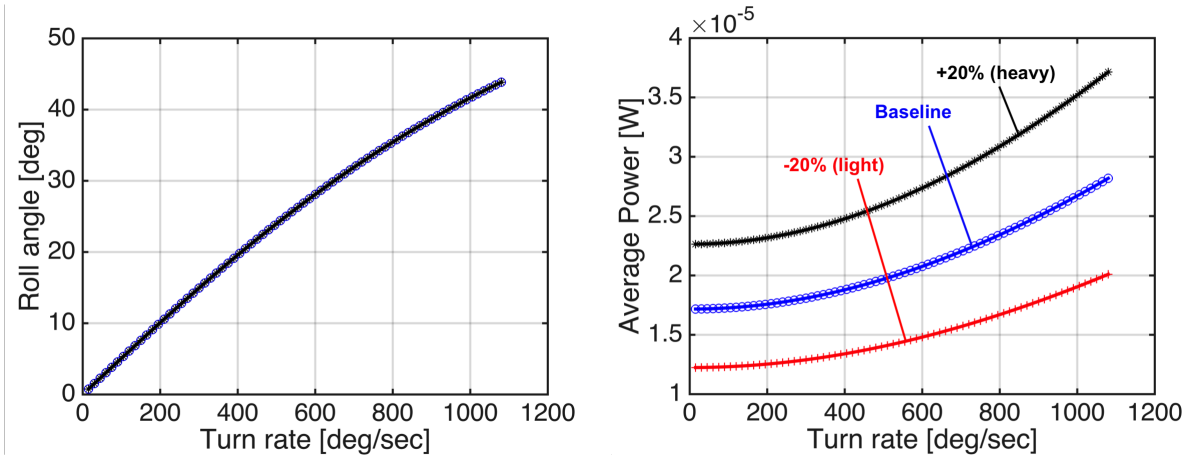

(a) Body Roll Attitude

(b) Aerodynamic Power Required

Figure 7.45: Variation of (a) Roll Attitude (b) Aerodynamic Power Required in Turning Flight; Flight Speed = 0.5 m/s.

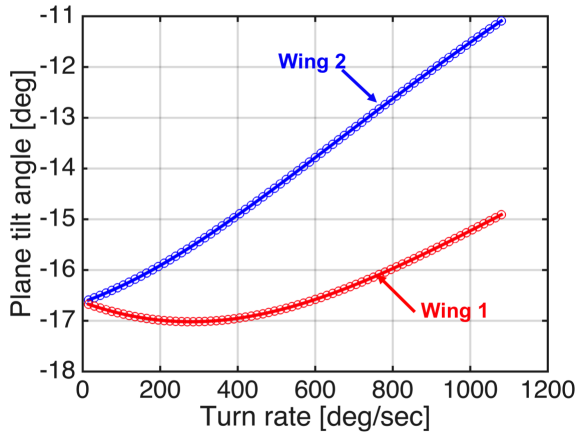

(a) Stroke Plane Tilt Angle β for Both Wings, Baseline

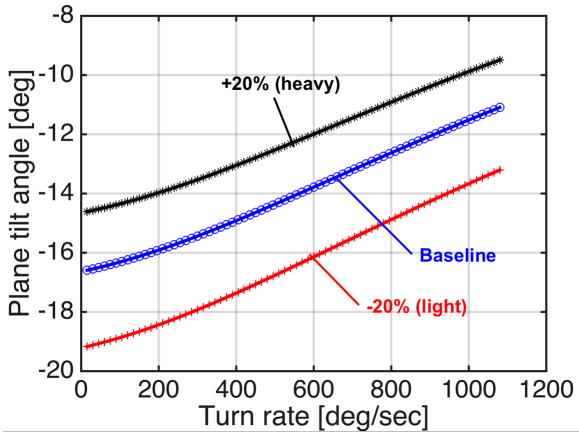

(b) Stroke Plane Tilt Angle β_2 for Various Weights

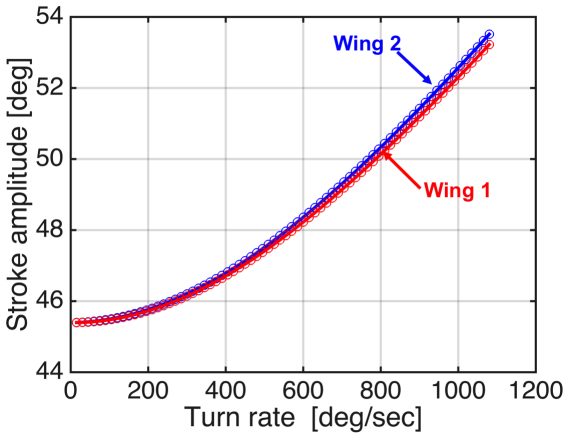

(c) Stroke Amplitude ϕ_{max} for Both Wings, Baseline

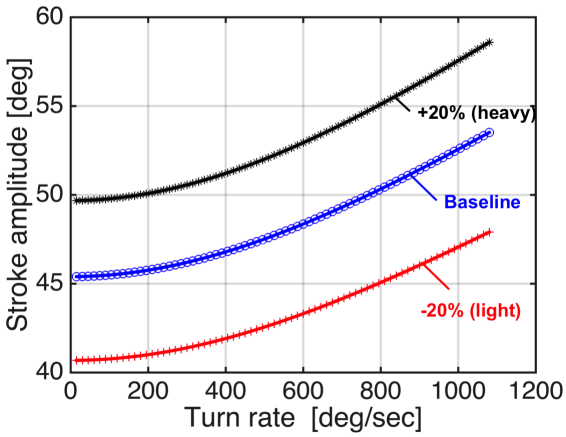

(d) Stroke Amplitude ϕ_{max_2} for Various Weights

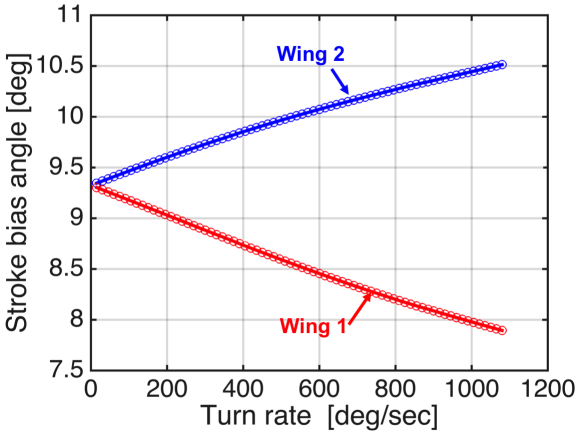

(e) Stroke Phase Offset ϕ_{off} for Both Wings, Baseline

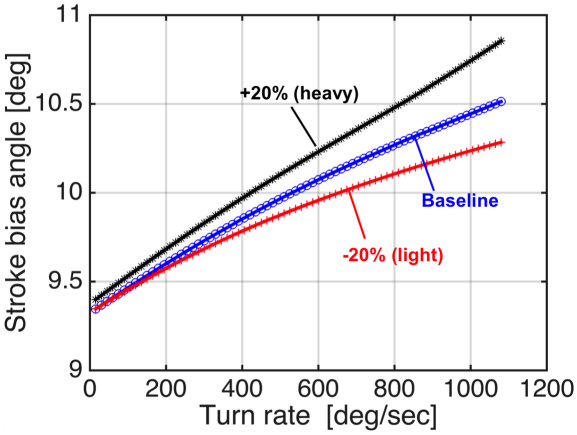

(f) Stroke Phase Offset ϕ_{off_2} for Various Weights

Figure 7.46: Variation of (a) Stroke Plane Tilt (b) Stroke Amplitude and (c) Stroke Phase Offset at Various Turn Rates, Flight Speed = 0.5 m/s.

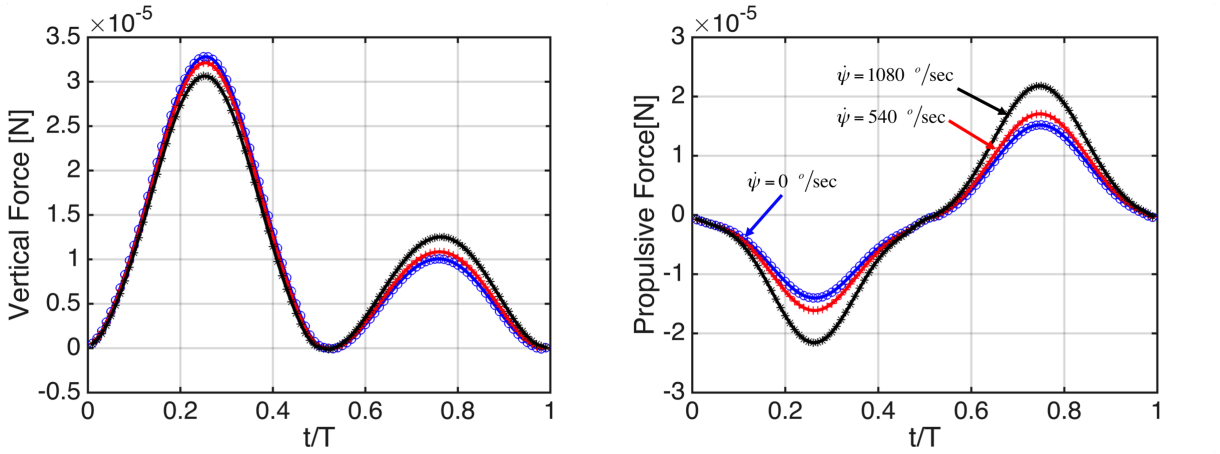

(a) Vertical Force

(b) Propulsive Force

(c) SideForce

(d) Aerodynamic Power Required

Figure 7.47: Variation of (a) Vertical Force , (b) Propulsive force, (c) Side Force and d) Aerodynamic Power Required within a Flap Cycle at Various Turn Rates; Flight Speed = 0.5 m/s.

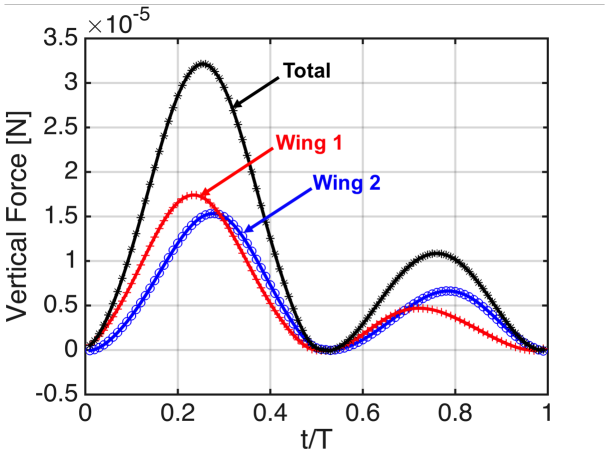

(a) Vertical Force

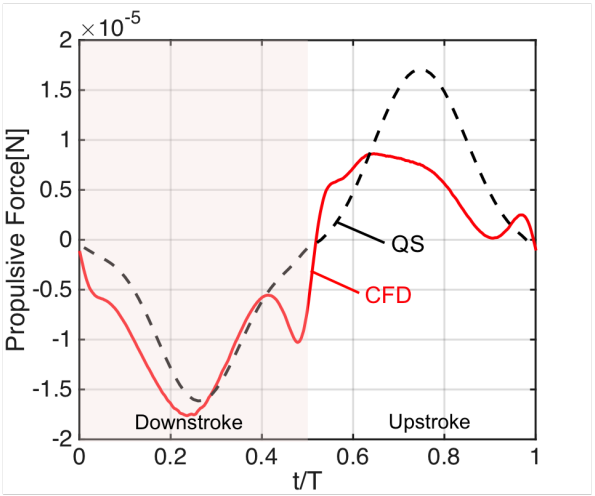

(b) Propulsive Force

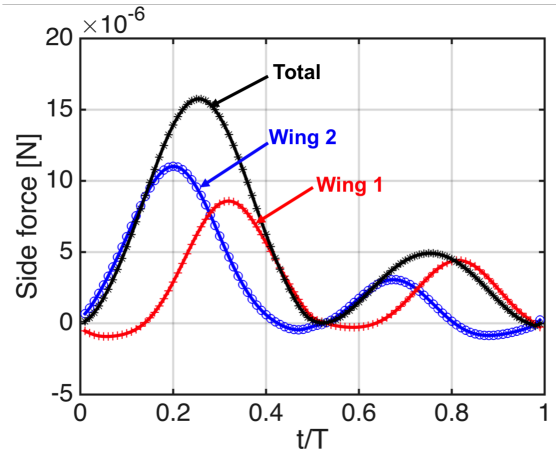

(c) SideForce

Figure 7.48: Variation of (a) Vertical Force , (b) Propulsive force and (c) Side Force within a Flap Cycle at Turn Rate of $540 deg/sec$; Flight Speed = 0.5 m/s.

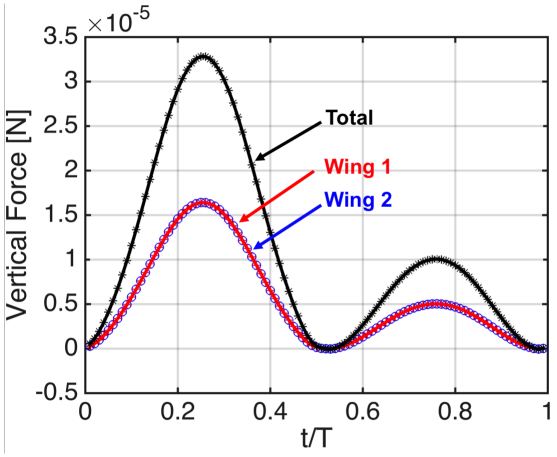

(a) Vertical Force

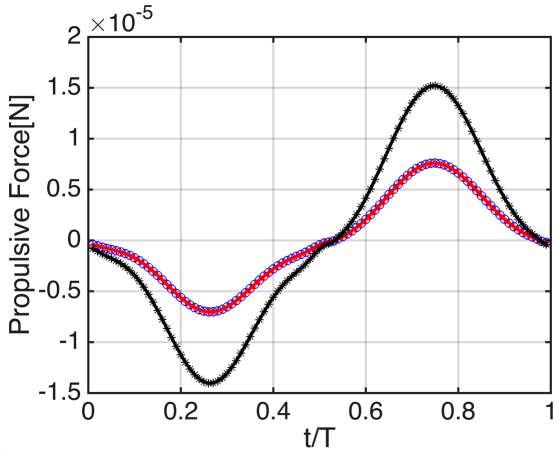

(b) Propulsive Force

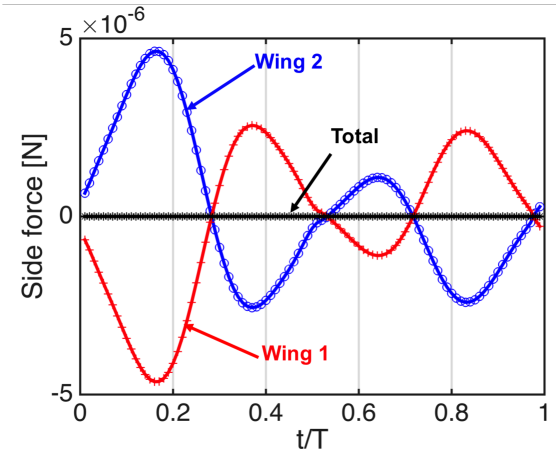

(c) SideForce

Figure 7.49: Variation of (a) Vertical Force , (b) Propulsive force and (c) Side Force within a Flap Cycle at Turn Rate of 0 deg/sec (forward flight); Flight Speed = 0.5 m/s.

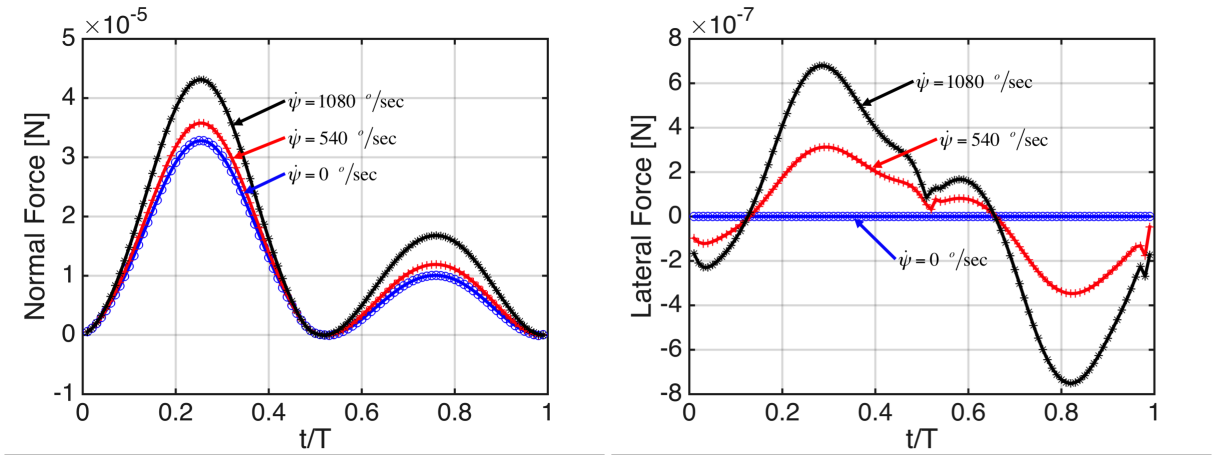

(a) Normal Force

(b) Lateral Force

Figure 7.50: Variation of (a) Normal Force and (b) Lateral Force within a lap-cycle at various turn rates; Flight Speed = 0.5 m/s.

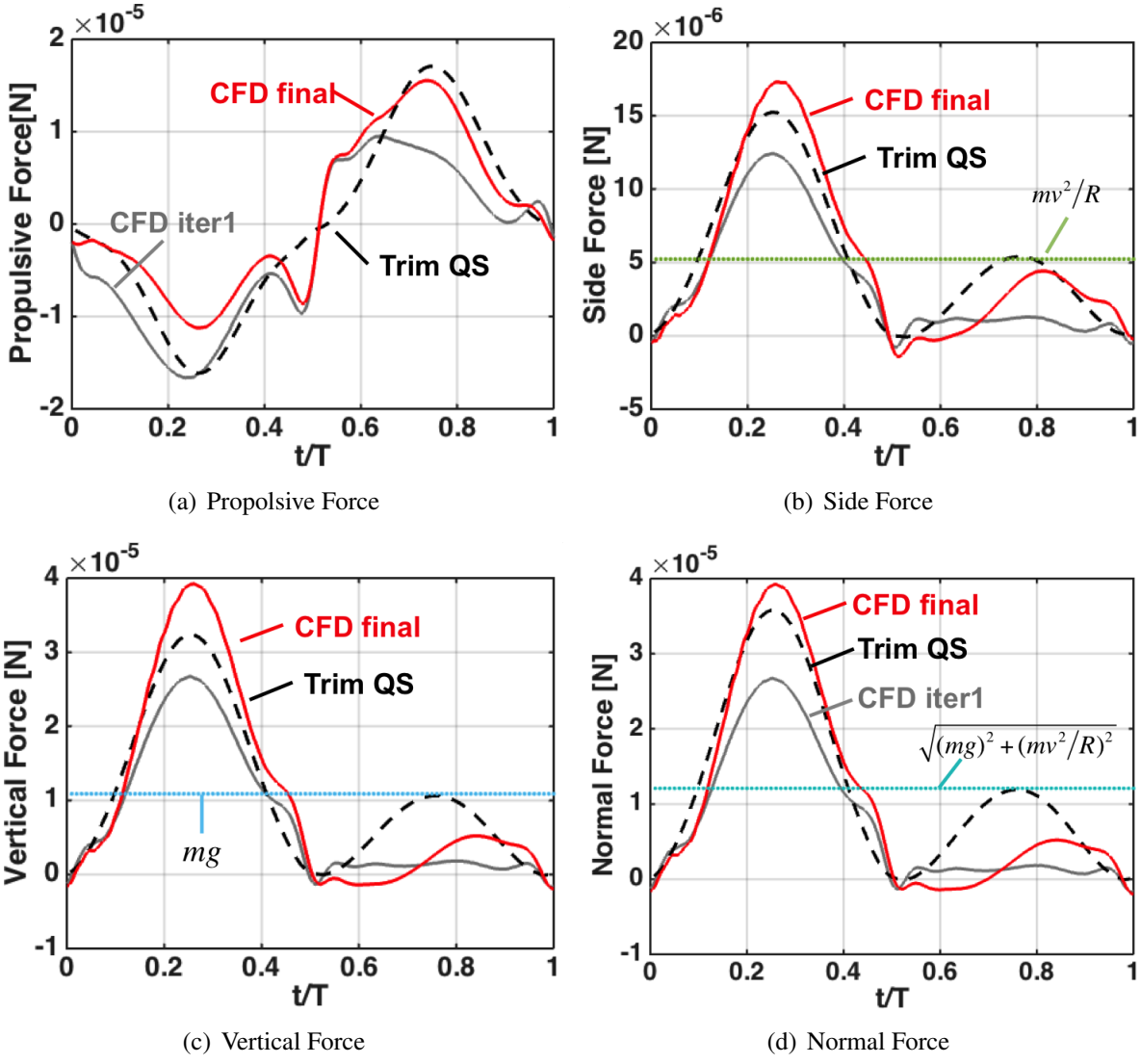

(a) Propolsive Force

(b) Side Force

(c) Vertical Force

(d) Normal Force

Figure 7.51: a,b,c : Variation of the forces within a flap cycle in the inertia frame at turn rate of $540 deg/sec$ and flight speed = 0.5 m/s; d: Normal force in the body frame.

7.5 Summary

Studies on a flapping-wing insect were conducted in trimmed hover and steady forward flight. A loose coupling strategy between the QS model with CFD was used to achieve rapid trim convergence within practical computational times while maintaining the high-fidelity of the simulations. The wing kinematic trim variables were studied as a function of forward flight speed and body incidence angle. Specific conclusion drawn from the study regrading the trim algorithm are discussed here.

The trim variables and aerodynamic loads are related and the following observations were made in forward flight

1. The balance in the z direction is dominated by half peak-to-peak stroke amplitude (ϕ_{max}) while the balance of drag in the x direction is mostly obtained by the change in the stroke plane angle (β). The pitch moment is primarily affected by the stroke bias angle (ϕ_{off}) and the stroke plane angle (β).

2. The stroke plane angle (β) increases (tilting the flapping stroke forward) with respect to the yz plane with an increase in forward speed. This angle is related to the ability to produce positive thrust during the upstroke.

3. The positive vertical force on the wing during the downstroke results from the wing lift and LEV, whereas during the upstroke positive thrust is produced primarily as a consequence of the wing drag (due to LEV).

4. At hover, the wing kinematics parameters produce linearly independent force and moment

components in the longitudinal plane. In forward flight, cross-couplings manifest between the individual wing kinematics parameters and the longitudinal forces and moments. Thus, the one-to-one correlation between forces and individual controls that exists at hover, is lost in forward flight.

5. At zero body pitch attitude, the body forces and pitching moment are negligible in comparison to the wing forces, except for drag at the higher forward flight speeds.

6. In the two-wing *diptera* configuration, equilibrium in forces and moments about the center of gravity (CG) was achieved through the variation in wing kinematics. In hover, the flapping strokes (upstroke and downstroke) are symmetrical, but because of the offset in the CG location from the mean centerline, the flapping stroke is slightly tilted to the horizontal line at roughly $\beta = 0.7$ degrees. This result from trim analysis agrees well with observed hovering flights of flies in nature.

7.5.1 Forces, Power and Wake Structure in Hover

- Wake: In hover, the wing wake convects downwards under the flapping stroke because of the vertical induced inflow from the shed vortices, which separate mainly from the tip, forming a trailed shed tip vortex, and from the root, forming a trailed shed root vortex.

- Forces:

    1. Because of the roughly horizontal stroke plane, the vertical force is similar in magnitude and trend during the downstroke and upstroke, and the horizontal force is equal in

magnitude with opposite trends.

2. During the translational portions, the peak in force is obtained around mid-downstroke/upstroke, where the rotational velocity is the maximum.

3. The local distribution of the vertical thrust (lift) along the span during the translational portions is "tip dominated", i.e., the force profile increases from wing root toward wing tip reaching a maximum at approximately 80% of the wing span at mid-downstroke/upstroke. This behavior is similar to the local vertical force obtained in hovering rotor blades as seen in rotorcraft.

- Power:

1. Required aerodynamic power can be divided into two components, i.e., shear force and pressure force.

2. The power due to the shear forces are nearly zero during the transition portions (t/T= 0.5, 1), and non-zero during the translational portions due to the formation of a boundary layer.

3. The aerodynamic power is mostly dominated by pressure forces. While the shear component of the total power may be relatively small, it cannot be neglected from the analysis.

4. It can be assumed that the aerodynamic power due to pressure is equivalent to induced power, and the profile power is equivalent to the power due to shear forces.

5. The local distribution of the power along the span during the translational portions are

also “tip dominated”, i.e., the power curve increases from wing root toward wing tip, to reach maxima at approximately 85% of the wing span at mid-downstroke/upstroke.

7.5.2 Forces, Power and Wake Structure in Trimmed Level Flight

- Wake: In trimmed level flight of 1 m/s, the wings wake convect backwards and downwards, with an increase in the vortical shed wake at the transition regime between downstroke to upstroke. The vorticity is shed from the wing from the tip and the root, forming tip and root trailed vortices.

- Forces:

    1. The majority of the required vertical force to balance the vehicle weight is obtained during downstroke, due to formation of the LEV and the circulatory lift. During the upstroke, the vertical force generated is minimal. Furthermore, the LEV is considerably smaller than the one obtained during downstroke.

    2. The two-wing *diptera* configuration in forward flight tilts its plane forward similar to rotary wing in level trimmed flight.

    3. During the translational portions, the peak force is obtained around the mid-downstroke where maximum resultant velocity was observed.

    4. During the transition from downstroke to upstroke, a local peak in vertical force is obtained because of the rapid rotational forces.

    5. The local distribution of the vertical thrust (lift) along the span during the translational

portions, is different than obtained in hover. The force profile increases rapidly from 35% span to reach a maxima at approximately 60% of the wing span at mid-downstroke and subsequently decrease towards the tip.

- Power:

  1. Required aerodynamic power can be divided into two components, one due to shear forces and one due to pressure forces. The required aerodynamic power is larger during downstroke than upstroke, where the main difference is in the power due to pressure forces; it is significantly smaller during upstroke.

  2. The power due to the shear forces are nearly zero during the transition portions (t/T= 0.5, 1), and non-zero during the translational portions due to the formation of a boundary layer.

  3. The local distribution of the power along the span during the translational portions, is similar to the vertical force distribution. The power profile is zero from the wing root to approximately 30% span, and then increases to reach a maxima at approximately 70% of the wing span at mid-downstroke and decreases after that toward the tip.

7.5.3 Trimmed Coordinated Turn

The quasi-steady flight dynamics model has been expanded to account for turning flight and some sample results have been demonstrated. The CFD solver and the delta-coupling approach were expanded and verified for level turning flight.

1. Turn coordination allows the flapping-wing vehicle to maintain a wider range of turning rate and turning radius. Without the appropriate roll attitude, the body cannot overcome centrifugal loads associated with higher airspeeds and rates of turn.

2. In a coordinated turn, the load factor increases according to $\sec\phi_B$, indicating that a faster turn rate may have trim characteristics similar to a heavier MAV in level. When the turn radius is significantly larger than the wing span, the variation of trim kinematics with load factor is similar to that observed for increasing weight. For example, the flap stroke amplitude (ϕ_{max}), a measure of force magnitude, increases with increasing turn rate.

3. Flap stroke bias (ϕ_{off}) is incrementally different between the two wings. This difference helps balance the body moments in a steady level turn, since the effective dynamic pressure of the outboard wing is marginally higher.

4. The stroke plane tilt of the wings decreases with increasing turn rate. This plane tilt angle represents the ratio of propulsive force to vertical force as resolved in the insect body axes. In a coordinated turn, the centrifugal force is overcome by increasing the total lift and rolling the body. To maintain the same propulsive force, the plane tilt is decreased to achieve trim.

5. The CFD forces do not match exactly with those generated by the quasi-steady model for the same wing kinematics. The quasi-steady model over-predicts the forces as compared to CFD.

6. CFD predictions of the force time history over one flap cycle are qualitatively similar to those obtained from the reduced-model, especially during the down-stroke. During the upstroke,

the vertical and side force are over-predicted by the reduced-order model, which is due to the wake interactions that are not accounted for by quasi-steady aerodynamics.

Chapter 8

Summary and Conclusions

An unsteady, three-dimensional, Navier–Stokes solver (OVERTURNS) was used to simulate insect flight with two flapping wings (*diptera* configuration). The OVERTURNS computational platform was extended to include insect-like kinematic simulations by adding the appropriate mesh motion terms to describe the wing flapping pattern. A nested overset mesh system was used to capture the flow physics, such as the leading edge vortex, viscous boundary layer, flow separation, and shedding of vorticity. To ensure that the OVERTURNS platform can accurately capture the flow around flapping wings at low Reynolds number, the solver was validated and verified for: 1. Laminar flow over a sphere, 2. An impulsively translated wing, and 3. An isolated wing undergoing unsteady motion.

A parametric study of a flapping wing was conducted to formulate efficiency metrics for flapping wings, and to investigate the effect of kinematic parameters on the resulting thrust and flow field characteristics. These efficiency metrics were determined by studying the averaged forces and power for different pitch angles over a range of Reynolds numbers. The CFD results were compared against the quasi-steady (QS) aerodynamic model predictions.

Studies on a flapping-wing insect were conducted in trimmed hover and steady forward flight. A loose coupling strategy between the QS and CFD models was used to achieve rapid trim convergence within practical computational times while maintaining the high fidelity of the simu-

lations. The wing kinematic trim variables were studied as a function of forward flight speed and body incidence angle. Specific key conclusions drawn from the parametric study and developments of the trim algorithm are discussed here.

8.1 Conclusions and Specific Contributions

- **Efficiency metric**: For fixed wing, where velocity is uniform and power is the product of integrated drag and velocity, L/D is equivalent to L/P. However, this relation does not hold for flapping or rotating wings where the velocity is time-varying and non-uniform along the wing span. It can therefore be concluded that to compare between flapping wings with different kinematics or geometrical parameters as well as to other micro-air vehicles, power loading as a function of averaged lift (L/P vs. L_{avg}) is more appropriate as an efficiency metric than is the L/D ratio. The proposed metric properly accounts for the required aerodynamic power and vertical thrust as a function of prescribed kinematics. The ratio L/P versus lift can be used to determine the performance. Power and vertical thrust are the key parameters for design and performance. In terms of efficiency metrics, the QS model fails to predict the values obtained by CFD, especially when L/D is considered. This results from the inadequate modeling of the unsteady mechanisms in the QS model. One specific outcome of the analysis is the conclusion that for the given flapping frequencies ranging from 100-300 Hz, a pitch angle of 40 degrees has a clear advantage over pitch angles of 30 and 60 degrees in terms of L/P versus lift.

- **Wake and induced inflow**: The flowfield dynamics of flapping wing were affected by the

wing pitch angle as well as the Reynolds number. For a given Reynolds number the LEV size, as well as the shed and trailed tip and root vortices, were more dominant for larger mid-stroke pitch angles. The formation of a LEV and vortical wake resulted in an enhancement of the lift force, but was limited to a pitch angle of up to 45°. For pitch angles larger than 45°, the drag component of the LEV becomes more significant when compared to the lift component, leading to low L/P ratio as well low L/D ratio. The vortical wake around the wing that resulted from the shed and trailed tip and root vortices had a significant effect on the forces through the effect of induced inflow. The induced inflow impacts the effective angle of attack experienced by the wing; this impact is a reduction in effective angle of attack, which might explain the 3D stability of the LEV during the translational portions. The effective angle of attack expanding by the was at least 15° lower than the geometrical angle of the wing.

- **Trim analysis**: A multi-fidelity approach for obtaining CFD-coupled trim solutions was adapted from rotary-wing analysis and applied to a flapping wing platform. Using a judicious number of CFD calculations to correct the quasi-steady aerodynamics so that trim is obtained with the CFD aerodynamics; thus, the detailed flowfield models can be incorporated into the analysis without incurring prohibitive run times. Wing flapping kinematics and longitudinal aerodynamic loads are cross-coupled in forward flight, i.e. one kinematic parameter affects multiple force/moment components and the sensitivity depends on the operating conditions (non-linearity). The methodology employed here considers the cross-coupling between these variables. The quasi-steady model is capable of obtaining qualitatively accurate and quanti-

tatively representative of the integrated wing loads and the trim Jacobian (i.e., sensitivity of airloads to the wing kinematics parameters), providing a good initial condition for the coupled process. The quasi-steady model is capable of obtaining reasonable representations of the integrated wing loads and the trim Jacobian, providing both a good initial condition for the coupled process and a stable matrix for the Newton-Raphson iterations. However, this simplified model over-predicts the wing lift and under-predicts power required, and cannot capture unsteady effects during wing rotation between the up-stroke and down-stroke. CFD is therefore required for the quantitatively accurate predictions of aerodynamic power and trim kinematics that are crucial for selection of wing geometry, battery, and determination of the actuator torque required and the vehicle flight envelope restrictions.

- **Forward flight**: The key feature in steady forward flight is that the flapping stroke plane is tilted forward, which leads to asymmetry in the forces produced and the power required during during the downstroke and the upstroke. The majority of the vertical thrust is produced during the downstroke, while the positive propulsive force is produced during the upstroke. The required aerodynamic power is larger during the downstroke, mostly due to the pressure drag resulting from flow separation presence of a LEV. The power required due to the shear forces is nearly zero during the supination and pronation because the LEV detaches and the flapping velocity slows down to zero, and non-zero during the translational portions due to the formation of a boundary layer.

The main contributions of this study to the further development of flapping wing MAVs, can be summarized as two key contributions:

1. A new efficiency metric is proposed. It is recommended evaluate designs based on the L/P ratio versus average lift to enable comparison between different platforms.

2. An alternative computationally efficient approach for trim analysis on insect-like flapping wing kinematics, has been developed and demonstrated.

8.2 Recommendation for Future Work

The research presented in this dissertation has demonstrated the use of a CFD computational platform coupled to a quasi-steady aerodynamics trim algorithm based on a loose coupling strategy. While the trim algorithm was successfully applied to obtained trimmed variables where the system satisfies the trim conditions of moments and forces, there are several issues that need to be addressed to improve its capabilities and applicability to a wide range of insect flight modes. This section will suggest ways in which these research findings may be leveraged in future work.

1. The CFD-QS trim coupled algorithm is computationally efficient when run on the HPC facilities. However, the computational cost can be further reduced by running the entire analysis on one or more GPUs. The current implementation uses a hole-cutting method to exchange information between multiple overset meshes that runs serially, incurring a high computational cost. Using a different method that can handle the data transfer in parallel will ultimately lead to a reduction in the computational time.

2. The kinematics pattern used in this study are combined from two simple harmonic functions. Various kinematic patterns can be investigated using the trim algorithm to optimize for power

reduction, maximum vertical thrust or greater horizontal thrust, during upstroke in forward flight. Examples of various kinematic patterns include figure-of-eight and asymmetrical flapping strokes (e.g., advanced and delayed rotation).

3. The present study uses a body angle of zero degrees with respect to the horizontal axis. In nature wing kinematics and body angle are most likely linked by the insect biology. This constraint can be added and investigated, which might affect the moment balance and possibly alter the CG location.

4. The trim algorithm, simplified model QS , and CFD should be coupled to a Structural Computational Dynamics (CSD) model to accurately represent the fluid/structure interactions that are present in these flexible wings. This additional capability will allow for the investigation of the effects of large deflections of flapping wings on both the aerodynamic performance and overall wake structure.

5. The high fidelity CFD solver can be used to study different flight features observed in biological insect flight, e.g. the effect of gusts on flapping wings.

Appendix A: Trim Jacobian

The trim Jacobian represents the sensitivity of the time-averaged longitudinal aerodynamic loads (propulsive force, vertical force and pitching moment) to the wing trim kinematics, and is given in Eqn. A.1.

$$J = \begin{bmatrix} \frac{\partial F_x}{\partial \phi_{\max}} & \frac{\partial F_x}{\partial \phi_{\text{off}}} & \frac{\partial F_x}{\partial \beta} \\ \frac{\partial F_z}{\partial \phi_{\max}} & \frac{\partial F_z}{\partial \phi_{\text{off}}} & \frac{\partial F_z}{\partial \beta} \\ \frac{\partial M_y}{\partial \phi_{\max}} & \frac{\partial M_y}{\partial \phi_{\text{off}}} & \frac{\partial M_y}{\partial \beta} \end{bmatrix} \tag{A.1}$$

If CFD is used to compute the trim Jacobian, the computational cost is 3 Million times larger compared the reduced-order model. Therefore, the present approach utilizes the quasi-steady aerodynamic model with *delta* corrections to drive the dynamics towards non-accelerating flight by adjusting the wing kinematics. For this multi-fidelity approach to achieve trim, the approximate Jacobian must be qualitatively and quantitatively representative of the *actual* trim Jacobian. This appendix provides numerical values of the trim Jacobian as obtained from the quasi-steady model and the CFD model at hover. Each of the trim variables was increased by 2%, the steady-state stroke-averaged loads were obtained from the two aerodynamic models and forward differences were used to compute the matrix in Eqn. A.1.

The quasi-steady (CFD) trim kinematics are $\phi_{\max} = 45.31^\circ$ (58.7°), $\phi_{\text{off}} = 8.89^\circ$ (11.98°) and $\beta = 0.0^\circ$ (0.79°). Trim Jacobians based on quasi-steady aerodynamics and CFD are given by

$$J_{QS} = 10^{-6} \begin{pmatrix} 0.0 & 0.0 & -0.1901 \\ -0.4830 & 0.0 & 0.0 \\ 0.0 & -0.0004 & 0.0001 \end{pmatrix} \tag{A.2}$$

$$J_{CFD} = 10^{-6} \begin{pmatrix} 0.0054 & 0.0044 & -0.1921 \\ -0.4156 & 0.0 & 0.0 \\ 0.0 & -0.0004 & 0.0001 \end{pmatrix} \tag{A.3}$$

$$J_{QS+\delta} = 10^{-6} \begin{pmatrix} 0.0055 & 0.0011 & -0.1921 \\ -0.3722 & 0.0 & 0.0008 \\ 0.0 & -0.0012 & 0.0001 \end{pmatrix} \tag{A.4}$$

Based on the numerical values of each of the trim Jacobian entries at hover, the following conclusions can be drawn:

- Propulsive force F_x depends dominantly on stroke plane tilt β
- Vertical force F_z is affected by stroke amplitude ϕ_{max}
- Pitching moment M_y is sensitive to the stroke phase offset ϕ_{off}
- The Jacobian obtained from the QS model (for both sets of reference kinematics) is a good approximation to that obtained from CFD. The additional cross-couplings between stroke amplitude and propulsive force/pitching moment are a result of non-zero stroke plane tilt for the CFD-coupled solution. To verify this dependence, the trim Jacobian was generated using the quasi-steady model using the CFD trim solution as the reference condition and is given in Eqn. A.4.
- The dependence of propulsive force on stroke plane tilt and stroke amplitude is very well predicted by the quasi-steady model. The dependence of vertical force on stroke amplitude

is also well represented by the quasi-steady model.

Appendix B: Loose Delta Coupling

The trim algorithm use delta loose coupling method, where the delta forces and delta moments are calculated and applied to the re-trim process. For illustration a simplified trim algorithm is shown in Fig. B.1. The delta-correction defined as: $\delta f_{w(t)} = f_{w(cfd)} - f_{w(QS)}$, the dimensional forces in the wing frame (Fig. B.2) for each wing are scaled by the same dynamic pressure that QS model is using. The difference between CFD and QS forces coefficient in the wing frame called "delta force coefficients": chord-wise, span-wise and normal forces coefficients ($\delta C_t(t)$,δC_r, $\delta C_n(t)$). Where $\delta C_t(t) = C_{t(cfd)} - C_{t(QS)}$, $\delta C_r = C_{r(cfd)} - C_{r(QS)}$ and $\delta C_n = C_{n(cfd)} - C_{n(QS)}$, the delta of each force coefficient is time dependent, and it will be added as a correction to the forces coefficient from the quasi steady in the retirm process.

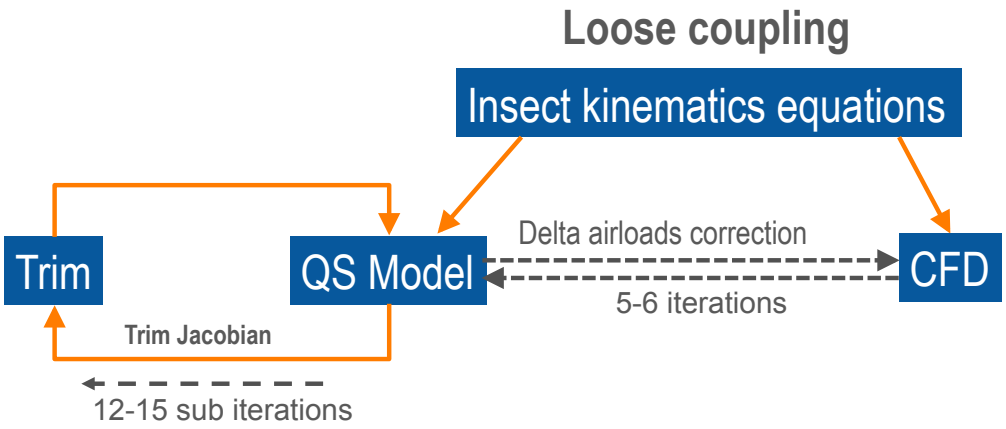

Figure B.1: The trim algorithm flow chart.

The new forces and moments are calculated now from the corrected force coefficient from previous step where $C_t(t) = C_{t(QS)} + \delta C_t(t)$, $C_r(t) = C_{r(QS)} + \delta C_r(t)$ and $C_n(t) = C_{n(QS)} + \delta C_n(t)$. For trim analysis flapping-cycle averaged X, Z, M in the body frame are considered, and the new corresponding trim variables are obtained using the trim algorithm described in Fig. B.1.

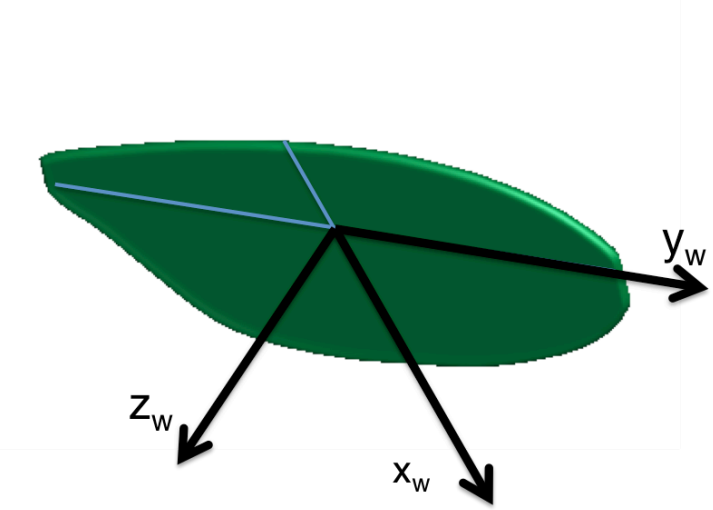

Figure B.2: The wing coordinated system.

The time variant delta coefficients for C_t, C_r and C_n, is added to the coefficient from the QS model for each wing, at every time step the trim code loop runs $\vec{C}_w(t) = \vec{C}_{w(QS)} + \vec{\delta}C_w(t)$.
The next step is to obtain the new trim variables, as mentioned in the trim algorithm. The process of retrimming and then running the CFD simulations are repeated until convergence is obtained. Convergence of the process is achieved when the trim conditions are satisfied and the trim variables change in a minor way and further more implies that the delta force coefficients become unchanged.

Figures B.3-B.5 show the delta-correction time histories in the normal, chordwise and spanwise direction at the 6 iterations for the case of level flight of 1 m/s. Every iteration represents the trim process and CFD simulation. The delta-coefficients show that the larger change between CFD and QS occurs at the first iteration. but after 3 iteration, the change between the delta forces becomes minor.

Convergence of the process will be achieved when: 1. The latest delta coefficient will be equal to the pre- vious delta, L2 norm of this change is applied to check this change, 2. the CFD

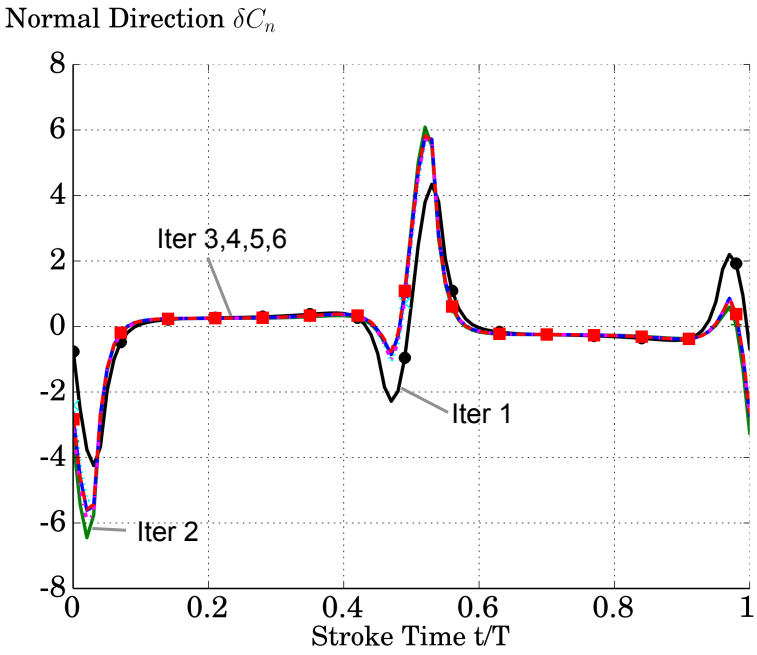

Figure B.3: Delta correction in the normal direction for the retrim iterations, u= 1 m/s.

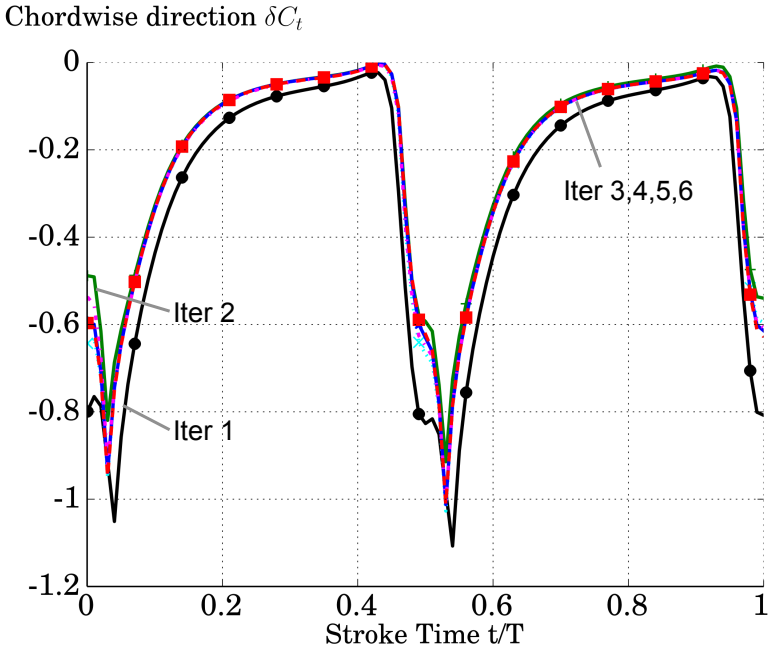

Figure B.4: Delta correction in the chordwise direction for the retrim iterations, u= 1 m/s.

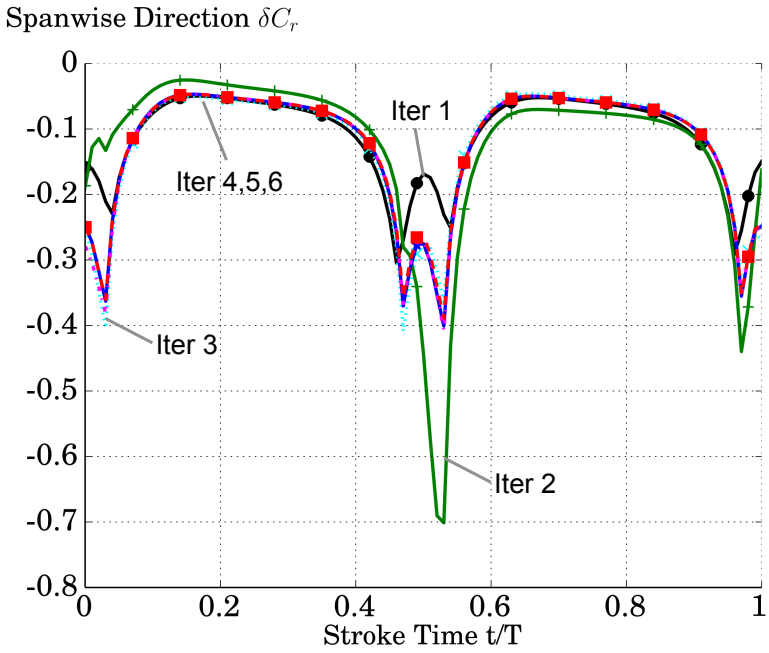

Figure B.5: Delta correction in the chordwise direction for the retrim iterations, u= 1 m/s.

averaged forces satisfy the equilibrium conditions, and 3. as a result of previous conditions change in trim variables will be minor.

Appendix C: Body Modeling

This chapter divided into two sections. First section investigates the effect of insect body shape and angle of incidence on the aerodynamic forces in forward flight. The insect body shape was compared with both a sphere and ellipsoid, and it was shown that an ellipsoid shape provides a reasonable approximation for the insect body as compared to a sphere, and the analytical correlation of drag and lift as a function of body angle of incidence and Reynolds number can be used in a quasi-steady evaluation of the forces. In the second section, the kinematic variables are obtained in trimmed hover and steady forward flight at different body angles of incidence. Using a loose coupling procedure where the quasi-steady model based on reduced-order aerodynamics is coupled to the OVERTURNS CFD solver to achieve insect body trim in practical computational times. The trimmed kinematics variables are the stroke amplitude ϕ_{max}, stroke flapping bias ϕ_{off} and the stroke plane angle β. It was observed that the wing kinematic variables are strongly dependent on the body angle of incidence (especially the flapping offset angle), and is a key feature in optimizing the flapping based MAV design.

C.1 Insect Body Modeling

The aim of this section is to identify a mathematical model that can serve as a close approximation to that of the insect body to predict the lift and drag coefficients as a function of the Reynolds number and angle of incidence to be used in the QS model. Such a goal to model the insect body shape can be achieved using multiple pathways. One approach can be to perform direct numerical simulations (DNS) simulations to obtain the required data, but simulating the flow

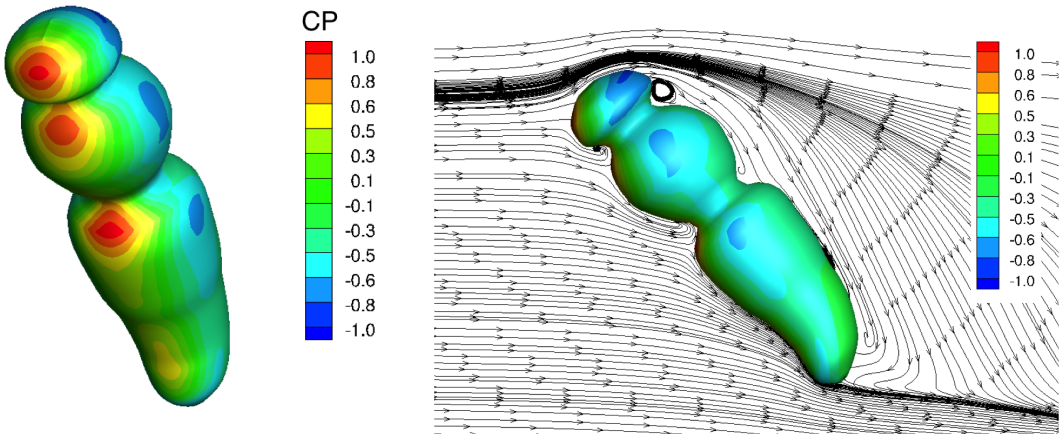

(a) Pressure coefficient on the body surface

(b) Flow stream-lines on the xz plane that cross the body CG

Figure C.1: (a)The pressure coefficient contours on the body surface at Reynolds number 300, (b) Streamlines cross the body parallel to xz plane

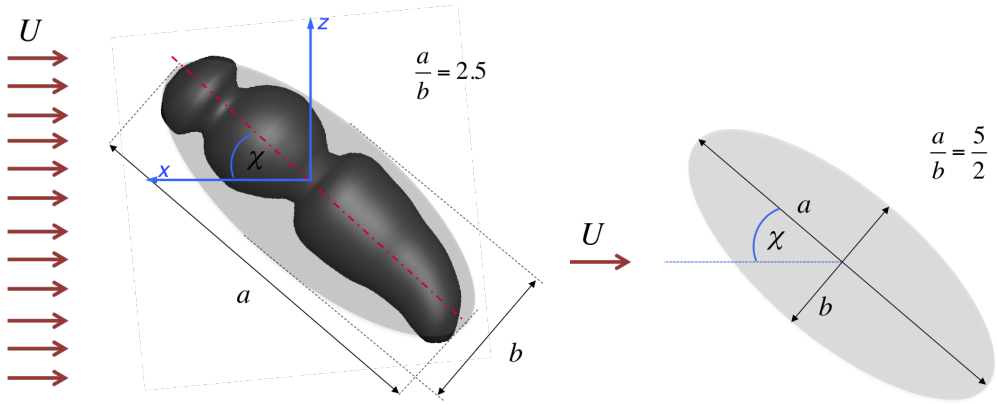

(a) Insect body shape

(b) Ellipsoid 1

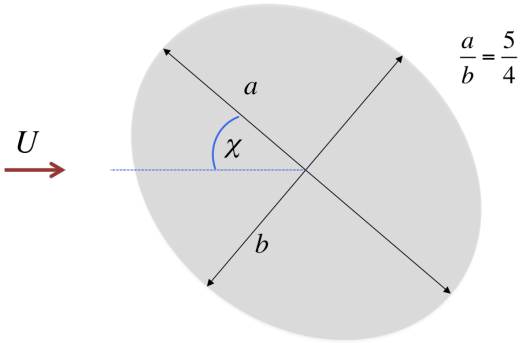

(c) Ellipsoid 2

Figure C.2: Blunt body shapes: (a) Insect body shape(fruit fly), the light gray represent the ellipsoid that can replace the insect shape (b) Ellipsoid 1 and (c) Ellipsoid 2 as given in the Ref. [11]. χ is the angle of incidence, and U is free-stream velocity component as seen in the body axis system

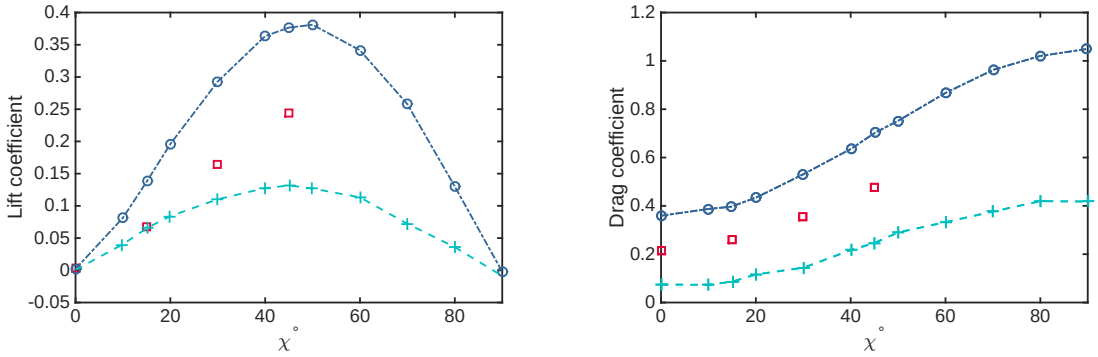

(a) Lift

(b) Drag

Figure C.3: Lift and drag coefficients as a function of angle of incidence (χ) of blunt bodies at Reynolds number 300. Ellipsoid 1 and 2 are obtained from Zastawny et. al correlation [11], the body insect results represent DNS simulations of insect body shape body shape(current study).

around body shape for a range of Reynolds numbers and body angles of incidence can be computationally consuming. The other approach is taking advantage of different studies that have been performed on blunt bodies at low Reynolds number and examine which approximation (if any) might be appropriate for the present scenario.

To identify a potential body of revolution to represent an insect body, simulations of the isolated body were conducted at two Reynolds number (140 and 300) at four different angles of incidence (0, 15, 30, and 45 degrees), as shown in Fig. C.2(a). Such a study can help identify the trends in lift and drag forces and the characteristic features observed in the flow field. The insect body shape has typical anatomical features of a fruit fly with three main parts, i.e., the head, thorax and abdomen. Figure C.1 shows the flowfield around the insect at a body incidence of 45° and Reynolds number of 300. Figure C.1(a) shows the surface pressure contours, where there are three stagnation points obtained on the front side of the body, where Cp is 1 in accordance with predictions from Bernoulli's law. Streamlines around the body are shown in Fig. C.1(b), and it was observed that the stream-lines remain attached to the body surface and there is no major flow separation or dominant vortical structures in the flow field. Similar behavior was observed at other body incidence angles and Reynolds numbers considered in this study. The drag coefficient obtained for the different incidence angles at Reynolds number of 300 were between 0.2 for $\chi = 0^\circ$ and 0.48 for $\chi = 45^\circ$. The lift and the drag coefficient converged in asymptotic behavior and are not shown here in the interest of brevity. The convergence criteria was determined as the flapping cycle when the change in the forces was less than 0.5% through the cycle.

Many studies have been conducted in the past focusing on the lift and drag of blunt bodies operating in low Reynolds numbers flows, such as a sphere, cylinder, ellipsoid and airfoil. Considerable work has been done on identifying the flow features past a sphere. Qualitatively and quantitatively analysis of the flow was experimentally performed by Taneda [7] including drag coefficient, location of the flow separation point, wake streamlines and the center of resulting vortices as a function of Reynolds numbers. The flow around a sphere is characterized by large scale vortical structures being shed over the sphere where the flow separates (for Reynolds number greater than 300). The typical drag coefficient of a sphere at Reynolds number order magnitude of 10^2 is 1. Therefore, a sphere might not provide the best approximation for the insect body.

The insect body more closely resembles an ellipsoid as shown in Fig. C.2. Zastawny et al. [11] derived an analytical correlation for the drag and lift coefficients for different bodies shapes as a functions of Reynolds number, angle of incidence and shape. They investigated non-spherical shapes such as ellipsoid, disc and fiber. The disc and fiber are not considered in the current study as these shapes are far from that of the insect body. The reference study [11] focused on two ellipsoids with the parameter a/b (ratio between the major axis a and the minor axis b of 2.5 for Ellipsoid-1, and 1.25 for Ellipsoid-2, as shown in Figs. C.2(b) and C.2(c).

The lift and drag coefficients from the current study are shown in Fig. C.3 along with the results that were obtained from the correlation of Zastawny. The non-dimensional forces lie between those of Ellipsoids-1 and -2 with a similar trend in the forces being predicted. The reason for this result can be explained by looking at the insect body, which can be encapsulated by an ellipsoid with a a/b ratio of 2.5, as shown in Fig. C.2(a). However, the insect is not a perfect ellipsoid and

the convex contours over the insect body contribute to the creation of small vortices, which affect the force coefficients; see Fig. C.1. The stream-lines around the ellipsoid stayed attached similarly for $\chi = 40$ similar to the streamlines around the insect body. Despite the difference in the values of the forces, as a first level approximation, representing the insect body as an ellipsoid would capture the appropriate behavior of the flow that an insect body would experience at low Reynolds numbers. Further studies will investigate the formulation of a mathematical model that could be used for various insect body shapes.

C.1.1 Body Forces

The insect body assumed in this study to be fixed with body angle of zero pitch attitude (relatively to x axis in the body system). The forces around the body are calculated but they are not considered in the trim analysis because they are small in comparison with the wings forces. Table. 4 summarizes the loads obtained from the body for different forward speeds. The dominant force is the drag, it is small relative to the insect weight; with increasing forward speed the drag increases and should be considered in the trim. A very small amount of lift is produced; with forward speed increases Z force increases, but the largest Z force at 1 m/s case is 0.56% of the required force. The stream lines around the body mid-section. There is no separation, and small vortices are created at joints between the insect body parts, and the wake from the wings has very minor interaction with body.

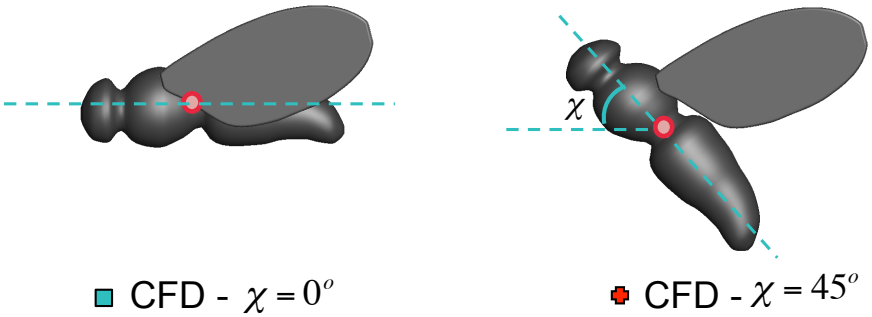

(a) Insect body at angle 0° (b) Insect body at angle 45°

Figure C.4: The obtained trim variables from QS analysis for different body angles, includes the predicted data from CFD for two case, hover at

C.1.2 Hover and Steady Level Flight

The aim of this section is to analyze the effect of body angle (χ) on the considered control variables, i.e., β, ϕ_{off} and ϕ_{max}, for steady flight conditions in hover and forward level flight. Currently, the results of insect trim in forward flight were obtained both with isolated QS model and the coupled CFD-QS model. While the QS model cannot capture any unsteady effects currently, it helps in the understanding of the physics behind insect flight.

Figure C.5 shows the variation of the control angles against flight speed for different body incidence angles. The body forces in the analysis are presented in Table C.1. Note that in the CFD simulations, the insect body operates under the downwash from the wings. From the data in Table C.1, it was observed that the body drag (horizontal) and the body vertical force increase with body angle, χ, and that these forces are negligible compared to the forces produced by the wing (less than 2%), especially at low speeds. Therefore, at low speeds, the effect of the body can be largely ignored. The control variable that had the largest variation as a function of the incidence angle was the stoke offset angle (ϕ_{off}), which is expected as the primary role of ϕ_{off} is to balance

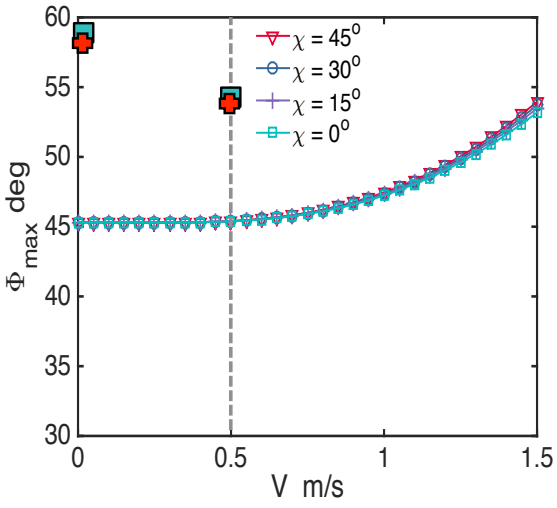

(a) Half peak-to-peak stroke amplitude angle

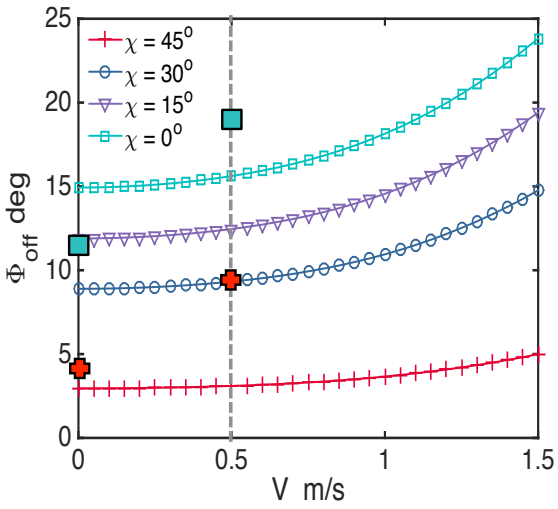

(b) Stroke flapping bias

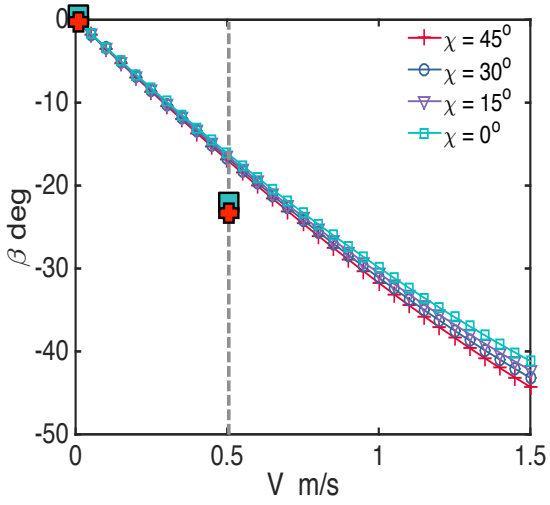

(c) Stroke plane angle

Figure C.5: The obtained trim variables from QS analysis for different body angles, includes the predicted data from CFD for two case, hover at

the pitching moment change caused by the change in incidence angle. In comparison, ϕ_{max} and β exhibit minor changes in response to different incidence angles as these variables are linked to the horizontal and vertical force, which do not change significantly with body angle. Furthermore, as the body angle increases for a given speed, the flapping stroke is shifted backward, which is reflected in the decrease in ϕ_{off}, as shown in Fig. C.5.

Table C.1: Body airloads in steady hover and steady level flight

Body Airloads		
CFD Results	X/mg %	Z/mg %
Hover (χ = 0°)	0.006	0.08
Hover (χ = 45°)	0.03	0.2
U = 0.5 m/s (χ = 0°)	1	0.8
U = 0.5 m/s (χ = 45°)	1.8	0.84

Note: mg is the insect weight ($1.0889 \times 10^{-5} N$)

Table C.2: Comparison of the trim control angles between QS model and CFD-QS coupled model

Hover (χ = 0°)			
	ϕ_{max}	ϕ_{off}	β
CFD-QS Coupling Trim	58.7	11.98	0.79
QS Trim	45.31	14.93	0
Hover (χ = 45°)			
	ϕ_{max}	ϕ_{off}	β
CFD-QS Coupling Trim	59.1	1.98	0.8
QS Trim	45.31	2.95	0
Forward Flight (χ = 0°)			
	ϕ_{max}	ϕ_{off}	β
CFD-QS Coupling Trim	54.4	19.01	-22.95
QS Trim	45.38	15.61	-16.07
Forward Flight (χ = 45°)			
	ϕ_{max}	ϕ_{off}	β
CFD-QS Coupling Trim	54.8	9.9	-22.5
QS Trim	45.4	3.1	-16.91

Note: All angles are in degrees.

For the insect flight in hover, the loose coupling procedure was performed where the corrected airloads from CFD were prescribed as "delta" corrections to the QS model to aid convergence of the control variables in trim. Four cases were investigated for this purpose; two in hover and two in forward flight (0.5 m/sec). For each flight condition, the body incidence angles (χ) of 0° and 45° were considered. It takes 5-6 coupling iterations to obtain convergence, the convergence in this case is the change in the control variables less than 5%. This condition is equivalent to that the "delta" forces not changing from iteration to the next.

The results are summarized in Tables C.2. Overall, a significant discrepancy in the control angles between the two procedures was observed. Such a result was expected as the simpler QS model will not capture the flow physics as accurately as CFD. However, for the hover cases performed, the difference in β between QS and CFD-QS was much smaller compared that to the discrepancy in ϕ_{off} and ϕ_{max}. While the angles of the QS trim analysis are not accurate, the trend in the control angles with a change in χ (see Fig. C.5) was reflected in the angles predicted by CFD-QS, lending further confidence in the developed QS model. The effect of χ on the control variables in forward flight was similar to the trend observed in hover, as shown in Table C.2, with ϕ_{off} changing significantly with a change in body incidence angle. The QS value of β is close to -16° and converges to a non-negligible (close to -22°) CFD-QS value in forward flight. As the forward speed of the insect increases, the flapping plane is tilted forward (β), to produce a positive thrust that balances the increased vehicle drag. Figure C.6 compares the instantaneous forces (horizontal and vertical) and the power required between steady forward flight and steady hover. These results were obtained at the end of the convergence cycles between CFD and QS

models. In hover, the upstroke and down-stroke was symmetric as can be seen in the vertical force, horizontal force and power, as expected. However, in forward flight, there was significant asymmetry in the observed instantaneous trends. The net force and moments balance the lift, drag and pitching moment of the wing, which manifests as an increase in the flapping plane incidence in forward flight; see Table C.2. Figure C.7 shows the average power required for steady level flight at different forward flight speeds as obtained using the QS model. The power was observed to first decrease as the flight speed increases, the trend of which is synonymous with a reduction in wing induced power. As the flight speed increases, the parasitic drag increases and the trend is reflected in the increasing power. Note that there was no change in the quasi-steady analysis for a variation in body angle. This result was attributed, partly, to the fact that the flat plate area of the body was not a function of body angle.

Most of the positive vertical force (Z) required for lift is produced in the down-stroke for forward flight. This vertical force balances the vehicle weight of the insect. The average of the integrated lift along the flapping cycle in forward flight and hover was equal under steady conditions. Note that this increased vertical lift during the down-stroke is also accompanied by an increase in power, whose origins lie in the drag force. The horizontal force (X) in hover and forward flight is divided into negative instantaneous force during down-stroke and positive instantaneous force during the up-stroke. In hover, these two portions were equal and opposite in direction such that net force in the horizontal direction was zero (trim conditions). In forward flight, the net force in the horizontal direction balances primarily the drag force, but the strokes are not symmetric because of the flapping plane tilt angle. At the end of pronation/supination when the wing undergoes reversal

(t/T= 0 or 0.5 or 1), higher frequency content was detected in the force and power histories, as shown in Fig. C.6.

The force production in forward flight results primarily from unsteady aerodynamic sources such as the circulatory lift contribution from the LEV and the wake. This persistent LEV causes a low pressure suction region on the upper surface of the wing, which results in the increased lift production seen in the time history of forces (see Fig. C.6(a)). The increased lift was also accompanied by an increase in drag, which causes the increased power required for flight during the down-stroke. In comparison, during the up-stroke and there was no evidence of a significant LEV. This lack of a sustained LEV was the cause of the reduced lift and drag production, as seen in Fig. C.6.

C.2 Conclusions

Studies on a flapping insect body-wing combination were conducted in hover and steady forward flight under trim conditions. Experiments were conducted using a single isolated wing in an oil tank and the forces were correlated with numerical predictions from OVERTURNS. A loose coupling was developed to interface a quasi-steady (QS) model with CFD to achieve rapid trim convergence in practical computational times while maintaining a high-fidelity of the simulations. Furthermore, based on CFD simulations, a simple model for the insect body was identified that could be incorporated into the quasi steady analysis in future works. Finally, the wing kinematic control variables were studied as a function of forward flight speed and body incidence angle.

The following specific conclusion were drawn from the study

1. The multi-fidelity approach, where QS calculation were combined with a limited number of CFD simulations, proved to be computationally efficient. The isolated QS model predicted similar trends in control angles for different flight conditions, although there were discrepancies in the magnitude of these angle, an artifact of the reduced aerodynamic model.

2. The ellipsoid was found to closely represent the insect body in shape and the lift and drag prediction from CFD (of the insect body) were found to lie within the measurement range available of ellipsoids from literature. This addition of the ellipsoid for the body model could further reduce the coupling cycles between QS and CFD.

3. Trends in control angles were obtained for different flight speeds and body angles and it was observed that the flapping offset (ϕ_{off}) had the most prominent effect, a consequence of the shifting CG as a function of body angle.

4. A physical understanding of the aerodynamic nature of unsteady lift and drag forces were extracted from the simulated results highlighting the role of the LEV and wake. It was observed that the persistence of the LEV in the down-stroke was key to the lift production over the flapping cycle.

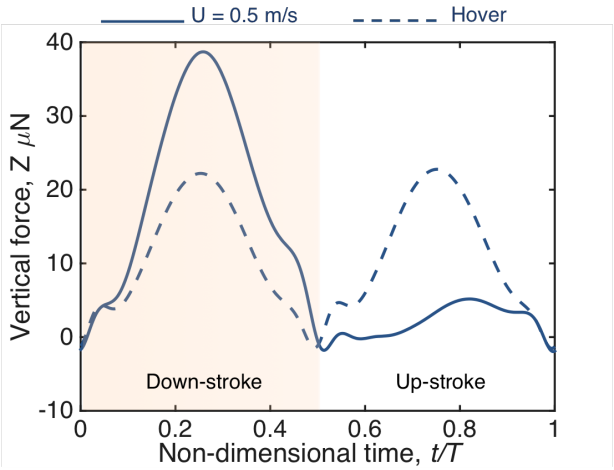

(a) Time dependent vertical forces

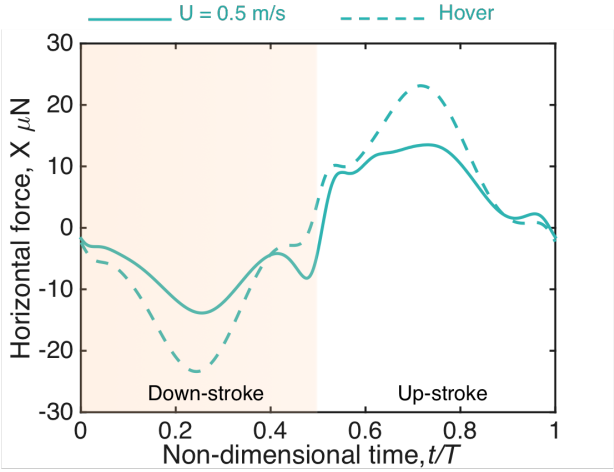

(b) Time dependent horizontal force

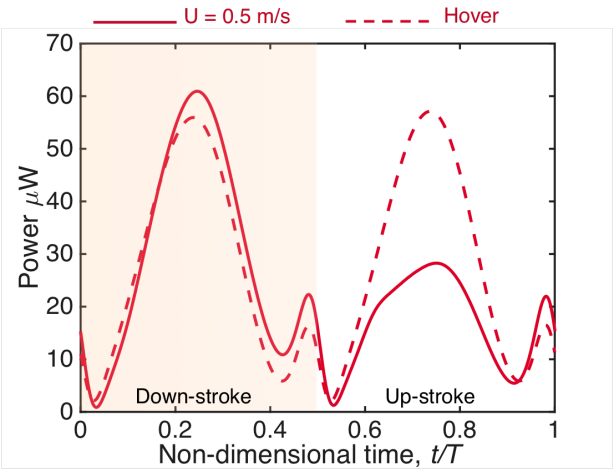

(c) Time dependent powe

Figure C.6: Insect air-loads in steady hover and steady forward flight in body axis system.

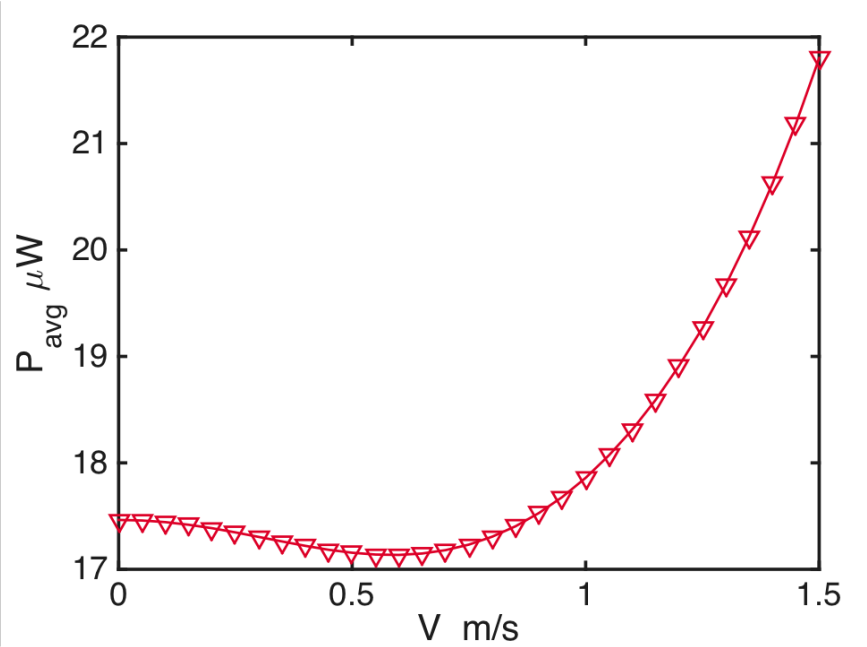

Figure C.7: Averaged power during a flapping cycle obtained from QS analysis.

Appendix D: Q-Criterion

A commonly used flow variable, "Q-Criterion", is detailed in this section. It was developed by Hunt et. al (1988) [78] and has shown to be very useful to identify regions of strong vorticity and highlight vortical structures. The formulation is given below, and it is the second invariant of the velocity gradient tensor.

$$Q = -\frac{1}{2}\frac{\partial u_i}{\partial x_j}\frac{\partial u_j}{\partial x_i} \tag{E.1}$$

$$Q = -\frac{1}{2}\sum_{j=1}^{3}\sum_{i=1}^{3}\bigtriangledown\vec{u}(i,j)\cdot\bigtriangledown\vec{u}(j,i) \tag{E.2}$$

$$\bigtriangledown\vec{u} = \begin{bmatrix} \frac{\partial u}{\partial x} & \frac{\partial u}{\partial y} & \frac{\partial u}{\partial z} \\ \frac{\partial v}{\partial x} & \frac{\partial v}{\partial y} & \frac{\partial v}{\partial z} \\ \frac{\partial w}{\partial x} & \frac{\partial w}{\partial y} & \frac{\partial w}{\partial z} \end{bmatrix} \tag{E.3}$$

$$Q = -\frac{1}{2}\left(\left(\frac{\partial u}{\partial x}\right)^2 + \left(\frac{\partial v}{\partial y}\right)^2 + \left(\frac{\partial w}{\partial z}\right)^2 + 2\frac{\partial u}{\partial y}\frac{\partial v}{\partial x} + 2\frac{\partial u}{\partial z}\frac{\partial w}{\partial x} + 2\frac{\partial v}{\partial z}\frac{\partial w}{\partial y}\right) \tag{E.4}$$

Appendix E: Aerodynamic loads and Wake in Trimmed Forward Flight

This Chapter shows the aerodynamic loads for insect in trimmed level flight with forward speed of 0.3 m/s and 0.5 m/s.

E.1 Steady Level Flight - 0.3 m/s

The first step in trim algorithm is to obtain kinematics variables from the trim algorithm applied to QS model only to initiate the first CFD simulation. The reasons to start the CFD simulation with the kinematics from trimming the insect with QS is to have close educated guess and second to see how far or close QS can predict the insect air-loads. The first kinematic set is: $\phi_{\text{max}} = 45.17^{\circ}$, $\phi_{\text{off}} = 8^{\circ}$ (the averaged wing position moves backward Fig. 1(a)) and $\beta = 13.45^{\circ}$, and with this kinematics we obtain the accurate forces and moments from OVERTURNS, Fig. E.1 shows the time history of the forces, pitch moment and required aerodynamic power. From Fig. E.1(a) it can be seen that the majority of the vertical force is produced during the downstroke, similarly to results observed from experiments [83]. Drag (negative thrust) produced during the downstroke, and positive thrust is produced during the upstroke and it is contributed by the presence of the LEV (wing drag),Fig. E.1(b) . The trim algorithm consider the averaged forces and moments over a flapping cycle, flapping cycle defines as when the insect completes downstroke and upstroke. From the kinematics the y force is negligible along the stroke and thus also the average will be negligible as well; similarly for the roll and yaw moment. By averaging Z, X and M we can see how close the QS model trim variables achieve trim using CFD. The averaged Z force that obtained from the first CFD simulation is $6.6 \cdot 10^{-06} N$ which is 60% of the vertical force needed to balance

the vehicle weight. The averaged X supposed to be very small (magnitude order of 10^{-8} which is two order magnitude less than the typical produced forces),but from the first CFD X is approximately $5 \cdot 10^{-7} N$. In equilibrium the total pitching moment is supposed to be small (magnitude order $10^{(}-10)$), the computed averaged pitch moment from the CFD simulation is $-2.2 \cdot 10^{-9} Nm$. From these results, conclusion can be made that the trim variable from QS only are far from being trim variables in 3D CFD simulations. This discrepancy is expected for two reasons: 1) QS does not include the unsteady flow features especially during reversal. The comparison between CFD and QS time history forces in the chord-wise, span-wise and normal direction (wing frame), and the difference during the stroke reversal (pronation and supposition) is clear. 2) The used QS model is based on experiments conducted at hover conditions, that might explain the difference between the CFD and QS during the translational portions, although the trend of the QS predicted forces at the translational portion is similar to the CFD.

Two observations can be made here: There is positive correlation between stroke plane angle and forward speed, β increase with increasing the forward speed. For hover, the flapping stroke is almost horizontal and for forward speed the stroke plane tilted forward. The stroke angle affects mostly the horizontal force, and it is important for overcoming drag. A positive correlation between the stroke bias angle ϕ_{off} and the forward speed. ϕ_{off} mostly affects the moment balance. The more the insect increase its forward speed, the flapping stroke has bias toward backward. ϕ_{max} mostly affects the vertical force, and the trim requirements are identical for all cases half peak-to-peak stroke amplitude range from 58.7° for hover and 59.5° for $0.3 m/s$ forward speed. The obtained

trim variables for forward speed of 0.3 m/s are: $\phi_{max} = 59.5$, $\phi_{off} = 16.6$ (shifting the rotation point backward), $\beta = 12.8$ (flapping stroke tilts forward).

Shown in Fig. E.1 are the predictions of longitudinal loads and aerodynamic power required at hover as obtained from the quasi-steady model, the initial CFD solution (using wing kinematics from the quasi-steady trim solution) and the final CFD-coupled trim iteration. Figure 7.5(a) shows the time history of vertical force over the wing flap cycle. The most prominent feature of this plot is that the *force* predictions for the quasi-steady model and final CFD solution are almost identical. The quasi-steady model does not capture the unsteady effects during pronation and supination at the stroke reversal parts of the flap cycle. Thus, even though the trim kinematics are different, the airloads are very similar for the trimmed solutions as obtained using quasi-steady aerodynamics and CFD. If the wing kinematics as obtained from the quasi-steady trim solution are fed to the CFD model, the forces are severely underpredicted (almost 50% difference). Time histories of integrated airloads are not identical between the up-stroke and down-stroke in hover since the kinematics are symmetric.

Figure E.1(b) shows the time history over the flap cycle of the longitudinal propulsive force as predicted using the quasi-steady trim solution, final CFD-coupled trim solution and initial CFD solution. All three predictions show similarities in the locations of peaks and phase. The time-averaged propulsive force is zero. However, the order of magnitude of the transient longitudinal force is similar to that of the vertical force. Thus, the flapping kinematics chosen expend energy in producing this transient longitudinal force that is ultimately dissipated without performing useful work. Figure E.1(c) shows the time history over one flap cycle of body pitching moment. Dur-

ing the down-stroke, the effective center of lift is ahead of the CG as the wing moves forward, resulting in a nose-up pitching moment (negative according to the axes system chosen). During the up-stroke, the pitching moment is positive (nose-down) as the wing moves aft of the CG. Trim solutions obtained from the quasi-steady model and CFD evince very similar pitching moment time histories – both magnitude and phase – with the quasi-steady model having a slight under-prediction.

The time history over one flap cycle of aerodynamic power required to flap the wing is shown in Fig. E.1(d). The key refinement introduced by CFD over the quasi-steady tables is the accurate prediction of viscous and pressure forces resolved over the entire wing surface. Using the "initial CFD" as a reference, it is apparent that for the same kinematics, the quasi-steady model can capture qualitative trends in the power required, but severely under-predicts the magnitudes.

E.1.1 Wake Structure

The features of the flow structure can be observed in CFD simulations, it is important to look at the flow to verify and understand the physical phenomenon behind the obtained airloads and to investigate the vortex structure that corresponded to these loads. Figure E.2 plots the vorticity magnitude for forward speed of 0.5 m/sec at mid-span section over a flap cycle, the LEV during the downstroke is stronger in comparison to the up-stroke LEV. The vorticity contours indicates that the LEV is shed during supination and pronation, while it is able to be maintained stable during the translational portions. To see the vortical structure and the shedding path of the vortex that formed during the flap cycle, isovorticity can be plotted. Fig. E.2 shows the isovorticty with threshold of

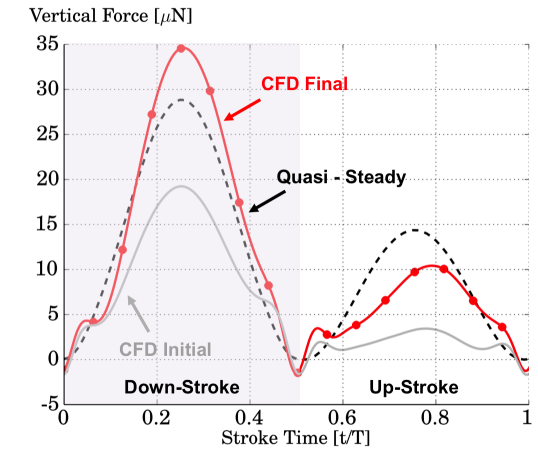

(a) Vertical force

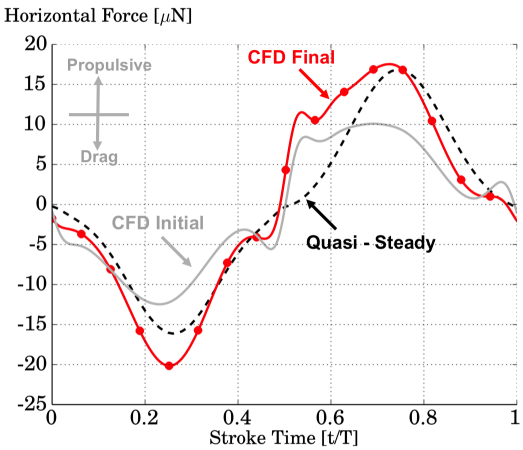

(b) Horizontal force

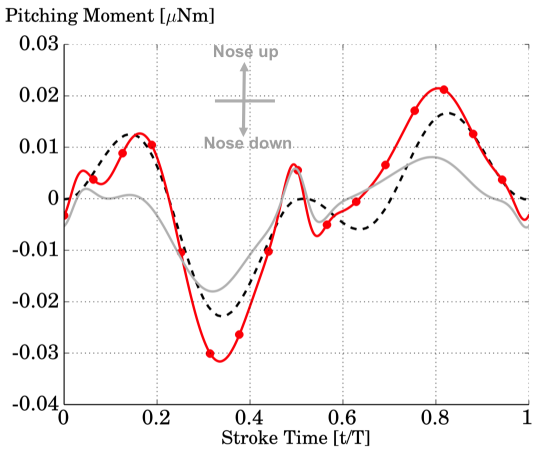

(c) Pitching moment about CG

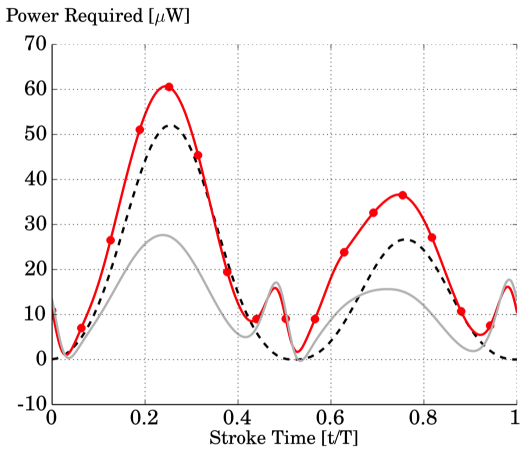

(d) Aerodynamic power required

Figure E.1: Time histories of aerodynamic loads during a flapping cycle in trimmed forward flight at 0.3 m/s: comparison of quasi-steady predictions with initial and final CFD

15 along the flap cycle for forward speed of 0.3 m/s. The stability of the LEV maintained along the span and during the translations periods, where the LEV drawn toward the tip, creating shedding tip vortex. Snapshots at the middle of the upstroke and downstroke ($T^* = 25\%; 75\%$) shows more vorticity at the downstroke relatively to the upstroke. During the upstroke the interaction of the wing with the

E.2 Steady Level Flight - 0.5 m/s

Trim analysis of insect with flapping wings in steady level flight with 0.5 m/s speed was performed. Trim variables and airloads were obtained that satisfy the conditions. Figure E.3(a & b) shows the vertical and propulsive force obtained from quasi-steady analysis, initial CFD case and the final CFD case. The forces obtained from the quasi-steady model were obtained with the following wing trim kinematics: ϕ_{max} is 45.4 degrees, ϕ_{off} is 9.3 degrees (shifted backward) and β is 16.6 degrees (tilted forward). The initial CFD results were obtained with prescribed wing kinematics obtained from the QS trim solution. The convergence process takes 6 coupling iterations, ad the final trim variables are ϕ_{max} is 54.4 degrees, ϕ_{off} is 18 degrees (shifted backward) and β is 22 degrees (tilted forward), which referred as CFD final in the Figure. Fig. E.3(c) shows the time history pitch moment during the flapping cycle. It is important to note the pitch moment curve trends in the downstroke and upstroke are similar. Which is important considering the fact that in CFD the moment is calculated at 3D wing, where in QS is treated as a point force at specific arm length. This similarity in trends contribute to the convergence of the process. Fig. E.3(d) shows the required aerodynamic power, as shown for various forward speeds, more power is required during

the downstroke.

E.2.1 Effect of Weight

Free-flight trim with quasi-steady aerodynamics was performed for various flight conditions, with insect weights set at 80%, 100% and 120% of the baseline value (1.11 mg). Figure E.4 (a)-(d) show, respectively, the variation of the stroke plane tilt, stroke amplitude, phase offset and and average aerodynamic power as a function of cruise velocity in level forward flight.

In forward flight, both wings exhibit identical kinematics. The stroke phase offset, stroke amplitude and stroke plane tilt angle increase monotonically with airspeed. The stroke amplitude, a measure of total thrust produced, increases with airspeed due to increased aerodynamic force requirements to balance both drag and weight, as shown in Fig. E.4(a). While heavier insects require more stroke amplitude at low speeds compared to lighter insects, the differences diminish at high speeds, since most of the wing force requirements are driven by aerodynamic drag. Analysis of the stroke-averaged aerodynamic power required for the 3 cases shows that the heavier insect requires 80% more power at hover compared to the lighter body. As the flight speed increases, the difference in power requirements between the heavy and light cases diminishes to 40% at 1.8 m/s. Beyond 1.8 m/s, the combination of stroke amplitude and stroke phase offset reach the physical limits of wing motion for the chosen wing flap frequency. This condition represents a kinematics-limited flight speed for this insect.

E.2.2 Wake Structure

Figure E.5 show the iso-surface vorticity colored by velocity magnitude during downstroke. By looking at the iso-surface vorticity, wake features can be identified such as: LEV during the translational portions, shed and trailed tip vortex, secondary vortex forming. Figure E.6 shows the vortical structure during the upstroke. Note that the LEV is smaller during the upstroke and the shed trailed vorticity is less intense than the downstroke, which emphasized as well at the supination and the pronation.

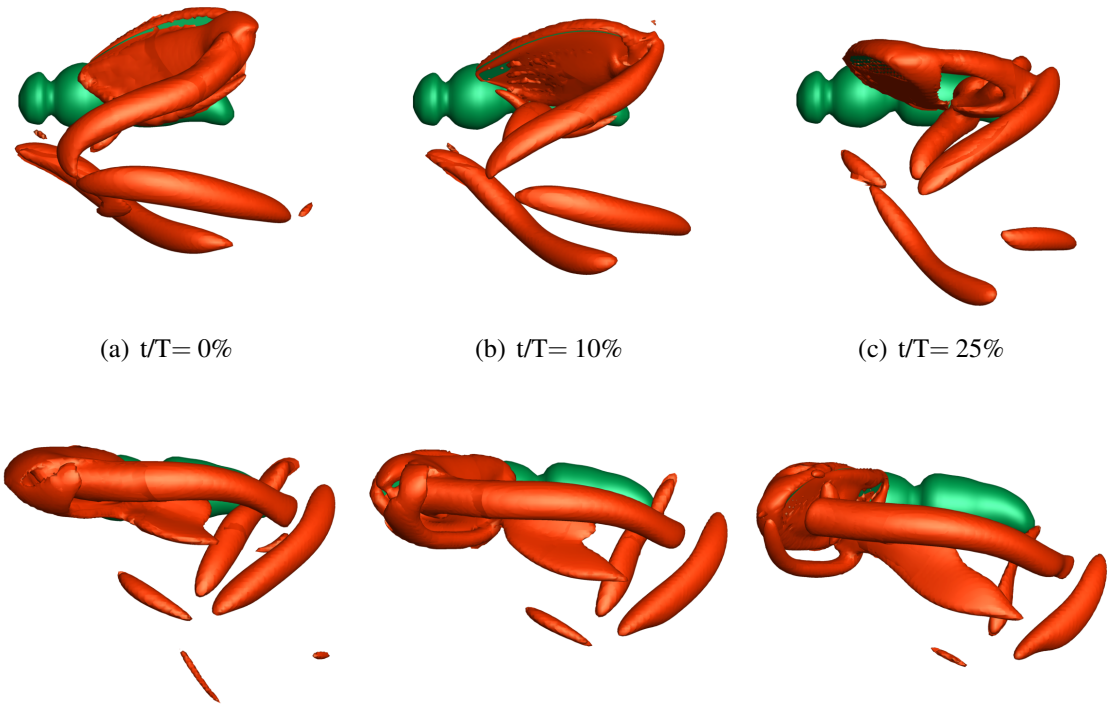

(a) t/T= 0% (b) t/T= 10% (c) t/T= 25%

(d) t/T= 40% (e) t/T= 50% (f) t/T= 60%

(g) t/T= 70% (h) t/T= 80% (i) t/T= 90%

Figure E.2: Vortex iso-surface during flapping stroke at trimmed forward flight of 0.3 m/s

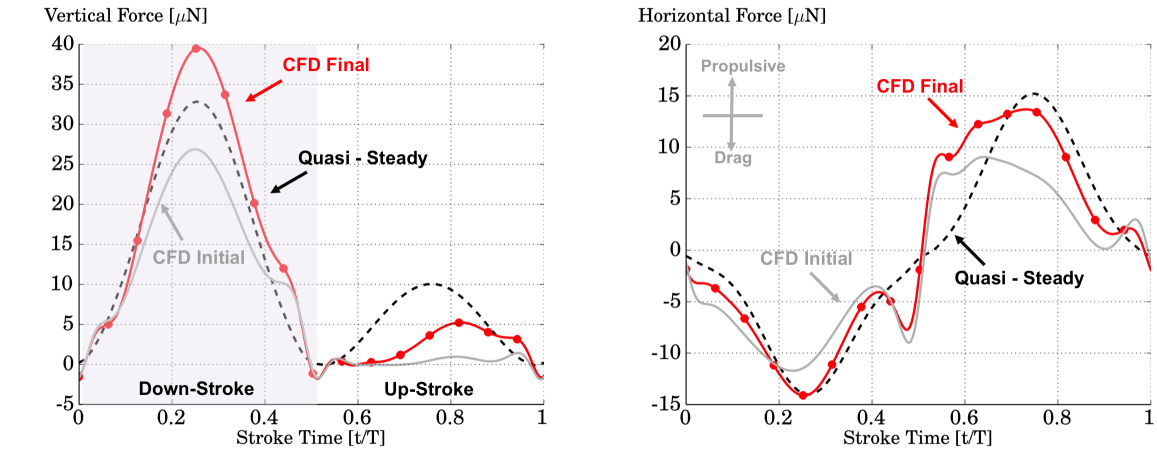

(a) Vertical force

(b) Horizontal force

(c) Pitching moment about CG

(d) Aerodynamic power required

Figure E.3: Time histories of aerodynamic loads during a flapping cycle in trimmed forward flight at 0.3 m/s: comparison of quasi-steady predictions with initial and final CFD

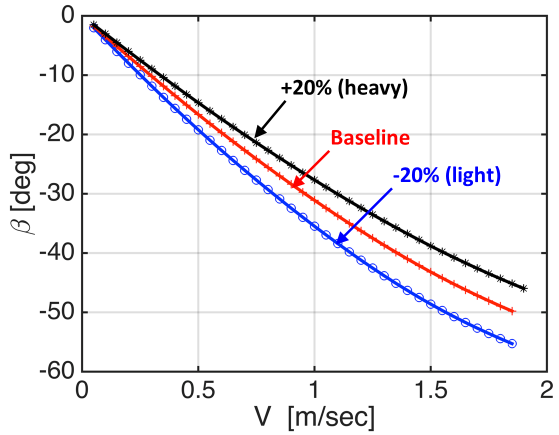

(a) Stroke Plane Tilt Angle β

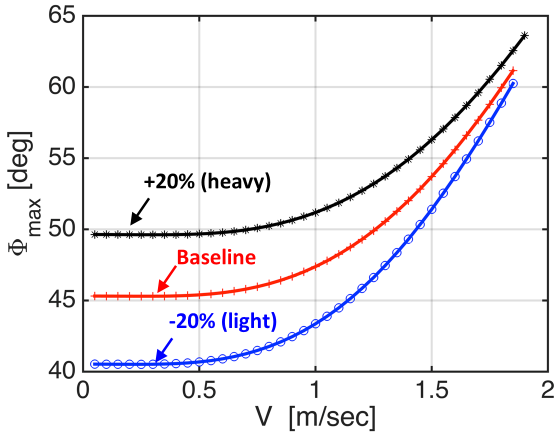

(b) Stroke Amplitude Angle ϕ_{max}

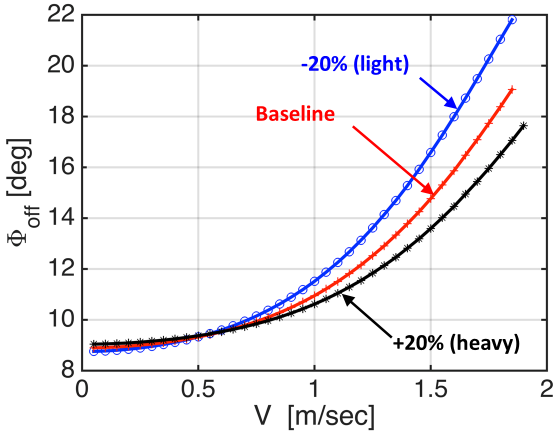

(c) Stroke Phase Offset Angle ϕ_{off}

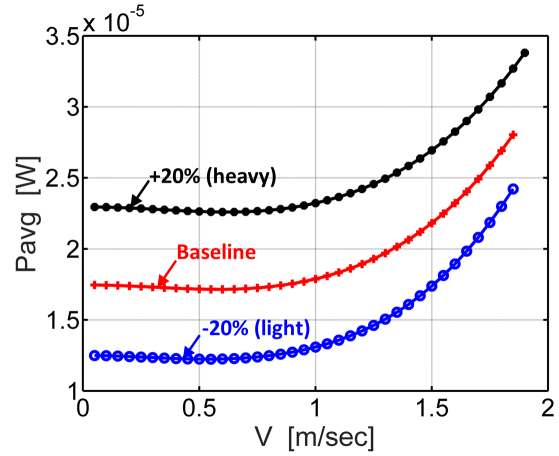

(d) Stroke-averaged Power in Steady Forward Flight

Figure E.4: Effect of Weight on Wing Kinematics and Stroke-averaged Power at Various Airspeeds in Steady Forward Flight

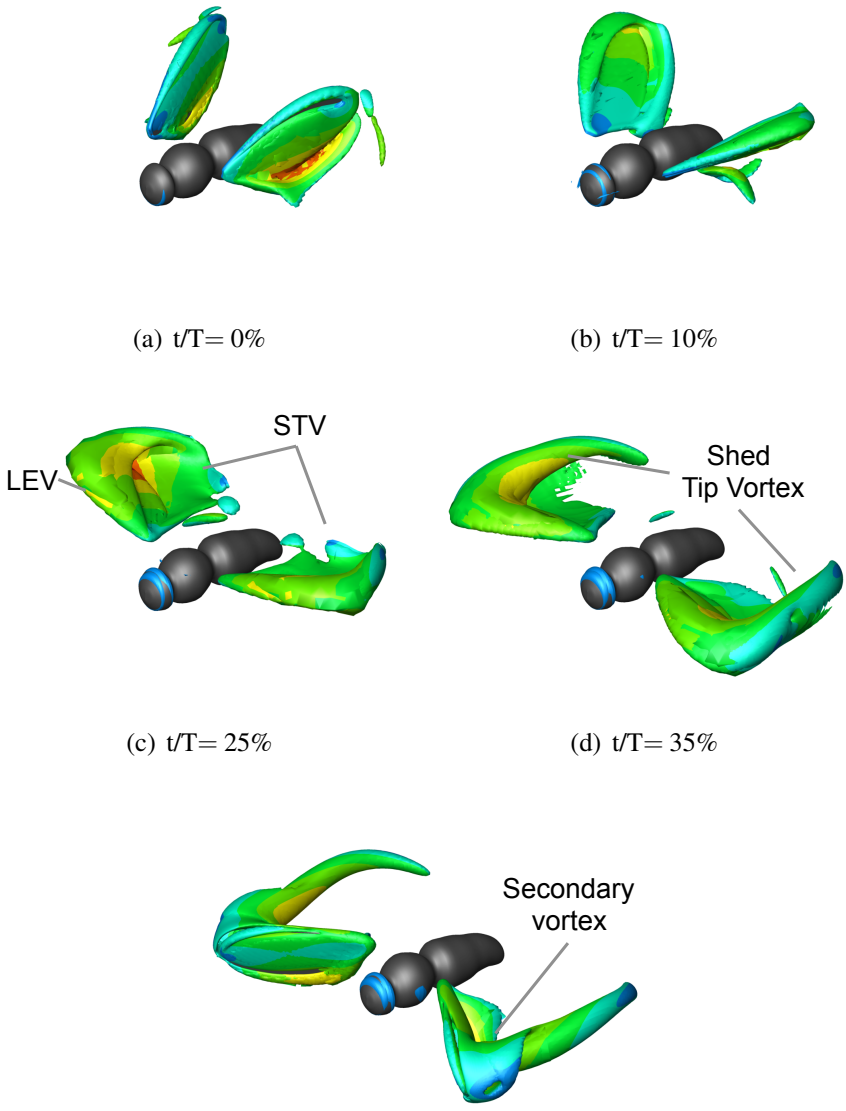

(a) t/T= 0%

(b) t/T= 10%

(c) t/T= 25%

(d) t/T= 35%

(e) t/T= 47%

Figure E.5: Vortex iso-surface colored by the velocity magnitude during flapping stroke at trimmed forward flight of 0.5 m/s, during downstroke.

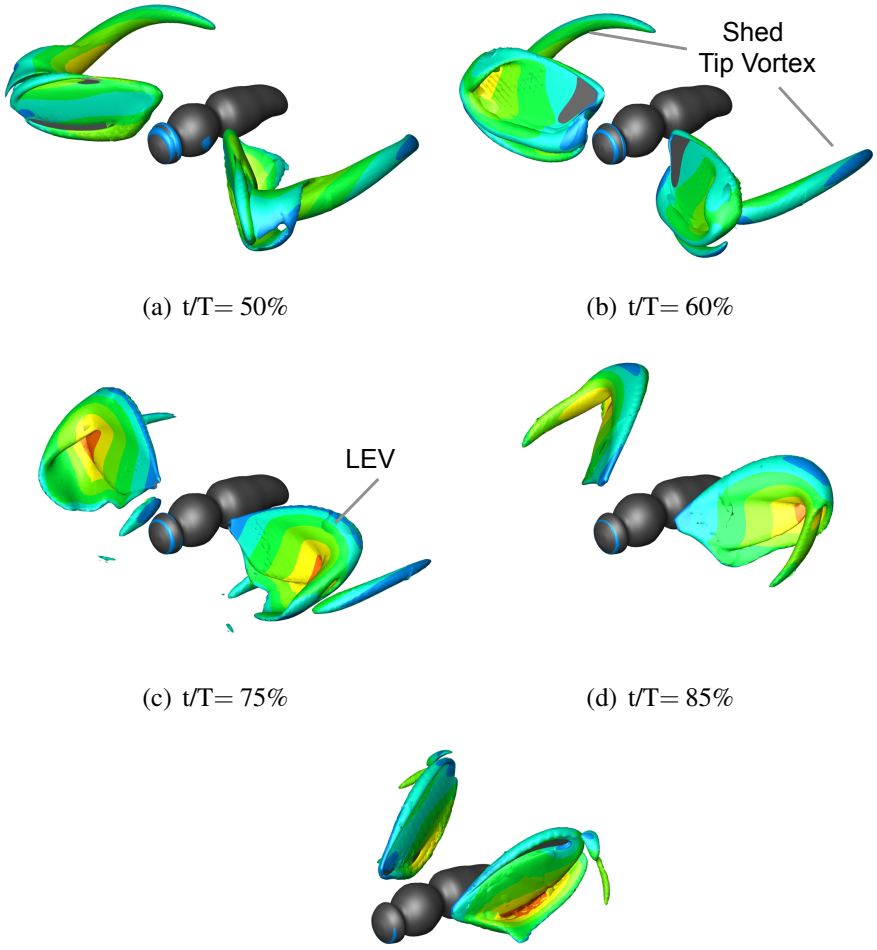

(a) t/T= 50%

(b) t/T= 60%

(c) t/T= 75%

(d) t/T= 85%

(e) t/T= 100%

Figure E.6: Vortex iso-surface colored by the velocity magnitude during flapping stroke at trimmed forward flight of 0.5 m/s, during upstroke.

Bibliography

[1] Pines,D. J. and Bohorquez, F., "Challenges Facing Future Micro-Air-Vehicle Development," *Journal of Aircraft*, Vol. 43, (2), March-April, 2006, pp. 290–305.

[2] Chopra, I., "Rotor-Based Micro Air Vehicles: Challenges & Opportunities," Presentation at First US-Asian Demonstration & Assessment of Micro-Aerial & Unmanned Ground Vehicle Technology, Agra, India, March 10–15, 2008.

[3] McMasters, J. H., and Henderson, M. L, "Low Speed Single Element Airfoil Synthesis," *Technical Soaring*, Vol. 6, (2), 1980, pp. 1–21.

[4] Shyy, W., Lian, Y., Tang, J., Viieru, D. and Liu, H. , *Aerodynamics of Low Reynolds Number Flyers*, Cambridge University Press, New York, USA, 2008.

[5] Dickinson, M. H.,Lehmann, F. H and Sane, S. P., "Wing Rotation and the Aerodynamic Basis of Insect Flight," *Science Journal*, Vol. 305, Jan.,1999, pp. 1954–1960.

[6] Sane S. P , T. and Dickinson M. H, " The Aerodynamic Effects of Wing Rotation and a Revised Quasi-steady Model of Flapping Flight," *The Journal of Experimental Biology*, Vol. 205, 2002, pp. 1087–1096.

[7] Taneda, S., "Experimental Investigation of the Wake Behind a Sphere at Low Reynolds Numbers," *Journal of the Physical Society of Japan*, Vol. 11, (10), 1956, pp. 1104–1108.

[8] Hoerner, S. F. , *Fluid Dynamic Drag*, Hoerner, USA, 1965.

[9] Taira, K. and Colonius, T., "Three-dimensional flows around low-aspect-ratio flat-plate wings at low Reynolds numbers," *Journal of Fluid Mechanics*, Vol. 623, 2009, pp. 187–297.

[10] Kroninger, M. C., Harrington, A., and Munson, M., "The Influence of Streamline Curvature on Low Aspect Ratio Rotating Wings," 45th AIAA Fluid Dynamics Conference, Dallas, TX, 22–26 June, 2015.

[11] Zastawny, M., Mallouppas, G., Zhao, F., and Wachem, B. V., "Derivation of Drag and Lift Force and Torque Coefficients for Non-spherical Particles," *International Journal of Multi Flow*, Vol. 39, 2012, pp. 227–239.

[12] Sun, M., "Insect Flight Dynamics: Stability and Control," *Reviews of Modern Physics*, Vol. 86, (2), 2014, pp. 615.

[13] Johnson, W., "A General Free Wake Geometry Calculation for Wings and Rotors," 51st Annual Forum Proceedings of the American Helicopter Society, Fort Worth, TX, May 9–11, 1995.

[14] Johnson, W., *Helicopter Theory*, Courier Corporation, 2012.

[15] McMichael, J. M. and Francis, Col. M. S., "Micro Air Vehicles Towards a New Dimension in Flight," Technical Report TTO document, USAF, DARPA, July,1996.

[16] Hylton, T., Martin, C., Tun, R. and Castelli, V., "The DARPA Nano Air Vehicle Program ," 50th AIAA Aerospace Sciences Meeting including the New Horizons Forum and Aerospace Exposition, Nashville, TN, Jan., 2010.

[17] "Micro Air Vehicles - Toward a New Dimension in Flight," , 1997.

[18] Grasmeyer, M. J., Keennon, T. M., and Aerovironment Inc, "Development of the Black Widow Micro Air Vehicle," 39th AIAA Aerospace Sciences Meeting and Exhibit, Reno, NV, Jan., 2001.

[19] "Mosquito Micro Unmanned Aerial Vehicle, Israel," , Accessed on July, 11, 2016.

[20] Grasmeyer, M. J., Keennon, T. M., and Aerovironment Inc, "Design and Development of a Quad Shrouded-Rotor Micro Air Vehicle," American Helicopter Society 65_{th} Annual Forum, Grapevine, Texas, 2009.

[21] Prinz, I., "The Mesicopter: A Meso-Scale Flight Vehicle," , Accessed on July, 14, 2016.

[22] Grasmeyer, M. J., Keennon, T. M., and Aerovironment Inc, "Fundamental Understanding of the Cycloidal-Rotor Concept for Micro Air Vehicle Applications," Ph.D Thesis, University of Maryland, College Park, 2010.

[23] "Controlled Flight of a Robotic Insect," , Accessed on July, 2016.

[24] Shyy, W., Kang, C.-k., Chirarattananon, P., Ravi, S., and Liu, H., "Aerodynamics, Sensing and Control of Insect-Scale Flapping-Wing Flight," Proc. R. Soc. A, Vol. 472, 2016.

[25] Brodsky, K., A., *The Evolution of Insect Flight*, Oxford University Press, New York, NY, 1994.

[26] Ellington, C. P., "The Aerodynamics of Hovering Insect Flight," *Philosophical Transactions of the Royal Society of London. Series B, Biological Science*, Vol. 305, (1122), Feb., 1984, pp. 1–181.

[27] Ellington, C. P., van den Berg, C., Willmott, A. P., and Thomas, A. L. R., "Leading-Edge Vortices in Insect Flight," *Nature*, Vol. 384, Dec., 1996, pp. 626–630.

[28] Dickinson, M. H, and Gotz, K. G., "Unsteady Aerodynamic Performance of Model Wings at Low Reynolds Numbers," *The Journal of Experimental Biology*, Vol. 174, Jan.,1993, pp. 45–64.

[29] Sane S. P , T. and Dickinson M. H, "The Control of Flight Force by a Flapping Wing: Lift and Drag Production," *The Journal of Experimental Biology*, Vol. 204, 2001, pp. 2607–2626.

[30] Birch, J. M., and Dickinson, M. H., "Spanwise Flow and the Attachment of the Leading-Edge Vortex on Insect Wings," *Nature Journal*, Vol. 412, 2001, pp. 729–733.

[31] Willmott, A. P. and Ellington, C. P., "The Mechanics of Flight in the Hawkmoth Manduca sexta. I. Kinematics of Hovering and Forward Flight," *The Journal of Experimental Biology*, Vol. 200, 1997, pp. 2705–2722.

[32] Usherwood, J. R. and Ellington, C. P., "The Aerodynamics of Revolving Wings I. Model Hawkmoth Wings," *Journal of Experimental Biology*, Vol. 205, 2002, pp. 1547–1564.

[33] Liu, H. and Kawachi, K., "A Numerical Study of Insect Flight," *Journal of Computational Physics*, Vol. 2146, March, 2003, pp. 2257–2272.

[34] Ansari, A. S., Phillips, N., Stabler, G., Wilkins, C. P., Zbikowski, R., "Experimental Investigation of Some Aspects of Insect-like Flapping Flight Aerodynamics for Application to Micro Air Vehicles," *Experiments in Fluids*, Vol. 46, (5), 2009, pp. 777–798.

[35] Bennett L., "Insect Flight: Lift and Rate of Change of Incidence," *Science*, Vol. 167, 1970, pp. 177–179.

[36] Kramer, M., "Die Zunahme des Maximalauftriebes von Tragfluglen bei plotzlicher Anstellwinkelvergrosserung (Boeneffect)," *Zeitschrift fur Flugtechnik und Motorluftschiffahrt*, Vol. 23, (7), 1932, pp. 185–189.

[37] Sun, T. and Tang, J., "Unsteady Aerodynamic Force Generation by a Model Fruit Fly Wing in Flapping Motion," *The Journal of Experimental Biology*, Vol. 205, Jan., 2002, pp. 55–70.

[38] Birch, J. M., and Dickinson, M. H., "The Influence of Wing Wake Interactions on the Production of Aerodynamic Forces in Flapping Flight," *The Journal of Experimental Biology*, Vol. 206, 1998, pp. 124–156.

[39] Wang, Z. J.,Birch, J. M., and Dickinson, M. H., "Unsteady Forces and Flows in Low Reynolds Number Hovering Flight: Two-Dimensional Computations vs Robotic Experiments," *Journal of Experimental Biology*, Vol. 207, 2007, pp. 449–460.

[40] Tang, J.,Viieru, D., and Shyy, W., "Effects of Reynolds Number and Flapping Kinematics on Hovering Aerodynamics," *AIAA Journal*, Vol. 46, (4), 2008, pp. 967–976.

[41] Weis-Fogh, T., "Quick Estimates of Flight Fitness in Hovering Animals, Including Novel Mechanisms For Lift Production," *Journal of Experimental Biology*, Vol. 59, 1973, pp. 169–230.

[42] Maxworthy, T., "Experiments on the Weis-Fogh Mechanism of Lift Generation by Insects in Hovering Flight .1.Dynamics of the Fling," *Journal of Fluid Mechanics*, Vol. 93, (01), 1979, pp. 47–63.

[43] Somps, C. and Luttges, M., "Dragonfly Flight - Novel Uses of Unsteady Separated Flows." *Science*, Vol. 228, 1985, pp. 1326–1329.

[44] Spedding, G. R. and Maxworthy, T., "The Generation of Circulation and Lift in a Rigid Two-Dimensional Fling," *Journal of Fluid Mechanics*, Vol. 165, 1986, pp. 247–272.

[45] Cooter, R. J. and Baker, P. S., "Weis-Fogh Clap and Fling Mechanism in Locusta," *Nature*, Vol. 269, 1977, pp. 53–54.

[46] Marden, J., "Maximum Lift Production During Takeoff in Flying Animals," *Journal of Experimental Biology*, Vol. 130, 1987, pp. 235–258.

[47] Sunada, S. and Ellington, C. P., "Approximate Added-Mass Method for Estimating Induced Power for Flapping Flight," *AIAA Journal*, Vol. 38, 2000, pp. 1313–1321.

[48] Katz, J., and Plotkin, A. , *Low-Speed Aerodynamics*, Cambridge University Press, Cambridge, UK, 2002.

[49] Lehmann, F. O., "The Mechanisms of Lift Enhancement in Insect Flight," *Naturwissenschaften*, Vol. 91, (3), 2004, pp. 101–122.

[50] Singh, B. and Chopra, I., "Insect-Based Hover-Capable Flapping Wings for Micro Air Vehicles: Experiments and Analysis," *AIAA Journal*, Vol. 46, (9), 2008, pp. 2115–2135.

[51] David, C. T., "The Relationship Between Body Angle and Flight Speed in Free-Flying Drosophila," *Physiol. Entomol.*, Vol. 13, 1978, pp. 191–195.

[52] Dickson, W. B. and Dickinson, M. H., "The Effect of Advance Ratio on the Aerodynamics of Revolving Wings," *The Journal of Experimental Biology*, Vol. 207, 2004, pp. 4269–4281.

[53] Nagai,H., Isogai, K. , Fujimoto, T. and Hayase, T., "Experimental and Numerical Study of Forward Flight Aerodynamics of Insect Flapping Wing," *AIAA Journal*, Vol. 47, (3), 2009, pp. 730–742.

[54] Weis-Fogh, T., "Energetic of Hovering Flight in Hummingbirds and in Drosophila," *Journal of Experimental Biology*, Vol. 56, 1972, pp. 79–104.

[55] Rayner, J. M. V., "A New Approach to Animal Flight Mechanics," *Journal of Experimental Biology*, Vol. 80, 1979a, pp. 17–54.

[56] Rayner, J. M. V., "A Vortex Theory of Animal Flight. Part 1. The Vortex Wake of a Hovering Animal," *Journal of Fluid Mechanics*, Vol. 91, 1979b, pp. 697–730.

[57] Weis-Fogh, T. and Jensen, M., "Biology and Physics of Locust Flight. I. Basic Principles in Insect Flight. A critical Review," *Philosophical Transactions of the Royal Society of London*, Vol. Series B 239, 1956, pp. 415–418.

[58] Ramamurti, R. and Sandberg, W, "Simulation of Flow about Flapping Airfoils using Finite Element Incompressible Flow Solver," *AIAA Journal*, Vol. 39, (2), Feb., 2001, pp. 253–260.

[59] Ramasamy, M., Leishman, J. G., and Lee, T. E., "Flow Field of Rotating Wing MAV," 62nd Annual National Forum Proceedings of the American Helicopter Society, Phoenix, AZ, May 9-11, 2006.

[60] Sun, M. and Xiong, Y., "Dynamic Flight Stability of a Hovering Bumblebee," *The Journal of Experimental Biology*, Vol. 208, (3), 2005, pp. 447–459.

[61] Stanford, B., Beran, P., Snyder, R., and Patil, M., "Stability and Power Optimality in Time-Perodic Flapping Wing Structure," *Journal of Fluids and Structures*, Vol. 38, 2013, pp. 238–254.

[62] Stanford, B., Kurdi, M., Beran, P., and McClung, A., "Shape, Structure, and Kinematic Parameterization of Power-Optimal Wing," *Journal of Aircraft*, Vol. 49, 2012, pp. 1687–1699.

[63] Oppenheimer, M., Doman, and D., Sigthorsson, , "Dynamics and Control of a Biomimetic Vehicle Using Biased Wingbeat Forcing Functions," *Journal of Guidance, Control and Dynamics*, Vol. 34, 2010, pp. 204–217.

[64] Leishman, J. G., *Principles of Helicopter Aerodynamics*, Cambridge University Press, New York, NY, 2006.

[65] Sedov, L. I., Libby, Paul A., " Two-Dimensional Problems in Hydrodynamics and Aerodynamics," *Journal of Applied Mechanics*, Vol. 33, (1), 1950, pp. 237.

[66] Lakshminarayan, V. K., *Computational Investigation of Micro-Scale Coaxial Rotor Aerodynamics in Hover*, Doctor of philosophy, Department of Aerospace Engineering, University of Maryland, College Park, MD, 2009.

[67] Amiraux, M., *Numerical Simulation and Validation of Helicopter Blade-Vortex Interaction Using Coupled CFD/CSD and The Levels of Aerodynamic Modeling*, Doctor of philosophy, Department of Aerospace Engineering, University of Maryland, College Park, MD, 2014.

[68] Malhan, R. P., *Investigation of Aerodynamics of Flapping Wings for Micro Air Vehicle Applications*, Doctor of philosophy, Department of Aerospace Engineering, University of Maryland, College Park, MD, 2013.

[69] White, F. M., *Viscous Fluid Flow*, McGraw-Hill, 1991.

[70] Koren, B., , "Upwind Schemes, Multigrid and Defect Correction for the Steady Navier-Stokes Equations," The 11th International Conference on Numerical Methods in Fluid Dynamics, Willansburg, VA, June 1988.

[71] Ghosh, D., Medida, S. and Baeder, J. D., "Compact-Reconstruction Weighted Essentially Non-Oscillatory Schemes for Unsteady Navier-Stokes Equations," 42nd AIAA Fluid Dynamics Conference and Exhibit, New Orleans, LA, June 25-28, 2012.

[72] Roe, P., "Approximate Riemann Solvers, Parameter Vectors and Difference Schemes," *Journal of Computational Physics*, Vol. 135, (2), August 1997, pp. 250–258.

[73] Turkel, E., "Preconditioning Techniques for Solving the Incompressible and Low Speed Compressible Equations," *Journal of Computational Physics*, Vol. 72, (2), October 1987, pp. 277–298.

[74] Turkel, E., "Preconditioning Techniques in Computational Fluid Dynamics," *Annual Review of Fluid Mechanics*, Vol. 31, January 1999, pp. 385–416.

[75] "UMD High Performance Computing, Deepthought2," , Accessed on Sep., 2016.

[76] Johnson, T. A., and Patel, V. C., "Flow Past a Sphere up to a Reynolds Number of 300," *Journal of Fluid Mechanics*, Vol. 378, 1999.

[77] "F/T Sensor: Nano17 -ATI Industrial Automation," , Accessed on Sep., 2016.

[78] Hunt, J. C., Wray, A. and Mon, P., "Eddies, stream, and convergence zones in turbulent flows," Technical Report TR 178-1, CTR-S88, 1988.

[79] Faruque, I. and Humbert, J.S., "Dipteran Insect Flight Dynamics. Part 1: Longitudinal Motion About Hover," *The Journal of Theoretical Biology*, Vol. 264, (02), 2010, pp. 538–552.

[80] MacFarlane, K. et al., "Quasi-Steady and Computational Aerodynamics Applied to Hovering *Drosophila* Dynamics," AIAA Applied Aerodynamics Conference, Honolulu, HI, June 27 - 30, 2011.

[81] Tung, C., Cardonna, F.X., and Johnson, W.R., "The Prediction of Transonic Flows on an Advancing Rotor," *Journal of the American Helicopter Society*, Vol. 31, (3), 1986, pp. 4–9.

[82] Datta, A.,Sitaraman, J.,Chopra, I. and Baeder, D. J., "CFD/CSD Prediction of Rotor Vibratory Loads in High-Speed Flight," *Journal of Aircraft*, Vol. 43, (6), 2006, pp. 1698–1709.

[83] Sun, M. and Wu, J. H. , "Aerodynamic Force Generation and Power Requirements in Forward Flight in a Fruit Fly with Modeled Wing Motion," *The Journal of Experimental Biology*, Vol. 206, 2003, pp. 3065–3083.